Excitons in a dilute magnetic semiconductor in the presence of an inhomogeneous magnetic field

Styth, Melissa

Award date:
2014

Awarding institution:
University of Bath

Excitons in a dilute magnetic semiconductor in the presence of an inhomogeneous magnetic field

submitted by

Melissa Styth

for the degree of Doctor of Philosophy

of the

University of Bath

Department of Physics

October 2013

Abstract

Dilute magnetic semiconductors (DMSs) are ideal candidates for spintronic devices as they exhibit both semiconducting and magnetic properties. The defining feature of a DMS material is the exchange interactions between the magnetic ions and the band electrons and holes, which leads to many of the spin behaviours observed. A fundamental property of DMSs is that a relatively small external magnetic field can cause enormous Zeeman splittings of the electronic energy levels, which allows separating of states with different spins. The giant Zeeman effect present in the DMS systems also leads to the possibility of trapping quasiparticles in an inhomogeneous magnetic field.

In this thesis the effect of inhomogeneous magnetic fields on excitons in a DMS quantum well is investigated. We look at the possibility of trapping excitons in hybrid structures composed of a DMS quantum well placed a few nanometres below a nanoscale and microscale ferromagnetic disk and a ferromagnetic strip. Quasiparticles in a DMS quantum well are shown to undergo a splitting between band states for different spin components due to the giant Zeeman interaction. Due to the inhomogeneous magnetic field created by a nanoscale ferromagnetic disk in the vortex state the quasiparticles are found to be confined in a small region on the quantum well. The behaviours of excitons in the presence of both a homogeneous and inhomogeneous magnetic field is then discussed. The binding energy of a heavy hole exciton in a finite DMS quantum well in the presence of a homogeneous is calculated. The study is extended to look at excitons in the presence of an inhomogeneous magnetic field. The behaviour of excitons in the presence of a inhomogeneous magnetic field, is found to depend on the type of magnetic field, and is shown to be different for a magnetic field created by a microscale and nanoscale ferromagnetic disk and a ferromagnetic strip.

Acknowledgements

I would like to thank my supervisor, Dr Simon Crampin, for giving me the opportunity to work in the Condensed Matter Theory group, and providing me assistance, support and guidance. I would also like to thank the staff and students in the Department of Physics for comfortable research environment. Further thanks go to the Leverhulme trust for all their financial support. Finally, I would like to thank my beloved family and friends for all their encouragement over the years.

Contents

Chapter 1

Introduction

The success of semiconductor electronics has been built on the charge degree of freedom, and therefore the key parameter is the charge of the electrons or holes. Integrated circuits operate by controlling the flow of carriers through the semiconductor by applied electric fields, and until recently, the spin of the electron was ignored in mainstream charge based electronics. However, currently there is considerable interest in a new type of spin electronics called spintronics, where not just the electron charge but also the electron spin carries information, and this offers opportunities for a new generation of devices [1][2]. The discovery in 1988 of the giant magnetoresistive effect (GMR) is considered the beginning of this new spin based electronics [3].

Spintronics exploits the intrinsic spin of the electron and its associated magnetic moment, in addition to its fundamental electronic charge. Either adding the spin degree of freedom to conventional charge based electronic devices or using the spin alone has the potential advantages of non volatility, increased data processing speed, decreased electric power consumption, and increased integration densities compared with conventional semiconductor devices [1]. Traditional approaches to using spin are based on the alignment of a spin (either up or down) relative to a reference (an applied magnetic field or magnetisation orientation). Device operations then proceed with some quantity (e.g electrical current) that depends in a predictable way on the degree of alignment. There are two directions for semiconductor spintronics; one is semiconductor magneto electronics, where the magnetisation direction is important, and the other is quantum information technology based on the spin degree of freedom in semiconductors [4].

A valuable testing ground for spintronics, for various theoretical ideas and device applications, comes from dilute magnetic semiconductors (DMSs), which simultaneously exhibit both semiconducting and ferromagnetic properties [5][6]. DMSs are created by dilute doping of magnetic ions (usually a few percent, and usually transition metals) into the semiconductor, giving rise to localised magnetic moments in the semiconductor [7][8]. In physics, quasiparticles are characterised as that of a single particle in a system, including the effect the particle has on the system. It can be roughly defined as the combination of a particle and its influence on the local environment. The most well known quasiparticles are the electron, hole and exciton quasiparticle. Due to the giant Zeeman interaction in a DMS, an inhomogeneous magnetic field produced by a nanoscale/microscale ferromagnetic disk can act as an effective potential that can trap quasiparticles in the quantum well.

This thesis looks at $Cd_{1-x}Mn_xTe$ DMS quantum wells, as an interesting system for studying excitons in a DMS quantum well in the presence of an inhomogeneous magnetic

field. Chapters 2, 3, 4 and 5 cover the main results of this work. Chapter 2 looks at the bandstructure of the conduction and valence band in a semiconductor within the framework of $\vec{k} \cdot \vec{p}$ theory which forms the framework for later work. Two models within this theory will be discussed, namely the Kane and Luttinger Kohn model. Chapter 3 looks at the splitting between band states for different spin components of quasiparticles in a DMS quantum well placed a few nanometres below a nanoscale ferromagnetic disk in the vortex state. The magnetic field profile for a single vortex from this ferromagnetic disk is also discussed. Chapter 4 and 5 looks at the behaviours of excitons in these systems, in the presence of both a homogeneous and inhomogeneous magnetic field. Chapter 6 concludes the work with an overview of the findings, and an outlook for the future of research in this area. In all chapters lengthy derivations are demoted to appendices.

1.1 Dilute magnetic semiconductors

As mentioned previously DMSs are non magnetic semiconductors doped with a few percent of magnetic elements, usually transition metals, which produce localised magnetic moments in the semiconductor, Figure (1-1). These magnetic moments usually originate from the 3d or 4f shells of the transition metals. The presence of such ions randomly distributed in the host lattice gives rise to two kinds of interactions, firstly the sp-d (sp-f) exchange interaction between the localised d (f) electrons of the magnetic ions and the delocalised electrons (s orbital like) and holes (p orbital like). Secondly is the d-d (f-f) interaction between the ions themselves. When a semiconductor contains localised magnetic moments, its band structure will be modified by the exchange interaction of these moments with the band electrons. DMSs exhibit a variety of effects via these spin exchange interactions that are not present in nonmagnetic semiconductors [7].

1.1.1 Properties of $Cd_{1-x}Mn_xTe$

In their crystal structure, as well as mechanical, optical and electrical properties, DMSs are qualitatively similar to their non magnetic parent compounds. Hence the crystal structure of $Cd_{1-x}Mn_xTe$, in which a fraction x of the Cd atoms are substituted by Mn^{2+}, resembles that of CdTe. Similar to CdTe, $Cd_{1-x}Mn_xTe$ crystallises in the zincblende structure, and is a direct gap semiconductor with the band extrema at the Γ point, Figure (1-2). There is a limit to the concentration of magnetic ions that can be incorporated into the compound without the resulting alloy changing its crystal structure to a form other than zincblende. For $Cd_{1-x}Mn_xTe$ values of x less than 0.77 respectively are necessary to ensure a zincblende structure [7]. $Cd_{1-x}Mn_xTe$ is one of the most intensively studied of the $A^{II}_{1-x}Mn_xB^{VI}$ type DMSs. These $A^{II}_{1-x}Mn_xB^{VI}$ type DMSs are interesting subjects of spintronics for the three following reasons. Firstly, the parameters which determine the band structure of the material such as the energy gap, and the lattice parameter can be varied by appropriately changing the Mn concentration x in the crystal. With increasing x the energy gap E_g increases, to the point that the originally opaque material eventually becomes transparent to the visible. This variation is given by

$$\begin{aligned} E_g(300\text{K}) &= (1.528 + 1.316x)\ \text{eV}, \\ E_g(4.2\text{K}) &= (1.606 + 1.592x)\ \text{eV}, \end{aligned} \tag{1.1}$$

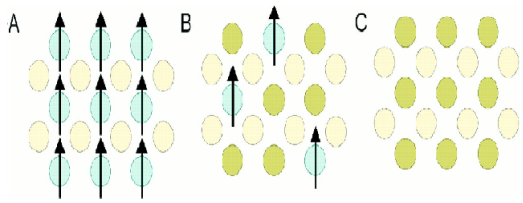

Figure 1-1: Three types of semiconductors: (a) a magnetic semiconductor with a periodic array of magnetic elements; (b) a dilute magnetic semiconductor containing a fraction of magnetic ions; (c) a nonmagnetic semiconductor which contains no magnetic ions. Adapted from from Ref. [9].

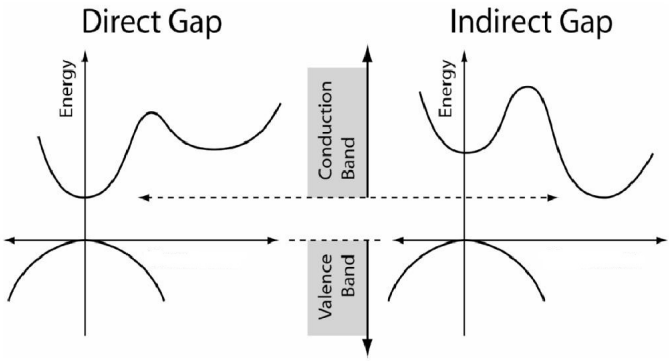

Figure 1-2: Schematic diagram showing the difference between a direct and indirect bandgap semiconductor.

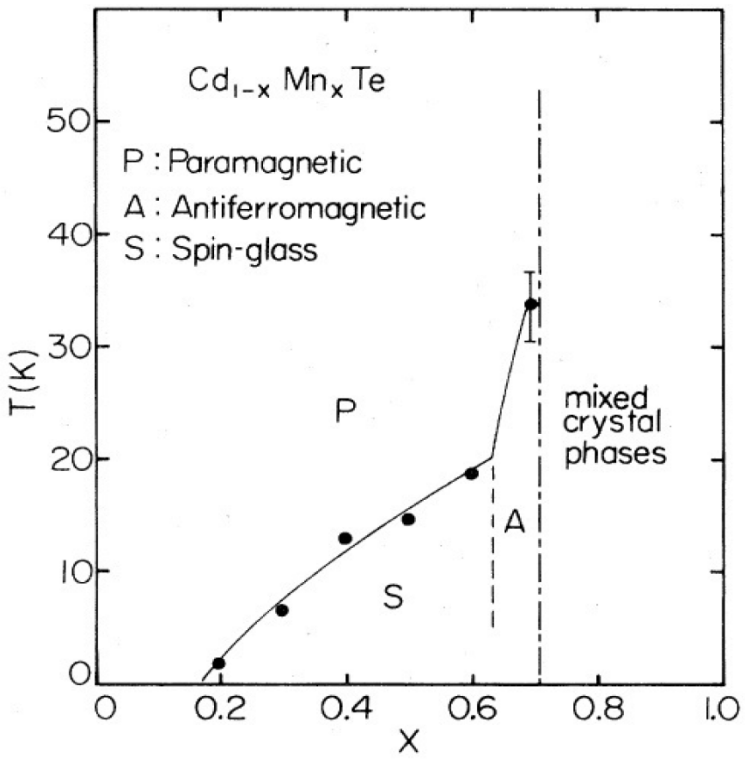

Figure 1-3: Phase diagram for $Cd_{1-x}Mn_xTe$ showing the paramagnetic, spin glass and antiferromagnetic phase. Taken from Ref. [10].

for $x < 0.77$ [7]. The lattice parameter of $Cd_{1-x}Mn_xTe$ obeys Vegard's law [11] and is given by

$$a_0 = (1-x)a_{\mathrm{CdTe}} + xa_{\mathrm{MnTe}}, \tag{1.2}$$

where $a_{\mathrm{CdTe}} = 6.4810$ Å and $a_{\mathrm{MnTe}} = 6.338$ Å are the lattice parameters of CdTe and the hypothetical zincblende MnTe [7][12][13]. The lattice parameter decreases linearly with increasing Mn^{2+} content. Secondly, the magnetic properties of these DMSs include paramagnetic, spin glass and antiferromagnetic behaviour, depending upon the magnetic ion concentration and temperature. Thirdly is the exchange interaction between the localised magnetic moments of the Mn^{2+} ions and the conduction and valence band electrons which results in a series of features which are unique to DMS, most importantly of which is the giant spin splittings of the electronic states which will be discussed below [7].

1.1.2 Magnetic Properties of $Cd_{1-x}Mn_xTe$

As already mentioned, depending on the magnetic ion concentration and temperature $Cd_{1-x}Mn_xTe$ can have a paramagnetic, antiferromagnetic, or spin glass magnetic phase as shown in Figure (1-3) [14][10][15]. The regions marked P, S, and A can be loosely identified as paramagnetic, spin glass, and antiferromagnetic regions. For small values of x the system behaves in the paramagnetic fashion, and the Mn^{2+} spins can be regarded as isolated and independent from one another. In the paramagnetic state this magnetisation is related to the manganese concentration and to the average value of the manganese spin component $\langle S_z \rangle$ as [7]

$$M(x,B,T) = -g_{Mn}\mu_B N_0 x \langle S_z \rangle, \tag{1.3}$$

where $g_{Mn} = 2$ is the magnetic ion Mn^{2+} g factor, μ_B is the Bohr magneton, and N_0 is the number of unit cells per unit volume. When the concentration of the Mn^{2+} ions is small $\langle S_z \rangle$ may be expressed by the standard Brillouin function as [10]

$$\langle S_z \rangle = JB_J\left(\frac{Jg_{Mn}\mu_B B_z}{k_B T}\right), \tag{1.4}$$

where $J = 5/2$ is the total angular momentum of the Mn^{2+} ions, k_B is the Boltzmann constant, T is the temperature, B_z is the magnetic field, and the Brillouin function

$$B_J(x) = \frac{2J+1}{2J}\coth\left(\frac{2J+1}{2J}x\right) - \frac{1}{2J}\coth\left(\frac{1}{2J}x\right). \tag{1.5}$$

As x is increased, the antiferromagnetic interactions between the magnetic ions become important and the magnetisation M is no longer described by the standard Brillouin function. The magnetic ion concentration x and temperature T need to be replaced by effective values x_{eff} and T_{eff}, and the magnetisation then becomes [7]

$$M(x,B,T) = g_{Mn}\mu_B N_0 x_{eff} JB_J\left(\frac{Jg_{Mn}\mu_B B_z}{k_B T_{eff}}\right), \tag{1.6}$$

where x_{eff} and T_{eff} are phenomenological fitting parameters. The Mn^{2+} distribution can be isolated atoms (singlets), pairs, triplets and larger clusters. The number of different

types of clusters depends on the Mn^{2+} concentration. The effective manganese concentration is the concentration of magnetic ions that remain in (unpaired) spin singlet states, defined as

$$x_{eff} = \frac{\text{number of singlet states}}{\text{total number of cations}}. \tag{1.7}$$

For higher values of x and lower temperatures, DMSs pass from the paramagnetic region into a new phase, called the spin glass state. The spin glass behaviour, attributed to the frustration of the antiferromagnetic interactions between the Mn^{2+} ions, arises from the lattice topology of the $A^{II}_{1-x}Mn_xB^{VI}$ alloys. The spin glass state becomes possible when the magnetic ion concentration exceeds a percolation threshold of $x \cong 0.19$, for a dilute magnetic with nearest neighbour interactions only. However the spin glass phase can form for arbitrarily small x at sufficiently low temperatures. For $Cd_{1-x}Mn_xTe$ with $x > 0.65$, there is a long range (antiferromagnetic) ordered phase.

1.1.3 The sp-d exchange interaction

A critical distinguishing characteristic of a DMS is the sp-d exchange interaction. Therefore, confirmation of the sp-d exchange interaction is essential in judging whether or not the synthesised material is a DMS. The strong spin dependent coupling of the effective mass carriers to the localised d electrons of the magnetic ions was first discovered in $Cd_{1-x}Mn_xTe$ [16] and $Hg_{1-x}Mn_xTe$ [17].

If localised Mn^{2+} magnetic ions are incorporated into the semiconductor, the band structure is significantly influenced by the sp-d exchange coupling. The sp-d exchange contribution to the band structure can be expressed by an additional Kondo like exchange term [7][18]

$$\mathcal{H}_{sp-d} = \sum_{\vec{R}_i} [\hat{J}_{sp-d}(\vec{r} - \vec{R}_i)] \vec{S}_i \cdot \vec{\sigma}, \tag{1.8}$$

where $\vec{S}_i$ is the total spin operator of the magnetic ion at $\vec{R}_i$, $\vec{\sigma}$ is the spin operator of an electron at position $\vec{r}$, and $\hat{J}_{sp-d}(\vec{r} - \vec{R}_i)$ is an appropriate exchange constant that designates the exchange interaction coupling integral for the sp-d exchange. The summation is over all lattice sites occupied by the Mn^{2+} ions.

To simplify $\mathcal{H}_{sp-d}$ the following two approximations can be made. Firstly, since the electron wavefunction is greatly extended the electrons interact with a large number of magnetic ions, and so the molecular field approximation, which replaces $\vec{S}_i$ by the thermal average $\langle S_z \rangle$ taken over all Mn^{2+} ions, can be used. Secondly, since the electronic wavefunction spans a large number of lattice sites, the term $\hat{J}_{sp-d}(\vec{r} - \vec{R}_i)$ is replaced by $x\hat{J}_{sp-d}(\vec{r} - \vec{R})$. The summation is carried out over all sites of the sub lattice denoted by $\vec{R}$, but weighted with the Mn^{2+} ion content x. The resulting Hamiltonian

$$\mathcal{H}_{sp-d} = \langle S_z \rangle \, \sigma_z x \sum_{\vec{R}} [\hat{J}_{sp-d}(\vec{r} - \vec{R})] \tag{1.9}$$

then has the periodicity of the lattice, which allows the use of the same wavefunctions as the non magnetic crystal lattice Hamiltonian, and can thus be incorporated into the total Hamiltonian of the semiconductor [7][18]. The modifications of the band structure from the sp-d exchange interaction is determined by the values of the exchange constant $\hat{J}_{sp-d}$. If the magnetic field is zero then $\langle S_z \rangle = 0$ and the material behaves like a typical nonmagnetic semiconductor.

The main effect of the sp-d exchange interaction is the modification of the band structure in the presence of an external magnetic field. This sp-d exchange interaction leads to a splitting between band states for different spin components. When a magnetic field is applied to a semiconductor, the energy of the electrons and holes with their spin magnetic moments parallel to the field is lowered, and the energy of those with spin magnetic moments antiparallel to the field is raised. The difference in energy between opposite spin polarisations is known as the Zeeman splitting. Thus in addition to the regular Zeeman coupling present in nonmagnetic semiconductors, the electrons and holes feel a large magnetisation from the magnetic ions. This results in a Zeeman splitting that can be hundreds of times larger than that in non magnetic semiconductors [7].

In order to understand the effects involving the sp-d exchange it is sufficient to only consider how the exchange affects the top of the valence band (p-like) and the bottom of the conduction band (s-like). The exchange Hamiltonian can be written as two separate terms for the conduction and valence band respectively as

$$\mathcal{H}_{s,p-d} = \mathcal{H}_{s-d} + \mathcal{H}_{p-d}. \tag{1.10}$$

Using the appropriate basis (which will be discussed in the next Chapter), the exchange Hamiltonian for the conduction band can then be written as [7]

$$\mathcal{H}_{s-d} = \begin{pmatrix} 3A & 0 \\ 0 & -3A \end{pmatrix}, \tag{1.11}$$

where the exchange interaction results in a splitting of $\pm 3A$, independent of the orientation of the external magnetic field. In the valence band the exchange splitting depends on the orientation of the external magnetic field. For a magnetic field in the z direction the exchange Hamiltonian for the valence band is [7]

$$\mathcal{H}_{p-d} = \begin{pmatrix} 3B & 0 & 0 & 0 \\ 0 & B & 0 & 0 \\ 0 & 0 & -B & 0 \\ 0 & 0 & 0 & -3B \end{pmatrix}, \tag{1.12}$$

where there is a splitting of $\pm 3B$ and $\pm B$ for the heavy and light hole respectively [19]. The corresponding result for a magnetic field in the xy plane may be found in Ref. [20]. Here A and B are given by

$$A = \frac{1}{6} N_0 \alpha x_{eff} \langle S_z \rangle , \tag{1.13}$$

$$B = \frac{1}{6} N_0 \beta x_{eff} \langle S_z \rangle , \tag{1.14}$$

where $N_0\alpha$ and $N_0\beta$ are the conduction electron and valence band exchange integrals. For $Cd_{1-x}Mn_xTe$ the values for the exchange integrals are given in Appendix K. The values of α and β are of the same order for all the II-VI compounds containing manganese, and are not sensitive to the magnetic ion concentration. The size of the exchange interaction is influenced by two competing effects. According to the present understanding of the exchange interaction between band carriers and the d electrons of the Mn^{2+} ions, a positive contribution is given by the parallel (ferromagnetic) alignment of the spins, which comes from the Coulomb exchange between the band electrons and the Mn^{2+} d electrons.

The exchange constant α arises almost exclusively from this direct ferromagnetic s-d exchange and is therefore positive. A negative contribution is given by the so called kinetic exchange, originating from the hybridisation of the Mn^{2+} d electrons with the s and p band electrons leading to an antiferromagnetic alignment of the spins of the Mn^{2+} ions and the band electrons. The p-d exchange constant β contains both positive (β_{dir}) and negative (β_{hyb}) contributions, the latter of the two being dominant and connected with the antiferromagnetic p-d hybridisation. Thus, one may write that $\beta = \beta_{dir} + \beta_{hyb}$ with $\beta_{dir} \approx \alpha$.

It is conventional to write the resulting exchange energy Hamiltonian as

$$\mathcal{H}_{s-d} = -N_0 \alpha x_{eff} \langle S_z \rangle S_{e,z}, \tag{1.15}$$

for electrons, and

$$\mathcal{H}_{p-d} = -\frac{1}{3} N_0 \beta x_{eff} \langle S_z \rangle S_{h,z}, \tag{1.16}$$

for holes, where $S_{e,z}$, and $S_{h,z}$ are the spins of the electron ($\pm\frac{1}{2}$) and hole ($\pm\frac{3}{2}$ for heavy holes, and $\pm\frac{1}{2}$ for light holes) [21][22][23]. The Zeeman splitting for the valence band using Eq. (1.16) for one spin component is plotted in Figure (1-4) as a function of the magnetic field for different Mn^{2+} concentrations and temperatures. It can be seen that increasing the Mn^{2+} concentration increases the energy splitting, as does decreasing the temperature.

The solution for the energies of electrons in the conduction band incorporating the s-d exchange of Eq. (1.11), for $\vec{k} \approx 0$, where the band is assumed to be parabolic, is given by

$$\begin{aligned} E_c &= E_g + E_{\text{Landau}}(l) + E_{\text{Zeeman}}(S_{e,z}) + E_{\text{giantZeeman}}(S_{e,z}) \\ &= E_g + \left(l + \frac{1}{2}\right)\hbar\omega_c + S_{e,z}\left(g_e \mu_B B_z - N_0 \alpha x_{eff} \langle S_z \rangle\right), \end{aligned} \tag{1.17}$$

where E_g is the energy gap, $l = 0, 1, 2 \ldots$ is the Landau quantum number, ω_c is the cyclotron frequency, and g_e is the band electron g factor [7]. The Landau ladder $(l+\frac{1}{2})\hbar\omega_c$ originates from the operator $(e/m_0 c)\vec{p}\cdot\vec{A}$. The equivalent term for the valence band is

$$E_v = \left(l + \frac{1}{2}\right)\hbar\omega_c + S_{h,z}\left(g_h \mu_B B_z - \frac{1}{3} N_0 \beta x_{eff} \langle S_z \rangle\right), \tag{1.18}$$

where g_h is the hole g factor. Then Eqs. (1.17) and (1.18) can be rewritten as

$$E_c = E_g + \left(l + \frac{1}{2}\right)\hbar\omega_c + g^e_{eff}\mu_B B_z S_{e,z}, \tag{1.19}$$

$$E_v = \left(l + \frac{1}{2}\right)\hbar\omega_c + g^h_{eff}\mu_B B_z S_{h,z}, \tag{1.20}$$

where $g^{e(h)}_{eff}$ are the effective g factors [7], used to describe Zeeman splittings of the conduction and valence bands and are given by

$$g^e_{eff} = g_e - \frac{N_0 \alpha x_{eff} \langle S_z \rangle}{\mu_B B_z}, \tag{1.21}$$

for electrons, and

$$g^h_{eff} = g_h - \frac{1}{3}\frac{N_0 \beta x_{eff} \langle S_z \rangle}{\mu_B B_z}, \tag{1.22}$$

for holes [7].

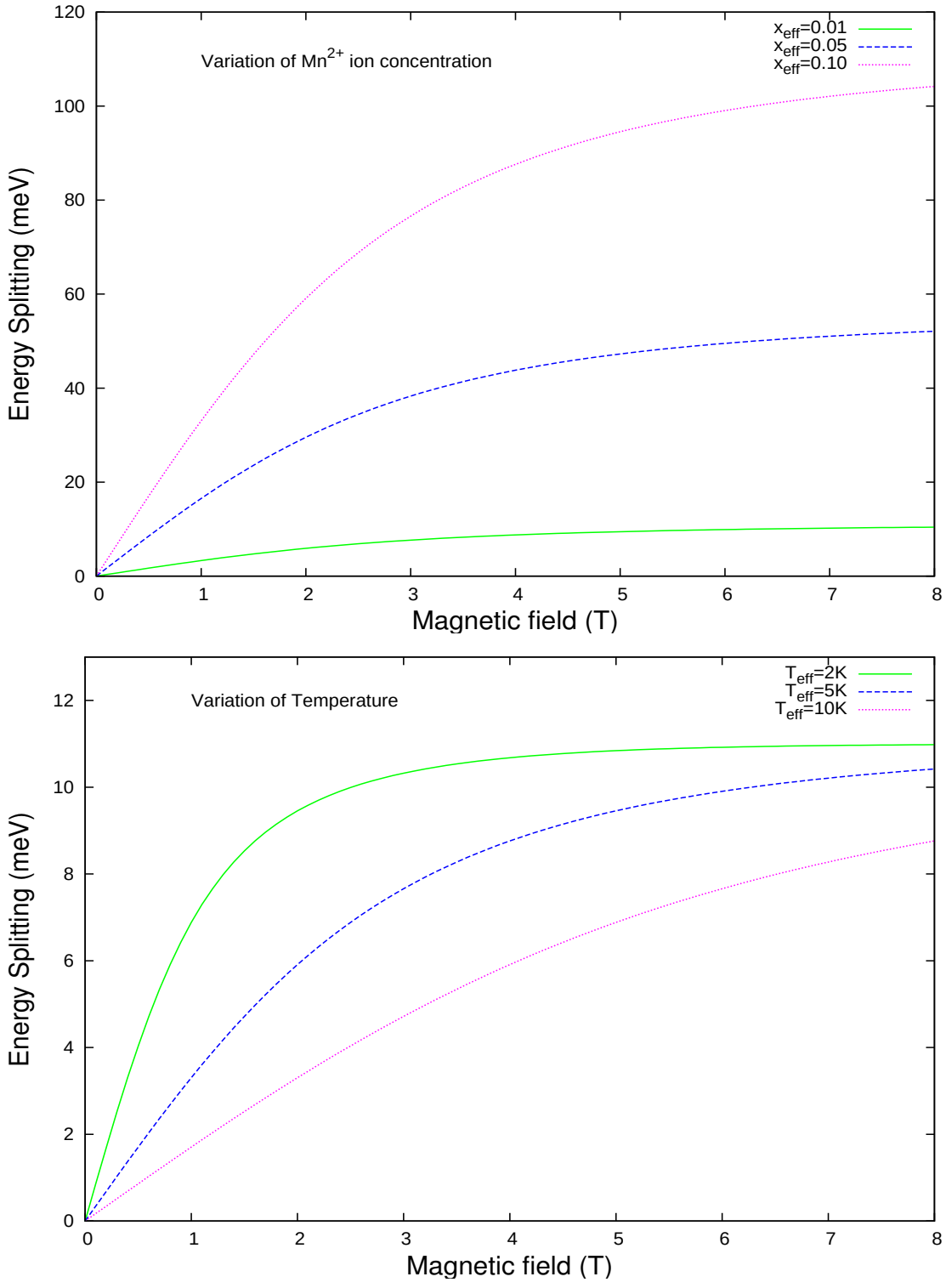

Figure 1-4: The Zeeman splitting for a heavy hole as a function of the magnetic field for various Mn^{2+} concentrations at a temperature of 5 K (top), and for various temperatures for a Mn^{2+} concentration of $x = 0.01$ (bottom).

1.1.4 The d-d exchange interaction

The half-filled 3d shell of Mn^{2+} is highly localised at the ion site, and contains five electrons with aligned spins, giving each individual ion a magnetic moment of five Bohr magnetons. The Mn^{2+} ions, and their interactions among themselves, determine the magnetic properties of the DMS. These properties are interesting, giving insight into the behaviour of a disordered magnetic system. This section outlines the interactions that couple the spins of magnetic ions, discussed comprehensively in reference [24]. There are several microscopic mechanisms that lead to the spin-spin (d-d) interactions between two Mn^{2+} magnetic ions. The d-d exchange interaction between the magnetic ions can be introduced with the following spin Hamiltonian operator [25][24]

$$\mathcal{H}_{d-d} = -\sum_{i \neq j} \sum_{\alpha,\beta} \vec{S}_{i,\alpha} \hat{J}^{\alpha,\beta}_{d-d}(\vec{R}_{ij}) \vec{S}_{j,\beta}, \tag{1.23}$$

where $\hat{J}^{\alpha,\beta}_{d-d}$ denotes the exchange tensor, $\vec{R}_{ij} = \vec{R}_i - \vec{R}_j$ is the vector separating spins, $\vec{S}_{i,\alpha}$ and $\vec{S}_{j,\beta}$ correspond to the components α and β of the Mn^{2+} spins i at $\vec{R}_i$ and j at R_j.

There are four main mechanisms that lead to the spin-spin magnetic ion interactions. Firstly the superexchange interaction, resulting from the sp-d hybridisation, is by far the dominant spin-spin interaction for short distances. The superexchange interaction can be explained in the following way; as a result of the aforementioned sp-d exchange interaction, the electrons residing in the sp bands are either attracted to or repulsed by a given magnetic ion, depending on their spin orientation. This results in a spatial separation of the spin down and spin up electrons if the bands are entirely occupied. Such a separation leads to an antiferromagnetic interaction between neighbouring localised spins. Indeed, in the absence of holes, localised spins are antiferromagnetically coupled in Mn^{2+} based $A^{II}_{1-x}Mn_xB^{VI}$ DMSs [11][24]. The second interaction is know as the Bloembergen-Rowland mechanism, an indirect Mn^{2+}-Mn^{2+} coupling resulting from fully occupied band states that are polarised by the sp-d exchange interaction [24][10]. This long ranged Bloembergen Rowland mechanism is an order of magnitude less effective than the superexchange interaction. Thirdly is the Ruderman Kittel Kasuya Yosida interaction (RKKY), which originates from the indirect exchange interaction via electrons. For the case of the RKKY interaction, the Mn^{2+}-Mn^{2+} coupling proceeds via spin polarisation of partly filled bands, which is achieved by free carriers (due to doping of the material). Since the spins of all carriers can assume the same direction if the band is unfilled, a ferromagnetic ordering can emerge [24][26][27][28][29]. The superexchange between more distant pairs of Mn^{2+} gives an antiferromagnetic coupling that competes with RKKY as soon as free carriers are present. Lastly is the double exchange which couples magnetic ions in different charge states by a virtual hopping of an extra electron from one ion to the other. This mechanism operates if the width of the carrier band is smaller than the exchange energy, a situation expected for bands formed from d states.

1.2 Conclusion

Now we have briefly reviewed the magnetic properties of DMSs, and in particular the existence of a giant Zeeman interaction, in the next Chapter we give an overview of the theoretical description of semiconductor band structures, which provide the framework within which the later work on excitons is performed.

Chapter 2

Semiconductor bandstructure

To understand the properties of excitons in a DMS semiconductor quantum well, one has to first study the electronic band structure. In this Chapter, the bandstructure of the conduction and valence band in a semiconductor will be considered. All the details of the bulk band structure can be described within the framework of $\vec{k} \cdot \vec{p}$ theory, which is very useful for calculating the band structure of a direct band gap semiconductor near a particular point in the Brillouin zone. Two models within this theory will be discussed, namely the Kane and the Luttinger Kohn model. The effect of strain can be easily added to the Luttinger Kohn model, with the use of the Pikus Bir Hamiltonian.

In a crystalline solid the motion of electrons is characterised by energy bands $E_n(\vec{k})$, with band index n, and wave vector $\vec{k}$ which labels the energy levels in the band. Most physical phenomena (electronic, optical and magnetic) in semiconductors can be understood by looking at a small portion of the band structure. Therefore, it is sufficient only to consider the bottom of the conduction band, and the top of the valence band, assumed to be at the Γ point, the $\vec{k} = 0$ point in k space. In most compound semiconductors, the maximum of the valence band and the minimum of the conduction band occur at the same point in the k space, making them direct gap semiconductors, Figure (1-2). The conduction band is s orbital like, and the valence band is p orbital like with heavy hole and light hole band maxima.

2.1 k·p method

An elementary model for the band structure of a direct band semiconductor close to the fundamental energy gap is an isotropic parabolic dispersion for the conduction band $E_c(\vec{k})$ and for the valence band $E_v(\vec{k})$ where

$$E_{c/v}(\vec{k}) = \pm \left(\frac{E_g}{2} + \frac{\hbar^2 k^2}{2m^*_{e/h}} \right), \tag{2.1}$$

where E_g is the band gap, and m^*_e and m^*_h are the effective masses for the conduction and valence band. This model neglects the non parabolicity of the conduction band, anisotropy, and coupling between the light and heavy holes [30]. A better approach is to use the $\vec{k} \cdot \vec{p}$ method which can calculate the semiconductor band structure near the band edges. This theory is for the energy eigenstates and wavefunctions in the region of any $\vec{k}$ value, and particularly for $\vec{k} = 0$. For this method one needs to know the $\vec{k} = 0$ eigenstates [30].

In an ideal crystal the ions occupy positions which form a regular periodic structure. The potential $V(\vec{r})$ is thus a periodic function, where the periodicity is that of the corresponding Bravais lattice

$$V(\vec{r}+\vec{R}) = V(\vec{r}), \tag{2.2}$$

where $\vec{R}$ is a lattice vector. The Schrödinger equation for electrons moving in such a potential is (ignoring spin orbit effects)

$$\mathcal{H}\phi_{n\vec{k}}(\vec{r}) = \left[\frac{p^2}{2m_0} + V(\vec{r})\right]\phi_{n\vec{k}}(\vec{r}) = E_n(\vec{k})\phi_{n\vec{k}}(\vec{r}), \tag{2.3}$$

where $\vec{p}$ is the momentum operator, m_0 is the electron rest mass, $E_n(\vec{k})$ is the energy, and n refers to the band. Since the lattice has translational symmetry the energy eigenfunctions obey Bloch's theorem [30], so that

$$\phi_{n\vec{k}}(\vec{r}) = \exp\left\{i\vec{k}\cdot\vec{r}\right\} u_{n\vec{k}}(\vec{r}), \tag{2.4}$$

where the function $u_{n\vec{k}}(\vec{r})$ is lattice periodic, $u_{n\vec{k}}(\vec{r}+\vec{R}) = u_{n\vec{k}}(\vec{r})$. Then one can write the Schrödinger equation for the periodic parts of the Bloch functions as [31]

$$\mathcal{H}u_{n\vec{k}}(\vec{r}) = \left[\frac{p^2}{2m_0} + \frac{\hbar}{m_0}\vec{k}\cdot\vec{p} + V(\vec{r})\right]u_{n\vec{k}}(\vec{r}) = \left[E_n(\vec{k}) - \frac{\hbar^2k^2}{2m_0}\right]u_{n\vec{k}}(\vec{r}), \tag{2.5}$$

which can be expanded near a particular point of interest in the band structure [31]. If this is $\vec{k}=0$ we can write

$$\left[\mathcal{H}_0 + \frac{\hbar}{m_0}\vec{k}\cdot\vec{p}\right]u_{n\vec{k}}(\vec{r}) = \left[E_n(\vec{k}) - \frac{\hbar^2k^2}{2m_0}\right]u_{n\vec{k}}(\vec{r}), \tag{2.6}$$

where

$$\mathcal{H}_0 = \frac{p^2}{2m_0} + V(\vec{r}), \tag{2.7}$$

$$\mathcal{H}_0 u_{n0}(\vec{r}) = E_n(0)u_{n0}(\vec{r}). \tag{2.8}$$

2.1.1 k·p method for one band

If one is interested in the band edge of a single band, such as the conduction band, and the couplings to the other bands are weak, then time independent perturbation theory can be used to solve Eq. (2.6). The eigenstates are divided into weakly interacting subsets A and B, where one is primarily interested in set A. Here the band of interest is labelled n and is contained in class A whilst class B contains all the other bands in the system, labelled n' [31]. Then to second order in the perturbation $(\hbar/m_0)\vec{k}\cdot\vec{p}$

$$E_n(\vec{k}) = E_n(0) + \frac{\hbar^2k^2}{2m_0} + \frac{\hbar}{m_0}\vec{k}\cdot\vec{p}_{nn} + \frac{\hbar^2}{m_0^2}\sum_{n'\neq n}\frac{\left|\vec{k}\cdot\vec{p}_{nn'}\right|^2}{E_n(0)-E_{n'}(0)}, \tag{2.9}$$

and the wavefunction to first order in the perturbation is

$$u_{n\vec{k}}(\vec{r}) = u_{n0}(\vec{r}) + \sum_{n'\neq n}\left[\frac{\hbar}{m_0}\frac{\vec{k}\cdot\vec{p}_{n'n}}{E_n(0)-E_{n'}(0)}\right]u_{n'0}(\vec{r}) = \sum_{n'}a_{n'}u_{n'0}(\vec{r}). \tag{2.10}$$

The momentum matrix elements appearing here are given by

$$\vec{p}_{nn'} = \int_{\text{unit cell}} u^*_{n0}(\vec{r})\vec{p}u_{n'0}(\vec{r})d^3\vec{r}. \tag{2.11}$$

If $E_n(\vec{k})$ has an extremum at $\vec{k} = 0$ then $E_n(\vec{k})$ will vary quadratically away from $\vec{k} = 0$ and $\vec{p}_{nn} = 0$ [31]. One can then write

$$E_n(\vec{k}) - E_n(0) = \frac{\hbar^2}{2}\sum_{\alpha,\beta}\left(\frac{1}{m^*}\right)_{\alpha\beta} k_\alpha k_\beta, \tag{2.12}$$

where

$$\left(\frac{1}{m^*}\right)_{\alpha\beta} = \frac{1}{m_0}\delta_{\alpha\beta} + \frac{2}{m_0^2}\sum_{n'\neq n}\frac{p^\alpha_{nn'}p^\beta_{n'n} + p^\beta_{nn'}p^\alpha_{n'n}}{E_n(0) - E_{n'}(0)}, \tag{2.13}$$

with $\alpha, \beta = (x, y, z)$. The effective mass of the band is seen to be related to momentum matrix elements connecting the band to other bands in the system [31].

2.2 Kane model

The Kane model is a simple model that describes the electron states in the vicinity of the band gap in a direct semiconductor using $\vec{k}\cdot\vec{p}$ theory, and also includes the spin orbit interaction in the form of the Pauli spin orbit term, which enters into the Hamiltonian from a non relativistic approximation to the Dirac equation [30]. The spin orbit interaction (also referred to as spin orbit coupling) is the interaction between orbital and spin degrees of freedom of an electron. Although this interaction has an essentially relativistic nature it nevertheless can give rise to an observable modification of the band structure of a semiconductor. For example in semiconductors the spin orbit interaction gives rise to a splitting of the topmost valence bands which are split by an energy gap Δ_{so}, resulting in a heavy hole band, light hole band and spin orbit split off band. The spin orbit interaction term can be written as

$$\mathcal{H}_{so} = \frac{\hbar}{4m_0^2c^2}\vec{p}\cdot\vec{\sigma}\times(\nabla V(\vec{r})), \tag{2.14}$$

where $\vec{\sigma} = \sigma_x\hat{i} + \sigma_y\hat{j} + \sigma_z\hat{k}$ is the vector of Pauli spin matrices, and c is the speed of light [31].

The Kane model considers the effect on the conduction and valence band states as one moves away from the Γ point ($\vec{k} = 0$), and considers the effect of the spin orbit interaction on them. The conduction and valence band states are solved exactly using the matrix formalism based on a convenient basis choice. Using Eq. (2.3) the Hamiltonian near the zone centre $\vec{k} = 0$ is then written as

$$\mathcal{H}_K = \mathcal{H}_0 + \mathcal{H}_{so}. \tag{2.15}$$

The Schrödinger equation for the Bloch states $\phi_{n\vec{k}}(\vec{r})$ then leads to the following equation for the cell periodic function $u_{n\vec{k}}(\vec{r})$,

$$\begin{aligned}\mathcal{H}_K u_{n\vec{k}}(\vec{r}) &= \left[\mathcal{H}_0 + \frac{\hbar}{m_0}\vec{k}\cdot\vec{p} + \frac{\hbar^2}{4m_0^2c^2}\vec{k}\cdot\vec{\sigma}\times(\nabla V(\vec{r})) + \frac{\hbar}{4m_0^2c^2}\vec{p}\cdot\vec{\sigma}\times(\nabla V(\vec{r}))\right]u_{n\vec{k}}(\vec{r}) \\ &= \left[E_n(\vec{k}) - \frac{\hbar^2k^2}{2m_0}\right]u_{n\vec{k}}(\vec{r}).\end{aligned} \tag{2.16}$$

The $\vec{k}$ dependent spin interaction (the third term) can normally be neglected compared to the fourth term, since the crystal momentum $\hbar\vec{k}$ is small compared to the atomic momentum [31]. Then

$$\mathcal{H}_K u_{n\vec{k}}(\vec{r}) = \left[\mathcal{H}_0 + \frac{\hbar}{m_0}\vec{k}\cdot\vec{p} + \frac{\hbar}{4m_0^2c^2}\vec{p}\cdot\vec{\sigma}\times(\nabla V(\vec{r}))\right] u_{n\vec{k}}(\vec{r}) = \left[E_n(\vec{k}) - \frac{\hbar^2k^2}{2m_0}\right] u_{n\vec{k}}(\vec{r}). \tag{2.17}$$

This equation is solved using a basis of band edge states found in the absence of the spin orbit term, where $|S\uparrow\rangle, |S\downarrow\rangle$ are the two fold degenerate conduction band states with eigenenergy E_s, and the six fold degenerate valence band states are written as $|X\uparrow\rangle |X\downarrow\rangle, |Y\uparrow\rangle, |Y\downarrow\rangle, |Z\uparrow\rangle, |Z\downarrow\rangle$ with eigenenergy E_p. Here $|X\rangle$, $|Y\rangle$, and $|Z\rangle$ are functions with the periodicity of the host lattice, and which transform like p_x, p_y and p_z orbitals. $|\uparrow\rangle$ and $|\downarrow\rangle$ are the spin eigenfunctions.

For convenience the following linear combinations are constructed and used to create basis states $|u_i\rangle, i = 1, 2, \ldots 8$:

$$\begin{aligned} &|iS\downarrow\rangle, \frac{1}{\sqrt{2}}|(X-iY)\uparrow\rangle, |Z\downarrow\rangle, \frac{1}{\sqrt{2}}|-(X+iY)\uparrow\rangle, \\ &|iS\uparrow\rangle, \frac{1}{\sqrt{2}}|-(X+iY)\downarrow\rangle, |Z\uparrow\rangle, \frac{1}{\sqrt{2}}|(X-iY)\downarrow\rangle, \end{aligned} \tag{2.18}$$

where the first four are degenerate with their spin counterparts [31]. With this choice one obtains the Hamiltonian matrix [32]

$$\mathcal{H}_K = \begin{pmatrix} \overline{\mathbf{H}} & 0 \\ 0 & \overline{\mathbf{H}} \end{pmatrix}, \qquad \overline{\mathbf{H}} = \begin{pmatrix} E_s & 0 & kP' & 0 \\ 0 & E_p - \frac{\Delta_{so}}{3} & \frac{\sqrt{2}\Delta_{so}}{3} & 0 \\ kP' & \frac{\sqrt{2}\Delta_{so}}{3} & E_p & 0 \\ 0 & 0 & 0 & E_p + \frac{\Delta_{so}}{3} \end{pmatrix}, \tag{2.19}$$

where $E_s = E_g$ is the band gap energy, and $E_p = -\Delta_{so}/3$ (the top of the valence band is taken to be the zero of energy). The Kane parameter P' is given by

$$P' = \frac{\hbar}{m_0}\langle u_i|p_z|u_j\rangle \equiv -i\frac{\hbar}{m_0}\langle S|p_z|Z\rangle, \tag{2.20}$$

and the spin orbit split off energy is given by

$$\Delta_{so} \equiv \frac{3i\hbar}{4m_0^2c^2}\left\langle X\left|\frac{\partial V}{\partial x}p_y - \frac{\partial V}{\partial y}p_x\right|Y\right\rangle. \tag{2.21}$$

The full derivation is given in Appendix A. The band structure obtained from the Hamiltonian (Eq. (2.19)) is displayed in Figure (2-1).

For small $\vec{k}$ it can be shown that the energy bands are given by

$$\begin{aligned} E_c(k) &= E_g + \frac{\hbar^2k^2}{2m_0} + \frac{k^2P'^2(3E_g+2\Delta_{so})}{3E_g(E_g+\Delta_{so})}, \\ E_{hh}(k) &= \frac{\hbar k^2}{2m_0}, \\ E_{lh}(k) &= \frac{\hbar k^2}{2m_0} - \frac{2k^2P'^2}{3E_g}, \\ E_{so}(k) &= -\Delta_{so} + \frac{\hbar k^2}{2m_0} - \frac{k^2P'^2}{3(E_g+\Delta_{so})}, \end{aligned} \tag{2.22}$$

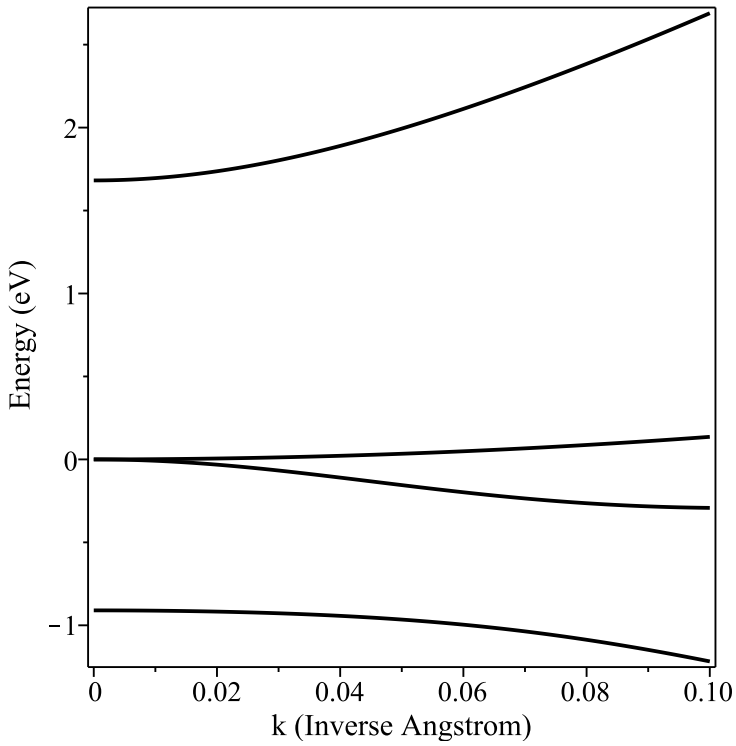

Figure 2-1: Band structure for $Cd_{1-x}Mn_xTe$ obtained using the Kane model showing the conduction band, heavy hole, light hole, and spin orbit split off band. This has been calculated using the values given in Appendix K, for $x = 0.05$.

(Appendix A), with corresponding eigenfunctions

$$\begin{aligned}
\phi_{c,\alpha} &= |iS\downarrow\rangle, \qquad \phi_{c,\beta} = |iS\uparrow\rangle, \\
\phi_{hh,\alpha} &= -\frac{1}{\sqrt{2}}|(X+iY)\uparrow\rangle, \qquad \phi_{hh,\beta} = \frac{1}{\sqrt{2}}|(X-iY)\downarrow\rangle, \\
\phi_{lh,\alpha} &= \frac{1}{\sqrt{6}}|(X-iY)\uparrow\rangle + \sqrt{\frac{2}{3}}|Z\downarrow\rangle, \qquad \phi_{lh,\beta} = -\frac{1}{\sqrt{6}}|(X+iY)\downarrow\rangle + \sqrt{\frac{2}{3}}|Z\uparrow\rangle, \\
\phi_{so,\alpha} &= \frac{1}{\sqrt{3}}|(X-iY)\uparrow\rangle - \frac{1}{\sqrt{3}}|Z\downarrow\rangle, \qquad \phi_{so,\beta} = \frac{1}{\sqrt{3}}|((X+iY)\downarrow)\rangle + \frac{1}{\sqrt{3}}|Z\uparrow\rangle,
\end{aligned} \tag{2.23}$$

where c denotes the conduction band, lh the light hole, hh the heavy hole, and so the split off band. The Kane parameter can be seen to be related to the effective mass of the conduction electrons by using Eq. (2.22) with [31]

$$P'^2 = \left(1 - \frac{m_e^*}{m_0}\right)\frac{\hbar^2 3E_g(E_g+\Delta_{so})}{2m_e^*(3E_g+2\Delta_{so})}. \tag{2.24}$$

In principle knowledge of the zone centre energies and conduction band effective mass (i.e from spectroscopic measurements) allows the parameters entering the model to be established, after which it can be used to predict other properties of the electronic structure. However, one can see from Eq. (2.22) that the Kane model also predicts that the heavy

hole band disperses upwards, which is contrary to experiments. Therefore a more accurate band model is required. This is given by the Luttinger Kohn Hamiltonian, obtained by using Löwdin's Renormalisation.

2.3 Löwdin's Renormalisation

Löwdin's Renormalisation is a technique in perturbation theory. The couplings to other bands are included and it continues from the previous idea where the placing of bands into two different sets was introduced, with set A containing the bands of interest and set B containing all the other bands in the system. In this case, unlike in Section 2.1.1, set A will include both conduction and valence bands. The eigenstate equation is written as

$$\sum_{n=1}^{N}(\mathcal{H}_{mn} - E\delta_{mn})a_n = 0, \tag{2.25}$$

assuming an orthonormalised basis set of unperturbed states [31]. This partitioning means Eq (2.25) can be rewritten as

$$(E - \mathcal{H}_{mm})a_m = \sum_{n\neq m}^{A} \mathcal{H}_{mn}a_n + \sum_{\alpha\neq m}^{B} \mathcal{H}_{m\alpha}a_\alpha, \tag{2.26}$$

or

$$a_m = \sum_{n\neq m}^{A} \frac{\mathcal{H}_{mn}}{E - \mathcal{H}_{mm}}a_n + \sum_{\alpha\neq m}^{B} \frac{\mathcal{H}_{m\alpha}}{E - \mathcal{H}_{mm}}a_\alpha. \tag{2.27}$$

Since only the coefficients a_m for m in class A are of interest, those in class B are eliminated by an iteration procedure, where the coefficients for B on the right are replaced as follows

$$a_m = \sum_{n\neq m}^{A} \frac{\mathcal{H}_{mn}}{E - \mathcal{H}_{mm}}a_n + \sum_{\alpha\neq m}^{B} \frac{\mathcal{H}_{m\alpha}}{E - \mathcal{H}_{mm}} \left(\sum_{n\neq \alpha}^{A} \frac{\mathcal{H}_{\alpha n}}{E - \mathcal{H}_{\alpha\alpha}}a_n + \sum_{\beta\neq \alpha}^{B} \frac{\mathcal{H}_{\alpha\beta}}{E - \mathcal{H}_{\alpha\alpha}}a_\beta \right).$$

Grouping terms with the same coefficients together and replacing the coefficients that are not in class A, eventually an equation that only depends on the coefficients in class A is obtained, where

$$a_m = \sum_{n}^{A} \frac{(U^A_{mn} - \mathcal{H}_{mn}\delta_{mn})}{E - \mathcal{H}_{mm}}a_n, \tag{2.28}$$

and

$$U^A_{mn} = \mathcal{H}_{mn} + \sum_{\alpha\neq m}^{B} \frac{\mathcal{H}_{m\alpha}\mathcal{H}_{\alpha n}}{E - \mathcal{H}_{\alpha\alpha}} + \sum_{\alpha\neq m}^{B}\sum_{\beta\neq n}^{B} \frac{\mathcal{H}_{m\alpha}\mathcal{H}_{\alpha\beta}\mathcal{H}_{\beta n}}{(E - \mathcal{H}_{\alpha\alpha})(E - \mathcal{H}_{\beta\beta})} + \dots \quad . \tag{2.29}$$

The second, and subsequent terms account for the effect of bands in class B on class A in series form [31]. Clearing fractions in Eq. (2.28)

$$\begin{aligned}(E - \mathcal{H}_{mm})a_m &= \sum_{n}^{A}(U^A_{mn} - \mathcal{H}_{mn}\delta_{mn})a_n \\ &= \sum_{n}^{A} U^A_{mn}a_n - \mathcal{H}_{mm}a_m. \end{aligned} \tag{2.30}$$

Hence

$$\sum_{n}^{A}(U_{mn}^{A} - E\delta_{mn})a_n = 0. \tag{2.31}$$

A necessary condition for the expansion of Eq. (2.29) to be convergent is

$$|\mathcal{H}_{m\alpha}| \ll |E - \mathcal{H}_{\alpha\alpha}|\,. \tag{2.32}$$

In practice, to second order in perturbation, E may be replaced by E_A in Eq. (2.29) (where E_A is an average energy of states in class A), and then the series in Eq. (2.29) can be truncated at the second order term. If class A consists of only a single nondegenerate state n, then class B consists of the rest, and Eq. (2.31) gives only on equation

$$E = U_{nn}^{A} = \mathcal{H}_{nn} + \sum_{\alpha\neq n}\frac{\mathcal{H}_{n\alpha}\mathcal{H}_{\alpha n}}{E - \mathcal{H}_{\alpha\alpha}} + \sum_{\alpha,\beta\neq n}\frac{\mathcal{H}_{n\alpha}\mathcal{H}_{\alpha\beta}\mathcal{H}_{\beta n}}{(E - \mathcal{H}_{\alpha\alpha})(E - \mathcal{H}_{\beta\beta})} + \ldots. \tag{2.33}$$

If $\mathcal{H}$ is separated into $\mathcal{H}^{(0)}$ and a perturbation $\mathcal{H}'$, then to second order in $\mathcal{H}'$

$$E = E_n(0) + \mathcal{H}'_{nn} + \sum_{\alpha\neq n}\frac{\mathcal{H}'_{n\alpha}\mathcal{H}'_{\alpha n}}{E_n(0) - E_\alpha(0)}, \tag{2.34}$$

where $E_n(0) = \mathcal{H}^{(0)}_{nn}$. If the states in class A are degenerate, then the diagonal elements are almost or exactly the same with differences of the first and higher orders, and then we can write [31]

$$U_{mn}^{A} = \mathcal{H}_{mn} + \sum_{\alpha}^{B}\frac{\mathcal{H}'_{m\alpha}\mathcal{H}'_{\alpha n}}{E_A - \mathcal{H}_{\alpha\alpha}}, \tag{2.35}$$

This is now applied to the Luttinger Kohn Hamiltonian to include the influence of the other bands.

2.4 Luttinger Kohn Hamiltonian

The Kane model includes all 4 bands treated exactly, but the coupling to the other bands is neglected. Within this approximation the heavy hole band has the wrong sign and value when compared to experimental data. Therefore a better model is required, for which the Luttinger Kohn Hamiltonian is used for degenerate bands, with the spin orbit interaction included [33]. This Hamiltonian can be extended to include all 4 bands via Löwdins renormalisation. The heavy and light hole bands are labelled as the Γ_{8v} valence band, while the spin orbit split off band is labelled as the Γ_{7v} valence band. The lowest conduction band is labelled as the Γ_{6c} conduction band, and the next highest conduction bands are labelled as Γ_{7c} and Γ_{8c}, shown in Figure (2-2). The bands are separated into two classes, where the bands of interest are placed in class A (either all or some of the 4 bands that contains the lowest conduction band, the heavy hole, light hole and spin orbit split off band within the valence band). All other bands in the system are placed in class B, which influences the bands in class A. The Hamiltonian in Eq. (2.16) is rewritten by

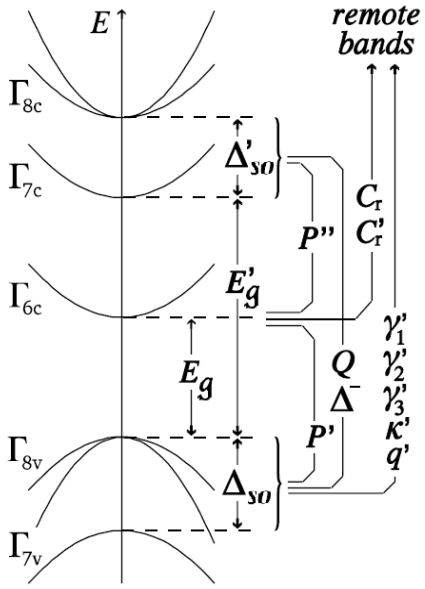

Figure 2-2: Schematic diagram of the band structure, showing energy separations and coupling parameters. Taken from Ref. [30].

dropping the band index n as

$$\mathcal{H}u_{\vec{k}}(\vec{r}) = \left[\mathcal{H}_0 + \frac{\hbar^2 k^2}{2m_0} + \frac{\hbar}{4m_0^2c^2}\nabla V(\vec{r}) \times \vec{p}\cdot\vec{\sigma} + H'\right] u_{\vec{k}}(\vec{r}) = E(\vec{k})u_{\vec{k}}(\vec{k}), \tag{2.36}$$

where

$$\mathcal{H}' = \frac{\hbar}{m_0}\vec{k}\cdot\Pi, \tag{2.37}$$

and

$$\Pi = \vec{p} + \frac{\hbar}{4m_0c^2}\vec{\sigma}\times\nabla V(\vec{r}). \tag{2.38}$$

The function $u_{\vec{k}}(\vec{r})$ is expanded into two sets for A and B

$$u_{\vec{k}}(\vec{r}) = \sum_{j'}^{A} a_{j'}(\vec{k}) u_{j'0}(\vec{r}) + \sum_{\gamma}^{B} a_{\gamma}(\vec{k}) u_{\gamma 0}(\vec{r}), \tag{2.39}$$

where class B affects class A when a perturbation is applied. Class A contains states labelled by Roman indices j and class B contains states labelled by Greek indices γ. The eigenvalue problem (see Section 2.3)

$$\sum_{j'}^{A} (U^{A}_{jj'} - E\delta_{jj'}) a_{j'}(\vec{k}) = 0 \tag{2.40}$$

needs to be solved, where (Eq. (2.35))

$$U^{A}_{jj'} = \mathcal{H}_{jj'} + \sum_{\gamma}^{B} \frac{\mathcal{H}_{j\gamma}\mathcal{H}_{\gamma j'}}{E_0 - E_\gamma} = \mathcal{H}_{jj'} + \sum_{\gamma}^{B} \frac{\mathcal{H}'_{j\gamma}\mathcal{H}'_{\gamma j'}}{E_0 - E_\gamma}, \tag{2.41}$$

with

$$\mathcal{H}_{jj'} = \langle u_{j0} | \mathcal{H} | u_{j'0} \rangle = \left[E_j(0) + \frac{\hbar^2 k^2}{2m_0} \right] \delta_{jj'}, \tag{2.42}$$

$$\mathcal{H}'_{j\gamma} = \left\langle u_{j0} \left| \frac{\hbar}{m_0} \vec{k} \cdot \vec{p} \right| u_{\gamma 0} \right\rangle \cong \sum_{\alpha} \frac{\hbar k_\alpha}{m_0} p^{\alpha}_{j\gamma}, \tag{2.43}$$

since $\Pi_{jj'} = 0$ for j and j' in class A, and $\Pi^{\alpha}_{j\gamma} \cong p^{\alpha}_{j\gamma}$ for j in class A and γ in class B. Adding the unperturbed part to the perturbed part in $\mathcal{H}'_{j\gamma}$ does not effect the results (i.e $\mathcal{H}_{j\gamma} = \mathcal{H}'_{j\gamma}$), due to the fact that $\gamma \neq j$. Then one obtains

$$\begin{aligned} U^{A}_{jj'} &= \left[E_j(0) + \frac{\hbar^2 k^2}{2m_0} \right] \delta_{jj'} + \frac{\hbar^2}{m_0^2} \sum_{\gamma}^{B} \sum_{\alpha,\beta} \frac{k_\alpha k_\beta p^{\alpha}_{j\gamma} p^{\beta}_{\gamma j'}}{E_0 - E_\gamma} \\ &= E_j(0)\delta_{jj'} + \sum_{\alpha,\beta} D^{\alpha\beta}_{jj'} k_\alpha k_\beta, \end{aligned} \tag{2.44}$$

where

$$D^{\alpha\beta}_{jj'} = \frac{\hbar^2}{2m_0} \left(\delta_{jj'}\delta_{\alpha\beta} + \frac{1}{m_0} \sum_{\gamma}^{B} \frac{p^{\alpha}_{j\gamma} p^{\beta}_{\gamma j'} + p^{\beta}_{j\gamma} p^{\alpha}_{\gamma j'}}{E_0 - E_\gamma} \right) \tag{2.45}$$

The summation is over all others states γ, and α and β run over x, y and z. This equation is similar to Eq. (2.13), but has been generalised so as to now also include the degenerate bands. The Luttinger Kohn Hamiltonian is then

$$(\mathcal{H}_{LK})_{jj'} = E_j(0)\delta_{jj'} + \sum_{\alpha,\beta} D^{\alpha\beta}_{jj'} k_\alpha k_\beta. \tag{2.46}$$

2.4.1 4×4 Luttinger Kohn Hamiltonian

The 4×4 Luttinger Kohn Hamiltonian only explicitly includes the light and heavy hole bands (the Γ_{8v} valence band), and these bands are placed in class A and have the following basis functions

$$\begin{aligned}
|u_{10}\rangle &= \left|\frac{3}{2}, \frac{3}{2}\right\rangle = -\frac{1}{\sqrt{2}} |(X + iY) \uparrow\rangle , \\
|u_{20}\rangle &= \left|\frac{3}{2}, \frac{1}{2}\right\rangle = -\frac{1}{\sqrt{6}} |(X + iY) \downarrow\rangle + \sqrt{\frac{2}{3}} |Z \uparrow\rangle , \\
|u_{30}\rangle &= \left|\frac{3}{2}, -\frac{1}{2}\right\rangle = \frac{1}{\sqrt{6}} |(X - iY) \uparrow\rangle + \sqrt{\frac{2}{3}} |Z \downarrow\rangle , \\
|u_{40}\rangle &= \left|\frac{3}{2}, -\frac{3}{2}\right\rangle = \frac{1}{\sqrt{2}} |(X - iY) \downarrow\rangle ,
\end{aligned} \tag{2.47}$$

from the eigenfunctions in Eq. (2.23) [34]. To formulate the matrix elements in Eq. (2.45) the following quantities are defined

$$\begin{aligned}
A_0 &= \frac{\hbar^2}{2m_0} + \frac{\hbar^2}{m_0^2} \sum_{\gamma}^{\beta} \frac{p_{x\gamma}^x p_{\gamma x}^x}{E_0 - E_\gamma}, \\
B_0 &= \frac{\hbar^2}{2m_0} + \frac{\hbar^2}{m_0^2} \sum_{\gamma}^{\beta} \frac{p_{x\gamma}^y p_{\gamma x}^y}{E_0 - E_\gamma}, \\
C_0 &= \frac{\hbar^2}{m_0^2} \sum_{\gamma}^{\beta} \frac{p_{x\gamma}^x p_{\gamma y}^y + p_{x\gamma}^y p_{\gamma y}^x}{E_0 - E_\gamma},
\end{aligned} \tag{2.48}$$

and the band structure γ parameters are defined as

$$\begin{aligned}
\frac{\hbar^2}{2m_0}\gamma_1 &= -\frac{1}{3}(A_0 + 2B_0), \\
\frac{\hbar^2}{2m_0}\gamma_2 &= -\frac{1}{6}(A_0 - B_0), \\
\frac{\hbar^2}{2m_0}\gamma_3 &= -\frac{C_0}{6}.
\end{aligned} \tag{2.49}$$

The parameters γ_1, γ_2 and γ_3 describe the coupling between the p like valence band states and the remote bands.

Using Eq. (2.46) with the basis functions in Eq. (2.47) the 4×4 Luttinger Kohn Hamiltonian becomes

$$\mathcal{H}_{LK} = -\begin{pmatrix} P+Q & -b & c & 0 \\ -b^* & P-Q & 0 & c \\ c^* & 0 & P-Q & b \\ 0 & c^* & b^* & P+Q \end{pmatrix}, \tag{2.50}$$

with

$$\begin{aligned} P &= \left(\frac{\hbar^2}{2m_0}\right)\gamma_1\left(k_x^2+k_y^2+k_z^2\right), \\ Q &= \left(\frac{\hbar^2}{2m_0}\right)\gamma_2\left(k_x^2+k_y^2-2k_z^2\right), \\ c &= \left(\frac{\hbar^2}{2m_0}\right)\left[-\sqrt{3}\gamma_2(k_x^2-k_y^2)+i2\sqrt{3}\gamma_3 k_x k_y\right], \\ b &= \left(\frac{\hbar^2}{2m_0}\right)\gamma_3 2\sqrt{3}(k_x-ik_y)k_z. \end{aligned} \tag{2.51}$$

From a practical point of view, the γ parameters in Eq. (2.49) can be determined from the effective masses of the various bands, which themselves can be determined from experimental observation of the energy bands, via the relations

$$\begin{aligned} \frac{m_{hh}^{*[001]}}{m_0} &= \frac{1}{\gamma_1-2\gamma_2}, \qquad \frac{m_{lh}^{*[001]}}{m_0} = \frac{1}{\gamma_1+2\gamma_2}, \\ \frac{m_{hh}^{*[111]}}{m_0} &= \frac{1}{\gamma_1-2\gamma_3}, \qquad \frac{m_{lh}^{*[111]}}{m_0} = \frac{1}{\gamma_1+2\gamma_3}, \end{aligned} \tag{2.52}$$

so that

$$\begin{aligned} \gamma_1 &= \frac{1}{2}\left(\frac{1}{m_{hh}^{*[001]}}+\frac{1}{m_{lh}^{*[001]}}\right), \\ \gamma_2 &= \frac{1}{4}\left(\frac{1}{m_{lh}^{*[001]}}-\frac{1}{m_{hh}^{*[001]}}\right), \\ \gamma_3 &= \frac{1}{4}\left(\frac{1}{m_{hh}^{*[001]}}+\frac{1}{m_{lh}^{*[001]}}\right)-\frac{1}{2m_{hh}^{*[111]}}, \end{aligned} \tag{2.53}$$

where [001] and [111] indicate the band directions [35][36].

The 4×4 Luttinger Kohn Hamiltonian in Eq. (2.50) can be block diagonalised and rewritten as [34]

$$\mathcal{H}_{LK} = -\begin{pmatrix} H^U & 0 \\ 0 & H^L \end{pmatrix}, \tag{2.54}$$

where

$$H^U = -\begin{pmatrix} P+Q & R \\ R^* & P-Q \end{pmatrix}, \qquad H^L = -\begin{pmatrix} P-Q & R \\ R^* & P+Q \end{pmatrix}, \tag{2.55}$$

and $R = |c| - i|b|$. The derivation is given in Appendix B. For the Hamiltonian in Eq. (2.54), the valence bands from $\det\left|\mathcal{H}_{LK}(\vec{k})-E\right| = 0$ are given by

$$E(\vec{k}) = -P \pm \sqrt{Q^2+|c^2|+|b^2|}. \tag{2.56}$$

From the small k expansion one obtains

$$E_{hh}(\vec{k}) \approx -P-Q \approx -\left(\frac{\hbar^2}{2m_0}\right)\left[(\gamma_1+\gamma_2)k_{||}^2+(\gamma_1-2\gamma_2)k_z^2\right], \tag{2.57}$$

and

$$E_{lh}(\vec{k}) \approx -P + Q \approx -\left(\frac{\hbar^2}{2m_0}\right)\left[(\gamma_1 - \gamma_2)k_{||}^2 + (\gamma_1 + 2\gamma_2)k_{\perp}^2\right], \tag{2.58}$$

where $k_{||} = \sqrt{k_x^2 + k_y^2}$, and $k_{\perp} = k_z$, from which one can immediately obtain the effective masses parallel or perpendicular to the xy plane (which is the (001) plane of the crystal) as

$$\begin{aligned} \frac{m^*_{hh,\perp}}{m_0} &= \frac{1}{\gamma_1 - 2\gamma_2}, \qquad \frac{m^*_{hh,||}}{m_0} = \frac{1}{\gamma_1 + \gamma_2} \\ \frac{m^*_{lh,\perp}}{m_0} &= \frac{1}{\gamma_1 + 2\gamma_2}, \qquad \frac{m^*_{lh,||}}{m_0} = \frac{1}{\gamma_1 - \gamma_2}. \end{aligned} \tag{2.59}$$

The band structure for $Cd_{1-x}Mn_xTe$ using the 4×4 Luttinger Kohn Hamiltonian can be seen in Figure (2-3). In contrast to the Kane model the masses here are of the correct sign, so the heavy hole band disperses downwards.

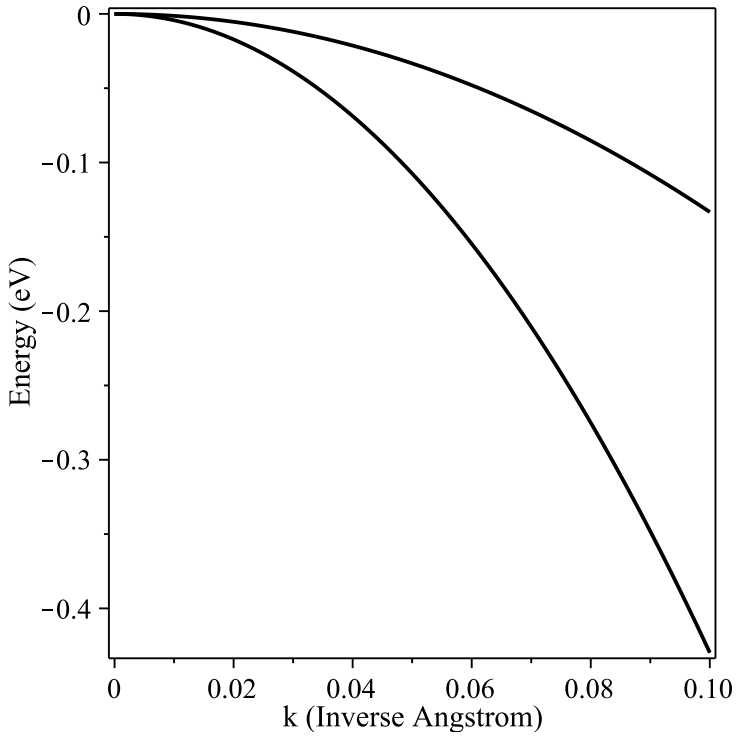

Figure 2-3: Band structure for $Cd_{1-x}Mn_xTe$ obtained using the 4×4 Luttinger Kohn model. This has been calculated using the values in Appendix K, for $x = 0.05$.

2.4.2 6×6 Luttinger Kohn Hamiltonian

This model extends the 4×4 Luttinger Kohn Hamiltonian to include the spin orbit split off band. The following basis functions for the states in class A are used

$$\begin{aligned}
u_{10} &= \left|\frac{3}{2}, \frac{3}{2}\right\rangle = -\frac{1}{\sqrt{2}} \left|(X+iY)\uparrow\right\rangle, \\
u_{20} &= \left|\frac{3}{2}, \frac{1}{2}\right\rangle = -\frac{1}{\sqrt{6}} \left|(X+iY)\downarrow\right\rangle + \sqrt{\frac{2}{3}} \left|Z\uparrow\right\rangle, \\
u_{30} &= \left|\frac{3}{2}, -\frac{1}{2}\right\rangle = \frac{1}{\sqrt{6}} \left|(X-iY)\uparrow\right\rangle + \sqrt{\frac{2}{3}} \left|Z\downarrow\right\rangle, \\
u_{40} &= \left|\frac{3}{2}, -\frac{3}{2}\right\rangle = \frac{1}{\sqrt{2}} \left|(X-iY)\downarrow\right\rangle, \\
u_{50} &= \left|\frac{1}{2}, \frac{1}{2}\right\rangle = \frac{1}{\sqrt{3}} \left|(X+iY)\downarrow\right\rangle + \frac{1}{\sqrt{3}} \left|Z\uparrow\right\rangle, \\
u_{60} &= \left|\frac{1}{2}, -\frac{1}{2}\right\rangle = \frac{1}{\sqrt{3}} \left|(X-iY)\uparrow\right\rangle - \frac{1}{\sqrt{3}} \left|Z\downarrow\right\rangle.
\end{aligned} \tag{2.60}$$

Using Eq. (2.46) with these basis functions, the 6×6 Luttinger Kohn Hamiltonian is

$$\mathcal{H}_{LK} = -\begin{pmatrix}
P+Q & -b & c & 0 & -\frac{1}{\sqrt{2}}b & \sqrt{2}c \\
-b^* & P-Q & 0 & c & -\sqrt{2}Q & \sqrt{\frac{3}{2}}b \\
c^* & 0 & P-Q & b & \sqrt{\frac{3}{2}}b^* & \sqrt{2}Q \\
0 & c^* & b^* & P+Q & -\sqrt{2}c^* & -\frac{1}{\sqrt{2}}b^* \\
-\frac{1}{\sqrt{2}}b^* & -\sqrt{2}Q & \sqrt{\frac{3}{2}}b & -\sqrt{2}c & P+\Delta_{so} & 0 \\
\sqrt{2}c^* & \sqrt{\frac{3}{2}}b^* & \sqrt{2}Q & -\frac{1}{\sqrt{2}}b & 0 & P+\Delta_{so}
\end{pmatrix}, \tag{2.61}$$

where P, Q, b and c are as before. The effective masses parallel or perpendicular to the xy plane for the heavy and light hole are still given by Eq. (2.59), and the effective masses of the split off band by

$$\frac{m^*_{so,\perp}}{m_0} = \frac{m^*_{so,||}}{m_0} = \frac{1}{\gamma_1}. \tag{2.62}$$

The band structure for $Cd_{1-x}Mn_xTe$ using the 6×6 Luttinger Kohn Hamiltonian can be seen in Figure. (2-4).

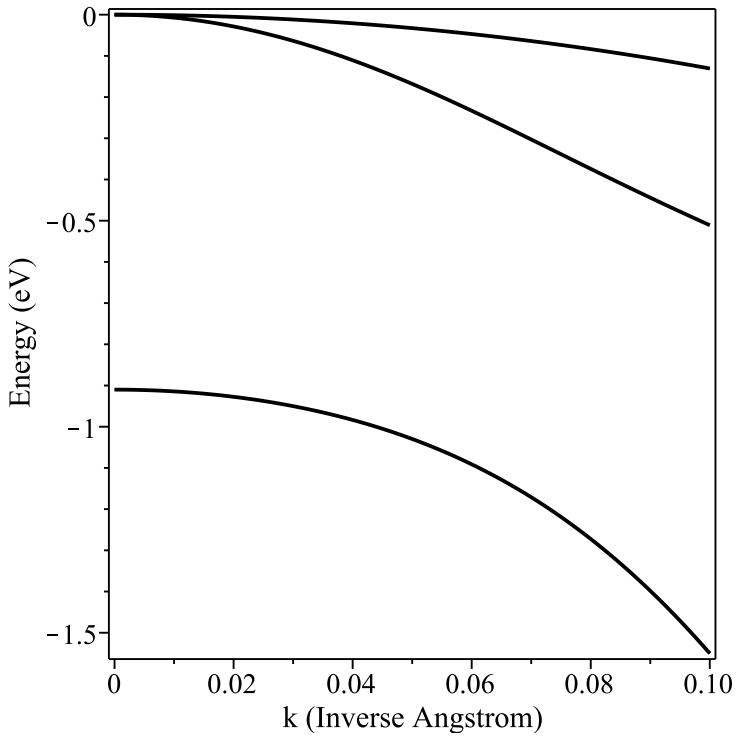

Figure 2-4: Band structure for $Cd_{1-x}Mn_xTe$ obtained using the 6×6 Luttinger Kohn model. This has been calculated using the values in Appendix K, for $x = 0.05$.

2.4.3 8×8 Luttinger Kohn Hamiltonian

Finally, the previous Luttinger Kohn Hamiltonian can be extended to include the lowest conduction band (Γ_{6c}), for which the following additional basis functions are used

$$\begin{aligned} u_{70} &= \left|\frac{1}{2}, \frac{1}{2}\right\rangle = |iS\uparrow\rangle\,, \\ u_{80} &= \left|\frac{1}{2}, -\frac{1}{2}\right\rangle = |iS\downarrow\rangle\,. \end{aligned} \tag{2.63}$$

The new Hamiltonian presented with these basis functions (u_{70}, u_{80}, u_{10}, u_{20}, u_{30}, u_{40}, u_{50}, u_{60}) is written as

$$\mathcal{H}_{LK} = \begin{pmatrix} E_g + \frac{\hbar^2 k^2}{2m_e^*} & 0 & -\frac{1}{\sqrt{2}}P'k_+ & \sqrt{\frac{2}{3}}P'k_z \\ 0 & E_g + \frac{\hbar^2 k^2}{2m_e^*} & 0 & -\frac{1}{\sqrt{6}}P'k_+ \\ -\frac{1}{\sqrt{2}}P'k_- & 0 & -P-Q & b \\ \sqrt{\frac{2}{3}}P'k_z & -\frac{1}{\sqrt{6}}P'k_- & b^* & -P+Q \\ \frac{1}{\sqrt{6}}P'k_+ & \sqrt{\frac{2}{3}}P'k_z & -c^* & 0 \\ 0 & \frac{1}{\sqrt{2}}P'k_+ & 0 & -c^* \\ -\frac{1}{\sqrt{3}}P'k_z & -\frac{1}{\sqrt{3}}P'k_- & -\frac{1}{\sqrt{2}}b^* & -\sqrt{2}Q \\ -\frac{1}{\sqrt{3}}P'k_+ & \frac{1}{\sqrt{3}}P'k_z & \sqrt{2}c^* & \sqrt{\frac{3}{2}}b^* \end{pmatrix}$$

$$\begin{pmatrix}
\frac{1}{\sqrt{6}}P'k_- & 0 & -\frac{1}{\sqrt{3}}P'k_z & -\frac{1}{\sqrt{3}}P'k_- \\
\sqrt{\frac{2}{3}}P'k_z & \frac{1}{\sqrt{2}}P'k_- & -\frac{1}{\sqrt{3}}P'k_+ & \frac{1}{\sqrt{3}}P'k_z \\
-c & 0 & -\frac{1}{\sqrt{2}}b & \sqrt{2}c \\
0 & -c & -\sqrt{2}Q & \sqrt{\frac{3}{2}}b \\
-P+Q & -b & \sqrt{\frac{3}{2}}b^* & \sqrt{2}Q \\
-b^* & -P-Q & -\sqrt{2}c^* & -\frac{1}{\sqrt{2}}b^* \\
\sqrt{\frac{3}{2}}b & -\sqrt{2}c & -P-\Delta_{so} & 0 \\
\sqrt{2}Q & -\frac{1}{\sqrt{2}}b & 0 & -P-\Delta_{so}
\end{pmatrix}, \tag{2.64}$$

with [37]

$$\begin{aligned}
P &= \left(\frac{\hbar^2}{2m_0}\right)\gamma_1'\left(k_x^2+k_y^2+k_z^2\right), \\
Q &= \left(\frac{\hbar^2}{2m_0}\right)\gamma_2'\left(k_x^2+k_y^2-2k_z^2\right), \\
c &= \left(\frac{\hbar^2}{2m_0}\right)\left[-\sqrt{3}\gamma_2'(k_x^2-k_y^2)+i2\sqrt{3}\gamma_3'k_xk_y\right], \\
b &= \left(\frac{\hbar^2}{2m_0}\right)\gamma_3'2\sqrt{3}(k_x-ik_y)k_z, \\
k_\pm &= k_x \pm k_y.
\end{aligned} \tag{2.65}$$

The Kane parameter describing the coupling between the conduction and valence bands P' is given by Eq. (2.20), and Δ_{so} is given by Eq. (2.21) [38]. Once again, the effective masses can be found by diagonalising $\mathcal{H}_{LK}$ and expanding about $\vec{k}=0$, or by applying perturbation theory. The effective mass of the conduction band electron can be found from Eq. (2.13). The number of bands taken into account, as well as the addition of higher order terms in the perturbation theory, effects the degree of accuracy to which m_e^* is calculated. Staying with only second order terms, and including the effects of the closest Γ_8^v and Γ_7^v valence bands on the lowest energy Γ_6^c conduction gives the following effective mass,

$$\frac{m_0}{m_e^*} = 1 + \frac{P'^2}{3}\left(\frac{2}{E_g}+\frac{1}{E_g+\Delta_{so}}\right), \tag{2.66}$$

or including the more remote Γ_8^c and Γ_7^c conduction bands gives [39]

$$\frac{m_0}{m_e^*} = 1 + \frac{P'^2}{3}\left(\frac{2}{E_g}+\frac{1}{E_g+\Delta_{so}}\right) - \frac{P''^2}{3}\left(\frac{2}{E(\Gamma_8^c)-E_g}+\frac{1}{E(\Gamma_7^c)-E_g}\right)+C, \tag{2.67}$$

with

$$P'' \equiv -i\frac{\hbar}{m_0}\left\langle S\left|p_z\right|Z'\right\rangle \tag{2.68}$$

and $C=-2$, an empirically chosen dimensionless constant generally acceptable for all materials. The Luttinger Kohn parameters γ_1', γ_2' and γ_3' have an additional contribution from the conduction band [40]:

$$\gamma_1' = \gamma_1 - \frac{2}{3}\frac{m_0}{\hbar^2}\left(\frac{P'^2}{E_g}\right), \tag{2.69}$$

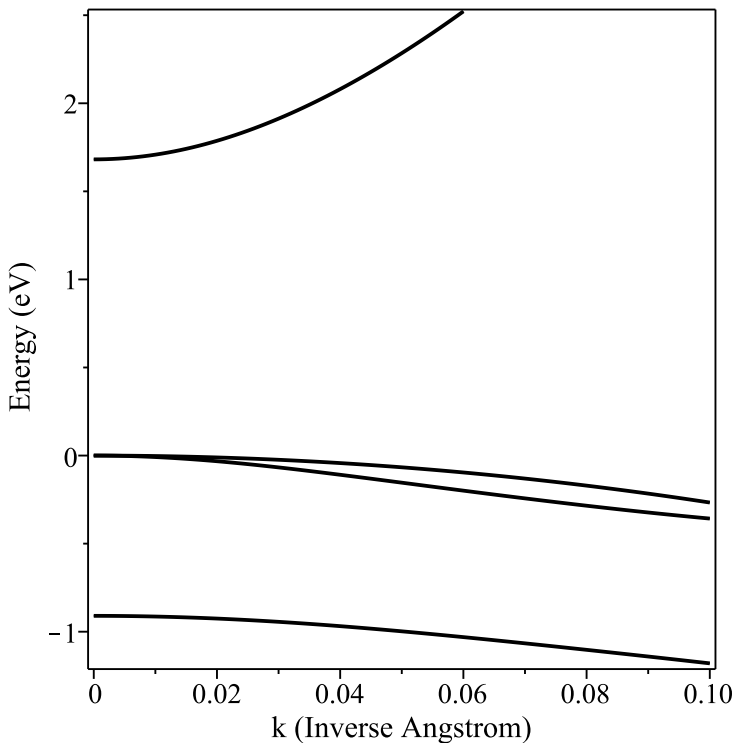

Figure 2-5: Band structure for $Cd_{1-x}Mn_xTe$ obtained using the 8×8 Luttinger Kohn model. This has been calculated using the values in Appendix K, for $x = 0.05$.

$$\gamma_2' = \gamma_2 - \frac{1}{3}\frac{m_0}{\hbar^2}\left(\frac{P'^2}{E_g}\right), \tag{2.70}$$

$$\gamma_3' = \gamma_3 - \frac{1}{3}\frac{m_0}{\hbar^2}\left(\frac{P'^2}{E_g}\right). \tag{2.71}$$

Then the effective masses of the heavy hole, light hole and the split off band are given by

$$\frac{m^*_{hh,\perp}}{m_0} = \frac{1}{\gamma_1' - 2\gamma_2'}, \qquad \frac{m^*_{hh,||}}{m_0} = \frac{1}{\gamma_1' + \gamma_2'}, \tag{2.72}$$

$$\frac{m^*_{lh,\perp}}{m_0} = \frac{1}{\gamma_1' + 2\gamma_2'}, \qquad \frac{m^*_{lh,||}}{m_0} = \frac{1}{\gamma_1' - \gamma_2'}, \tag{2.73}$$

$$\frac{m^*_{so,\perp}}{m_0} = \frac{m^*_{so,||}}{m_0} = \frac{1}{\gamma_1'}. \tag{2.74}$$

The band structure for $Cd_{1-x}Mn_xTe$ using the 8×8 Kohn Luttinger Hamiltonian can be seen in Figure. (2-5).

2.5 Pikus Bir (Strain) Hamiltonian

Strain in crystals is created by deformation and is defined as a relative lattice displacement. Figure (2-6) illustrates this concept; under a small uniform deformation of the lattice, the position vector $\vec{r}$ is distorted in both orientation and length. The strain coefficients ε_{ij} (where $i, j = x, y, z$) define the deformation of the lattice and are dimensionless [31].

Strain modifies the valence band structure, including the band edge energies and the effective masses, which are among the most important parameters characterising any semiconductor material. In addition, strain also introduces additional coupling between the heavy hole bands, light hole bands, and the spin orbit split-off bands. Strain however can be useful for modifying the band structure of semiconductors in a beneficial and predictable way.

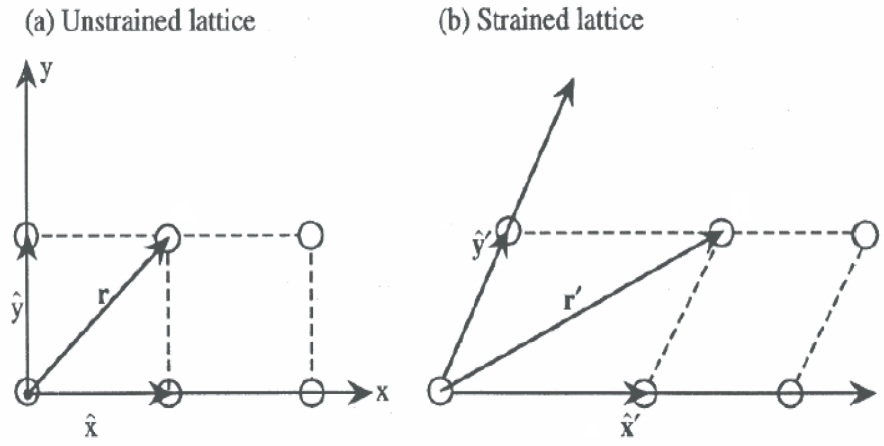

Figure 2-6: Comparison of the unstrained lattice with position vector $\vec{r}$, and the strained lattice with position vector $\vec{r}\,'$. Under a small uniform deformation of the lattice, the position vector $\vec{r}$ is distorted in both orientation and length. Taken from Ref. [31].

When a material with a smaller band gap is embedded inbetween a material with a larger band gap a quantum well is formed, Figure (2-7) (which shows a quantum well where $Cd_{1-x}Mn_xTe$ forms the well material and $Cd_{1-y}Mg_yTe$ forms the barrier material). This can create strain due to the lattice mismatch between the material forming the well and the barrier. The use of lattice mismatched materials in semiconductor devices provides an advantage over lattice matched materials, due to the greater degree of freedom in adjusting the band structure of the heterostructure device. Any strain can be decomposed into either hydrostatic strain or shear strain. The hydrostatic strain does not break the crystal symmetry and only shifts energy levels without lifting the band degeneracy. When a compressive hydrostatic stress is applied, the semiconductor bandgap widens, and when a tensile hydrostatic stress is applied the bandgap diminishes. The most important effect arising from lattice mismatch is a lifting of the degeneracy of the heavy and light holes in the valence band at the Γ point, which leads to a splitting of the heavy and light holes bands. This is due to the shear strain, which breaks the cubic symmetry of the lattice [41][42]. The nature of this splitting depends on whether it is brought on by either tensile or compressive strain.

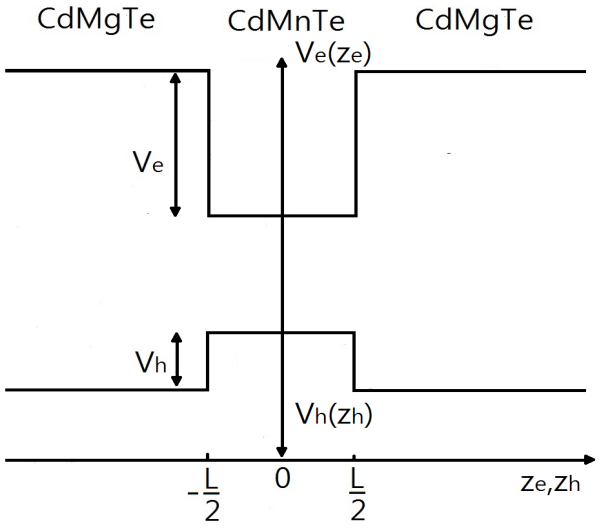

Figure 2-7: Schematic diagram of a $Cd_{1-x}Mn_xTe/Cd_{1-y}Mg_yTe$ finite quantum well of length L, with offsets V_e and V_h for the conduction and valence band.

Figure (2-8) illustrates that in a quantum well in the presence of compressive (tensile) strain the bottom of the conduction band is shifted up (down) by the value of the hydrostatic strain. For the case of the holes, at the Γ point the valence band for the heavy and light hole is shifted up or down depending on the tensile or compressive hydrostatic strain, and is also shifted by a value which depends on the shear strain. A general stress will induce both hydrostatic and shear strain; two important stress examples are the biaxial and uniaxial stress, see Figure (2-9).

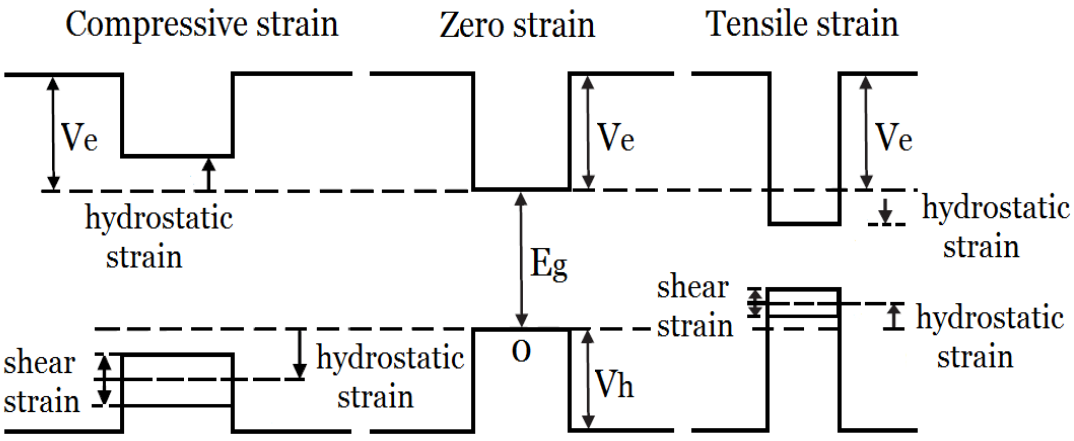

Figure 2-8: Comparison showing a quantum well under compressive strain, an unstrained quantum well, and a quantum well under tensile strain.

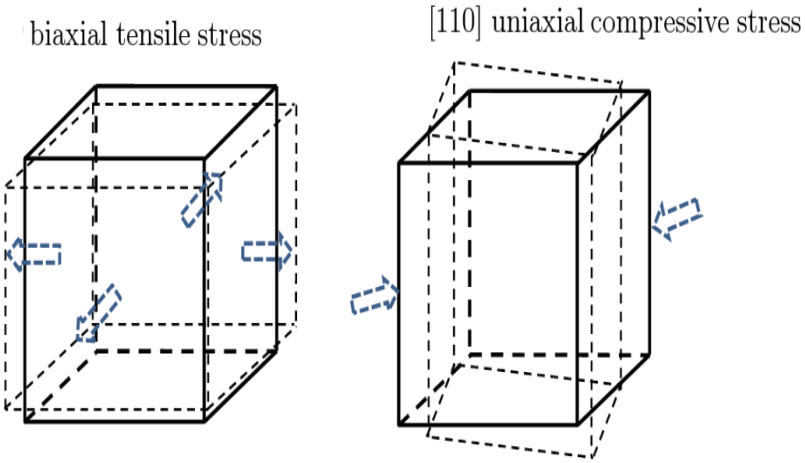

Figure 2-9: Cubic crystal under in plane biaxial tensile stress. Under this type of stress, the x-y plane is still a square, but the x,y-z plane becomes a rectangle (left). Cubic crystal under [110] uniaxial compressive stress. Under this type of stress, the x-y plane becomes a rhombus, and the x,y-z plane becomes a rectangle (right). Taken from Ref. [43].

In this section we will discuss how the previously introduced Luttinger Kohn Hamiltonian needs to be modified in order to incorporate strain. We consider the particular case relevant for the quantum well systems studied in later chapters in which the inplane strain produced by mismatching lattice constants in the well and the barrier region is given by the strain coefficients

$$\begin{aligned}
\varepsilon_{xx} &= \varepsilon_{yy} = \varepsilon_{||} = \frac{a_x - a_0}{a_x}, \\
\varepsilon_{zz} &= -\frac{2C_{12}}{C_{11}}\varepsilon_{||}, \\
\varepsilon_{xy} &= \varepsilon_{yz} = \varepsilon_{zx} = 0,
\end{aligned} \tag{2.75}$$

where a_x and a_0 are the lattice constants of the well and the barrier material, and C_{11} and C_{12} the stiffness constants. The biaxial compressive strain can be divided into a hydrostatic component and a shear strain component. The hydrostatic component is [44][45]

$$\begin{aligned}
\delta E_{hy} &\equiv -a(\varepsilon_{xx} + \varepsilon_{yy} + \varepsilon_{zz}) \\
&= -2a\left[1 - \frac{C_{12}}{C_{11}}\right]\varepsilon_{||},
\end{aligned} \tag{2.76}$$

where a is the hydrostatic deformation potential. Since this component of the strain just raises or lowers the whole band uniformly, it can be included in the band gap energy. The shear strain component is written as [44][45]

$$\begin{aligned}
\delta E_{sh} &\equiv -b(\varepsilon_{xx} + \varepsilon_{yy} - 2\varepsilon_{zz}) \\
&= -2b\left[1 + \frac{2C_{12}}{C_{11}}\right]\varepsilon_{||},
\end{aligned} \tag{2.77}$$

where b is the shear deformation potential. Since this strain component leads to a lifting of the degeneracy and influences the position of the heavy and light hole it needs to be added to the Luttinger Kohn Hamiltonian. The shear component of the strain for the heavy and light hole can be added to the 4×4 Hamiltonian in Eq. (2.50) (using the same basis functions), by writing it as [46]

$$\mathcal{H}_\zeta = \begin{pmatrix} -\zeta & 0 & 0 & 0 \\ 0 & \zeta & 0 & 0 \\ 0 & 0 & \zeta & 0 \\ 0 & 0 & 0 & -\zeta \end{pmatrix}, \tag{2.78}$$

where

$$\zeta = \frac{1}{2}\delta E_{sh} = -b\left[1 + \frac{2C_{12}}{C_{11}}\right]\varepsilon_{||}. \tag{2.79}$$

The band structure which now includes the effect of strain (calculated by using both Hamiltonians in Eq. (2.50) and (2.78)) along both the k_x and k_z direction for both compression ($\zeta < 0$) and tensile ($\zeta > 0$) strain for a $Cd_{1-x}Mn_xTe$ /$Cd_{1-y}Mg_yTe$ quantum well is shown in Figure (2-10) and (2-11). The lattice constants are given by

$$\begin{aligned} a_x &= (1-x)a_{\mathrm{CdTe}} + x a_{\mathrm{MnTe}} \\ &= (6.4810 - 0.143x)\mathring{A}, \end{aligned} \tag{2.80}$$

for $Cd_{1-x}Mn_xTe$ from Eq. (1.2), and

$$\begin{aligned} a_0 &= (1-y)a_{\mathrm{CdTe}} + x a_{\mathrm{MgTe}} \\ &= (6.418 - 0.061y)\mathring{A}, \end{aligned} \tag{2.81}$$

for $Cd_{1-y}Mg_yTe$, where $a_{\mathrm{CdTe}} = 6.4810$ Å [13], $a_{\mathrm{MnTe}} = 6.338$ Å [12], and $a_{\mathrm{MgTe}} = 6.420$ Å [13]. Comparing Figure (2-3) with Figures (2-10)-(2-11) it can be seen that the heavy hole and light hole band degeneracy has been lifted due to strain, and there is a splitting between the light and heavy hole for both tensile and compressive strain which is not present when there is no strain. As show in Figure (2-10) for the case of compressive strain the heavy hole band is now above the light hole band at $\vec{k} = 0$ for both the k_x and k_z directions, while for tensile strain the light hole band is shifted above the heavy hole band for both the k_x and k_z directions. For tensile strain in the k_z direction at a point away from $\vec{k} = 0$, the heavy hole band crosses the light hole band, as shown in Figure (2-11). Since the strain can lift the degeneracy of the heavy and light hole and can move the light hole band above the heavy hole it should be included in the next Chapter, which will look at trapping quasiparticles in a DMS quantum well.

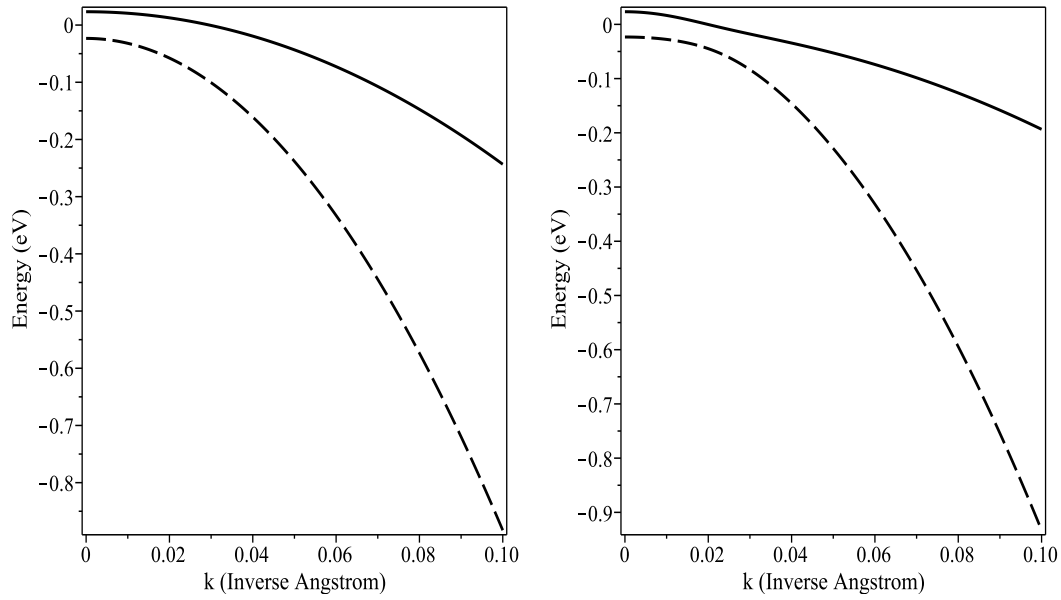

Figure 2-10: Band structure of the heavy (solid line) and light (dashed line) hole for compressive strain in both the k_z (left) and k_x (right) direction. These were calculated using the deformation potentials given in Appendix K for a $Cd_{1-x}Mn_x$/Te $Cd_{1-y}Mg_y$Te quantum well with $x = 0.05$, and $y = 0.05$.

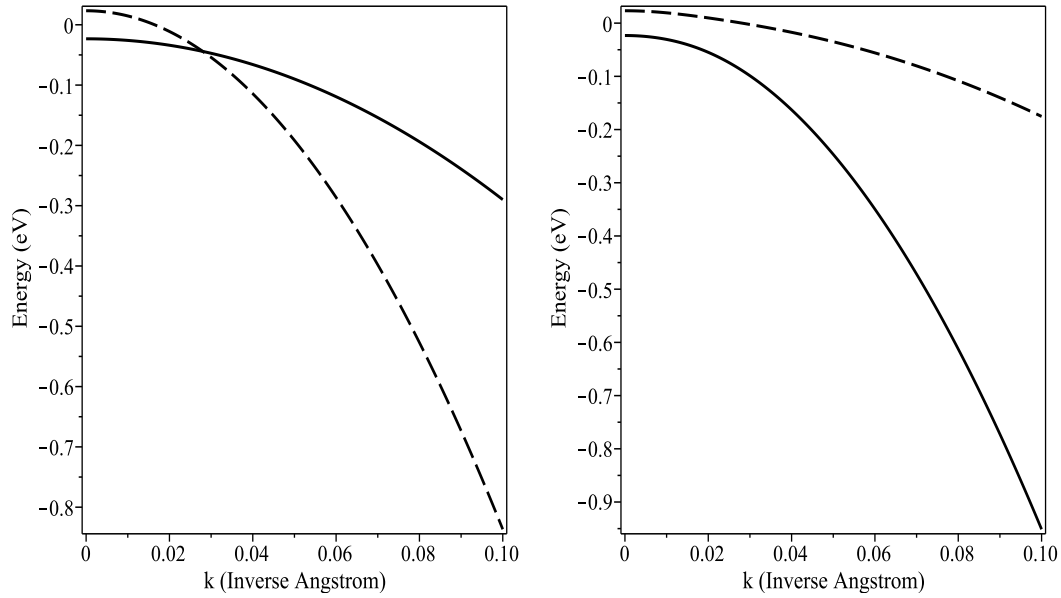

Figure 2-11: Band structure of the heavy (solid line) and light (dashed line) hole for tensile strain in both the k_z (left) and k_x (right) direction. These were calculated using the deformation potentials given in Appendix K for a $Cd_{1-x}Mn_x$Te/$Cd_{1-y}Mg_y$Te quantum well with $x = 0.05$, and $y = 0.05$.

2.6 Conclusion

To conclude, the bandstructure of the conduction and valence bands in a semiconductor has been considered within the framework of $\vec{k} \cdot \vec{p}$ theory. Firstly the Kane model was discussed, but it predicts that the heavy hole band disperses upwards, contrary to the finding of experiments. To rectify this the Luttinger Kohn Hamiltonian was investigated and shown to be an improvement. The relationship between Hamiltonian parameters and effective masses, available from experiment, was considered, for the Luttinger Kohn Hamiltonian extended to include the conduction, heavy hole, light hole and split off band. The effect of strain was also added to the Luttinger Kohn model, with the use of the Pikus Bir Hamiltonian. The compressive strain and tensile strain for both the heavy and light hole was calculated for a $Cd_{1-x}Mn_xTe$ /$Cd_{1-y}Mg_yTe$ quantum well. A splitting at $\vec{k} = 0$ between the light and heavy hole, for both tensile and compressive strain occurs which is not present in the absence of strain. Since the strain can lift the degeneracy of the heavy and light hole, and can move the light hole band above the heavy hole it is necessary to include it in subsequent studies described in the next Chapter. This looks at the trapping of quasiparticles in a DMS quantum well in the presence of an inhomogeneous magnetic field.

Chapter 3

Zero dimensional magnetic traps for quasiparticles

As mentioned previously due to the sp-d exchange interaction in a DMS there is a giant Zeeman splitting of the electronic states that can be hundreds of times larger than that in non magnetic semiconductors in the presence of an applied magnetic field. A relatively small external magnetic field can cause a sizeable Zeeman splitting of the electronic energy levels. This feature has be utilised in another way, by taking advantage of the large effective g factor present in a DMS, and combining it with a spatially inhomogeneous applied magnetic field, to create a spatially varying Zeeman potential that acts as a confining potential for quasiparticles [6][47][48][49][50]. Inhomogeneous magnetic fields with nanoscale spatial variation can be provided by a variety of systems, such as microscale ferromagnets [47][48][49], where the microscale ferromagnet is deposited on top of the DMS quantum well. They have been used as a source of an inhomogeneous magnetic field [51][52], for example for the case of a microscale ferromagnetic disk placed above a non magnetic semiconductor. In this case, the inhomogeneous magnetic field modifies the exciton kinetic energy operator, and excitons were found to be weakly confined in the semiconductor. In the case of DMSs, these have been considered in the vicinity of microscale ferromagnets with a variety of shapes (i.e circular, rectangular, and squares), and depending on the shape and orientation of the ferromagnet, different nonuniform fields are generated, which have been shown to give rise to various types of confined electron and hole states [47][48][49]. The confinement in these cases was found to be a result of the Zeeman interaction, which is hundreds of times stronger than the variation of the kinetic energy. Another possibility for obtaining inhomogeneous magnetic fields is through the use of nanoscale or mesoscopic superconductors, or the Abrikosov vortices that appear in type-II superconductors [6], which has been the subject of both theoretical and experimental studies [6][53]. Of particular interest is the magnetic vortex state of a nanoscale ferromagnetic disk [47][54], which can confine quasiparticles in a DMS quantum well within the magnetic vortex.

In this Chapter the inhomogeneous magnetic field created from a nanoscale ferromagnetic disk in the vortex state will be studied, firstly by looking at the energy contributions in a ferromagnet, and then the conditions needed for a magnetic vortex to form. Before the properties of excitons in a DMS in the presence of a magnetic field is studied, we first consider the effect the inhomogeneous magnetic field has upon the valence band holes, and the splitting of the heavy and light holes in the DMS quantum well.

3.1 Energy contributions in ferromagnets

Ferromagnetic materials like nickel, iron, cobalt and compounds containing these elements exhibit a collective interaction between the electron spins. This phenomenon causes a permanent magnetic moment, and due to the exchange interaction individual magnetic moments will attempt to align with other magnetic moments within a material. If the magnetic moments align in a parallel fashion, the material is ferromagnetic; if the magnetic moments align antiparallel, the material is antiferromagnetic [55].

While the exchange interaction forces nearby spins to align into a uniform distribution, the demagnetising field has the opposite effect on the long range scale. The magnetisation generates a magnetic stray field which influences the magnetisation itself and is expressed in terms of a demagnetisation energy [56]. The demagnetisation energy forces the magnetisation to align parallel to the sample's surface, in order to minimise the surface charges [57]. The resulting competition creates regions containing atoms with aligned magnetic moments called domains, whose orientation differs from that in adjacent domains. In the absence of an applied magnetic field, the domains are randomly oriented so that the net macroscopic magnetisation is zero. In the presence of an applied magnetic field, the domains align themselves with the applied field.

3.2 Vortex states

In very small ferromagnetic systems, however, the formation of domain walls is not energetically favoured. When the lateral dimensions of ferromagnetic materials shrink to the submicron regime, instead of the aggregate of magnetic domains, the magnetisation can arrange in a single, highly nonuniform pattern or a magnetic vortex.

Due to the competition between the exchange energy and the demagnetisation energy, the magnetisation essentially aligns with the disk geometry as much as possible and lies in the plane of the ferromagnet disk [54]. In this curling configuration, the spin directions change gradually in plane so as not to lose too much exchange energy, see Figure (3-1 (a)). If the spin directions remain confined in plane in the vicinity of the dot centre the angle between adjacent spins becomes increasingly large, which costs energy. Therefore, at the core of the vortex structure, the magnetisation turns out of the plane to reduce energy, see Figure (3-1 (b)). The region containing a strong out of plane magnetisation component is called the vortex core, and is typically only a few nanometres in diameter [49]. It has been observed in circular ferromagnetic disks with diameters ranging between the nm scale and up to 1 μm [54][58]. Figures (3-2 (a)) and (3-2 (b)) respectively show magnetic force microscopy images of vortex formation in ferromagnetic permalloy $Ni_{80}Fe_{20}$ disks and permalloy $Ni_{80}Fe_{20}$ disks with a variety of diameters.

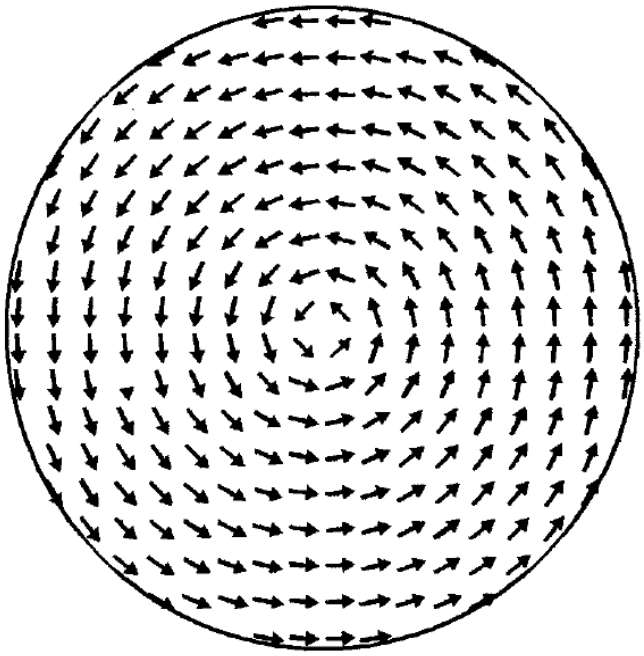

(a)

(b)

Figure 3-1: (a) The spin configuration in a nanoscale ferromagnetic disk. Far away from the centre of the disk the magnetisation continuously curls around the centre with a 'curling configuration', that aligns with the disk geometry and lies in the plane of the ferromagnet disk. (b) In the centre of the ferromagnetic disk the magnetisation turns out of the plane and forms a magnetic vortex. Taken from Ref. [59] and [60].

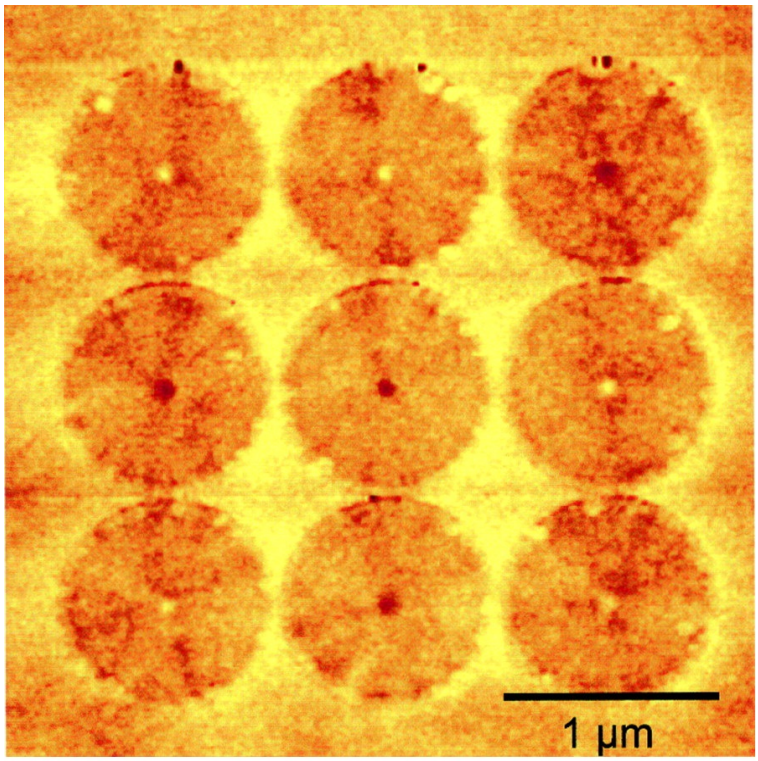

(a)

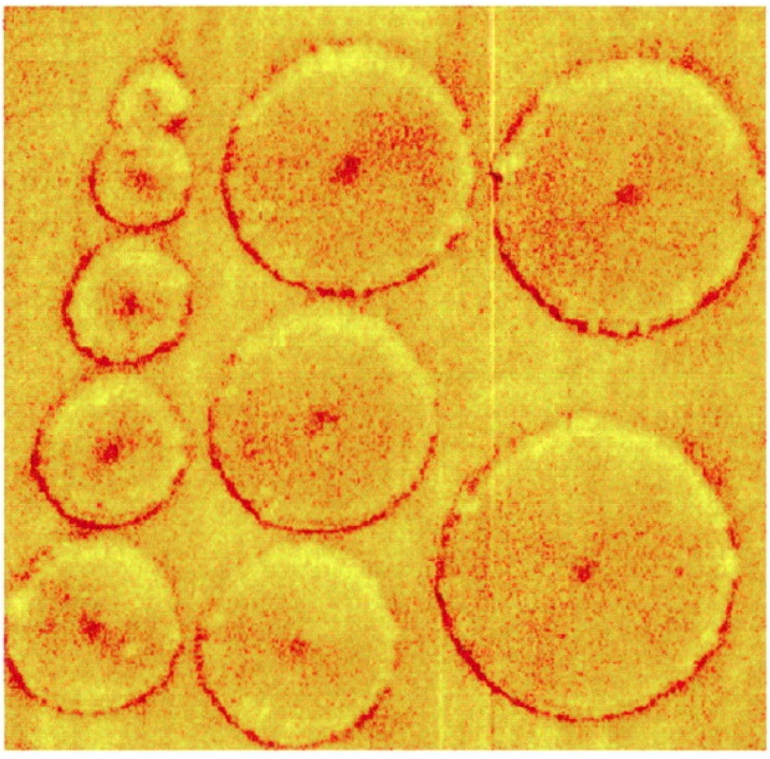

(b)

Figure 3-2: (a): Magnetic force microscopy image of vortex formation in an array of ferromagnetic permalloy $Ni_{80}Fe_{20}$ disks with a diameter of 1 μm and a thickness of 50 nm. The central dot in each disk shows the evidence of the vortex formation. (b): Magnetic force microscopy image of vortex formation in an array of ferromagnetic permalloy $Ni_{80}Fe_{20}$ disks with a thickness of 50 nm, with diameters ranging from 0.1 μm to 1 μm after an external magnetic field of 1.5 T has been applied. Taken from Ref. [58]

3.3 Magnetic field created by a nanoscale ferromagnetic disk

As mentioned previously quasiparticles can be trapped in a DMS quantum well by an inhomogeneous magnetic field created by a nanoscale ferromagnetic disk in the vortex state placed a few nanometres above the DMS [49], see Figure (3-3).

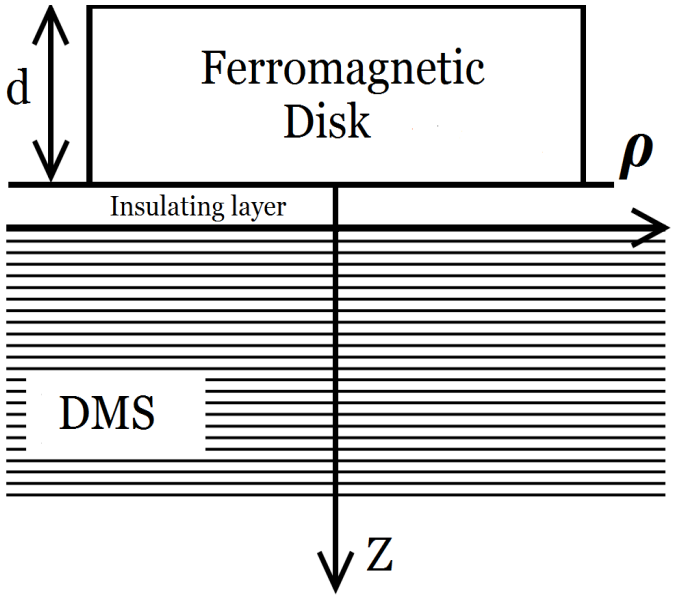

Figure 3-3: Diagram depicting a nanoscale ferromagnetic disk (of height d) in the vortex state placed a few nanometres above a DMS quantum well, using cylindrical coordinates.

The magnetic field created from this ferromagnetic disk in the vortex state can be calculated using the magnetisation profile of the vortex and the magnetostatic Maxwell equations. For a magnetic disk of height d which is small compared to the radius, the vortex magnetisation can be written as

$$\vec{M}(\vec{r}) = M_\varphi(\rho)\vec{e}_\varphi + M_z(\rho)\vec{e}_z, \tag{3.1}$$

where cylindrical coordinates $\vec{r} = (\rho, \varphi, z)$ are used [61] . Then using Maxwell's equations the resulting magnetic field in an adjacent DMS, is given by $\vec{B}(\vec{r}) = \vec{b}(\vec{r}) - \vec{b}(\vec{r} + d\vec{e}_z)$, where [62]

$$b_\rho(\rho, z) = \frac{\mu_0}{2\pi\rho}\int_0^{\rho_c} \frac{\rho' M_z(\rho')d\rho'}{\sqrt{(\rho+\rho')^2+z^2}}\left\{K(k) - E(k)\frac{[\rho'^2+z^2-\rho^2]}{[(\rho-\rho')^2-z^2]}\right\}, \tag{3.2}$$

$$b_\varphi(\rho, z) = 0, \tag{3.3}$$

and

$$b_z(\rho, z) = \frac{\mu_0 z}{\pi}\int_0^{\rho_c} \frac{\rho' M_z(\rho')d\rho'}{(\rho-\rho')^2+z^2}\frac{E(k)}{\sqrt{(\rho+\rho')^2+z^2}}, \tag{3.4}$$

with $K(k)$ and $E(k)$ the usual elliptical integrals [63], and $k = \sqrt{4\rho\rho'/[(\rho+\rho')^2+z^2]}$. The derivation of $b_z(\rho, z)$ is given in Appendix C. To calculate the magnetic fields we

need to know $M_z(\rho')$, and for this the magnetisation in the disk. This can be fitted to the results of micromagnetic simulations [60], using the parameterisation [61][64][65]

$$\left|M_z(\rho')\right|/M_s = \begin{cases} (\rho_c^2 - \rho'^2)(\rho_c^2 + \rho'^2) & \rho' \leq \rho_c \\ 0 & \rho' > \rho_c \end{cases}, \tag{3.5}$$

where ρ_c is the vortex core radius, and M_s is the saturation magnetisation. The saturation magnetisation of a ferromagnetic material is a measure of the maximum amount of field that can be generated by a material, resulting from all the magnetic moments being mutually aligned with the external field; beyond this no further increase in magnetisation occurs. The radius of the magnetic core is about 30 nm in permalloy $Ni_{80}Fe_{20}$ disks [58][59] and 10 nm in Fe disks [60], and $\mu_0 M_s = 1.06$ T in permalloy $Ni_{80}Fe_{20}$ disks. A plot of the magnetic field as a function of ρ for different z values, calculated assuming M_z given by Eq. (3.5), is given in Figure (3-4). It can be seen that $B_z(\rho, z)$ is largest at $\rho = z = 0$, which corresponds to the centre of the vortex. It decreases for increasing ρ and z, and becomes negligible for distances beyond the core radius. The quasiparticles are trapped by the z component of the magnetic field within the vortex. $B_r(\rho, z)$ is equal to zero when $\rho = 0$, and reaches a maximum at a distance ρ close to the value of ρ_c. This maximum value is roughly half that of $B_z(\rho, z)$ for the same z value.

The giant Zeeman effect in the DMS has the possibility of trapping quasiparticles in the strong magnetic field near the disk surface. The eigenstates of a quasiparticle placed in a magnetic field are given by the Schrödinger equation [47]

$$\left\{ \frac{\hbar^2}{2m^*_{e(h)}} \left\{ -i\nabla_{e(h)} + \frac{e}{\hbar c}\vec{A}(\vec{r}_{e(h)}) \right\}^2 - \frac{1}{2} g^{e(h)}_{eff} \mu_B \vec{\sigma} \cdot \vec{B}(\vec{r}_{e(h)}) \right\} \phi_m(\rho, \varphi, z) = E\phi_m(\rho, \varphi, z). \tag{3.6}$$

We use here the simple parabolic band model of the conduction and valence band. Given the symmetries of the magnetic field, solutions of this equation have the form [47]

$$\phi_m(\rho, \varphi, z) = \exp(im\varphi) \begin{pmatrix} \phi^m_\uparrow(\rho, z) \\ \phi^{m+1}_\downarrow(\rho, z)\exp(i\varphi) \end{pmatrix}, \tag{3.7}$$

where the angular momentum quantum number m is an integer (Appendix D). The extra phase $\exp(i\varphi)$ in the spin down component has two significant consequences. Firstly σ_z is not a good quantum number, a consequence of the radial component of the magnetic field. Secondly the (usually expected) degeneracy between states with $\pm m$ is now lifted, since the presence of the magnetic field breaks the time reversal symmetry responsible for this degeneracy.

To demonstrate the lifting of the $\pm m$ degeneracy the magnetic fields can be approximated by removing the terms involving the vector field $\vec{A}(\vec{r})$ (negligible compared to the Zeeman term) and by applying a Taylor series for small (ρ, z) (when one is only interested in the most strongly bound states, localised at small (ρ, z)) so that

$$B_\rho(\rho, z) = \mu_0 M_s B\left(\frac{z}{\rho_c}\right)\frac{\rho}{\rho_c}, \tag{3.8}$$

$$B_z(\rho, z) = \mu_0 M_s \left[A\left(\frac{z}{p_c}\right) - b_3 \frac{\rho^2}{p_c^2} \right], \tag{3.9}$$

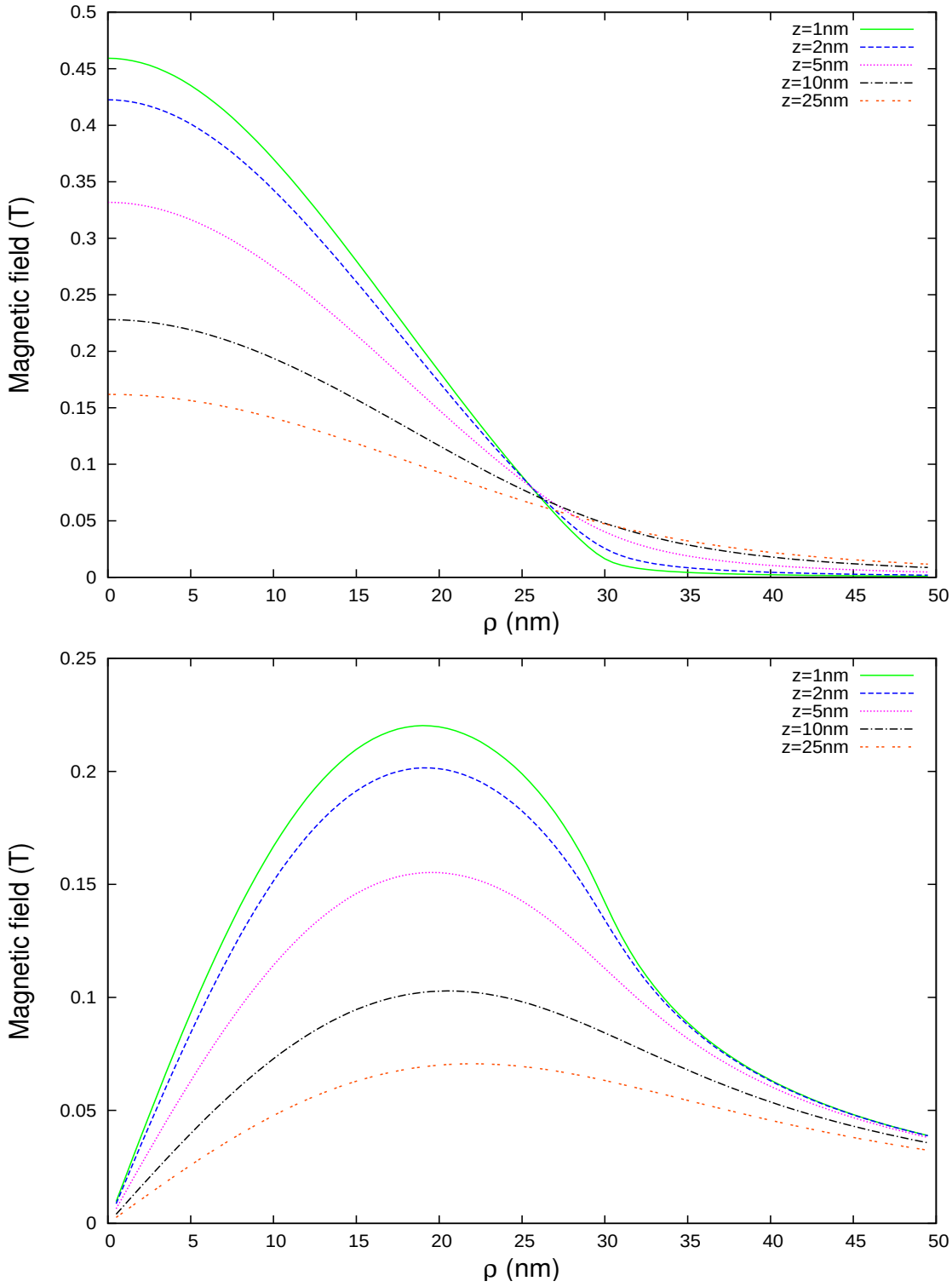

Figure 3-4: Top: Magnetic field component $B_z(\rho, z)$ for a nanoscale ferromagnetic disk in the vortex state as function of ρ for several values of z. Bottom: Magnetic field component $B_\rho(\rho, z)$ for a nanoscale ferromagnetic disk in the vortex state as function of ρ for several values of z. With a vortex core radius of $\rho_c = 30$ nm, a disk height of $d = 50$ nm, and $\mu_0 M_s = 1.06$ T (found in permalloy $Ni_{80}Fe_{20}$ disks).

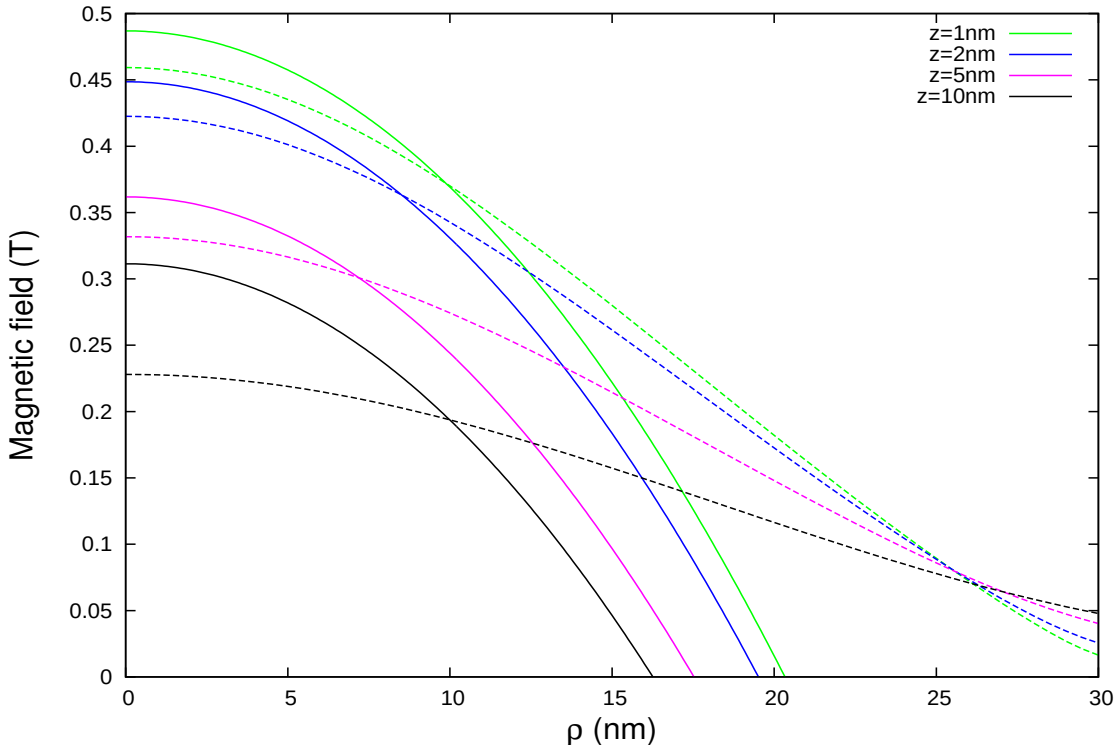

Figure 3-5: Comparison of the magnetic field component $B_z(\rho, z)$ for a nanoscale ferromagnetic disk in the vortex state as function of ρ for several values of z using both Eq. (3.4) (dashed line) and the approximation in Eq. (3.9) (solid line). With a vortex core radius of $\rho_c = 30$ nm, a disk height of $d = 50$ nm, and $\mu_0 M_s = 1.06$ T (found in permalloy $Ni_{80}Fe_{20}$ disks).

where

$$A(z) = b_1 - b_2 z + 2b_3 z^2, \tag{3.10}$$

and

$$B(z) = \frac{b_2}{2} - 2b_3 z, \tag{3.11}$$

with $b_1 = 1/2$, $b_2 = (\pi + 2)/4$ and $b_3 = 1$ [47]. These are only accurate for the magnetic fields where the wavefunction is localised for $\rho \ll p_c$ and $z \ll p_c$, so for values of 15 nm or less for z and ρ, which can be seen in Figure (3-5) where the approximation for the magnetic field using Eq. (3.9) is plotted as a function of ρ.

The following eigenfunction ansatz for Eq. (3.7) is used

$$\phi_{\uparrow}^{m}(\rho, z) = a_1(z/p_c)\left(\frac{\rho}{p_c}\right)^{|m|} \exp\left(-\frac{\rho^2}{b^2 p_c^2}\right), \tag{3.12}$$

$$\phi_{\downarrow}^{m}(\rho, z) = a_2(z/p_c)\left(\frac{\rho}{p_c}\right)^{|m+1|} \exp\left(-\frac{\rho^2}{b^2 p_c^2}\right), \tag{3.13}$$

where a_1 and a_2 are both functions to be determined, as is the decay constant b. Substituting these approximations into Eq. (3.6) gives 2 sets of equations from the different spin components in the Schrödinger equation, and then depending on the value of m the

following set of coupled equations are obtained

$$\left[\frac{4(|m|+1)}{b^2} - \frac{d^2}{dz^2} - \alpha A(z)\right] a_1(z) - \frac{s-1}{2}\alpha B(z) a_2(z) = e_m a_1(z), \tag{3.14}$$

$$\left(\frac{4}{b^4} - \alpha\right) a_1(z) + \frac{s+1}{2}\alpha B(z) a_2(z) = 0, \tag{3.15}$$

$$\left[\frac{4(|m|+s+1)}{b^2} - \frac{d^2}{dz^2} + \alpha A(z)\right] a_2(z) - \frac{s+1}{2}\alpha B(z) a_1(z) = e_m a_2(z). \tag{3.16}$$

$$-\left(\frac{4}{b^4} + \alpha\right) a_2(z) + \frac{s-1}{2}\alpha B(z) a_1(z) = 0. \tag{3.17}$$

where $s = 1$ if $m \geq 0$ and $s = -1$ if $m < 0$, $E_0 = \hbar^2/(2m^*_{e(h)}\rho_c^2)$, $e_m = E/E_0$ and $\alpha = g^{e(h)}_{eff}\mu_B\mu_0 M_s/2E_0$ [47]. If $s = 1$ then the solutions of these equations are obtained from Eq. (3.17) if $4/b^4 = -\alpha$; possible only if $\alpha < 0$. This being the case when $M_s < 0$ (when the z axis disk magnetisation M_z points away from the DMS surface). Eq. (3.15) has the solution $a_1(z) = \frac{1}{2}B(z)a_2(z)$ when $b^2 = \sqrt{4/|\alpha|}$. Substituting this answer into Eq. (3.16) gives

$$\left[2\sqrt{|m|}(|m|+2)\right] a_2(z) - \frac{d^2}{dz^2}a_2(z) + \alpha\left(\frac{(6-\pi)(10+\pi)}{128}\right) a_2(z) = e_m a_2(z). \tag{3.18}$$

The solution is found to be $a_2(z) = \exp(-kz)$ (assuming $z > 0$), with eigenenergy $e_m = 2\sqrt{|\alpha|}(m+2) + \alpha\frac{(6-\pi)(10+\pi)}{128} - k^2$. Finally Eq. (3.14) gives $k = -0.321\sqrt{|\alpha|} + 0.127|\alpha|$ (with $k > 0$ satisfied for $|\alpha| > 1.56$) with $e_m = 2\sqrt{|\alpha|}m$ [47]. This is similar to a harmonic oscillator ($s = 1$, and therefore $m \geq 0$). These solutions are only valid up to z^2 since the expansion for $B_\rho(\rho, z)$ and $B_z(\rho, z)$ was truncated after the second term in the Taylor series. This in turn means that the a_1 and a_2 terms are also only valid up to z^2, and therefore the second derivative of a_1 is only valid up to z^0.

To summarise for $M_z < 0$ there is only a solution when $s = +1$ or $m \geq 0$, proving that the $\pm m$ degeneracy is indeed lifted in this simplified case. These simple solutions only hold for small values of m, where the wavefunctions are localised at small ρ and z and the Taylor series for the magnetic fields are valid [47].

3.4 Electronic states in a quantum well

Quantum wells were briefly introduced in Chapter 2, so before we look at a new effective Hamiltonian for holes in a DMS quantum well a more detailed discussion about quantum wells is needed. This thesis looks at the DMS quantum well system $Cd_{1-x}Mn_xTe$/ $Cd_{1-y}Mg_yTe$, with a layer of $Cd_{1-x}Mn_xTe$ embedded in between $Cd_{1-y}Mg_yTe$, see Figure (2-7). This creates a confinement potential for both conduction band electrons and valence band holes arising from the energy difference between the larger band gap of the barrier $Cd_{1-y}Mg_yTe$ and the smaller band gap of the well material $Cd_{1-x}Mn_xTe$. In a quantum well the energetically low lying electrons and holes states are confined in the z direction to a region of length L (lengths around 100 Å), which is considerably larger than the lattice constant, but sufficiently small that the electron and hole wavefunctions become

quantised. The translational motion in the xy plane perpendicular to the confinement direction is unrestricted.

Within the framework developed in the preceding section using $\vec{k}_e \rightarrow -i\vec{\nabla}_e$, $\vec{k}_h \rightarrow -i\vec{\nabla}_h$ the electron and hole confinement in the z direction can be described by the one dimensional Schrodinger equation with Hamiltonian

$$\mathcal{H}_e^{\perp}(z_e) = -\frac{\hbar^2}{2m_{e,\perp}^*}\frac{\partial^2}{\partial z_e^2} + V_e(z_e), \tag{3.19}$$

for electrons, and

$$\mathcal{H}_h^{\perp}(z_h) = -\frac{\hbar^2}{2m_{h,\perp}^*}\frac{\partial^2}{\partial z_h^2} + V_h(z_h), \tag{3.20}$$

for holes, where $m_{e,\perp}^*$ and $m_{h,\perp}^*$ are the effective masses of the electron and hole (heavy or light) in the z direction. For the case of an infinite well where the excited electrons are completely confined in the quantum well the wavefunction has to vanish at the interface between the well and barrier. Standing waves are established. There is an infinite ladder of states and no unbound states. This is the case when the potentials $V(z_e)$ and $V(z_h)$ are given by

$$V_e(z_e) = \begin{cases} 0 & -L/2 \leq z_e \leq L/2 \\ \infty & \text{elsewhere} \end{cases}, \tag{3.21}$$

for electrons, and

$$V_h(z_h) = \begin{cases} 0 & -L/2 \leq z_h \leq L/2 \\ \infty & \text{elsewhere} \end{cases}, \tag{3.22}$$

for holes. The eigenfunctions of the one particle Hamiltonians of the quantum well for an infinite well, satisfying

$$\mathcal{H}_e^{\perp}(z_e)\phi_e(z_e) = E_e^{\perp}(z_e)\phi_e(z_e), \qquad \mathcal{H}_h^{\perp}(z_h)\phi_h(z_h) = E_h^{\perp}(z_h)\phi_h(z_h), \tag{3.23}$$

are then

$$\phi_e(z_e) = \begin{cases} \sqrt{\frac{2}{L}}\cos\left(\frac{n_e\pi z_e}{L}\right) & \text{for odd } n_e \\ \sqrt{\frac{2}{L}}\sin\left(\frac{n_e\pi z_e}{L}\right) & \text{for even } n_e \end{cases}, \qquad \phi_h(z_h) = \begin{cases} \sqrt{\frac{2}{L}}\cos\left(\frac{n_h\pi z_h}{L}\right) & \text{for odd } n_h \\ \sqrt{\frac{2}{L}}\sin\left(\frac{n_h\pi z_h}{L}\right) & \text{for even } n_h \end{cases}, \tag{3.24}$$

where $n_e, n_h = 1, 2, ...$, with corresponding eigenenergies

$$\begin{aligned} E_e^{\perp} &= \frac{\hbar^2\pi^2 n_e^2}{2m_{e,\perp}^* L^2} \qquad \text{for electrons,} \\ E_h^{\perp} &= \frac{\hbar^2\pi^2 n_h^2}{2m_{h,\perp}^* L^2} \qquad \text{for holes.} \end{aligned} \tag{3.25}$$

For a finite square quantum well the well depth seen by electrons and holes can differ (see Figure (2-7)), described by the conduction and valence band offsets given by

$$V_{e(h)}(z_{e(h)}) = \begin{cases} V_{e(h)} & z_{e(h)} < -L/2 \\ 0 & -L/2 \leq z_{e(h)} \leq L/2 \\ V_{e(h)} & z_{e(h)} > L/2 \end{cases}. \tag{3.26}$$

When the total energy is larger than the height of the potential, the energy becomes continuous (not quantised); when the energy is less than $V_{e(h)}$ the states are bound, with a finite number of quantised states. The wider and/or more shallow the potential, the lower the energies of the quantum states. The eigenfunctions for the finite quantum well can be divided into even and odd parity solutions. For even parity

$$\phi_{e(h)}(z_{e(h)}) = \begin{cases} C_{e(h)} \exp(\kappa_{e(h)} z_{e(h)}), & z_{e(h)} < -L/2 \\ A_{e(h)} \cos(k_{e(h)} z_{e(h)}), & -L/2 < z_{e(h)} < L/2 \\ C_{e(h)} \exp(-\kappa_{e(h)} z_{e(h)}), & z_{e(h)} > L/2 \end{cases}, \tag{3.27}$$

and

$$\phi_{e(h)}(z_{e(h)}) = \begin{cases} C_{e(h)} \exp(\kappa_{e(h)} z_{e(h)}), & z_{e(h)} < -L/2 \\ B_{e(h)} \sin(k_{e(h)} z_{e(h)}), & -L/2 < z_{e(h)} < L/2 \\ -C_{e(h)} \exp(-\kappa_{e(h)} z_{e(h)}), & z_{e(h)} > L/2 \end{cases}, \tag{3.28}$$

for odd parity, where $\phi_{e(h)}(z_{e(h)})$ spreads out beyond the well (and decays exponentially), with

$$k_{e(h)} = \sqrt{2m^*_{e(h),w} E^{\perp}_{e(h)}/\hbar^2}, \tag{3.29}$$

$$\kappa_{e(h)} = \sqrt{2m^*_{e(h),b} (V_{e(h)} - E^{\perp}_{e(h)})/\hbar^2}, \tag{3.30}$$

and $E^{\perp}_{e(h)}$ the eigenenergy, found by requiring smooth solutions to Eq. (3.23). Here $m^*_{e(h),w}$ ($m^*_{e(h),b}$) is the associated mass in the quantum well (barrier) in the confinement direction. Coefficients $C_{e(h)}$ ensures continuity at $z_{e(h)} = L/2$, and the normalisation constants are

$$\begin{aligned} A_{e(h)} &= \left[\frac{L}{2} + \frac{\sin(k_{e(h)} L)}{2k_{e(h)}} + \frac{\cos^2(k_{e(h)} L)}{\kappa_{e(h)}} \right]^{-1/2}, \\ B_{e(h)} &= \left[\frac{L}{2} - \frac{\sin(k_{e(h)} L)}{2k_{e(h)}} + \frac{\sin^2(k_{e(h)} L)}{\kappa_{e(h)}} \right]^{-1/2}. \end{aligned} \tag{3.31}$$

3.5 New effective Hamiltonian for a dilute magnetic semiconductor quantum well

This section will discuss the derivation of an effective Hamiltonian to show the splitting of the heavy and light holes in a DMS quantum well in the presence of an inhomogeneous magnetic field that is both parallel and perpendicular to the z direction. This is due to the Zeeman splitting of the valence band depending on the direction of the magnetic field with respect to the quantum well growth direction (taken to be the z direction) [19].

The 4×4 Luttinger Kohn Hamiltonian in Eq. (2.50) that models the heavy and light hole bands can be rewritten by rearranging the basis as

$$\mathcal{H}_{LK} = -\begin{pmatrix} P+Q & c & -b & 0 \\ c^* & P-Q & 0 & b \\ -b^* & 0 & P-Q & c \\ 0 & b^* & c^* & P+Q \end{pmatrix}, \tag{3.32}$$

where the matrix elements are still given by Eq. (2.51). For a quantum well structure we use the following four component spinor

$$\phi(\vec{r}) = \begin{pmatrix} \phi_{\frac{3}{2}}(\vec{r}) \\ \phi_{-\frac{1}{2}}(\vec{r}) \\ \phi_{\frac{1}{2}}(\vec{r}) \\ \phi_{-\frac{3}{2}}(\vec{r}) \end{pmatrix} = \begin{pmatrix} \phi_{hh}(z_h)\phi_{\frac{3}{2}}(x,y) \\ \phi_{lh}(z_h)\phi_{-\frac{1}{2}}(x,y) \\ \phi_{lh}(z_h)\phi_{\frac{1}{2}}(x,y) \\ \phi_{hh}(z_h)\phi_{-\frac{3}{2}}(x,y) \end{pmatrix}, \tag{3.33}$$

where the functions $\phi_n(x,y)$ are undetermined at present. The ground state functions $\phi_{hh}(z_h)$ and $\phi_{lh}(z_h)$ satisfy the following Schrödinger eigenequations from Eq. (3.20) and Eq. (3.23):

$$\mathcal{H}^{\perp}_{hh}(z_h)\phi_{hh}(z_h) = \left(-\frac{\hbar^2(\gamma_1 - 2\gamma_2)}{2m_0}\frac{\partial^2}{\partial z_h^2} + V_h(z_h)\right)\phi_{hh}(z_h) = E^{\perp}_{hh}\phi_{hh}(z_h), \tag{3.34}$$

for heavy holes, where $\phi_{hh}(z_h)$ is the envelope function for the heavy hole band, and for the light hole envelope function

$$\mathcal{H}^{\perp}_{lh}(z_h)\phi_{lh}(z_h) = \left(-\frac{\hbar^2(\gamma_1 + 2\gamma_2)}{2m_0}\frac{\partial^2}{\partial z_h^2} + V_h(z_h)\right)\phi_{lh}(z_h) = E^{\perp}_{lh}\phi_{lh}(z_h). \tag{3.35}$$

The potential well $V_h(z_h)$ is given by Eq. (3.26). The functions $\phi_{hh}(z_h)$ and $\phi_{lh}(z_h)$ that satisfy Eqs. (3.34) and (3.35) are even functions given by Eq. (3.27), and fulfill the relation $\int \phi^*_{hh}(z_h)p_z\phi_{lh}(z_h)dz_h = 0$.

For a quantum well we don't use the previous $\vec{k}\cdot\vec{p}$ theory as before with $\vec{p}$, instead we use $\hbar\vec{k} = -i\hbar\vec{\nabla}$ and treat the z direction differently by working in the space of the lowest confinement state. The 4×4 Luttinger Kohn Hamiltonian needs to be turned into a set of differential equations. This can be achieved with the following integral which is separated into two directions, one perpendicular (the x and y direction) and one parallel to the z direction:

$$\tilde{\mathcal{H}}_{LK} = \int dxdy\phi^*_n(x,y)\tilde{\mathcal{H}}\phi_n(x,y) \tag{3.36}$$

where

$$\tilde{\mathcal{H}} = \int dz_h \phi^*_{hh(lh)}(z_h)\mathcal{H}_{LK}\phi_{hh(lh)}(z_h) \tag{3.37}$$

Then by integrating out the z degree of freedom the Luttinger Kohn Hamiltonian can be rewritten as [49]

$$\tilde{\mathcal{H}}_{LK}(x,y) = -\begin{pmatrix} H_{hh} & cI_{hl} & 0 & 0 \\ c^*I^*_{hl} & H_{hl} & 0 & 0 \\ 0 & 0 & H_{hl} & c^I_{hl} \\ 0 & 0 & c^*I^*_{hl} & H_{hh} \end{pmatrix}, \tag{3.38}$$

where

$$\begin{aligned} H_{hh} &= \frac{\hbar^2}{2m_0}(\gamma_1+\gamma_2)\left(-\frac{\partial^2}{\partial x^2}-\frac{\partial^2}{\partial y^2}\right)+E^{\perp}_{hh}, \\ H_{lh} &= \frac{\hbar^2}{2m_0}(\gamma_1-\gamma_2)\left(-\frac{\partial^2}{\partial x^2}-\frac{\partial^2}{\partial y^2}\right)+E^{\perp}_{lh}, \\ c &= \frac{\hbar^2}{2m_0}\sqrt{3}\left[\gamma_2\left(\frac{\partial^2}{\partial x^2}-\frac{d^2}{dy^2}\right)-2i\gamma_3\frac{\partial}{\partial x}\frac{\partial}{\partial y}\right], \end{aligned}$$

and the overlap integral is

$$I_{hl} = \int_{-L/2}^{L/2} \phi^*_{hh}(z_h)\phi_{lh}(z_h)dz_h. \tag{3.39}$$

The term b reduces to zero from the relation $\int_{-L/2}^{L/2}\phi^*_{hh}(z_h)p_z\phi_{lh}(z_h)dz_h = 0$, since p_z vanishes between states of equal symmetry, for a symmetric quantum well between $L/2$ and $-L/2$ [49].

As already mentioned the inhomogeneous magnetic field from the nanoscale ferromagnetic disk acts as an effective potential that can trap quasiparticles in the DMS quantum well due to the Zeeman interaction [49]. The Zeeman Hamiltonian for the valence band is

$$\mathcal{H}_{zeeman}(\vec{r}) = g^h_{eff}\mu_B\vec{B}(\vec{r})\cdot\vec{S}_{e(h)}, \tag{3.40}$$

where $\vec{S}_{e,h} = (S_{e(h),x}, S_{e(h),y}, S_{e(h),z})$ is the spin operator (defined in Appendix E) [47]. If the quantum well is narrow then one can rewrite it as

$$\tilde{\mathcal{H}}_z(x,y) = g^h_{eff}\mu_B\vec{B}_{av}(d)\cdot\vec{S}_{e(h)}, \tag{3.41}$$

where d is distance between the quantum well and the nanoscale ferromagnetic disk, and $\vec{B}_{av}$ is the average value of the magnetic field over the thickness of the well [49]. Then the valence band effective Hamiltonian can be written as

$$\tilde{\mathcal{H}}(x,y) = \tilde{\mathcal{H}}_{LK}(x,y) + \tilde{\mathcal{H}}_z(x,y). \tag{3.42}$$

The Zeeman splitting of the valence band depends on the direction of the magnetic field with respect to the z direction. Reordering the basis as

$$\phi(\vec{r}) = \begin{pmatrix} \phi_{\frac{3}{2}}(\vec{r}) \\ \phi_{-\frac{1}{2}}(\vec{r}) \\ \phi_{\frac{1}{2}}(\vec{r}) \\ \phi_{-\frac{3}{2}}(\vec{r}) \end{pmatrix} \rightarrow \begin{pmatrix} \phi_{\frac{3}{2}}(\vec{r}) \\ \phi_{-\frac{3}{2}}(\vec{r}) \\ \phi_{\frac{1}{2}}(\vec{r}) \\ \phi_{-\frac{1}{2}}(\vec{r}) \end{pmatrix}, \tag{3.43}$$

the new valence band effective Hamiltonian for a magnetic field in the z direction can be written as

$$\tilde{\mathcal{H}}(x,y) = \begin{pmatrix} \frac{1}{2}g^h_{eff}\mu_B B_z & 0 & 0 & 0 \\ 0 & -\frac{1}{2}g^h_{eff}\mu_B B_z & 0 & 0 \\ 0 & 0 & -\Delta_{lh} + \frac{1}{6}g^h_{eff}\mu_B B_z & 0 \\ 0 & 0 & 0 & -\Delta_{lh} - \frac{1}{6}g^h_{eff}\mu_B B_z \end{pmatrix}, \tag{3.44}$$

for the edge (at the Γ point) of the valence band quantum well. Where the energy splitting $\Delta_{lh} = |E^{\perp}_{lh} - E^{\perp}_{hh}|$ is due to the quantum well confinement. The energy of the heavy hole splits by a factor of $|g^h_{eff}\mu_B B_z|$, while the energy of the light hole splits by a factor of $|\frac{1}{3}g^h_{eff}\mu_B B_z|$. For a magnetic field perpendicular to the z direction, chosen here to be along $\hat{x}$, the valence band effective Hamiltonian is

$$\tilde{\mathcal{H}}(x,y) = \begin{pmatrix} 0 & 0 & \frac{1}{2\sqrt{3}}g^h_{eff}\mu_B B_x & 0 \\ 0 & 0 & 0 & \frac{1}{2\sqrt{3}}g^h_{eff}\mu_B B_x \\ \frac{1}{2\sqrt{3}}g^h_{eff}\mu_B B_x & 0 & -\Delta_{lh} & \frac{1}{3}g^h_{eff}\mu_B B_x \\ 0 & \frac{1}{2\sqrt{3}}g^h_{eff}\mu_B B_x & \frac{1}{3}g^h_{eff}\mu_B B_x & -\Delta_{lh} \end{pmatrix}. \tag{3.45}$$

with corresponding eigenvalues

$$E^{\mp}_{hh} = -\frac{\Delta_{lh}}{2} \mp -\frac{g^h_{eff}\mu_B B_x}{6} + \frac{1}{6}\sqrt{9\Delta^2_{lh} \pm 6\Delta_{lh}g^h_{eff}\mu_B B_x + 4(g^h_{eff}\mu_B B_x)^2}, \tag{3.46}$$

$$E^{\mp}_{lh} = -\frac{\Delta_{lh}}{2} \mp -\frac{g^h_{eff}\mu_B B_x}{6} - \frac{1}{6}\sqrt{9\Delta^2_{lh} \pm 6\Delta_{lh}g^h_{eff}\mu_B B_x + 4(g^h_{eff}\mu_B B_x)^2}. \tag{3.47}$$

When $\Delta_{lh} >> |g^h_{eff}\mu_B B_x|$ then up to terms quadratic in the external field B_x, the eigenvalues in Eq. (3.46) and (3.47) can be simplified to

$$E^{\mp}_{hh} \approx \frac{1}{12}\frac{g^h_{eff}\mu_B B_x}{\Delta_{lh}} g^h_{eff}\mu_B B_x, \tag{3.48}$$

$$E^{\mp}_{lh} \approx -\Delta_{lh} \mp \frac{g^h_{eff}\mu_B B_x}{3} - \frac{1}{12}\frac{g^h_{eff}\mu_B B_x}{\Delta_{lh}} g^h_{eff}\mu_B B_x, \tag{3.49}$$

where the full derivation is given in Appendix F. If the mixing between the light and heavy holes is emitted then the heavy holes don't split and the light holes split by $|\frac{2}{3}g^h_{eff}\mu_B B_x|$ [49]. Figure (3-6) shows the splitting between the heavy and light holes for both magnetic configurations. It can be seen that when the magnetic field is in the z direction the heavy holes split by 3 times the amount of the light holes, and the energy splitting has a linear relationship with respect to the magnetic field, while for a magnetic field perpendicular to the z direction the light holes split considerably more than the heavy holes, and the behaviour is not linear due to the mixing between the bands.

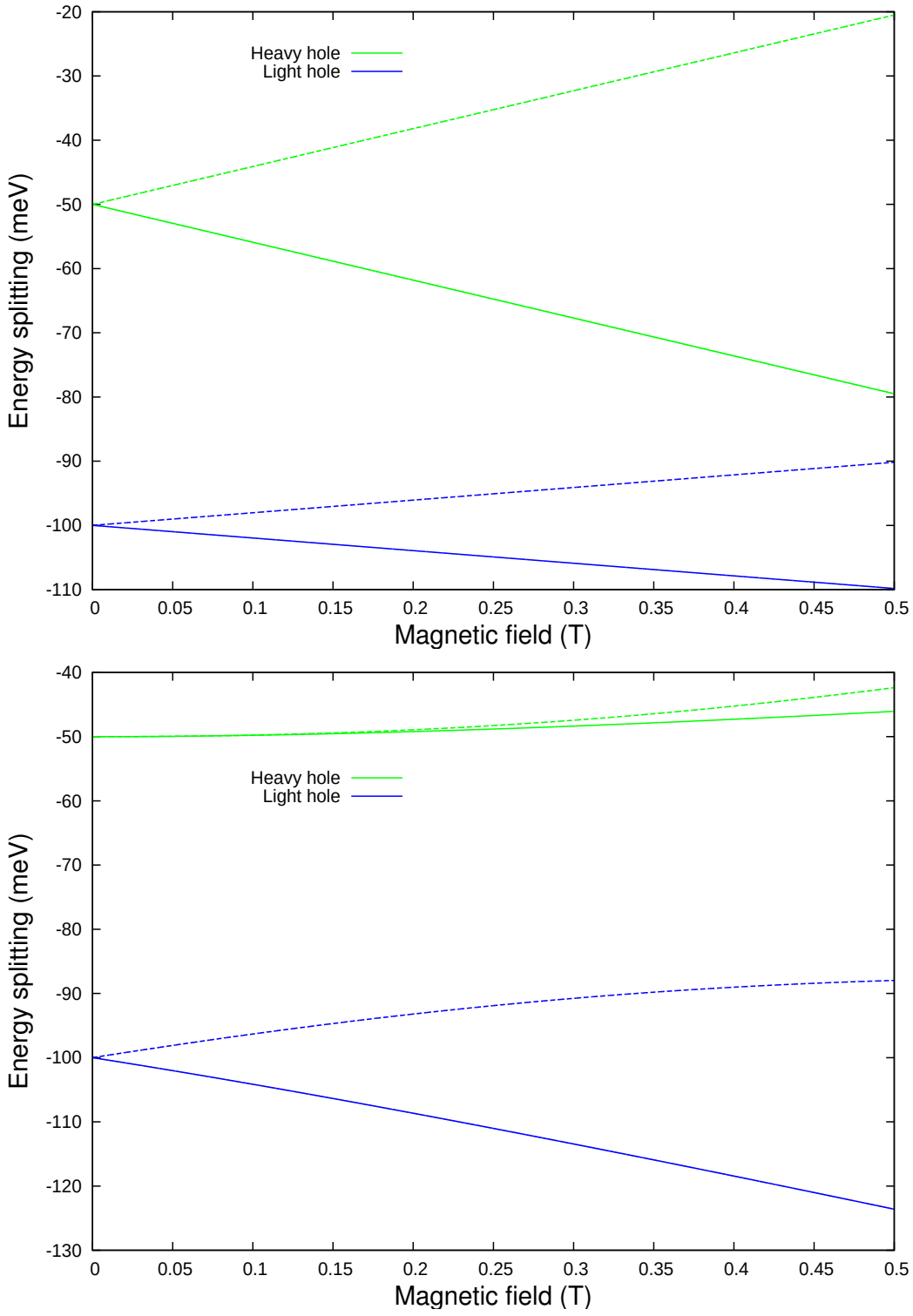

Figure 3-6: Top: Energy splitting of the heavy and light holes in a $Cd_{1-x}Mn_xTe/Cd_{1-y}Mg_yTe$ quantum well as a function of the magnetic field in the z direction. Bottom: Energy splitting of the heavy and light holes in a $Cd_{1-x}Mn_xTe/Cd_{1-y}Mg_yTe$ quantum well as a function of the magnetic field in the x direction. Parameters for $Cd_{1-x}Mn_xTe$ are given in the Table in Appendix K, $x = 0.05$, and Δ_{lh}=50 meV [49] have been assumed.

To include the effect of strain to the effective Hamiltonian in Eq. (3.42) we can write

$$\tilde{\mathcal{H}}(x,y) = \tilde{\mathcal{H}}_{LK}(x,y) + \tilde{\mathcal{H}}_z(x,y) + \mathcal{H}_\zeta, \tag{3.50}$$

where $\mathcal{H}_\zeta$ is given by Eq. (2.78). For a magnetic field in the z direction the new valence band effective Hamiltonian with the inclusion of strain is

$$\tilde{\mathcal{H}}(x,y) = \begin{pmatrix} \frac{1}{2}g^h_{eff}\mu_B B_z - \zeta & 0 & 0 & 0 \\ 0 & -\frac{1}{2}g^h_{eff}\mu_B B_z - \zeta & 0 & 0 \\ 0 & 0 & -\Delta_{lh} + \frac{1}{6}g^h_{eff}\mu_B B_z + \zeta & 0 \\ 0 & 0 & 0 & -\Delta_{lh} - \frac{1}{6}g^h_{eff}\mu_B B_z + \zeta \end{pmatrix}, \tag{3.51}$$

with corresponding eigenvalues

$$E^{\pm}_{hh} = \pm\frac{1}{2}g^h_{eff}\mu_B B_z - \zeta, \tag{3.52}$$

$$E^{\pm}_{lh} = -\Delta_{lh} \pm \frac{1}{6}g^h_{eff}\mu_B B_z + \zeta. \tag{3.53}$$

For a magnetic field perpendicular to the z direction the valence band effective Hamiltonian with the inclusion of strain is

$$\tilde{\mathcal{H}}(x,y) = \begin{pmatrix} -\zeta & 0 & \frac{1}{2\sqrt{3}}g^h_{eff}\mu_B B_x & 0 \\ 0 & -\zeta & 0 & \frac{1}{2\sqrt{3}}g^h_{eff}\mu_B B_x \\ \frac{1}{2\sqrt{3}}g^h_{eff}\mu_B B_x & 0 & -\Delta_{lh} + \zeta & \frac{1}{3}g^h_{eff}\mu_B B_x \\ 0 & \frac{1}{2\sqrt{3}}g^h_{eff}\mu_B B_x & \frac{1}{3}g^h_{eff}\mu_B B_x & -\Delta_{lh} + \zeta \end{pmatrix}, \tag{3.54}$$

with corresponding eigenvalues

$$E^{\mp}_{hh} = -\frac{\Delta_{lh}}{2} \mp -\frac{g^h_{eff}\mu_B B_x}{6} + \frac{1}{6}\sqrt{9\Delta^2_{lh} \pm 6\Delta_{lh}g^h_{eff}\mu_B B_x + 4(g^h_{eff}\mu_B B_x)^2 + 36\zeta^2 \mp 12B_x\zeta g^h_{eff}\mu_B - 36\zeta\Delta_{lh}}, \tag{3.55}$$

$$E^{\mp}_{lh} = -\frac{\Delta_{lh}}{2} \mp -\frac{g^h_{eff}\mu_B B_x}{6} - \frac{1}{6}\sqrt{9\Delta^2_{lh} \pm 6\Delta_{lh}g^h_{eff}\mu_B B_x + 4(g^h_{eff}\mu_B B_x)^2 + 36\zeta^2 \mp 12B_x\zeta g^h_{eff}\mu_B - 36\zeta\Delta_{lh}}. \tag{3.56}$$

Figure (3-7) shows a comparison plot for the splitting between the heavy and light holes for both magnetic configurations with and without the inclusion of strain. It can be seen that the strain has little effect on the splitting compared to the effect of the giant Zeeman interaction due to the sp-d exchange interaction in a DMS. Due to this fact for simplification the strain will be omitted in the next Chapters when discussing excitons in a DMS quantum well in the presence of a magnetic field.

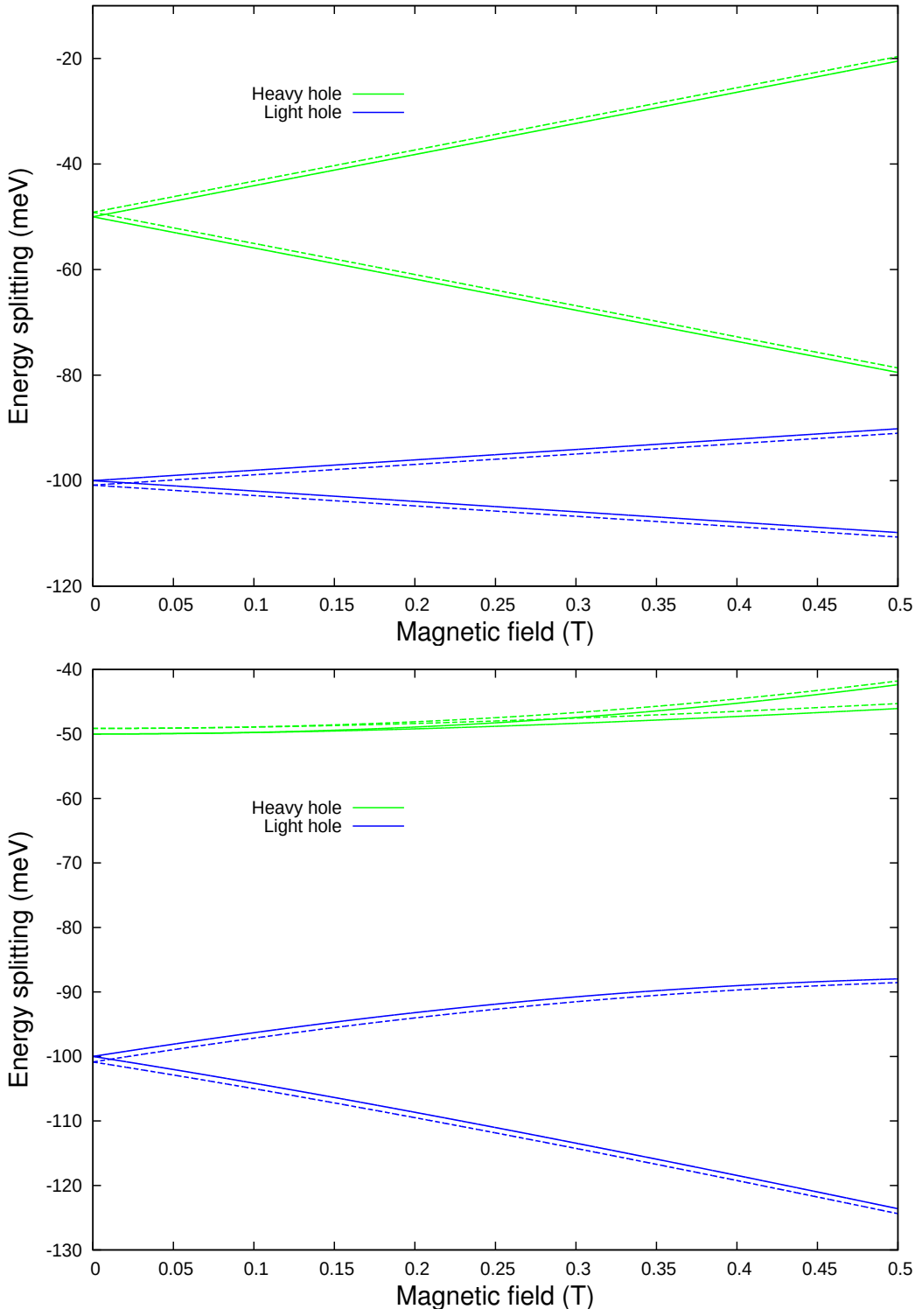

Figure 3-7: Top: Comparison of the energy splitting of the heavy and light holes in a $Cd_{1-x}Mn_xTe/Cd_{1-y}Mg_yTe$ quantum well with (dashed) and without (solid) the inclusion of the strain as a function of the magnetic field in the z direction. Bottom: Comparison of the energy splitting of the heavy and light holes in a $Cd_{1-x}Mn_xTe/ Cd_{1-y}Mg_yTe$ quantum well with (dashed) and without (solid) the inclusion of the strain as a function of the magnetic field in the x direction. Parameters for $Cd_{1-x}Mn_xTe$ are given in the Table in Appendix K, $x = 0.05$ and Δ_{lh}=50 meV [49] have been assumed.

3.6 Conclusion

To conclude, in this Chapter the effect of an inhomogeneous magnetic field from a nanoscale ferromagnetic disk in the vortex state upon the valance band has been studied. This was done by deriving a new effective Hamiltonian to describe the splitting of the holes in a DMS quantum well in the presence of a magnetic field either parallel and perpendicular to the z direction. When the magnetic field is in the z direction the splitting of the heavy holes is 3 times that of the light holes splitting, while for a magnetic field perpendicular to the z direction the light holes split much more than the heavy holes, and there is mixing between the bands. The effect of the strain in the case of $Cd_{1-x}Mn_xTe/Cd_{1-y}Mg_yTe$ is negligible compared to the giant Zeeman interaction due to the sp-d exchange interaction in the DMS. Therefore the strain will be omitted in the next Chapters where excitons in a DMS quantum well in the presence of a magnetic field will be considered.

Chapter 4

Excitons in the presence of a homogeneous magnetic field

When photons of energy comparable to the band gap are incident on a semiconductor, they can be absorbed by electrons providing them with enough energy to be excited from the valence band to the conduction band. A hole state is then created in the valence band which behaves like a positively charged particle. At low enough temperatures there will be insufficient free carriers to screen the electron and hole, and they can lower their energy by approaching one another and binding together. The electron and hole interact via the Coulomb interaction and this bound electron-hole pair is called an exciton.

In the previous Chapter the band structure for electrons in the conduction band and holes in the valence band, and the splitting of heavy and light holes in a DMS quantum well due to a magnetic field from a nanoscale ferromagnetic disk in the vortex state was discussed. The Coulomb interaction between the hole and electron in the DMS quantum well has been ignored up until now. In this Chapter the fundamental properties of excitons in a bulk semiconductor, and in a quantum well, will be discussed. A variational approach will be followed to calculate the binding energies for both a heavy and light hole exciton as a function of the quantum well size. Then, excitons in a DMS quantum well in the presence of a homogeneous magnetic field will be studied, to look at a simple picture for the behaviour of the exciton binding energy, before excitons in the presence of an inhomogeneous magnetic field are studied. The binding energy for both a heavy and light hole exciton is calculated, as well as a look at how the binding energy changes as a function of the well width for different values of the magnetic field. Results are reported for a $Cd_{1-x}Mn_xTe/Cd_{1-y}Mg_yTe$ quantum well, which has not previously been studied in this way, and the majority of studies looking at the material $Cd_{1-x}Mn_xTe$ have $Cd_{1-x}Mn_xTe$ as the barrier material instead of the well material [66][67][68].

4.1 Excitons in bulk semiconductors

Here the basic Schrödinger equation for an exciton in a bulk semiconductor will be discussed. The electron hole system of the exciton is analogous to a hydrogen atom, since the mass of the hole is generally much greater than the electron. Using the effective mass

theory, the electrons and holes obey

$$\mathcal{H}_{ex}\phi_{ex} = \left[-\frac{\hbar^2}{2m_e^*}\nabla_e^2 - \frac{\hbar^2}{2m_h^*}\nabla_h^2 - \frac{e^2}{4\pi\varepsilon_0\varepsilon_r\left|\vec{r}_e - \vec{r}_h\right|}\right]\phi_{ex} = E_{ex}\phi_{ex}, \tag{4.1}$$

where m_e^* and m_h^* are the effective masses of the electron and hole, ε_0 is the permittivity of free space, ε_r is the dielectric constant of the material, $\vec{r}_e$ and $\vec{r}_h$ are the positions of the electron and hole, and $|\vec{r}_e - \vec{r}_h|$ the distance between them. The terms in this equation are the kinetic energy of the conduction electron, the kinetic energy of the hole, and the Coulomb interaction between the electron and hole [69].

This equation can be separated into two parts, one for the centre of mass motion and the other for the relative motion of the electron hole system, by defining

$$\vec{R} = \frac{m_e^*\vec{r}_e + m_h^*\vec{r}_h}{m_e^* + m_h^*}, \tag{4.2}$$

and

$$\vec{r} = \vec{r}_e - \vec{r}_h. \tag{4.3}$$

In terms of these variables, the Hamiltonian becomes [70]

$$\mathcal{H}_{ex} = \left[-\frac{\hbar^2}{2(m_e^* + m_h^*)}\nabla_{\vec{R}}^2\right] + \left\{-\frac{\hbar^2}{2\mu}\nabla_{\vec{r}}^2 - \frac{e^2}{4\pi\varepsilon_0\varepsilon_r\vec{r}}\right\}, \tag{4.4}$$

with reduced mass

$$\mu = \frac{m_e^* m_h^*}{m_e^* + m_h^*}. \tag{4.5}$$

The two resulting equations are

$$\left[-\frac{\hbar^2}{2(m_e^* + m_h^*)}\nabla_{\vec{R}}^2\right]\phi_K(\vec{R}) = E_K\phi_K(\vec{R}), \tag{4.6}$$

for the centre of mass, and

$$\left\{-\frac{\hbar^2}{2\mu}\nabla_{\vec{r}}^2 - \frac{e^2}{4\pi\varepsilon_0\varepsilon_r\vec{r}}\right\}\phi_n(\vec{r}) = E_X\phi_n(\vec{r}), \tag{4.7}$$

for the relative motion. The solution for the centre of mass motion is

$$\phi_K(\vec{R}) = \exp(i\vec{K}\cdot\vec{R}), \tag{4.8}$$

with energy

$$E_K = \frac{\hbar^2 K^2}{2(m_e^* + m_h^*)}, \tag{4.9}$$

the kinetic energy of the centre of mass. The solution for the relative motion follows the usual hydrogenic solution, where the wavefunction is written as a product of a radial function and the spherical harmonics

$$\phi_n(\vec{r}) = R_{n,l}(r)Y_{l,m}(\theta,\phi), \tag{4.10}$$

where $R_{n,l}$ are the Laguerre polynomials and $Y_{l,m}$ the spherical harmonics. The energy spectrum is then given by

$$E_X = -\frac{R_{ex}}{n^2}, \tag{4.11}$$

where R_{ex} is the excitonic Rydberg

$$R_{ex} = \frac{\mu e^4}{32\pi^2\hbar^2\varepsilon_0^2\varepsilon_r^2}. \tag{4.12}$$

The radial solutions are characterised by a Bohr radius [69]

$$a_B^* = \frac{4\pi\varepsilon_0\varepsilon_r\hbar^2}{\mu e^2}. \tag{4.13}$$

For bulk $Cd_{1-x}Mn_xTe$ the heavy hole exciton binding energy is $E_X = 10.05$ meV, while the bulk light hole exciton binding energy is $E_X = 11.68$ meV (from Eq. (4.11), using $n = 1$). The Bohr radius for the heavy hole exciton is $a_B^* = 77$ Å, and $a_B^* = 66$ Å for the light hole exciton for bulk $Cd_{1-x}Mn_xTe$.

4.2 Excitons in a Quantum well

We now consider how this situation changes for an exciton confined within a quantum well. The Hamiltonian in this case can be expressed in the effective mass approximation as

$$\mathcal{H}_{ex} = -\frac{\hbar^2}{2m_e^*}\nabla_e^2 + \mathcal{H}_{LK} + V_e(z_e) + V_h(z_h) - \frac{e^2}{4\pi\varepsilon_0\varepsilon_r r}, \tag{4.14}$$

where the second term for the kinetic energy of the hole is determined from the Luttinger Kohn Hamiltonian given in Eq. (2.50), and $V_e(z_e)$, and $V_h(z_h)$ are the confining potentials for the electrons and holes. They are assumed to be square wells, and for a finite well they are given by Eq. (3.26).

An exact solution to the Schrödinger equation corresponding to the exciton Hamiltonian in Eq. (4.14) is not possible. Therefore a variational approach is considered, which neglects the valence band coupling and which produces a highly non-parabolic subband structure which can lead to an underestimation of the binding energy [71][72]. Ignoring the off-diagonal terms of the Luttinger Kohn Hamiltonian leads to the formation of two types of excitons, the heavy hole and the light hole exciton. With this approximation the Hamiltonian of a heavy (light) hole exciton in a quantum well reduces to [69][71]

$$\mathcal{H}_{ex} = \mathcal{H}_e^{\perp}(z_e) + \mathcal{H}_h^{\perp}(z_h) + \mathcal{H}_r(\rho, z, \varphi), \tag{4.15}$$

where $\mathcal{H}_e^{\perp}(z_e)$ and $\mathcal{H}_h^{\perp}(z_h)$ are the one particle Hamiltonians for the conduction and valence bands of the quantum well

$$\mathcal{H}_e^{\perp}(z_e) = -\frac{\hbar^2}{2m_{e,\perp}^*}\frac{\partial^2}{\partial z_e^2} + V_e(z_e), \qquad \mathcal{H}_h^{\perp}(z_h) = -\frac{\hbar^2}{2m_{h,\perp}^*}\frac{\partial^2}{\partial z_h^2} + V_h(z_h). \tag{4.16}$$

The last term in Eq. (4.15) is composed of two terms, the kinetic energy of the relative motion of the electron and hole in the xy plane, and the Coulombic interaction:

$$\mathcal{H}_r(\rho, z, \varphi) = -\frac{\hbar^2}{2\mu}\left[\frac{1}{\rho}\frac{\partial}{\partial\rho}\rho\frac{\partial}{\partial\rho} + \frac{1}{\rho^2}\frac{\partial^2}{\partial\varphi^2}\right] - \frac{e^2}{4\pi\varepsilon_0\varepsilon_r r}, \tag{4.17}$$

where $r = \sqrt{\rho^2 + z^2}$ and (ρ, φ, z) are the relative coordinates separating the electron and hole in cylindrical coordinates. The effective masses here for the hole and the reduced mass in terms of the Luttinger Kohn parameters, γ_1 and γ_2 are

$$\begin{aligned} \frac{1}{m^*_{h,\perp}} &= \frac{1}{m_0}(\gamma_1 - 2\gamma_2) \qquad \text{for heavy holes,} \\ \frac{1}{m^*_{h,\perp}} &= \frac{1}{m_0}(\gamma_1 + 2\gamma_2) \qquad \text{for light holes,} \end{aligned} \tag{4.18}$$

and

$$\begin{aligned} \frac{1}{\mu} &= \frac{1}{m^*_{e,||}} + \frac{1}{m_0}(\gamma_1 + \gamma_2) \qquad \text{for heavy holes,} \\ \frac{1}{\mu} &= \frac{1}{m^*_{e,||}} + \frac{1}{m_0}(\gamma_1 - \gamma_2) \qquad \text{for light holes,} \end{aligned} \tag{4.19}$$

from Eq. (2.59).

The exciton wavefunction is chosen to have the following form,

$$\phi_{ex} = \phi_e(z_e)\phi_h(z_h)\phi_r(\rho, z, \varphi), \tag{4.20}$$

where the variational wavefunction $\phi_r(\rho, z, \varphi)$ accounts for the internal motion of the excitons, and $\phi_e(z_e)$ and $\phi_h(z_h)$ are eigenfunctions of the one particle Hamiltonians of the quantum well (ground state solutions of the electrons and holes in the quantum well)

$$\mathcal{H}^\perp_e(z_e)\phi_e(z_e) = E^\perp_e(z_e)\phi_e(z_e), \qquad \mathcal{H}^\perp_h(z_h)\phi_h(z_h) = E^\perp_h(z_h)\phi_h(z_h). \tag{4.21}$$

For a finite well they are given by Eqs. (3.27) and (3.28).

The expectation value of $\mathcal{H}_{ex}$ is [69]

$$E_{ex} = \frac{\langle \phi_{ex}|\mathcal{H}_{ex}|\phi_{ex}\rangle}{\langle \phi_{ex}|\phi_{ex}\rangle} = \frac{\int_0^{2\pi}\int_\nu^\mu\int_\nu^\mu\int_0^\infty \phi^*_{ex}\mathcal{H}_{ex}\phi_{ex}\rho d\rho dz_e dz_h d\varphi}{\int_0^{2\pi}\int_\nu^\mu\int_\nu^\mu\int_0^\infty \phi^*_{ex}\phi_{ex}\rho d\rho dz_e dz_h d\varphi}. \tag{4.22}$$

The one particle wavefunctions $\phi_e(z_e)$ and $\phi_h(z_h)$ decay exponentially outside the well in the z direction, so it is only necessary to integrate over z_e and z_h between the limits μ and ν, which lie just outside the quantum wells. The denominator in Eq. (4.22) is

$$D = \langle \phi_{ex}|\phi_{ex}\rangle = \int_0^{2\pi}\int_\nu^\mu\int_\nu^\mu\int_0^\infty |\phi_e(z_e)|^2 |\phi_h(z_h)|^2 |\phi_r|^2 \rho d\rho dz_e dz_h d\varphi. \tag{4.23}$$

Given the three term Hamiltonian in Eq. (4.15) the numerator $\mathcal{N}$ for the expectation value of the exciton energy in Eq. (4.22) can be written as

$$\mathcal{N} = \langle \phi_{ex}|\mathcal{H}_{ex}|\phi_{ex}\rangle = \left\langle \phi_{ex}|\mathcal{H}^\perp_e(z_e)|\phi_{ex}\right\rangle + \left\langle \phi_{ex}|\mathcal{H}^\perp_h(z_h)|\phi_{ex}\right\rangle + \langle \phi_{ex}|\mathcal{H}_r(\rho, z, \varphi)|\phi_{ex}\rangle\,. \tag{4.24}$$

The first term can be written as

$$\left\langle \phi_{ex}|\mathcal{H}^\perp_e(z_e)|\phi_{ex}\right\rangle = \langle \phi_{ex}|\tau|\phi_{ex}\rangle + \langle \phi_{ex}|\upsilon|\phi_{ex}\rangle\,, \tag{4.25}$$

where τ and υ are the kinetic and potential terms of the one particle electron Hamiltonian $\mathcal{H}_e^{\perp}(z_e)$. The first part is

$$\langle\phi_{ex}|\tau|\phi_{ex}\rangle = -\frac{\hbar^2}{2m^*_{e,\perp}}\int_0^{2\pi}\int_\nu^\mu\int_\nu^\mu\int_0^\infty \phi_e^*(z_e)\phi_h^*(z_h)\phi_r^*\frac{\partial^2}{\partial z_e^2}\phi_e(z_e)\phi_h(z_h)\phi_r\rho d\rho dz_e dz_h d\varphi, \tag{4.26}$$

which after differentiating becomes

$$\begin{aligned}\langle\phi_{ex}|\tau|\phi_{ex}\rangle = & -\frac{\hbar^2}{2m^*_{e,\perp}}\int_0^{2\pi}\int_\nu^\mu\int_\nu^\mu\int_0^\infty \Big[\phi_e^*(z_e)\phi_e''(z_e)|\phi_h(z_h)|^2|\phi_r|^2 \\ & +2\phi_e^*(z_e)\phi_e'(z_e)|\phi_h(z_h)|^2\phi_r^*\phi_r' + |\phi_e(z_e)|^2|\phi_h(z_h)|^2\phi_r^*\phi_r''\Big]\rho d\rho dz_e dz_h d\varphi.\end{aligned} \tag{4.27}$$

The first term when normalised with the denominator gives the one particle kinetic energy of the electron, which when coupled with $\langle\phi|\upsilon|\phi\rangle$ in Eq. (4.25) results in the one particle electron energy $E_e^{\perp}(z_e)$, defined in Eq. (3.25). For stationary states within semiconductor microstructures the wavefunctions are real and the chain rule gives

$$\phi_e(z_e)\phi_e'(z_e) = \frac{1}{2}\frac{\partial\phi_e^2(z_e)}{\partial z_e}. \tag{4.28}$$

Thus Eq. (4.25) can be simplified to

$$\begin{aligned}\left\langle\phi_{ex}|\mathcal{H}_e^{\perp}(z_e)|\phi_{ex}\right\rangle = & E_e^{\perp}(z_e)D - \frac{\hbar^2}{2m_e^*}\int_0^{2\pi}\int_\nu^\mu\int_\nu^\mu\int_0^\infty\Bigg\{|\phi_h(z_h)|^2\left[\frac{\partial\phi_e^2(z_e)}{\partial z_e}\right]\phi_r^*\phi_r' \\ & +|\phi_e(z_e)|^2\,|\phi_h(z_h)|^2\,\phi_r^*\phi_r''\Bigg\}\rho d\rho dz_e dz_h d\varphi.\end{aligned} \tag{4.29}$$

Integrating by parts over dz_e for the first part in the integrand and substituting back into Eq. (4.29) gives

$$\begin{aligned}\left\langle\phi_{ex}|\mathcal{H}_e^{\perp}(z_e)|\phi_{ex}\right\rangle = & E_e^{\perp}(z_e)D - \frac{\hbar^2}{2m^*_{e,\perp}}\int_0^{2\pi}\int_\nu^\mu\int_0^\infty|\phi_h(z_h)|^2\Big\{\Big[|\phi_e(z_e)|^2\,\phi_r^*\phi_r'\Big]_\nu^\mu \\ & -\int_\nu^\mu\Big[|\phi_e(z_e)|^2\,\phi_r'^2 + |\phi_e(z_e)|^2\,\phi_r^*\phi_r'' - |\phi_e(z_e)|^2\,\phi_r^*\phi_r''\Big]dz_e\Big\}\rho d\rho dz_h d\varphi.\end{aligned} \tag{4.30}$$

The last two terms in the integration over z_e cancel out and examination of the first term on the right hand side shows that this will not contribute since $\phi_e(z_e)$ it vanishes at the limits μ and ν. Therefore

$$\begin{aligned}\left\langle\phi_{ex}|\mathcal{H}_e^{\perp}(z_e)|\phi_{ex}\right\rangle = & E_e^{\perp}(z_e)D \\ & +\frac{\hbar^2}{2m^*_{e,\perp}}\int_0^{2\pi}\int_\nu^\mu\int_\nu^\mu\int_0^\infty|\phi_e(z_e)|^2\,|\phi_h(z_h)|^2\,\phi_r'^2\rho d\rho dz_e dz_h d\varphi.\end{aligned} \tag{4.31}$$

An analogous equation exists for the one particle Hamiltonian for the valence band

$$\begin{aligned}\left\langle \phi_{ex}|\mathcal{H}_h^{\perp}(z_h)|\phi_{ex}\right\rangle &= E_h^{\perp}(z_h)D \\ &\quad +\frac{\hbar^2}{2m_{h,\perp}^*}\int_0^{2\pi}\int_\nu^\mu\int_\nu^\mu\int_0^\infty |\phi_e(z_e)|^2\,|\phi_h(z_h)|^2\,\phi_r'^2\rho d\rho dz_e dz_h d\varphi.\end{aligned} \tag{4.32}$$

The last term in the Hamiltonian in Eq. (4.15) can be written as

$$\begin{aligned}\langle\phi_{ex}|\mathcal{H}_r(\rho,z,\varphi)|\phi_{ex}\rangle &= -\frac{\hbar^2}{2\mu}\int_0^{2\pi}\int_\nu^\mu\int_\nu^\mu\int_0^\infty \phi_e^*(z_e)\phi_h^*(z_h)\phi_r^*\left[\frac{1}{\rho}\frac{\partial}{\partial\rho}\rho\frac{\partial}{\partial\rho}+\frac{1}{\rho^2}\frac{\partial^2}{\partial\phi^2}\right] \\ &\qquad \phi_e(z_e)\phi_h(z_h)\phi_r\rho d\rho dz_e dz_h d\varphi \\ &\quad -\frac{e^2}{4\pi\varepsilon_0\varepsilon_r}\int_0^{2\pi}\int_\nu^\mu\int_\nu^\mu\int_0^\infty \frac{1}{\vec{r}}|\phi_e(z_e)|^2|\phi_h(z_h)|^2|\phi_r|^2\rho d\rho dz_e dz_h d\varphi.\end{aligned} \tag{4.33}$$

The exciton binding energy E_X is then determined by the requirement that [69]

$$E_{ex} = E_e^{\perp}(z_e) + E_h^{\perp}(z_h) - E_X. \tag{4.34}$$

To determine E_X we use a variational wavefunction for ϕ_r and minimise E_{ex} as a function of the variational parameters [73][66][67][74][75][68]. The trial wavefunctions that will be discussed will be the Harrison and Greene and Bajaj wavefunction.

4.2.1 Harrison model

The Harrison trial wavefunction for φ_r is given by

$$\phi_r(\rho,z) = \exp\left(\frac{-\sqrt{\rho^2+\alpha^2 z^2}}{\lambda}\right), \tag{4.35}$$

where λ and α are variational parameters [69]. Using Eq. (4.35) in (4.20) it is possible to minimise the expectation value in Eq. (4.22) with respect to λ and α, and hence calculate the exciton binding energy for different quantum well widths. This was done using the downhill simplex method in multi-dimension for minimising functions with more than one variable [76]. The integration was performed using a weighted Simpson's integration in Fortran. The accuracy of the calculation is effected by the limit of the integrations and the discretisation. The binding energy and variational parameters were found to converge to a value accurate to 5 decimal places when the z_e and z_h integrals were integrated between $\pm(L/2 - \mathrm{Ln}(0.00001)/2\kappa_{e(h)})$ (this is sufficient distance for the wavefunction to have decayed outside the well). While the ρ integral was integrated from 0 to 10^4. The discretisation for the z integrals and ρ integrals was set to values to ensure the convergence of the binding energies and variational parameters to 5 decimal places.

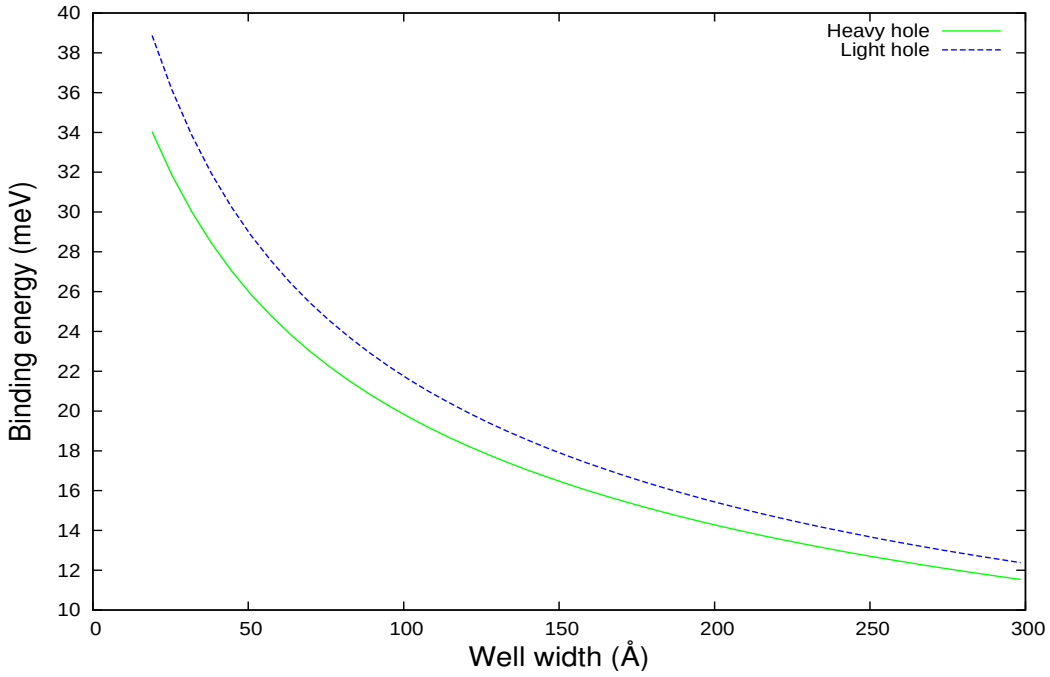

Figure 4-1: The exciton binding energy as a function of the quantum well width for excitons in a $Cd_{1-x}Mn_xTe$ infinite quantum well for both the heavy and light hole excitons using the Harrison model. The values of the physical parameters used for $Cd_{1-x}Mg_xTe$ are given in the table in Appendix K, and $x = 0.01$.

The binding energies for the heavy hole and light hole excitons in a $Cd_{1-x}Mn_xTe$ infinite well has been calculated as a function of the well width L, and is shown in Figure (4-1). It is seen that the values of the heavy hole and light hole exciton binding energy increase as L is reduced, the reason for this behaviour being that the exciton wavefunction is compressed in the quantum well as L is reduced, leading to increased binding. The binding energy of the heavy hole exciton is lower than the light hole exciton binding energy for an infinite well. This can be explained by looking at the binding energy for bulk $Cd_{1-x}Mn_xTe$, where he bulk heavy hole exciton binding energy is 10.05 meV and the bulk light hole exciton binding energy is 11.68 meV, calculated from Eq. (4.11) (using $n = 1$) . This is due to the light hole exciton having a greater reduced mass than the heavy hole exciton.

The values of the binding energies for the heavy and light hole exciton calculated as a function of the width of the $Cd_{1-x}Mn_xTe/Cd_{1-y}Mg_yTe$ quantum well (where $Cd_{1-x}Mn_xTe$ forms the well and $Cd_{1-y}Mg_yTe$ forms the barrier, see Figure (2-7)) for different Mg concentrations y is shown in Figure (4-2 (a)). The band gap for $Cd_{1-x}Mn_xTe$ in the well is taken to be

$$E_w = (1.606 + 1.592x) \text{ eV}, \tag{4.36}$$

from Eq. (1.1), and for the band gap of $Cd_{1-y}Mg_yTe$

$$E_b = (1.606(1 - y) + 3.2y) \text{ eV}. \tag{4.37}$$

The conduction and valence band offsets are (Eq. (3.26))

$$V_e = 0.7(E_b - E_w), \qquad V_h = 0.3(E_b - E_w). \tag{4.38}$$

The subband energies are determined by numerically solving the transcendental equations for a finite square well

$$\left[\frac{E_e^{\perp}}{V_e}\right]^{1/2} = \cos\left(\left(\frac{m_{e,\perp}^{*}E_e^{\perp}}{2\hbar^2}\right)^{1/2} L\right), \tag{4.39}$$

and

$$\left[\frac{E_h^{\perp}}{V_h}\right]^{1/2} = \cos\left(\left(\frac{m_{h,\perp}^{*}E_h^{\perp}}{2\hbar^2}\right)^{1/2} L\right). \tag{4.40}$$

It can be seen from Figure (4-2 (a)) that for a given value of y, the value of the exciton binding energy increases as the well width L is reduced until it reaches a maximum and then it starts to drop. This is from the fact that as L is decreased the exciton wavefunction is compressed in the quantum well leading to increased binding, until it reaches a certain value of L where the wavefunction starts spilling into the surrounding $Cd_{1-y}Mg_yTe$ layers, at which point the binding energy starts to approach the bulk value of $Cd_{1-y}Mg_yTe$. This behaviour is exhibited by both light and heavy hole excitons. Due to the wavefunction spilling into the barriers the exciton binding energy is a lot larger for the infinite potential barrier than the finite potential barrier for $L < 100$ Å. The binding energy is also greater for a given value of L for a higher value of y, for both the heavy and light hole exciton. The reason for this is that the electron and hole subband energies increase with increasing y because V_e and V_h increase with increasing y. For $L < 100$ Å the maximum of the heavy hole exciton binding energy is larger than that of the light hole exciton binding energy. This can be explained by looking at the compression for the exciton wavefunction. The well width dependence of the spatial separation of excitons in the z direction is calculated using [77]

$$\langle z \rangle = \left\langle \phi_{ex} | (z_e - z_h)^2 | \phi_{ex} \right\rangle^{1/2}. \tag{4.41}$$

This separation $\langle z \rangle$ shown in Figure (4-3), has a minimum for small L and increases with increasing L. For heavy hole excitons $\langle z \rangle$ is smaller than for light hole excitons. The interpretation for this is that the heavy hole excitons receive stronger confinement than the light hole excitons owing to the band offset potentials [77][78]. Therefore the heavy hole exciton has a higher binding energy than the light hole exciton for small L. As the well width increases the excitons become less confined and the light hole exciton binding energy becomes higher than the heavy hole exciton binding energy, as they start to approach their bulk values. This is seen in Figure (4-2 (a)), where the heavy and light hole excitons reach the bulk binding energy values, and the light hole exciton binding energy is higher than the heavy hole exciton binding energy as the well width is increased.

The variational parameter α in Eq. (4.35) is expected to equal 1 for an exciton in the bulk, and λ equal the Bohr radius in atomic units, which is approximately 145 for heavy hole excitons. This can be seen in Figure (4-2 (b)) as α approaches 1 for well widths of $L > 500$ Å. For higher values of the Mg concentration y the parameter α peaks at a lower value, but converges to 1 as the well width is increased. Figure (4-2 (c)) shows the variational parameter λ closely approaching the bulk value of the Bohr radius of the heavy hole as the well width reaches 300 Å for all values of y. For higher values of y the parameter λ peaks at a lower value.

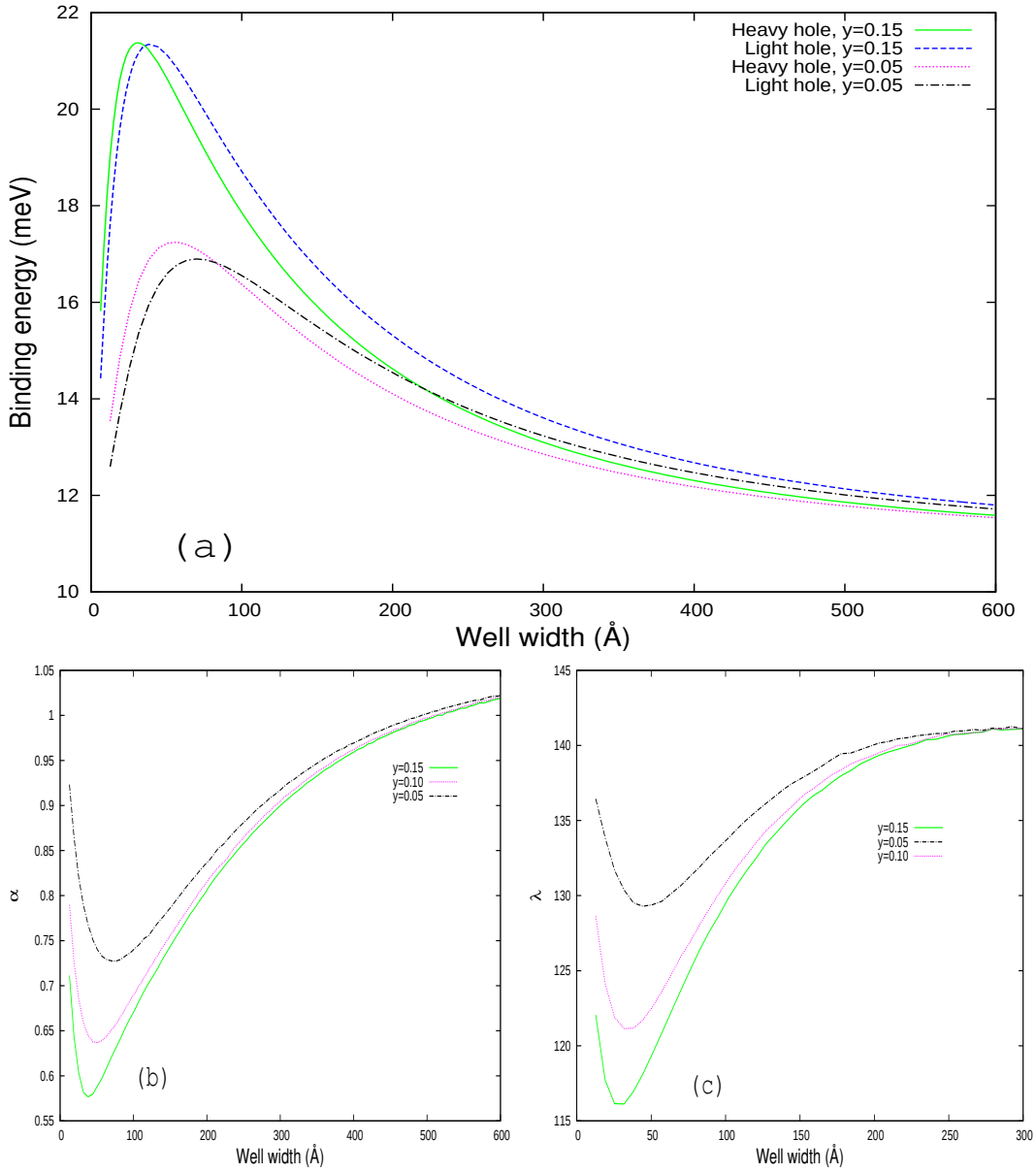

Figure 4-2: (a) The exciton binding energy as a function of the quantum well width for excitons in a $Cd_{1-x}Mn_xTe/Cd_{1-y}Mg_yTe$ finite well for both the heavy and light hole excitons for different values of the Mg concentration y using the Harrison model. (b) The variational parameter α as a function of the quantum well width for a heavy hole exciton in a $Cd_{1-x}Mn_xTe/Cd_{1-y}Mg_yTe$ finite well for different values of the Mg concentration y. (c) The variational parameter λ as a function of the quantum well width for a heavy hole exciton in a $Cd_{1-x}Mn_xTe/Cd_{1-y}Mg_yTe$ finite well for different values of the Mg concentration y. The values of the physical parameters used for $Cd_{1-x}Mg_xTe$ are given in the table in Appendix K, and $x = 0.01$.

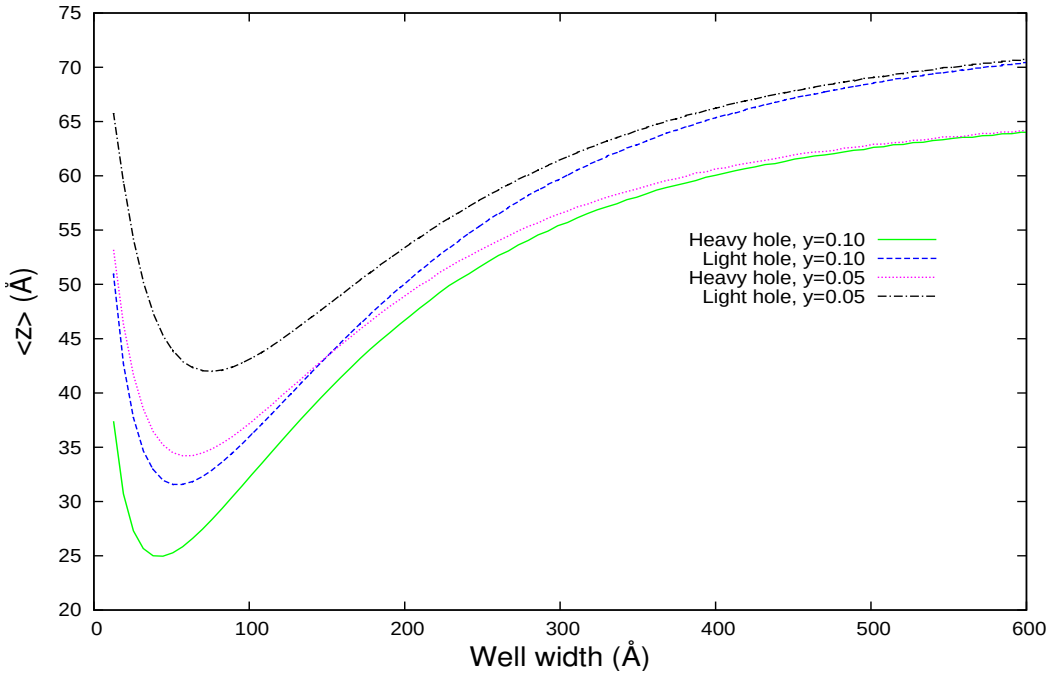

Figure 4-3: The separation $\langle z \rangle$ as a function of the quantum well width for excitons in a $Cd_{1-x}Mn_xTe/Cd_{1-y}Mg_yTe$ finite well for both the heavy and light hole excitons for different values of the Mg concentration y. The values of the physical parameters used for $Cd_{1-x}Mg_xTe$ are given in the table in Appendix K, and $x = 0.01$.

Figure (4-4 (a)) shows how the binding energy varies for different values of the magnetic ion concentration x for a heavy hole exciton. As x increases the binding energy is reduced for small values of the well width L, since the potentials V_e and V_h are smaller for higher values of x. The binding energies start to converge to the same value as the well width reaches 200 Å. The variational parameters peak at a higher value as x is increased but all converge to the bulk value, as shown in Figure (4-5 (b)) and (4-5 (c)). Figure (4-5 (a)) shows how the binding energy varies for different conduction and valence band offsets for a heavy hole exciton. As the valence band offset increases the binding energy decreases for small well widths, but starts to converge to the same value for well widths above 200 Å. This is due to the electron subband energy making a bigger contribution than the hole subband energy due to the difference in the mass of the electron and hole. The variational parameters peak at higher values as the valence band offset is increased but they converges to the bulk value, shown in Figure (4-5 (b)) and (4-5 (c)).

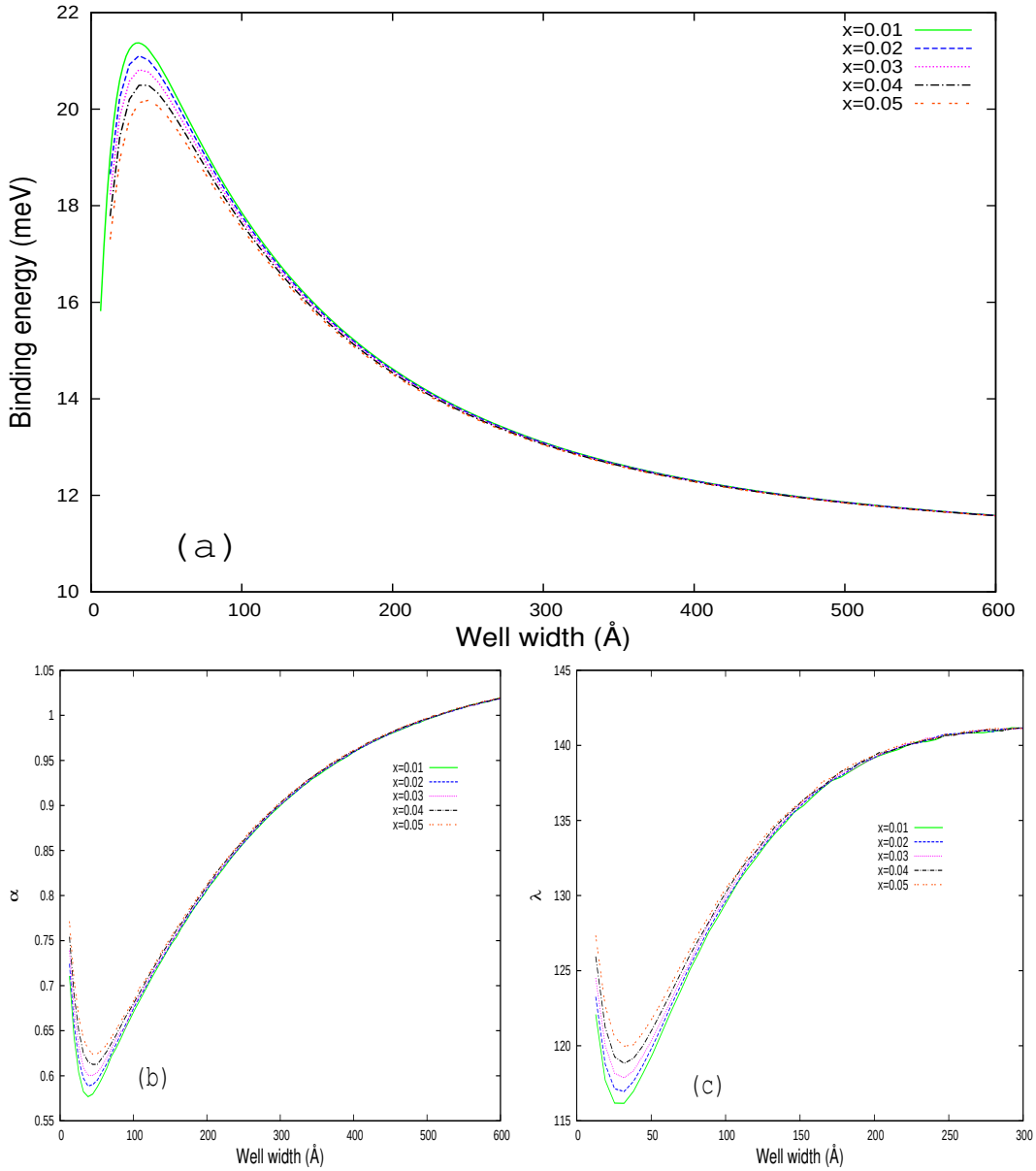

Figure 4-4: (a) The exciton binding energy as a function of the quantum well width for heavy hole excitons in a $Cd_{1-x}Mn_xTe/Cd_{1-y}Mg_yTe$ finite well for different values of the magnetic ion concentration x using the Harrison model. (b) The variational parameter α as a function of the quantum well width for heavy hole excitons in a $Cd_{1-x}Mn_xTe/Cd_{1-y}Mg_yTe$ finite well for different values of the magnetic ion concentration x. (c) The variational parameter λ as a function of the quantum well width for heavy hole excitons in a $Cd_{1-x}Mn_xTe/Cd_{1-y}Mg_yTe$ finite well for different values of the magnetic ion concentration x. The values of the physical parameters used for $Cd_{1-x}Mg_xTe$ are given in the table in Appendix K, and $y = 0.15$.

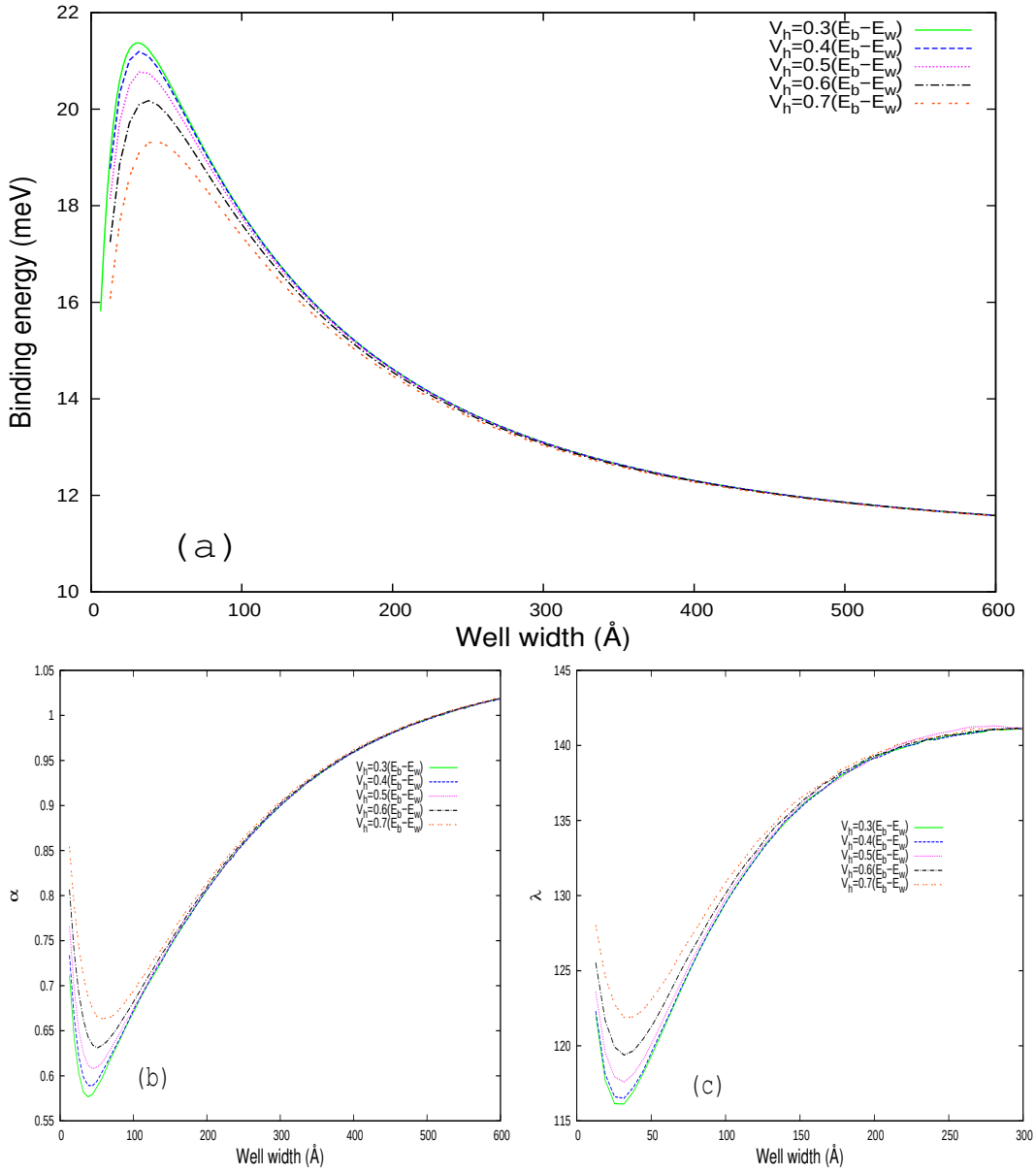

Figure 4-5: (a) The exciton binding energy as a function of the quantum well width for heavy hole excitons in a $Cd_{1-x}Mn_xTe/Cd_{1-y}Mg_yTe$ finite well for different values of the valence band offset V_h and conduction band offset V_e using the Harrison model. (b) The variational parameter α as a function of the quantum well width for heavy hole excitons in a $Cd_{1-x}Mn_xTe/Cd_{1-y}Mg_yTe$ finite well for different values of the valance band offset V_h and conduction band offset V_e. (c) The variational parameter λ as a function of the quantum well width for heavy hole excitons in a $Cd_{1-x}Mn_xTe/Cd_{1-y}Mg_yTe$ finite well for different values of the valance band offset V_h and conduction band offset V_e. The values of the physical parameters used for $Cd_{1-x}Mg_xTe$ are given in the table in Appendix K, with $x = 0.01$, and $y = 0.15$.

4.2.2 Greene and Bajaj model

Greene and Bajaj [79] were the first to calculate the binding energies of heavy and light hole excitons as a function of well size for finite values of the barrier height. Their trial wavefunction for φ_r is given by

$$\phi_r(\rho, z) = (1 + \alpha z^2) \exp\left(-\delta\sqrt{\rho^2 + z^2}\right), \tag{4.42}$$

where α and δ are the variational parameters [79]. Calculations were repeated using this trial form, and the binding energies for the heavy and light hole excitons for a $Cd_{1-x}Mn_xTe/Cd_{1-x}Mg_xTe$ finite well calculated as a function of the well width are shown in Figure (4-6). The band gaps and offsets are as before. The exciton binding energy again increases as the well width L is reduced until it reaches a maximum and then it starts to drop, and this behaviour is exhibited by both the heavy and light hole exciton. The binding energy is higher for the heavy hole exciton for small L, again explained by the fact that the heavy hole excitons receive stronger confinement for small L than the light hole excitons. As the well width increases the excitons become less confined and the light hole exciton binding energy becomes higher than the heavy hole exciton binding energy, as they start to approach their bulk values. As can be seen in Figure (4-6) both the Harrison model and Greene and Bajaj model display the same shape and differ only slightly for small L, but both converge to the same value as L is increased. Since there is little difference to the binding energy for both models it does not matter which model will be used for calculating binding energies for excitons in the presence of a homogeneous magnetic field.

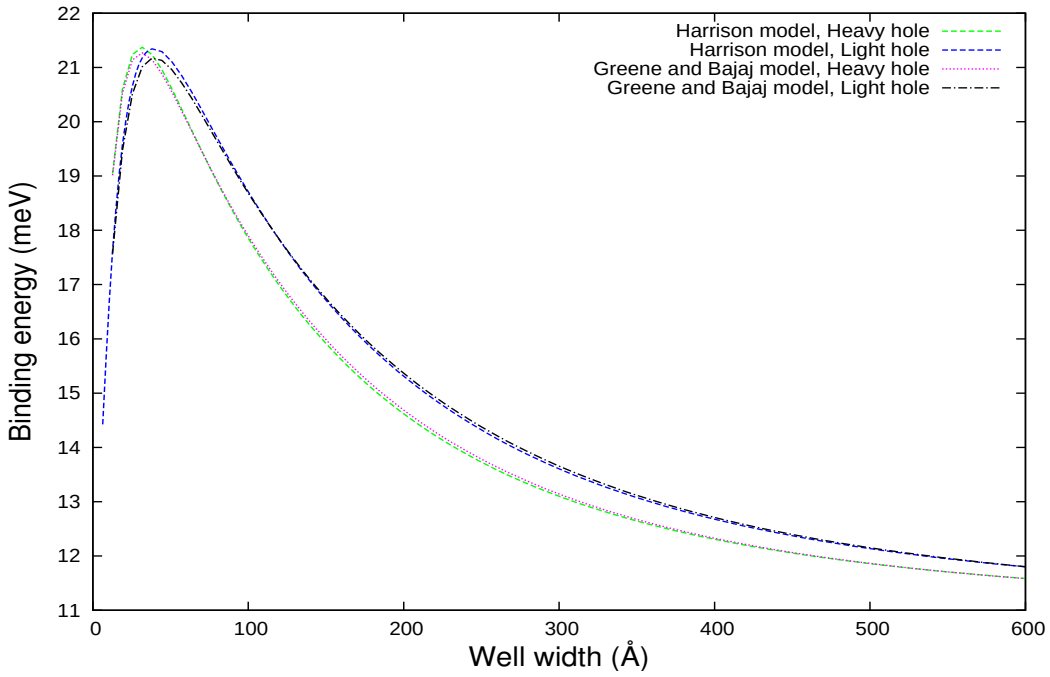

Figure 4-6: The binding energy as a function of the well width in a finite $Cd_{1-x}Mn_xTe/Cd_{1-y}Mg_yTe$ DMS quantum well using the Harrison model and Greene and Bajaj model for both a heavy and light hole exciton. The values of the physical parameters used for $Cd_{1-x}Mg_xTe$ are given in the table in Appendix K, with $x = 0.01$ and $y = 0.15$.

4.2.3 Excitons in a dilute magnetic semiconductor in the presence of a homogeneous magnetic field

So far, the effect of the magnetic field on an exciton in a DMS quantum well, and the sp-d interaction term for a DMS semiconductor, have been ignored. They will now be discussed here. The Hamiltonian for an exciton in a DMS well in the presence of a homogeneous magnetic field can be written in cylindrical coordinates in the effective mass approximation

$$\begin{aligned}\mathcal{H}_{ex} &= -\frac{\hbar^2}{2m^*_{e,\perp}}\frac{\partial^2}{\partial z_e^2} + V_e(z_e) - \frac{\hbar^2}{2m^*_{h,\perp}}\frac{\partial^2}{\partial z_h^2} + V_h(z_h) - \frac{\hbar^2}{2\mu}\left[\frac{1}{\rho}\frac{\partial}{\partial\rho}\rho\frac{\partial}{\partial\rho} + \frac{1}{\rho^2}\frac{\partial^2}{\partial\phi^2}\right] \\ &\quad -\frac{e^2}{4\pi\varepsilon_0\varepsilon_r r} + \frac{1}{8}\frac{1}{\mu}e^2\rho^2B_z^2 + g^e_{eff}\mu_B B_z S_{e,z}\Theta(L/2-|z_e|) \\ &\quad +g^h_{eff}\mu_B B_z S_{h,z}\Theta(L/2-|z_h|). \end{aligned} \tag{4.43}$$

where the first six terms are the same as those for the Hamiltonian in Eq. (4.15). The last terms correspond to the diamagnetic shift, the linear Zeeman effects (containing the electron and hole g factors), and the sp-d exchange interaction for the electron and hole present in the DMS. The effective g factors are defined in Eq. (1.21) and (1.22). The electron and hole g factors in the barrier material have been ignored, since they are negligible in comparison to the effective g factors in a DMS. We again use the Harrison wavefunction defined in Eq. (4.35) to calculate the binding energy as a function of the magnetic field for a $Cd_{1-x}Mn_xTe/Cd_{1-y}Mg_yTe$ dilute magnetic semiconductor. The variational parameters were found as before. We label σ^+ a heavy hole exciton (light hole exciton) with spins $S_{e,z} = \frac{1}{2}$, $S_{h,z} = \frac{3}{2}$ ($S_{e,z} = \frac{1}{2}$, $S_{h,z} = \frac{1}{2}$), and for spins $S_{e,z} = -\frac{1}{2}$, $S_{h,z} = -\frac{3}{2}$ ($S_{e,z} = -\frac{1}{2}$, $S_{h,z} = -\frac{1}{2}$) we use σ^-.

The binding energy in a $Cd_{1-x}Mn_xTe/Cd_{1-y}Mg_yTe$ quantum well calculated as a function of the well width for different values of the magnetic field for a σ^+ heavy hole exciton is shown in Figures (4-7 (a)) and (4-7 (b)) for two different values of the magnetic ion concentration x. It can be seen that the presence of the magnetic field leads to a reduction in the binding energy for a heavy hole with σ^+ spins in the DMS quantum well, and the binding energy decreases as the magnetic field increases for both values of x. The binding energy varies more for small well widths of $L < 200$ as x increases, due to the sp-d interaction making a bigger contribution. For $L > 300$ the binding energy converges to the same value for both values of x, and the main effect on the binding energy is the diamagnetic shift. The binding energy in a $Cd_{1-x}Mn_xTe/Cd_{1-y}Mg_yTe$ quantum well as a function of the well width for different values of the magnetic ion concentration x for a σ^+ heavy hole exciton is shown in Figure (4-8) for one value of the magnetic field. The binding energy varies below $L < 200$, which decreases as x increases, but it converges to the same value as the well width increases.

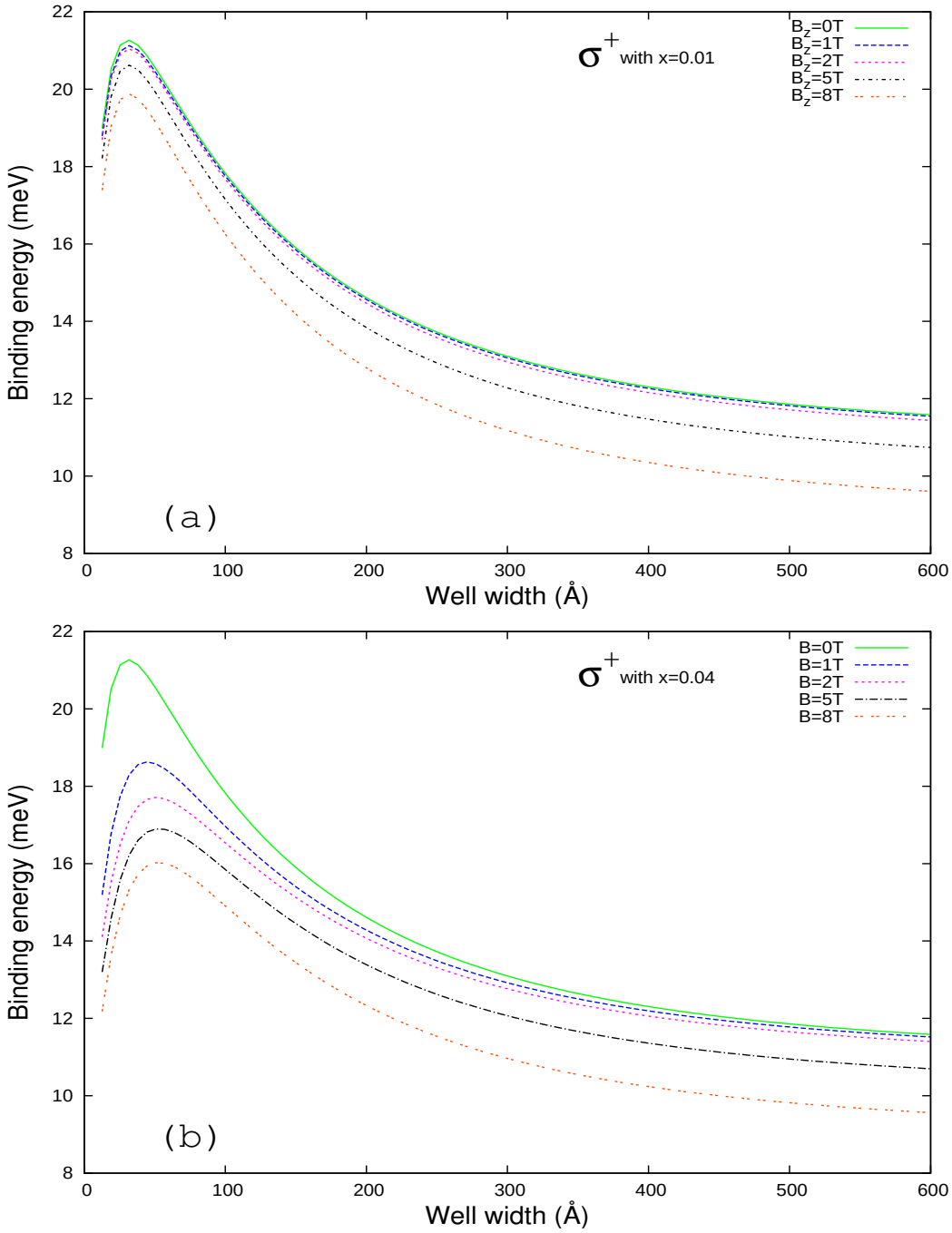

Figure 4-7: (a) The binding energy as a function of the well width in a finite $Cd_{1-x}Mn_xTe/Cd_{1-y}Mg_yTe$ DMS quantum well using the Harrison model for a heavy hole exciton with spins labelled by σ^+ for different values of the magnetic field, with a magnetic ion concentration of $x = 0.01$. (b) The binding energy as a function of the well width in a finite $Cd_{1-x}Mn_xTe/Cd_{1-y}Mg_yTe$ DMS quantum well using the Harrison model for a heavy hole exciton with spins labelled by σ^+ for different values of the magnetic field, with a magnetic ion concentration of $x = 0.04$. The values of the physical parameters used for $Cd_{1-x}Mg_xTe$ are given in the table in Appendix K, and $y = 0.15$.

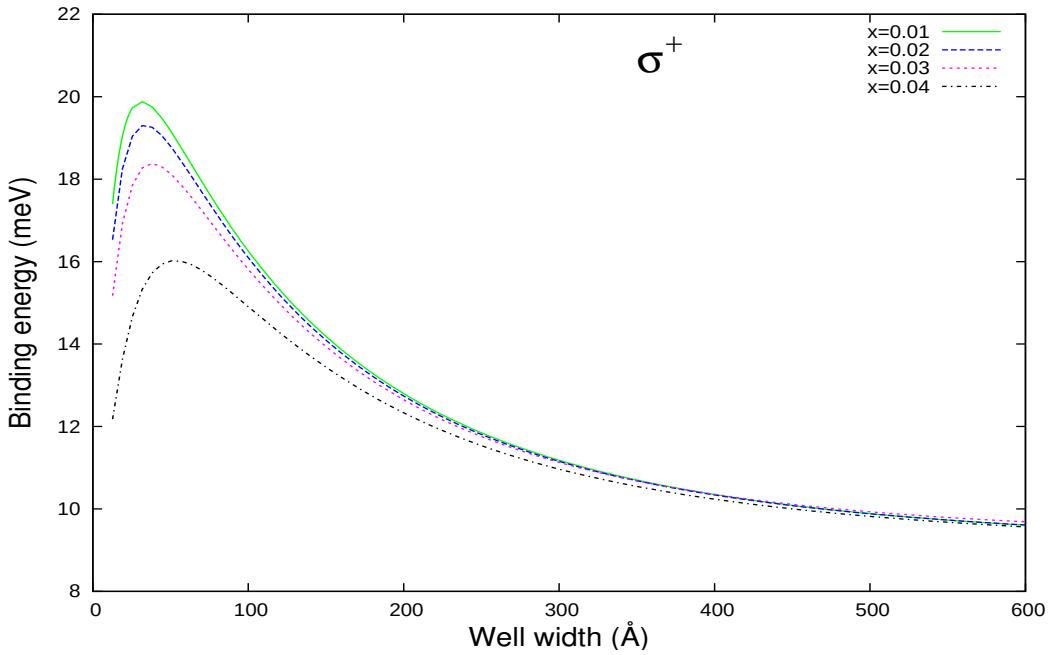

Figure 4-8: The binding energy as a function of the well width in a finite $Cd_{1-x}Mn_xTe/Cd_{1-y}Mg_yTe$ DMS quantum well using the Harrison model for a heavy hole exciton with spins labelled by σ^+ for different values of the magnetic ion concentration x. The values of the physical parameters used for $Cd_{1-x}Mg_xTe$ are given in the table in Appendix K, with $B_z = 8$ T and $y = 0.15$.

The binding energy in a $Cd_{1-x}Mn_xTe/Cd_{1-y}Mg_yTe$ quantum well calculated as a function of the well width for different values of the magnetic field for a σ^- heavy hole exciton is shown in Figure (4-9 (a)) and (4-9 (b)) for two different values of the magnetic ion concentration x. The presence of the magnetic field also leads to a reduction in the binding energy for a σ^- heavy hole exciton in the DMS quantum well. The binding energy varies more for small well widths of $L < 200$ as x increases, due to the sp-d interaction making a bigger contribution. The binding energy converges to the same value for $L > 300$ for both values of x. This is the same behaviour as the binding energy for σ^+ heavy hole excitons, but the binding energy varies more for σ^+ heavy hole excitons as x increases. This is due to the fact that the hole contribution of the sp-d interaction is positive which makes a bigger contribution than the electron contribution for σ^+ excitons, while for σ^- excitons the electron sp-d interaction contribution is positive and the hole contribution is negative. The binding energy in a $Cd_{1-x}Mn_xTe/Cd_{1-y}Mg_yTe$ quantum well as a function of the well width for different values of the magnetic ion concentration x for a σ^- heavy hole excitons is shown in Figure (4-10). Below $L < 200$ the binding energy varies for different values of x, which decreases as x increases, but it converges to the same value. For σ^+ heavy hole excitons the binding energy decreases more for increasing x than it does for σ^- heavy hole excitons. This is due to the hole contribution of the sp-d interaction for σ^+ excitons.

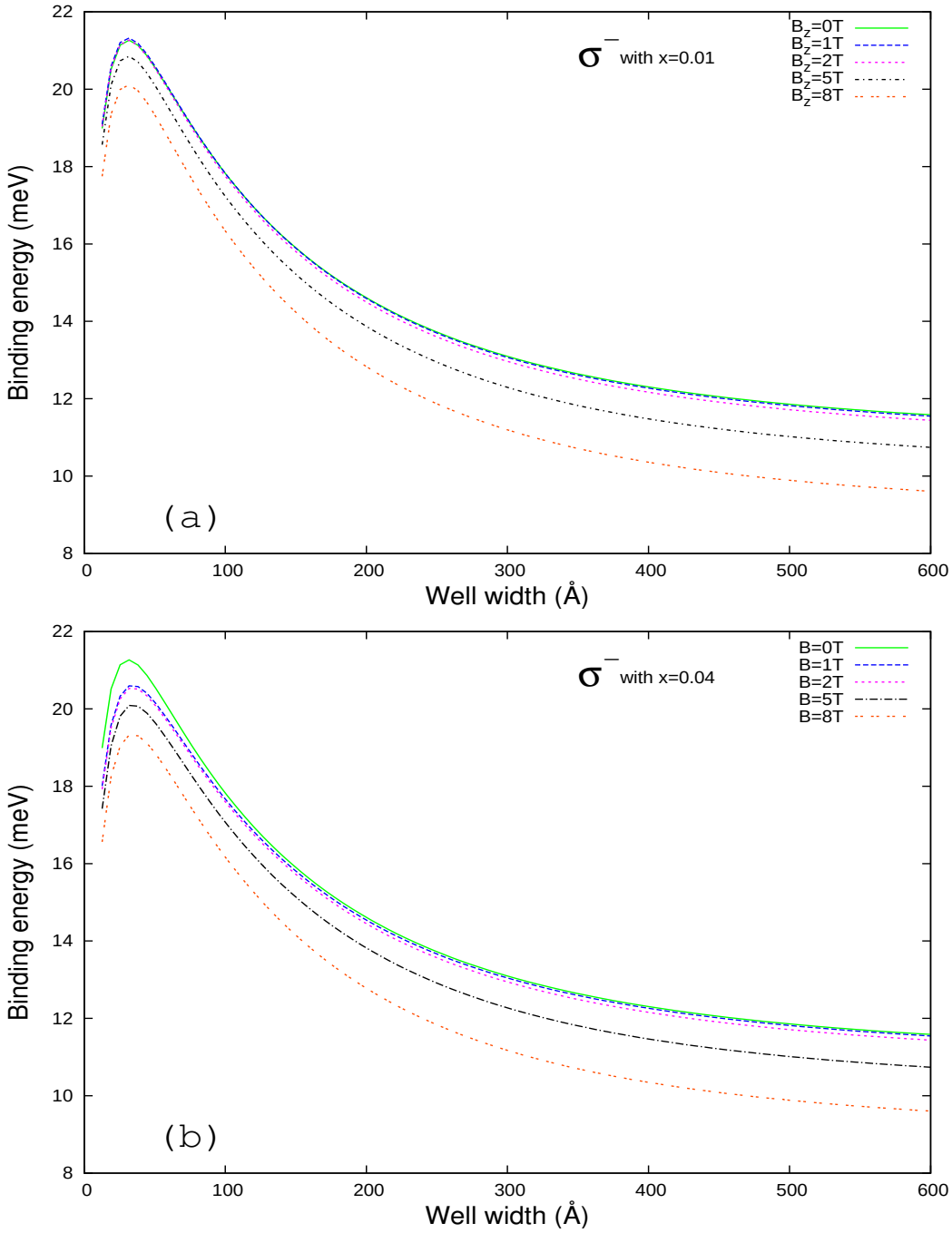

Figure 4-9: (a) The binding energy as a function of the well width in a finite $Cd_{1-x}Mn_xTe/Cd_{1-y}Mg_yTe$ DMS quantum well using the Harrison model for a heavy hole exciton with spins labelled by σ^- for different values of the magnetic field, with a magnetic ion concentration of $x = 0.01$. (b) The binding energy as a function of the well width in a finite $Cd_{1-x}Mn_xTe/Cd_{1-y}Mg_yTe$ DMS quantum well using the Harrison model for a heavy hole exciton with spins labelled by σ^- for different values of the magnetic field, with a magnetic ion concentration of $x = 0.04$. The values of the physical parameters used for $Cd_{1-x}Mg_xTe$ are given in the table in Appendix K, and $y = 0.15$.

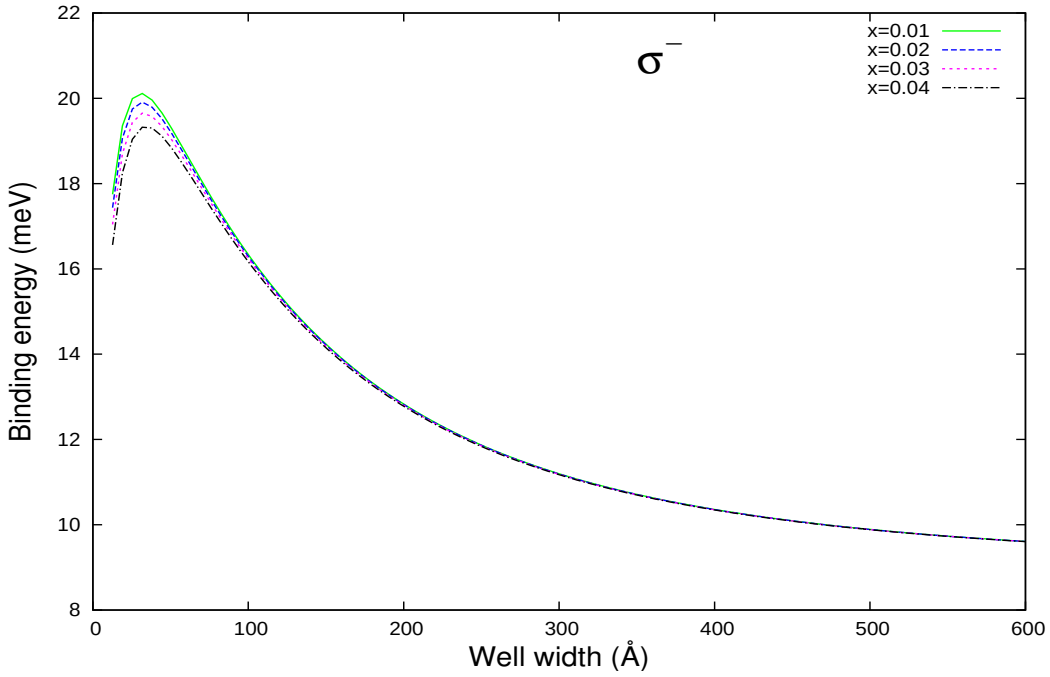

Figure 4-10: The binding energy as a function of the well width in a finite $Cd_{1-x}Mn_xTe/Cd_{1-y}Mg_yTe$ DMS quantum well using the Harrison model for a heavy hole exciton with spins labelled by σ^- for different values of the magnetic ion concentration x. The values of the physical parameters used for $Cd_{1-x}Mg_xTe$ are given in the table in Appendix K, with $B_z = 8$ T and $y = 0.15$.

The effect of the sp-d interaction on the binding energy can be seen in Figure (4-11 (a)), where the binding energy is plotted as a function of magnetic field for both σ^+ and σ^- heavy hole excitons in a $Cd_{1-x}Mn_xTe/Cd_{1-y}Mg_yTe$ quantum well for different values of x without the inclusion of the diamagnetic shift term. The spin up and spin down exciton components (σ^+ and σ^-) split as a function of the magnetic field and the splitting increases as the magnetic field increases until it starts to level off as the magnetic field is further increased. The binding energy decreases as the magnetic field increases for σ^+ heavy hole excitons, due to the hole contribution of the sp-d interaction being positive and making a bigger contribution than the electron contribution of the sp-d interaction. While the binding energy increases as the magnetic field increases for σ^- heavy hole excitons, due to the hole contribution of the sp-d interaction being negative. For σ^+ heavy hole excitons the binding energy changes more rapidly, due to the positive hole contribution of the sp-d interaction. The effect of the diamagnetic shift term can be seen in Figure (4-11 (b)) where its included in the calculation of the binding energy as a function of magnetic field for both σ^+ and σ^- heavy hole excitons in a $Cd_{1-x}Mn_xTe/Cd_{1-y}Mg_yTe$ quantum well. The binding energy decreases as the magnetic field increases for both σ^+ and σ^- heavy hole excitons. The binding energy is lower for the σ^+ heavy hole excitons for a given value of the magnetic field.

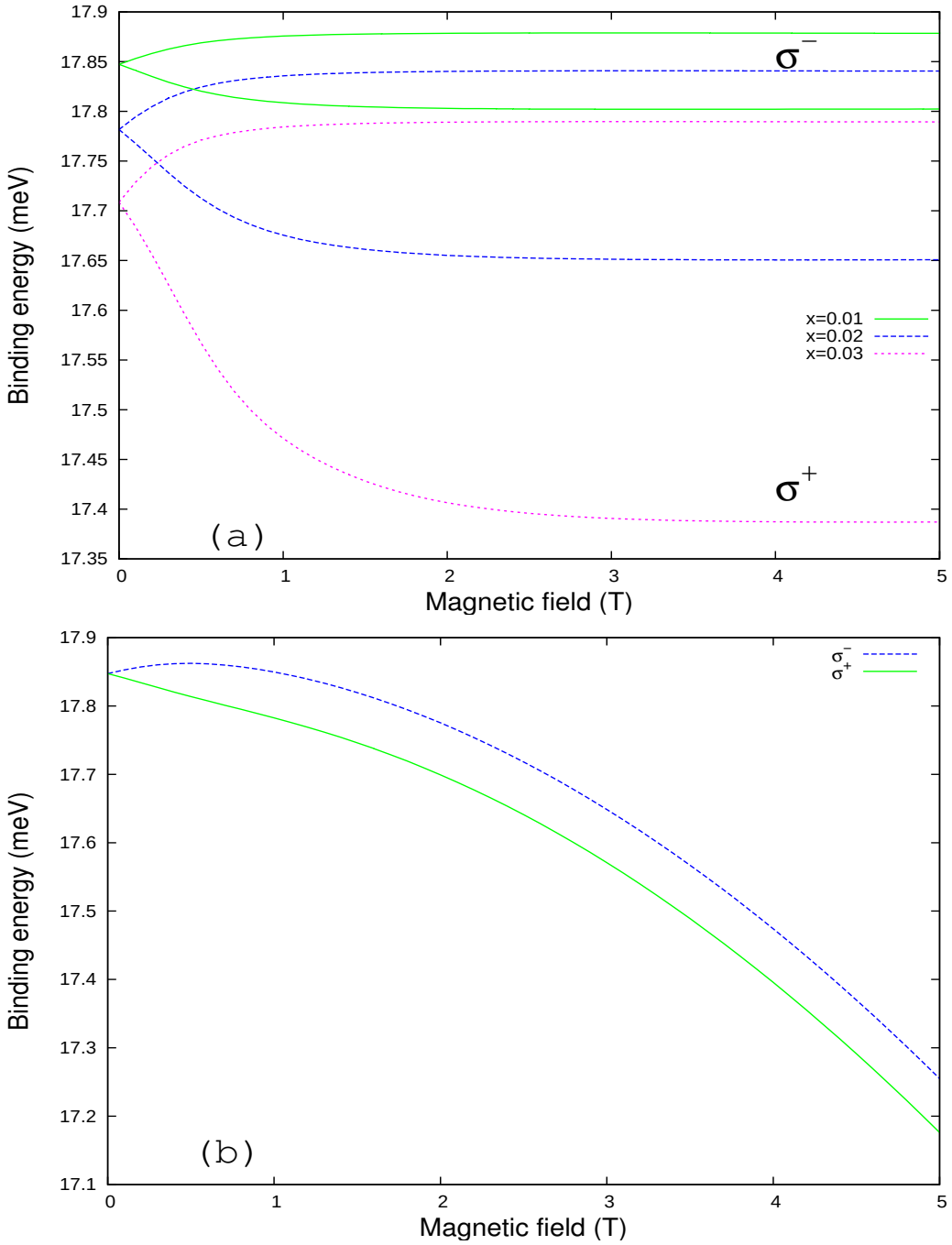

Figure 4-11: (a) The exciton binding energy as function of the magnetic field for a heavy hole exciton with both σ^+ and σ^- spins in a 100 Å finite $Cd_{1-x}Mn_xTe/Cd_{1-y}Mg_yTe$ DMS quantum well using the Harrison model for different values of the magnetic ion concentration x. Without the inclusion of the diamagnetic shift term. (b) The exciton binding energy as function of the magnetic field for a heavy hole exciton with both σ^+ and σ^- spins in a 100 Å finite $Cd_{1-x}Mn_xTe/Cd_{1-y}Mg_yTe$ DMS quantum well using the Harrison model, with $x = 0.01$. The values of the physical parameters used for $Cd_{1-x}Mg_xTe$ are given in the table in Appendix K, and $y = 0.15$.

4.3 Summary

To conclude, in this Chapter the binding energy of excitons in $Cd_{1-x}Mn_xTe/Cd_{1-y}Mg_yTe$ quantum wells has been considered. It is believed that this has not previously been studied in this way to calculate the binding energies for this material. The Harrison model was used to calculate binding energies in both an infinite and finite quantum well without the presence of a homogeneous magnetic field. For the infinite case the binding energy increases as the well width decreases, and for a given value of the well width the light hole exciton has a higher value for the binding energy. For the finite case the exciton binding energy increases as the well width L is reduced until it reaches a maximum and then it starts to drop, due to the wavefunction spilling into the surrounding barrier layers, which is exhibited by both light and heavy hole excitons. Due to the wavefunction spilling into the barriers the exciton binding energy is a lot larger for the infinite potential barrier than the finite potential barrier for around $L < 100$ Å. The heavy hole exciton has a higher binding energy than the light hole exciton for small L, due to the heavy hole excitons receiving stronger confinement than the light hole excitons owing to the band offset potentials. The Harrison model was compared to the Greene and Bajaj model, and the binding energy differs only slightly for small L, but for both models the binding energies converge to the same value as L is increased. The binding energy in a DMS quantum well in the presence of a homogeneous magnetic field was calculated using the Harrison model. For a heavy hole exciton with spins labelled by both σ^- and σ^+ the presence of the magnetic field leads to less binding and the main contribution is from the diamagnetic shift term for small values of the magnetic ion concentration x. The binding energy decreases for increasing x, and decreases more rapidly for σ^+ excitons. This approximation is only valid for a homogeneous magnetic field. In the next chapter excitons in the presence of an inhomogeneous magnetic field will be discussed.

Chapter 5

Excitons in a dilute magnetic semiconductor in the presence of an inhomogeneous magnetic field

In the previous Chapter the fundamental properties of excitons in a DMS quantum well were discussed, by considering a model to calculate the binding energy of excitons in a quantum well in the presence of a homogeneous magnetic field. Results were presented for $Cd_{1-x}Mn_xTe$, and the approximations used were valid for a homogeneous magnetic field. In this chapter we extend our study to look for the first time at excitons in $Cd_{1-x}Mn_xTe$ in the presence of an inhomogeneous magnetic field. Excitons can be forced into regions of low field gradient by means of inhomogeneous magnetic fields, creating a magnetic trap for the excitons [52][80]. The properties of excitons in an inhomogeneous magnetic field created by a microscale ferromagnetic disk, a nanoscale ferromagnetic disk in the vortex state, and a ferromagnetic strip, will be discussed. It is believed that excitons in a dilute magnetic semiconductor in the presence of these magnetic fields has not previously been studied in this way.

5.1 The excitonic Hamiltonian

We consider a DMS quantum well in which the electrons and holes are additionally trapped laterally by the presence of an inhomogeneous magnetic field, basing our analysis on the following Hamiltonian to describe the electron and hole motion

$$\mathcal{H}_{ex} = \mathcal{H}^{2D}(\vec{r_e}, \vec{r_h}) + \mathcal{H}^{\perp}(z_e, z_h) + W(\gamma) + \mathcal{H}_{ex}^{m_z}(\vec{r_e}, \vec{r_h}) + \mathcal{H}_{s,p-d}, \tag{5.1}$$

where $\mathcal{H}^{2D}(\vec{r_e}, \vec{r_h})$ is the 2D effective Hamiltonian, $\mathcal{H}^{\perp}(z_e, z_h)$ is the Hamiltonian describing the electron and hole confinement in the quantum well, $W(\gamma)$ is the difference between the 2D and 3D Coulomb interaction, $\mathcal{H}^{m_z}(\vec{r_e}, \vec{r_h})$ is the spin Hamiltonian and $\mathcal{H}_{s,p-d}$ is the sp-d exchange interaction. The first four terms are discussed in detail in the following sections.

5.1.1 The 2D effective Hamiltonian

In quantum wells the electron and hole motions along the z direction is quantised into discrete levels due to the presence of the confinement potential along this direction. For

simplicity the electron and hole motion in the well material will be regarded as pure two dimensional motion with quantisation along the z direction [81]. The two dimensional motion is then additionally restricted in a sufficiently small area by applying an inhomogeneous magnetic field, and the z direction is assumed to be unaffected by the magnetic field [82][52][83][84][80]. The first term in Eq. (5.1) is the Hamiltonian for a 2D system consisting of an electron in the conduction band and a hole in the valence band interacting via the Coulomb interaction in the xy plane, while moving in an inhomogeneous magnetic field, which is written as

$$\mathcal{H}^{\rm 2D}(\vec{r_e},\vec{r_h}) = \frac{\hbar^2}{2m^*_{e,||}}\left\{-i\nabla_e + \frac{e}{\hbar c}\vec{A}(\vec{r}_e)\right\}^2 + \frac{\hbar^2}{2m^*_{h,||}}\left\{-i\nabla_h - \frac{e}{\hbar c}\vec{A}(\vec{r}_h)\right\}^2 - \frac{\gamma e^2}{4\pi\varepsilon_0\varepsilon_r|\vec{r}_e-\vec{r}_h|}, \tag{5.2}$$

where $m^*_{e,||}$ and $m^*_{h,||}$ are the electron and hole effective masses in the xy direction. Notice that $\vec{r}_e$, $\vec{r}_h$ are 2D coordinates and give the xy plane position of the electron and hole, respectively, which is different to the 3D exciton Hamiltonian in Eq. (4.1), where $\vec{r}_e$ and $\vec{r}_h$ are 3D coordinates. The Coulomb interaction in this 2D effective Hamiltonian corresponds to the Coulomb interaction in the xy plane, called the 2D Coulomb interaction. The γ parameter is a variational parameter that will be used to make the difference between the 2D and 3D Coulomb interaction small, and will be discussed later on.

The Hamiltonian can be simplified by separating into the centre of mass coordinates, $\vec{R} = (m^*_{e,||}\vec{r}_e + m^*_{h,||}\vec{r}_h)/M$, and the relative motion coordinates, $\vec{r} = \vec{r}_e - \vec{r}_h$, where $M = m^*_{e,||} + m^*_{h,||}$ is the total mass of the exciton [52]. With these substitutions we get

$$\begin{aligned}\mathcal{H}^{\rm 2D}(\vec{R},\vec{r}) &= \frac{\hbar^2}{2m^*_{e,||}}\left\{-i\frac{m^*_{e,||}}{M}\nabla_R - i\nabla_r + \frac{e}{\hbar c}\vec{A}\left(\vec{R}+\frac{m^*_{h,||}}{M}\vec{r}\right)\right\}^2 \\ &\quad + \frac{\hbar^2}{2m^*_{h,||}}\left\{-i\frac{m^*_{h,||}}{M}\nabla_R + i\nabla_r - \frac{e}{\hbar c}\vec{A}\left(\vec{R}-\frac{m^*_{e,||}}{M}\vec{r}\right)\right\}^2 - \frac{\gamma e^2}{4\pi\varepsilon_0\varepsilon_r r}. \end{aligned}\tag{5.3}$$

The effect of the inhomogeneous magnetic field is accommodated by applying a wavefunction transformation analogous to the one used in reference [85] for the case of a homogeneous magnetic field

$$\Psi(\vec{R},\vec{r}) \to \exp\left\{-i(e/\hbar c)\vec{r}\cdot\vec{A}(\vec{R})\right\}\Psi(\vec{R},\vec{r}), \tag{5.4}$$

which leads to

$$\begin{aligned}\widetilde{\mathcal{H}}^{\rm 2D}(\vec{R},\vec{r}) &= \frac{\hbar^2}{2m^*_{e,||}}\left\{-i\frac{m^*_{e,||}}{M}\nabla_R - i\nabla_r + \frac{e}{\hbar c}\vec{A}\left(\vec{R}+\frac{m^*_{h,||}}{M}\vec{r}\right)\right. \\ &\qquad \left. -\frac{em^*_{e,||}}{\hbar cM}\nabla_R\{\vec{r}\cdot\vec{A}(\vec{R})\} - \frac{e}{\hbar c}\vec{A}(\vec{R})\right\}^2 \\ &\quad + \frac{\hbar^2}{2m^*_{h,||}}\left\{-i\frac{m^*_{h,||}}{M}\nabla_R + i\nabla_r - \frac{e}{\hbar c}\vec{A}\left(\vec{R}-\frac{m^*_{e,||}}{M}\vec{r}\right)\right. \\ &\qquad \left. -\frac{em^*_{h,||}}{\hbar cM}\nabla_R\{\vec{r}\cdot\vec{A}(\vec{R})\} + \frac{e}{\hbar c}\vec{A}(\vec{R})\right\}^2 - \frac{\gamma e^2}{4\pi\varepsilon_0\varepsilon_r r}, \end{aligned}\tag{5.5}$$

where $\mathcal{H}^{\rm 2D}(\vec{R},\vec{r}) = \exp\left\{i(e/\hbar c)\vec{r}\cdot\vec{A}(\vec{R})\right\}\widetilde{\mathcal{H}}^{\rm 2D}(\vec{R},\vec{r})\exp\left\{-i(e/\hbar c)\vec{r}\cdot\vec{A}(\vec{R})\right\}$, and the full derivation is given in Appendix G. Further progress is made by simplifying the equation

using an adiabatic expansion assuming that the size of the exciton is smaller than the length scale over which the magnetic field varies. In particular, the exciton relative motion is assumed to be faster than the centre of mass motion, and the relative coordinate smaller than the centre of mass motion. Note that in the case of a ferromagnetic disk placed above a quantum well, which is considered below, the magnetic vortex present at the centre of the disk and which penetrates into the quantum well has a core radius of approximately 30 nm (Chapter 3 for permalloy $Ni_{80}Fe_{20}$ disks), while the exciton radius is approximately 8 nm for $Cd_{1-x}Mn_xTe$ (Chapter 4 using Eq. (4.13)). In this case the vector potential can be expanded in a power series as

$$\vec{A}\left(\vec{R} \pm \frac{m^*_{h(e),||}\vec{r}}{M}\right) = \vec{A}(\vec{R}) \pm \frac{m^*_{h(e),||}}{M}\left(\vec{r}\cdot\nabla_R\right)\vec{A}(\vec{R}) + \ldots, \tag{5.6}$$

and truncated at second order [52][86]. This leads to the following expression for the exciton Hamiltonian

$$\widetilde{\mathcal{H}}^{2\mathrm{D}}(\vec{R},\vec{r}) = \frac{\hbar^2}{2\mu}\left(-i\nabla_r + \xi\frac{e}{\hbar c}\left\{(\vec{r}\cdot\nabla_R)\vec{A}(\vec{R})\right\}\right)^2 + \frac{\hbar^2}{2M}\left(i\nabla_R + \frac{e}{\hbar c}[\vec{r}\times\vec{B}(\vec{R})]\right)^2 - \frac{\gamma e^2}{4\pi\varepsilon_0\varepsilon_r r}, \tag{5.7}$$

where $\mu = m^*_{e,||}m^*_{h,||}/M$ is the exciton reduced mass, and $\xi = (m^*_{h,||} - m^*_{e,||})/M$. The gauge is chosen such that $(\vec{r}\cdot\nabla_R)\vec{A}(\vec{R}) = \vec{B}(\vec{R})\times\vec{r}/2 + \nabla_r\left[(\vec{r}\cdot\nabla_R)\left\{\vec{r}\cdot\vec{A}(\vec{R})\right\}\right]/2$, where $\vec{B}(\vec{R})$ is the magnetic field. Then the Hamiltonian is rewritten as

$$\begin{aligned}\widetilde{\mathcal{H}}^{2\mathrm{D}}(\vec{R},\vec{r}) &= \frac{\hbar^2}{2\mu}\left(-i\nabla_r + \xi\frac{e}{2\hbar c}\left\{\vec{B}(\vec{R})\times\vec{r}\right\} + \xi\frac{e}{2\hbar c}\nabla_r\left[(\vec{r}\cdot\nabla_R)\left\{\vec{r}\cdot\vec{A}(\vec{R})\right\}\right]\right)^2 \\ &\quad + \frac{\hbar^2}{2M}\left(i\nabla_R + \frac{e}{\hbar c}[\vec{r}\times\vec{B}(\vec{R})]\right)^2 - \frac{\gamma e^2}{4\pi\varepsilon_0\varepsilon_r r}.\end{aligned} \tag{5.8}$$

By applying a further wavefunction transformation

$$\Psi(\vec{R},\vec{r}) \to \exp\left\{-i\xi(e/\hbar c)\Omega(r)\right\}\Psi(\vec{R},\vec{r}), \tag{5.9}$$

where $\Omega(r) = (\vec{r}\cdot\nabla_R)\left\{\vec{r}\cdot\vec{A}(\vec{R})\right\}/2$, the exciton Hamiltonian becomes

$$\begin{aligned}\widetilde{\mathcal{H}}^{2\mathrm{D}}(\vec{R},\vec{r}) &= \frac{\hbar^2}{2\mu}\left(-i\nabla_r + \xi\frac{e}{2\hbar c}[\vec{B}(\vec{R})\times\vec{r}]\right)^2 + \frac{\hbar^2}{2M}\left(i\nabla_R\right. \\ &\quad \left. -\xi\frac{e}{2\hbar c}\nabla_R\left\{(\vec{r}\cdot\nabla_R)\left\{\vec{r}\cdot\vec{A}(\vec{R})\right\}\right\} + \frac{e}{\hbar c}[\vec{r}\times\vec{B}(\vec{R})]\right)^2 - \frac{\gamma e^2}{4\pi\varepsilon_0\varepsilon_r r},\end{aligned} \tag{5.10}$$

where $\mathcal{H}^{2\mathrm{D}}(\vec{R},\vec{r}) = \exp\left\{i\xi(e/\hbar c)\Omega(r)\right\}\widetilde{\mathcal{H}}^{2\mathrm{D}}(\vec{R},\vec{r})\exp\left\{-i\xi(e/\hbar c)\Omega(r)\right\}$. Expanding this out and ignoring terms of order r^3 leads to

$$\widetilde{\mathcal{H}}^{2\mathrm{D}}(\vec{R},\vec{r}) = -\frac{\hbar^2}{2\mu}\nabla_r^2 - \frac{\gamma e^2}{4\pi\varepsilon_0\varepsilon_r r} + W_1 + W_2 - \frac{\hbar^2}{2M}\nabla_R^2, \tag{5.11}$$

where

$$\begin{aligned}W_1 &= \frac{e}{2c\mu}\xi\vec{B}(\vec{R})\cdot\vec{L} + \frac{ie\hbar}{2Mc}\left\{\vec{B}(\vec{R})\times\nabla_R - \nabla_R\times\vec{B}(\vec{R})\right\}\cdot\vec{r}, \\ W_2 &= \frac{e^2}{8c^2\mu}\vec{B}(\vec{R})^2r^2,\end{aligned} \tag{5.12}$$

with the full derivation to be found in Appendix G. Here $\vec{L} = \vec{r} \times (-i\hbar\nabla_r)$ is the exciton relative angular momentum operator [52]. The above Hamiltonian describing the exciton motion in an inhomogeneous magnetic field now has position dependent terms, and an additional term (W_1 in Eq. (5.11)) not present for a homogeneous field [87].

The $\widetilde{\mathcal{H}}^{\mathrm{2D}}(\vec{R},\vec{r})$ Hamiltonian is separated into sum of a relative motion Hamiltonian and centre of mass Hamiltonian

$$\widetilde{\mathcal{H}}^{\mathrm{2D}}(\vec{R},\vec{r}) = \mathcal{H}^{\mathrm{CM}}(\vec{R}) + \mathcal{H}^{\mathrm{rel}}_{\gamma}(\vec{r},\vec{R},\nabla_R), \tag{5.13}$$

with

$$\mathcal{H}^{\mathrm{CM}}(\vec{R}) = -\frac{\hbar^2}{2M}\nabla^2_R \tag{5.14}$$

and

$$\mathcal{H}^{\mathrm{rel}}_{\gamma}(\vec{r},\vec{R},\nabla_R) = -\frac{\hbar^2}{2\mu}\nabla^2_r - \frac{\gamma e^2}{4\pi\varepsilon_0\varepsilon_r r} + W_1 + W_2. \tag{5.15}$$

The total exciton wavefunction is a product of wavefunctions describing centre of mass and relative motions

$$\Psi(\vec{R},\vec{r}) = \psi(\vec{R})\Phi_0^{n_r,m_r}(\vec{r}), \tag{5.16}$$

where the relative motion wavefunction obeys the Schrödinger equation

$$\left\{\mathcal{H}^{\mathrm{rel}}_{\gamma}(\vec{r},\vec{R},\nabla_R) - E^{\mathrm{rel}}(\gamma,\vec{R},\nabla_R)\right\}\Phi_0^{n_r,m_r}(\vec{r}) = 0. \tag{5.17}$$

The first two terms in the relative motion Hamiltonian, Eq. (5.15), describe a 2D hydrogenic system, which is exactly solvable, and the influence of the final two terms W_1 and W_2 will be treated as a perturbation to second order in the magnetic field. This assumption is valid in the weak field regime, $\hbar\omega_c^* < 2R_{ex}$, where $R_{ex} = \mu e^4/32\pi^2\varepsilon_0^2\varepsilon_r^2\hbar^2$ is the effective Rydberg, and $\omega_c^* = eB/\mu c$ is the cyclotron resonance frequency. For literature on excitons in an inhomogeneous magnetic field in the high field regime refer to reference [86]. From the zeroth order Hamiltonian

$$\mathcal{H}_0 = -\frac{\hbar^2}{2\mu}\nabla^2_r - \frac{\gamma e^2}{4\pi\varepsilon_0\varepsilon_r r}, \tag{5.18}$$

the zeroth order eigenvalues are

$$E_0(n_r,m_r) = -\lambda^2_{n_r}\gamma^2 R^*_y, \qquad \lambda_{n_r} = (n_r - 1/2)^{-1}, \tag{5.19}$$

and the zeroth order wavefunctions

$$\Phi_0^{n_r,m_r}(\vec{r}) = A_{n_r,m_r}\left(\frac{2\lambda_{n_r}\gamma r}{a^*_B}\right)^{|m_r|}\exp\left\{im_r\varphi - \frac{\lambda_{n_r}\gamma r}{a^*_B}\right\}\mathcal{L}^{2|m_r|}_{n_r-|m_r|-1}\left(\frac{2\lambda_{n_r}\gamma r}{a^*_B}\right), \tag{5.20}$$

where n_r is the radial relative motion quantum number, m_r is the angular relative motion quantum number, $\mathcal{L}^{(\alpha)}_n(x)$ is the associated Laguerre polynomial, and $a^*_B = 4\pi\varepsilon_0\varepsilon_r\hbar^2/\mu e^2$ is the exciton radius. The normalisation constant A_{n_r,m_r} is determined by $\langle\Phi_0^{n_r,m_r}|\Phi_0^{n_r,m_r}\rangle = 1$, with explicit values $A_{10} = 2\lambda_n\gamma/a^*_B$, $A_{20} = 2\lambda_n\gamma/\sqrt{3}a^*_B$, $A_{21} = 2\lambda_n\gamma/\sqrt{6}a^*_B$ [52][88]. Using standard perturbation theory [88][89], the first order equation (note we use a subscript to denote the order of the term in the series expansion of the eigenvalue E or wavefunction Φ^{n_r,m_r})

$$\{\mathcal{H}_0 - E_0(n_r,m_r)\}\,\Phi_1^{n_r,m_r}(\vec{r}) = \{E_1(n_r,m_r) - W_1\}\,\Phi_0^{n_r,m_r}(\vec{r}), \tag{5.21}$$

along with the orthogonality condition $\langle \Phi_1^{n_r,m_r} | \Phi_0^{n_r,m_r} \rangle = 0$, give for the first order eigenvalue correction

$$E_1(n_r, m_r) = \langle \Phi_0^{n_r,m_r} | W_1 | \Phi_0^{n_r,m_r} \rangle = \frac{e\hbar}{2\mu c} \xi B_z(\vec{R}) m_r, \tag{5.22}$$

while the second order correction is

$$\begin{aligned} E_2(n_r, m_r) &= \langle \Phi_0^{n_r,m_r} | W_2 | \Phi_0^{n_r,m_r} \rangle + \langle \Phi_0^{n_r,m_r} | [W_1 - E_1(n_r, m_r)] | \Phi_1^{n_r,m_r} \rangle \\ &= \beta_{m_r}^{n_r} \frac{e^2 a_B^{*2}}{8\mu c^2} \gamma^{-2} B_z(\vec{R})^2 + \alpha_{m_r}^{n_r} \frac{e^2 \hbar^2 a_B^{*2}}{2R_y^* M^2 c^2} \gamma^{-4} \nabla_R \left\{ B_z(\vec{R})^2 \nabla_R \right\}, \end{aligned} \tag{5.23}$$

where the full derivation is given in Appendix H. Thus one obtains the exciton relative motion energy

$$\begin{aligned} E^{\rm rel}(\gamma, \vec{R}, \nabla_R) &= \frac{e\hbar}{2\mu c} \xi B_z(\vec{R}) m_r + \beta_{m_r}^{n_r} \frac{e^2 a_B^{*2}}{8\mu c^2} \gamma^{-2} B_z(\vec{R})^2 \\ &\quad + \alpha_{m_r}^{n_r} \frac{e^2 \hbar^2 a_B^{*2}}{2R_y^* M^2 c^2} \gamma^{-4} \nabla_R \left\{ B_z(\vec{R})^2 \nabla_R \right\} - \lambda_n^2 \gamma^2 R_y^*. \end{aligned} \tag{5.24}$$

For a magnetic field perpendicular to the xy plane the following values are found for the numerical constants, $\alpha_{m_r}^{n_r}$ and $\beta_{m_r}^{n_r}$: $\alpha_0^1 = 21/128$, $\beta_0^1 = 3/8$, $\alpha_0^2 = 365/64$, $\beta_0^2 = 117/8$, and $\alpha_{\pm 1}^2 = 145/128$, $\beta_{\pm 1}^2 = 45/4$ (these values are derived in Appendix G).

5.1.2 Confined normal to the quantum well

The second term in the Hamiltonian in Eq. (5.1) describes the electron and hole confinement in the quantum well z direction, defined as

$$\mathcal{H}^{\perp}(z_e, z_h) = -\frac{\hbar^2}{2m_{e,\perp}^*} \frac{\partial^2}{\partial z_e^2} + V_e(z_e) - \frac{\hbar^2}{2m_{h,\perp}^*} \frac{\partial^2}{\partial z_h^2} + V_h(z_h), \tag{5.25}$$

given by Eqs. (3.19) and (3.20), where the potentials $V_e(z_e)$ and $V_h(z_h)$ are as previously discussed and given by Eqs. (3.21) and (3.22).

5.1.3 Difference between the 2D and 3D Coulomb interaction

In reality the electron and hole interact via the 3D Coulomb interaction, whilst $\mathcal{H}^{\rm 2D}$ considered in the previous section contains only a 2D inplane Coulomb term. The Hamiltonian in Eq. (5.1) has been divided into an unperturbed part $\mathcal{H}_0(\gamma) = \mathcal{H}^{\rm 2D}(\vec{r}_e, \vec{r}_h) + \mathcal{H}^{\perp}(z_e, z_h)$ given by Eq. (5.2) and (5.25), and a small perturbational part $W(\gamma)$ with the use of a variational parameter γ first introduced in reference [90]. The third term in Eq. (5.1) is the small perturbational term which is the difference between these 2D and 3D Coulomb interactions,

$$W(\gamma) = \frac{\gamma e^2}{4\pi\varepsilon_0\varepsilon_r r} - \frac{e^2}{4\pi\varepsilon_0\varepsilon_r [r^2 + (z_e - z_h)]^{1/2}}, \tag{5.26}$$

and contains the variational parameter γ which is chosen to make the magnitude of $W(\gamma)$ as small as possible [80]. The term $\gamma e^2 / 4\pi\varepsilon_0\varepsilon_r r$ has been added and subtracted to the

Hamiltonian in Eq. (5.1), which corresponds to the component of the electron hole interaction in the xy plane. This approach was used and proved to be reliable by Lee et al, in studies of impurity states in anisotropic crystals [90] and for the study of Wannier excitons in a thin crystal film [91], and later by Ekenberg and Altarelli [72] and Jiang [92] in the calculation of exciton binding energies in quantum wells.

The energy perturbation is written as

$$E = E_0(\gamma) + \Delta E(\gamma) = E_0(\gamma) + \Delta E_1(\gamma) + \Delta E_2(\gamma) + \ldots, \tag{5.27}$$

where

$$\begin{aligned} \Delta E_1(\gamma) &= \langle \Phi_0 \left| W(\gamma) \right| \Phi_0 \rangle, \\ \Delta E_2(\gamma) &= \sum_n \frac{|\langle \Phi_0 \left| W(\gamma) \right| \Phi_0^n \rangle|^2}{E_0 - E_0^n}, \end{aligned} \tag{5.28}$$

with

$$\mathcal{H}_0 \Phi_0 = E_0 \Phi_0. \tag{5.29}$$

First of all, it should be noted that γ is not a parameter in a variational trial wavefunction and therefore it should not be determined by minimising Eq. (5.27) with respect to γ. If the term $W(\gamma)$ is treated exactly, the total energy should not depend on the choice of the parameter γ, which only determines how the energy is divided between $\mathcal{H}_0(\gamma)$ and $W(\gamma)$. Therefore, the value of γ is chosen to render the solution of the perturbed part much smaller than that of the unperturbed part, with the optimum value of γ determined from minimising $|\Delta E(\gamma)/E_0(\gamma)|$ to ensure the fastest convergence of the perturbation series, Eq. (5.27). The first order perturbation to the ground state energy is $\Delta E_1(\gamma)$, and based on this first order perturbation energy, the optimum condition is found when [93][80]

$$\Delta E_1(\gamma) = \langle \Phi_0 \left| W(\gamma) \right| \Phi_0 \rangle = 0, \tag{5.30}$$

Once γ is found from this condition, it can then be used in determining the exciton relative motion energy in Eq. (5.24). The validity of the calculation can be judged by the dependence of $E = E_0(\gamma) + \Delta E(\gamma)$ on γ [90]. The less E is dependent upon γ, the more accurate the results.

Ideally this term in Eq. (5.30) should be as close to zero as possible when all the terms in the Hamiltonians $\mathcal{H}^{2D}(\vec{r}_e, \vec{r}_h)$, $\mathcal{H}^{\perp}(z_e, z_h)$ and $W(\gamma)$ are included, but here the effect of the magnetic field has been ignored to simplify the calculation. A similar approach was used successfully by Wei et al [94] to calculate binding energies. Therefore for the unperturbed Hamiltonian the solution in the xy direction is that given by the Hamiltonian $\mathcal{H}^{2D}(\vec{r}_e, \vec{r}_h)$ when no magnetic field is included. The electron and hole motion in the z direction is found from the one dimensional problem with the Hamiltonian of Eq. (5.25), and infinite potential barriers are also used to simplify the calculation. The binding energies were successfully calculated for an infinite quantum well using this perturbation variational method by Bajaj and Branis [93] and Wei et al [94]. Hence the wavefunctions for the unperturbed Hamiltonian are written as

$$\Phi_0(z_e, z_h, \vec{r}) = \phi_e(z_e)\phi_h(z_h)\Phi_0^{n_r, m_r}(\vec{r}) = \left(\frac{4}{L_e L_h}\right)^{1/2} \cos\left(\frac{n_e \pi z_e}{L_e}\right) \cos\left(\frac{n_h \pi z_h}{L_h}\right) \Phi_0^{n_r, m_r}(\vec{r}) \tag{5.31}$$

for odd n_e and n_h,

$$\Phi_0(z_e, z_h, \vec{r}) = \phi_e(z_e)\phi_h(z_h)\Phi_0^{n_r,m_r}(\vec{r}) = \left(\frac{4}{L_e L_h}\right)^{1/2} \sin\left(\frac{n_e \pi z_e}{L_e}\right) \sin\left(\frac{n_h \pi z_h}{L_h}\right) \Phi_0^{n_r,m_r}(\vec{r}) \tag{5.32}$$

for even n_e and n_h,

$$\Phi_0(z_e, z_h, \vec{r}) = \phi_e(z_e)\phi_h(z_h)\Phi_0^{n_r,m_r}(\vec{r}) = \left(\frac{4}{L_e L_h}\right)^{1/2} \cos\left(\frac{n_e \pi z_e}{L_e}\right) \sin\left(\frac{n_h \pi z_h}{L_h}\right) \Phi_0^{n_r,m_r}(\vec{r}) \tag{5.33}$$

for odd n_e and even n_h, and

$$\Phi_0(z_e, z_h, \vec{r}) = \phi_e(z_e)\phi_h(z_h)\Phi_0^{n_r,m_r}(\vec{r}) = \left(\frac{4}{L_e L_h}\right)^{1/2} \sin\left(\frac{n_e \pi z_e}{L_e}\right) \cos\left(\frac{n_h \pi z_h}{L_h}\right) \Phi_0^{n_r,m_r}(\vec{r}) \tag{5.34}$$

for even n_e and odd n_h, where n_e and $n_h = 1, 2, \ldots$, and L_e and L_h are the quantum well widths of the conduction and valence band, taken here to have the same value L.

For the ground state, the lowest subband exciton, where $n_r = n_e = n_h = 1$, and $m_r = 0$, the expectation value of $W(\gamma)$ is

$$\begin{aligned}
\Delta E_1(\gamma) &= \langle \Phi_0 | W(\gamma) | \Phi_0 \rangle \\
&= C \int_0^\infty \int_{-L/2}^{L/2} \int_{-L/2}^{L/2} r dr dz_e dz_h \left(\frac{\gamma e^2}{4\pi\varepsilon_0\varepsilon_r r} \right. \\
&\qquad \left. - \frac{e^2}{4\pi\varepsilon_0\varepsilon_r \sqrt{r^2 + (z_e - z_h)^2}} \right) \exp\left(-\frac{4\gamma r}{a_B^*}\right) \left(\mathcal{L}_0^0\left(\frac{4\gamma r}{a_B^*}\right)\right)^2 \\
&\qquad \cos^2\left(\frac{\pi z_e}{L}\right) \cos^2\left(\frac{\pi z_h}{L}\right),
\end{aligned} \tag{5.35}$$

where C contains normalisation constants. Then by setting $\tilde{r} = 4\gamma r / a_B^*$, and using the standard rule [95]

$$\int_0^\infty \frac{r dr}{\sqrt{r^2 + \beta_1^2}} \exp(-r) = -\beta_1 \left(1 - \frac{\pi}{2}\left[H_1(\beta_1) - N_1(\beta_1)\right]\right), \tag{5.36}$$

yields

$$\begin{aligned}
\Delta E_1(\gamma) &= \frac{e^2}{4\pi\varepsilon_0\varepsilon_r a_B^*} (4\gamma)^2 \left[\frac{1}{4} + \frac{1}{L^2\gamma} \int_{-L/2}^{L/2} dz_e \int_{-L/2}^{L/2} dz_h \cos^2\left(\frac{\pi z_e}{L}\right) \cos^2\left(\frac{\pi z_h}{L}\right) \right. \\
&\qquad \left. \beta_1 \left(1 - \frac{\pi}{2}[H_1(\beta_1) - N_1(\beta_1)]\right) \right],
\end{aligned} \tag{5.37}$$

where H_k is the Struve function of order k, N_k is the Neumann function of order k [95][93], and $\beta_1 = |4\gamma(z_e - z_h)/a_B^*|$. For $n_e = n_h = 1, n_r = 2$ and $m_r = 0$,

$$\begin{aligned}
\Delta E_1(\gamma) &= \langle \Phi_0 | W(\gamma) | \Phi_0 \rangle \\
&= C \int_0^\infty \int_{-L/2}^{L/2} \int_{-L/2}^{L/2} r dr dz_e dz_h \left(\frac{\gamma e^2}{4\pi\varepsilon_0\varepsilon_r r} \right. \\
&\qquad \left. - \frac{e^2}{4\pi\varepsilon_0\varepsilon_r \sqrt{r^2 + (z_e - z_h)^2}} \right) \exp\left(-\frac{4\gamma r}{3a_B^*}\right) \left(\mathcal{L}_1^0\left(\frac{4\gamma r}{3a_B^*}\right)\right)^2 \\
&\qquad \cos^2\left(\frac{\pi z_e}{L}\right) \cos^2\left(\frac{\pi z_h}{L}\right),
\end{aligned} \tag{5.38}$$

which with the following standard results [95],

$$\begin{aligned}
\int_0^\infty \frac{r^2 dr}{\sqrt{r^2+\beta_1^2}} \exp(-r) &= \frac{\pi}{2} N_0(\beta_1)\beta_1^2 + \beta_1 \frac{\pi}{2}\left(-\beta_1 H_0(\beta_1) - N_1(\beta_1) + H_1(\beta_1)\right), \\
\int_0^\infty \frac{r^3 dr}{\sqrt{r^2+\beta_1^2}} \exp(-r) &= \frac{\pi}{2} N_0(\beta_1)\beta_1^2 + \frac{\beta_1}{2}\Big(2\beta_1^2 - \pi\beta_1 H_0(\beta_1) \\
&\quad + (\beta_1^2 - 2)\pi\left[N_1(\beta_1) - H_1(\beta_1)\right]\Big), \qquad (5.39)
\end{aligned}$$

becomes

$$\begin{aligned}
\Delta E_1(\gamma) &= \frac{1}{9}\frac{e^2}{4\pi\varepsilon_0\varepsilon_r a_B^*}(4\gamma)^2\left[\frac{1}{4} + \frac{1}{L^2\gamma}\int_{-L/2}^{L/2} dz_e \int_{-L/2}^{L/2} dz_h \cos^2\left(\frac{\pi z_e}{L}\right)\cos^2\left(\frac{\pi z_h}{L}\right)\right. \\
&\quad \beta_1\left(1 - \beta_1^2 - \frac{\pi}{2}\left[H_1(\beta_1) + H_0(\beta_1)\beta_1 - H_1(\beta_1)\beta_1^2\right.\right. \\
&\quad \left.\left.\left. -N_1(\beta_1) - N_0(\beta_1)\beta_1 + N_1(\beta_1)\beta_1^2\right]\right)\Big], \qquad (5.40)
\end{aligned}$$

where β_1 is now defined as $\beta_1 = |4\gamma(z_e - z_h)/3a_B^*|$. Finally, for $n_e = n_h = 1, n_r = 2$ and $m_r = \pm 1$,

$$\begin{aligned}
\Delta E_1(\gamma) &= \langle\Phi_0|W(\gamma)|\Phi_0\rangle \\
&= C\int_0^\infty \int_{-L/2}^{L/2}\int_{-L/2}^{L/2} r^3 dr dz_e dz_h \left(\frac{\gamma e^2}{4\pi\varepsilon_0\varepsilon_r r}\right. \\
&\quad \left. -\frac{e^2}{4\pi\varepsilon_0\varepsilon_r\sqrt{r^2 + (z_e - z_h)^2}}\right)\exp\left(-\frac{4\gamma r}{3a_B^*}\right)\left(\mathcal{L}_0^2\left(\frac{4\gamma r}{3a_B^*}\right)\right)^2 \\
&\quad \cos^2\left(\frac{\pi z_e}{L}\right)\cos^2\left(\frac{\pi z_h}{L}\right), \qquad (5.41)
\end{aligned}$$

which becomes

$$\begin{aligned}
\Delta E_1(\gamma) &= \frac{1}{9}\frac{e^2}{4\pi\varepsilon_0\varepsilon_r a_B^*}(4\gamma)^2\left[\frac{1}{4} + \frac{1}{2L^2\gamma}\int_{-L/2}^{L/2} dz_e \int_{-L/2}^{L/2} dz_h \cos^2\left(\frac{\pi z_e}{L}\right)\cos^2\left(\frac{\pi z_h}{L}\right)\right. \\
&\quad \left\{\frac{\pi}{2} N_0(\beta_1)\beta_1^2 + \frac{\beta_1}{2}\Big(2\beta_1^2 - \pi\beta_1 H_0(\beta_1)\right. \\
&\quad \left.\left. +\ (\beta_1^2 - 2)\pi\left[N_1(\beta_1) - H_1(\beta_1)\right]\Big)\right\}\Big]. \qquad (5.42)
\end{aligned}$$

Figure (5-1) shows the calculated variation of the variational parameter γ as a function of the well width in a infinite $Cd_{1-x}Mn_xTe$ DMS quantum well for both the heavy and light hole exciton for the ground state ($n_r = n_e = n_h = 1, m_r = 0$). The values of γ where found by requiring Eq. (5.30) be satisfied, which was achieved by using the downhill simplex method for minimising a function with one variable [76]. The double z integrals where performed using the Simpson method in Fortran, with step sizes chosen to ensure convergence to 3 decimal places. Figure (5-2) shows the corresponding variation for both the heavy and light hole exciton for $n_r = 2$ and $m_r = 0$, whilst Figure (5-3) shows the results for $n_r = 2$ and $m_r = \pm 1$. As can be seen in these figures the variational parameter γ increases as the well width decreases for all the values of n_r and m_r considered. This

can be explained by looking at how the variational parameter is related to to the binding energy. The binding energy for the ground state exciton is given by $E_B = 4R_y^*\gamma^2$ [96][93], since the eigenenergy corresponding to the wavefunction for the unperturbed Hamiltonian (Eq. (5.31)-(5.34)) is

$$E^{(0)} = E_e^{\perp}(z_e) + E_h^{\perp}(z_e) + E_0(n_r, m_r) = \frac{\hbar^2\pi^2 n_e^2}{2m_{e,\perp}^* L^2} + \frac{\hbar^2\pi^2 n_h^2}{2m_{h,\perp}^* L^2} - \lambda_{n_r}^2\gamma^2 R_y^*. \tag{5.43}$$

So as the excitons become more compressed as the well width decreases, the variational parameter should increase. The value of γ also changes depending on the value of n_r and m_r, being greater for $n_r = 2$ and $m_r = 0$ compared to $n_r = 1$ and $m_r = 0$, and greater still for $n_r = 2$ and $m_r = \pm 1$. For a given value of the well width the variational parameter γ is largest for the heavy hole.

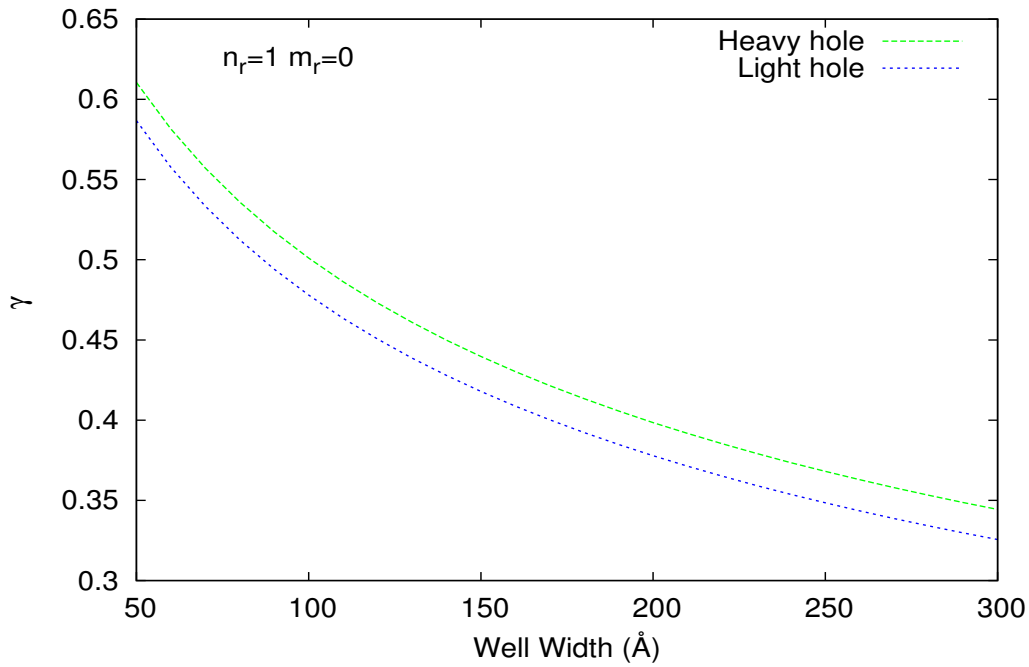

Figure 5-1: Variational parameter γ as a function of the well width for a heavy and light hole exciton in a infinite $Cd_{1-x}Mn_xTe$ DMS quantum well for $n_r = 1$ and $m_r = 0$. The values of the physical parameters used for $Cd_{1-x}Mn_xTe$ are given in the table in Appendix K.

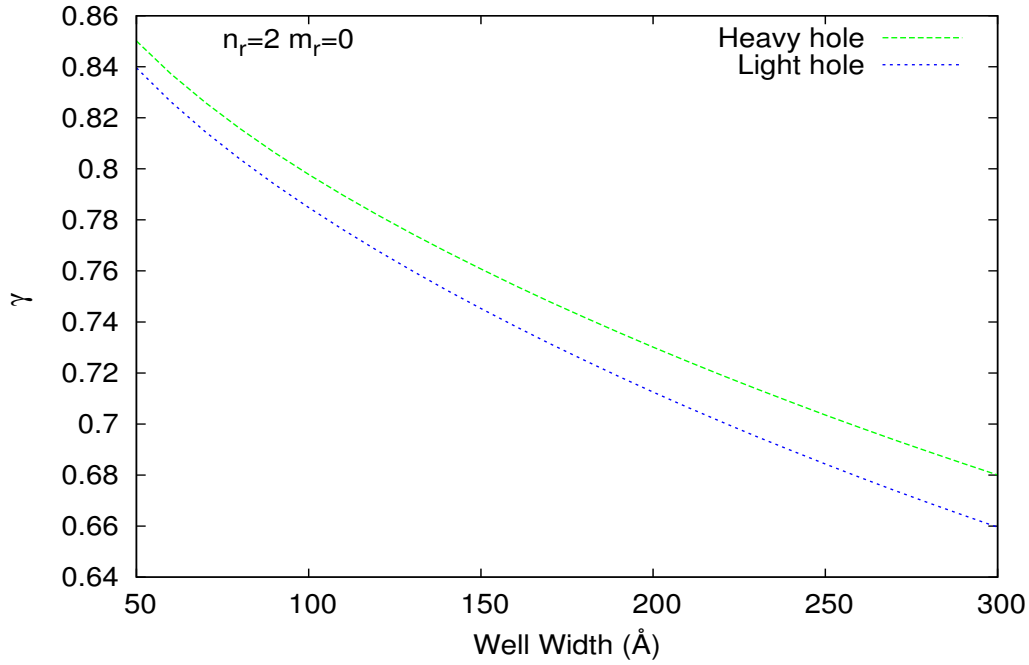

Figure 5-2: Variational parameter γ as a function of the well width for a heavy and light hole exciton in a infinite $Cd_{1-x}Mn_xTe$ DMS quantum well for $n_r = 2$ and $m_r = 0$. The values of the physical parameters used for $Cd_{1-x}Mn_xTe$ are given in the table in Appendix K.

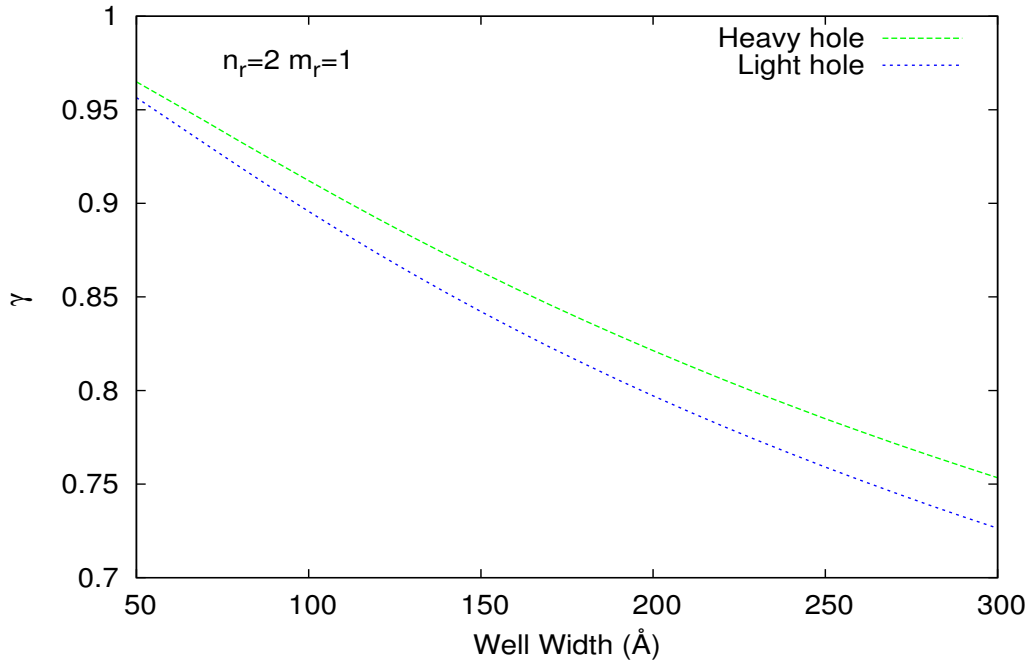

Figure 5-3: Variational parameter γ as a function of the well width for a heavy and light hole exciton in a infinite $Cd_{1-x}Mn_xTe$ DMS quantum well for $n_r = 2$ and $m_r = \pm 1$. The values of the physical parameters used for $Cd_{1-x}Mn_xTe$ are given in the table in Appendix K.

5.1.4 Spin Hamiltonian

We now consider the fourth term in the Hamiltonian in (5.1), which describes the interaction of the exciton spin with the magnetic field. The Zeeman splitting of the electron and hole in ordinary semiconductors is described by a spin Hamiltonian. In a bulk semiconductor, the ground state of the heavy hole exciton consists of an electron with spin $S_e = \pm\frac{1}{2}$, and a heavy hole with spin $J_h = \pm\frac{3}{2}$, while the round state of the light hole exciton consists of an electron with spin $S_e = \pm\frac{1}{2}$, and a light hole with spin $J_{h,z} = \pm\frac{1}{2}$. Zinc blende crystals have tetrahedral symmetry, and the total Hamiltonian must retain its scalar form under the coordinate transformations of the tetrahedral symmetry group. This results in the following spin Hamiltonian [97][98][99]

$$\mathcal{H}_{ex}^{m_z}(\vec{r}_e, \vec{r}_h) = \mathcal{H}_e + \mathcal{H}_h + \mathcal{H}_{e-h}, \tag{5.44}$$

describing the exciton spin interaction with the magnetic field, which is the fourth term of the Hamiltonian in Eq. (5.1), where

$$\mathcal{H}_e = \mu_B \sum_{i=x,y,z} g_{e,i} S_{e,i} B_i(\vec{r}_e) \tag{5.45}$$

and

$$\mathcal{H}_h = -2\mu_B \sum_{i=x,y,z} (\kappa_i J_{h,i} + q_i J_{h,i}^3) B_i(\vec{r}_h), \tag{5.46}$$

describing the Zeeman splittings of the electrons and holes, and

$$\mathcal{H}_{e-h} = -\sum_{i=x,y,z} (a_i J_{h,i} S_{e,i} + b_i J_{h,i}^3 S_{e,i}), \tag{5.47}$$

describing the spin coupling of the electron and hole forming the exciton. In these equations $g_{e(h),i}$ represents the electron (hole) g factor in the direction i, $S_{e,i}$ is the component of the electron spin, B_i is the component of the magnetic field, $J_{h,i}$ is the i component of total angular momentum of the hole, κ and q are the (Luttinger) Zeeman splitting constants for the hole, and a, b are the spin splitting coupling constants. For a quantum well, the heavy hole sub matrices have the property that $\tilde{J}_{h,x} = \tilde{J}_{h,y} = 0$ and $\tilde{J}_{h,z} = \frac{4}{9}\tilde{J}_{h,z}^3$. Using the relevant symmetry for a quantum well in the z direction the spin Hamiltonian for an electron and heavy hole can therefore be rewritten as [97]

$$\begin{aligned} \mathcal{H}_{ex}^{m_z}(\vec{r}_e, \vec{r}_h) \;=\; & \sum_{i=x,y} \left[\mu_B \left(g_{e,i} S_{e,i} - 2q_i \tilde{J}_{h,i}^3\right) B_i(\vec{r}_e, \vec{r}_h) - b_i S_{e,i} \tilde{J}_{h,i}^3\right] \\ & + \mu_B \left[g_{e,z} S_{e,z} - \left(\frac{8}{9}\kappa_z + 2q_z\right) \tilde{J}_{h,z}^3\right] B_z(\vec{r}_e, \vec{r}_h) - \left(\frac{4}{9}a_z + b_z\right) S_{e,z} \tilde{J}_{h,z}^3 \\ & , \end{aligned} \tag{5.48}$$

with $g_{e,x} = g_{e,y}$, $q_x = q_y$, and $b_x = b_y$. By using the following relations

$$\begin{aligned} & g_{h,x} = 3q_x, \qquad g_{h,y} = -3q_y, \qquad g_{h,z} = 6\kappa_z + 13.5q_z \\ & c_x = 1.5b_x, \qquad c_y = -1.5b_y, \qquad c_z = 3a_z + 6.75b_z, \end{aligned} \tag{5.49}$$

and

$$g_{h,x} = -g_{h,y}, \qquad c_x = -c_y, \tag{5.50}$$

for the D_{2d} point group symmetry of the quantum well. D_{2d} symmetry has a fourfold rotation reflection axis along the z direction which dictates $c_x = |c_y$ as well as $g_{e,x} = g_{e,y}$, and $g_{h,x} = -g_{h,y}$. If this symmetry is broken a zero field splitting $c_x + c_y$ appears. Eq. (5.48) can then be rewritten as

$$\mathcal{H}_{ex}^{m_z}(\vec{r}_e, \vec{r}_h) = \mu_B \sum_{i=x,y,z} \left[g_{e,i} S_{e,i} - \frac{1}{3} g_{h,i} \tilde{J}_{h,i} \right] B_i(\vec{r}_e, \vec{r}_h) - \frac{1}{3} \sum_{i=x,y,z} c_i S_{e,i} \tilde{J}_{h,i}. \tag{5.51}$$

The spin-spin coupling constant, c_i, is related to the zero field spin interaction. Assuming the field varies slowly on the scale of the exciton radius, this can be simplified using the adiabatic approximation, expanding the magnetic field to zero order in the relative coordinates, i.e., $\vec{B}(\vec{r}_e, \vec{r}_h) = \vec{B}(\vec{R})$. With this assumption, the exciton spin Hamiltonian takes the form [98]

$$\mathcal{H}_{ex}^{m_z}(\vec{R}) = \mu_B \sum_{i=x,y,z} \left[g_{e,i} S_{e,i} - \frac{1}{3} g_{h,i} J_{h,i} \right] B_i(\vec{R}) - \frac{1}{3} \sum_{i=1}^{3} c_i S_{e,i} J_{h,i}. \tag{5.52}$$

Neglecting the terms which do not depend on the magnetic field, c_z, and the terms c_x and c_y, which cancel because of symmetry considerations of the D_{2d} point symmetry group of the quantum well [84][100], the eigenenergy of the spin Hamiltonian for an electron and heavy hole ($J_{h,i} = 3/2$) is straightforwardly calculated from Eq. (5.52), by expanding the direct products of the spin matrices and simplified to

$$E_{ex}^{m_z}(\vec{R}) = \pm \frac{1}{2} \mu_B g_{ex} B_z(\vec{R}), \tag{5.53}$$

where $g_{ex} = g_{e,z} + g_{h,z}$ is the exciton g factor, and the $\pm$ refers to heavy hole excitons with plus ($S_e = \frac{1}{2}$, and $J_h = \frac{3}{2}$) or negative ($S_e = -\frac{1}{2}$, and $J_h = -\frac{3}{2}$) spins.

5.2 Centre of mass equation

The total exciton wavefunction satisfying the Schrödinger equation containing the Hamiltonian (5.1) can be written as a product of terms describing the decoupled motions [80]

$$\Psi(\vec{R}, \vec{r}, z_e, z_h) = \psi(\vec{R}) \Phi_0^{n_r, m_r}(\vec{r}) \phi_{e,h}(z_e, z_h) \mathcal{L}^{m_z}(\vec{R}), \tag{5.54}$$

where $\psi(\vec{R})$ is the wavefunction associated with the in plane centre of mass motion, $\Phi_0^{n_r, m_r}(\vec{r})$ is the exciton wavefunction associated with the in plane relative motion, $\phi_{e,h}(z_e, z_h)$ is the exciton wavefunction corresponding to the confinement in the quantum well, and $\mathcal{L}^{m_z}(\vec{R})$ is the exciton spin wavefunction.

It is assumed that there is no coupling between the exciton spin and its centre of mass and relative motion. The following Schrödinger equations are then obtained

$$\left\{ \mathcal{H}^{\mathrm{CM}}(\vec{R}) + E^{\mathrm{rel}}(\gamma, \vec{R}, \nabla_R) + E^{m_z}(\vec{R}) + E_{e,h}^{\perp} + H_{s,p-d}(\vec{R}) - E \right\} \psi(\vec{R}) = 0, \tag{5.55}$$

$$\left\{ \mathcal{H}_{\gamma}^{\mathrm{rel}}(\vec{r}, \vec{R}, \nabla_R) - E^{\mathrm{rel}}(\gamma, \vec{R}, \nabla_R) \right\} \Phi_0^{n_r, m_r}(\vec{r}) = 0, \tag{5.56}$$

$$\left\{ \mathcal{H}^{m_z}(\vec{R}) - E^{m_z}(\vec{R}) \right\} \mathcal{L}^{m_z}(\vec{R}) = 0. \tag{5.57}$$

$$\left\{\mathcal{H}^{\perp}(z_e,z_h)-E^{\perp}_{e,h}\right\}\phi_{e,h}(z_e,z_h)=0. \tag{5.58}$$

The energy of the exciton confinement in the quantum well direction (i.e. the eigenenergy of $\left\{\mathcal{H}^{\perp}(z_e,z_h)-E^{\perp}_{e,h}\right\}\phi_{e,h}(z_e,z_h)=0$), does not depend on the magnetic field, since only the exciton in the xy plane is being additionally restricted by applying the inhomogeneous magnetic field. Therefore the energy does not have to be calculated explicitly. This is due to the fact that the infinite well has been chosen to be used. All the well confinement related contribution to the exciton trapping is then determined through the γ parameter, and energies found give the exciton energy relation to $E^{\perp}_{e,h}$.

Now all the results of the exciton relative motion, well confinement, and spin interaction (Eqs. (5.24), (5.30), and (5.53) respectively) are used to solve the exciton centre of mass equation in Eq. (5.55)

$$\begin{aligned}\mathcal{H}^{CM}(\vec{R}) &= -\frac{\hbar^2}{2M}\nabla_R\left\{1-\alpha^{n_r}_{m_r}\frac{e^2a_B^{*2}}{Mc^2R_y^*}\gamma^{-4}B_z(\vec{R})^2\right\}\nabla_R+\beta^{n_r}_{m_r}\frac{e^2a_B^{*2}}{8\mu c^2}\gamma^{-2}B_z(\vec{R})^2\\ &\quad+\frac{e\hbar}{2\mu c}\xi B_z(\vec{R})m_r-\lambda^2_{n_r}\gamma^2R_y^*\pm\frac{1}{2}\mu_B g_{ex}B_z(\vec{R})+\mathcal{H}_{s,p-d}(\vec{R}),\end{aligned} \tag{5.59}$$

which describes the centre of mass motion of the exciton in an inhomogeneous magnetic field. The magnetic field is parallel to the z direction and for the magnetic disk systems has rotational symmetry, i.e., $B_z(\vec{R})=B_z(R)$. As a result, the exciton centre of mass wavefunction takes the form

$$\psi(\vec{R})=\frac{1}{\sqrt{2\pi}}\exp\left\{im_R\phi\right\}\psi(R), \tag{5.60}$$

where m_R is the exciton centre of mass angular momentum quantum number, and the radial wavefunction satisfies [52]

$$\left\{-\frac{\hbar^2}{2}\frac{1}{R}\frac{d}{dR}\left[\frac{R}{M^{eff}(R)}\frac{d}{dR}\right]+V^{eff}(R)-E\right\}\psi(R)=0, \tag{5.61}$$

where the effective mass

$$M^{eff}(R)=\frac{M}{1-\alpha^{n_r}_{m_r}c_1\gamma^{-4}B_z(R)^2}, \tag{5.62}$$

and the effective potential

$$\begin{aligned}V^{eff}(R) &= \frac{\hbar^2}{2M^{eff}(R)}\frac{m_R^2}{R^2}+\beta^{n_r}_{m_r}c_2\gamma^{-2}B_z(R)^2+m_rc_3B_z(R)-\lambda^2_{n_r}\gamma^2R_y^*\\ &\quad\pm\frac{1}{2}\mu_Bg_{ex}B_z(R)+H_{s,p-d}(R),\end{aligned} \tag{5.63}$$

with

$$c_1=\frac{e^2a_B^{*2}}{R_y^*Mc^2},\qquad c_2=\frac{e^2a_B^{*2}}{8\mu c^2},\qquad c_3=\frac{e\hbar}{2\mu c}\xi. \tag{5.64}$$

5.3 Results

In this section the possibilities of trapping excitons is illustrated using the magnetic field profiles created by microscale ferromagnetic disks and a nanoscale ferromagnetic disk in the vortex state placed on top of the DMS quantum well. The possibility of trapping excitons in a magnetic strip (linear magnetic traps) is also discussed. For this the exciton centre of mass equation is re-derived due to the different symmetry.

5.3.1 Microscale ferromagnetic disk

Here we discuss the magnetic field created by a microscale ferromagnetic disk. The microscale ferromagnetic disk is assumed to be very thin and is completely magnetised in the z direction, with the magnetisation given by

$$\vec{M}(\vec{R}) = h\mathcal{M}\delta(Z-d)\Theta(a-R)\vec{e}_Z, \tag{5.65}$$

where h is the disk thickness, a the disk radius, d the distance between the magnetic disk and the DMS quantum well, $\mathcal{M}$ the magnetisation, and $\Theta(X)$ the Heaviside step function. Z and $R = \sqrt{X^2+Y^2}$ are the cylindrical coordinates. The corresponding vector potential is found from the differential form of Amperes law. In cylindrical coordinates it only has an angular component

$$A_\varphi(R) = 4B_0^D\sqrt{\frac{a}{R}}\frac{1}{k}\left\{-E(k)+\left(1-\frac{k^2}{2}\right)K(k)\right\}, \tag{5.66}$$

where $E(k)$ and $K(k)$ are elliptic integrals and

$$k = \sqrt{\frac{4aR}{(a+R)^2+d^2}}. \tag{5.67}$$

$B_0^D = h\mathcal{M}$ is the field strength of the disk. The magnetic field $\vec{B}(\vec{R}) = \nabla\times\vec{A}(\vec{R})$ has z component

$$\begin{aligned} B_z(R) &= 2B_0^D\frac{(a+R)}{R\sqrt{(a+R)^2+d^2}}\left\{-E(k)+\left(1-\frac{k^2}{2}\right)K(k)\right\} \\ &\quad +B_0^D\frac{(a^2-R^2+d^2)}{R^2\sqrt{aR}}k^3\left\{-\frac{\partial}{\partial k^2}E(k)-\frac{1}{2}K(k)+\left(1-\frac{k^2}{2}\right)\frac{\partial}{\partial k^2}K(k)\right\}, \end{aligned} \tag{5.68}$$

where the full derivation may be found in Appendix I. Then the total magnetic field acting within the DMS quantum well is taken to be $B_z^{\text{Total}} = B_a + B_z(R)$, where B_a is an applied homogeneous magnetic field used to increase the confinement of the exciton [52].

Figure (5-4) shows the magnetic field profile created by a microscale ferromagnetic disk for different values of B_a and B_0^D, and Figure (5-5) illustrates how it varies with separation d and radius a. It can be seen that increasing the external applied magnetic field B_a simply increases the value of the magnetic field at a given point. By increasing B_0^D the magnetic field profile is shifted up and has a steeper curve, as seen in Figure (5-4). By increasing the distance from the microscale ferromagnetic disk to the DMS quantum well there is a reduction in the steepness of the magnetic profile, while increasing the disk radius results in the magnetic field profile being both broadened and reduced in magnitude in the central region, as seen in Figure (5-5).

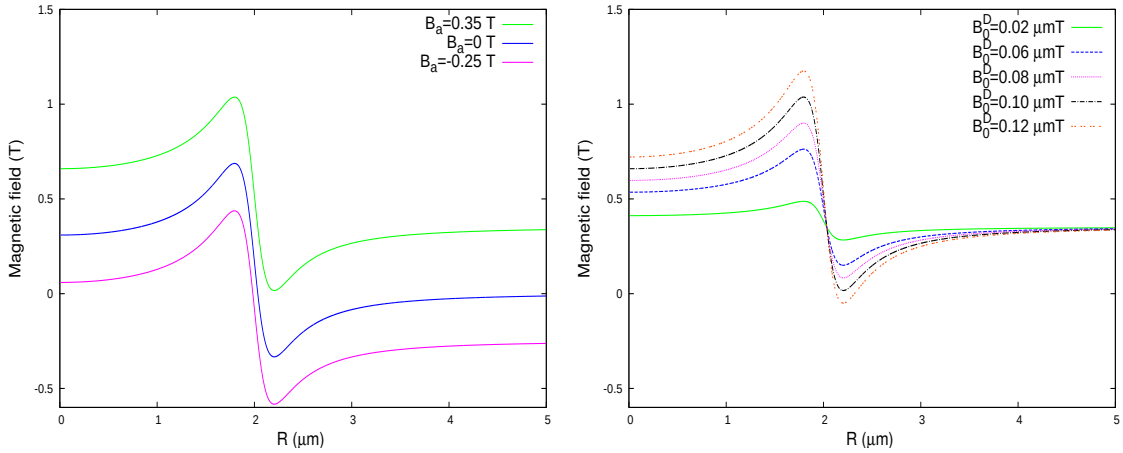

Figure 5-4: Left: Magnetic field in the presence of a microscale ferromagnetic disk as a function of the radial coordinate R for different applied magnetic fields, B_a, calculated with $B_0^D = 0.1$ μmT, $a = 2$ μm, and $d = 0.2$ μm. Right: Magnetic field in the presence of a microscale ferromagnetic disk as a function of the radial coordinate R for different strengths of the magnetisation of the disk, B_0^D, calculated with $B_a = 0.35$ T, $a = 2$ μm, and $d = 0.2$ μm.

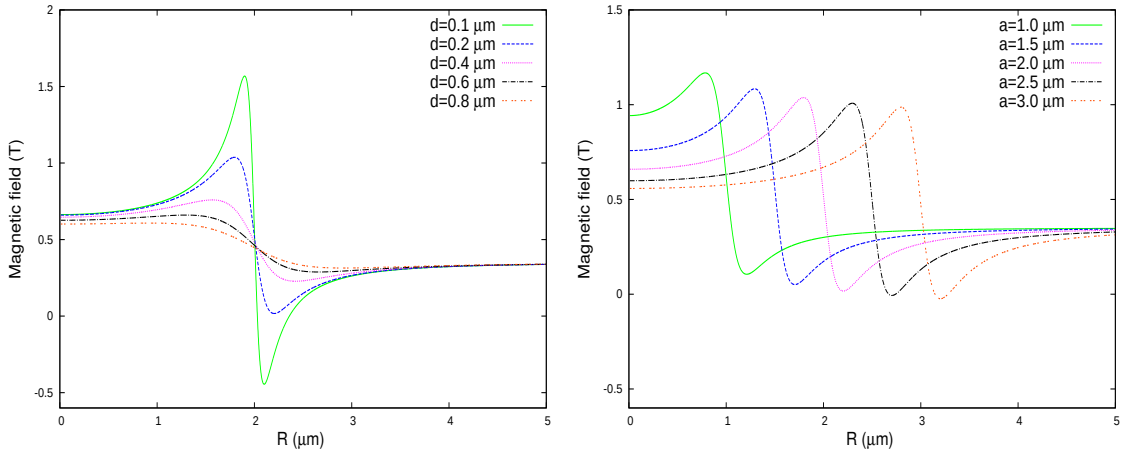

Figure 5-5: Left: Magnetic field in the presence of a microscale ferromagnetic disk as a function of the radial coordinate R for different distances of the disk to the DMS quantum well, d, calculated with $B_a = 0.35$ T, $B_0^D = 0.1$ μmT, and $a = 2$ μm. Right: Magnetic field in the presence of a microscale ferromagnetic disk as a function of the radial coordinate R for different disk radii, a, calculated with $B_a = 0.35$ T, $B_0^D = 0.1$ μmT, and $d = 0.2$ μm.

The effective potential given by Eq. (5.63) resulting from the magnetic field created by the microscale ferromagnetic disk is shown in Figures (5-6)-(5-9). Figure (5-6) illustrates how this potential varies for different values of the applied magnetic field, B_a, and the strength of the magnetisation of the disk, B_0^D, whilst Figure (5-7) shows the influence of the disk radius and distance between the disk and the DMS quantum well. The structure evident in the magnetic field plots, Figure (5-4), (5-5) is evident in the effective potential, Figure (5-6), (5-7), in particular the rapid variation near the disk radius creates a minimum in the effective potential just outside $R = a$, which it will be seen below traps excitons. The effective potential of the well width L on the effective potential can be seen in Figure (5-8). Increasing the well width raises the effective potential, meaning that the ground state energy of any trapped exciton will also increase with well width. The effective potential for different n_r, m_r and m_R quantum numbers is also shown in Figure (5-8), in the panel on the right. Increasing the radial relative motion quantum number n_r greatly increases the effective potential which can be seen by comparing the left plot in Figure (5-8) for $n_r = 1$ and $m_r = 0$ with the right plot in Figure (5-8) for $n_r = 2$ and $m_r = 0$. This can be explained by looking at the fourth term in the effective potential in Eq. (5.63), $-\lambda_{n_r}^2 \gamma^2 R_y^*$. The biggest negative contribution to the effective potential results from the zero field term $-\lambda_{n_r}^2 \gamma^2 R_y^*$ in the effective potential. It increases with increasing n_r, which is due to the $-\lambda_{n_r}^2 \gamma^2 R_y^*$ term having a lower negative contribution to the effective potential. The effective potential increases with the inclusion of the γ term in $-\lambda_{n_r}^2 \gamma^2 R_y^*$ which again results from $-\lambda_{n_r}^2 \gamma^2 R_y^*$ having a lower negative contribution to the effective potential. The effective potential is decreased when the m_r term is added due to the effect of the other terms, which can be seen in Figure (5-8). The first term in the effective potential equation, the centrifugal term, contains the exciton effective mass and the angular momentum of the centre of mass motion, and generally gives the smallest contribution to the effective potential. Varying like (m_R^2/R^2), it becomes significant as $R \to 0$, but is otherwise negligible, as can be seen in Figure (5-8), where the effective potential for $n_r = 2$, $m_r = 0$, $m_R = 1$ only differs from the effective potential for $n_r = 2$, $m_r = 0$, $m_R = 0$ when R becomes very small. The second term in the effective potential, the diamagnetic term, depends upon the square of the magnetic field. The third term, the orbital momentum term, makes a greater contribution than the diamagnetic term, but only contributes when $m_r \neq 0$. The fifth term, the spin contribution, is found to be slightly larger than the diamagnetic term. The sixth term, the sp-d interaction, is greater than the others. Figure (5-9) shows the effect of changing the magnetic ion concentration, x, and temperature, T, which influences the sp-d interaction term. Increasing x and decreasing T leads to a greater sp-d interaction term. The spin components in the sp-d interaction for a heavy hole exciton (light hole exciton) with both $S_{e,z} = \frac{1}{2}$, $S_{h,z} = \frac{3}{2}$ ($S_{e,z} = \frac{1}{2}$, $S_{h,z} = \frac{1}{2}$) are labelled by σ^+ and $S_{e,z} = -\frac{1}{2}$, $S_{h,z} = -\frac{3}{2}$ ($S_{e,z} = -\frac{1}{2}$, $S_{h,z} = -\frac{1}{2}$) are labelled by σ^-. The effective potentials for heavy and light hole excitons for both σ^+ and σ^- spin components are plotted in the inset of Figure (5-10).

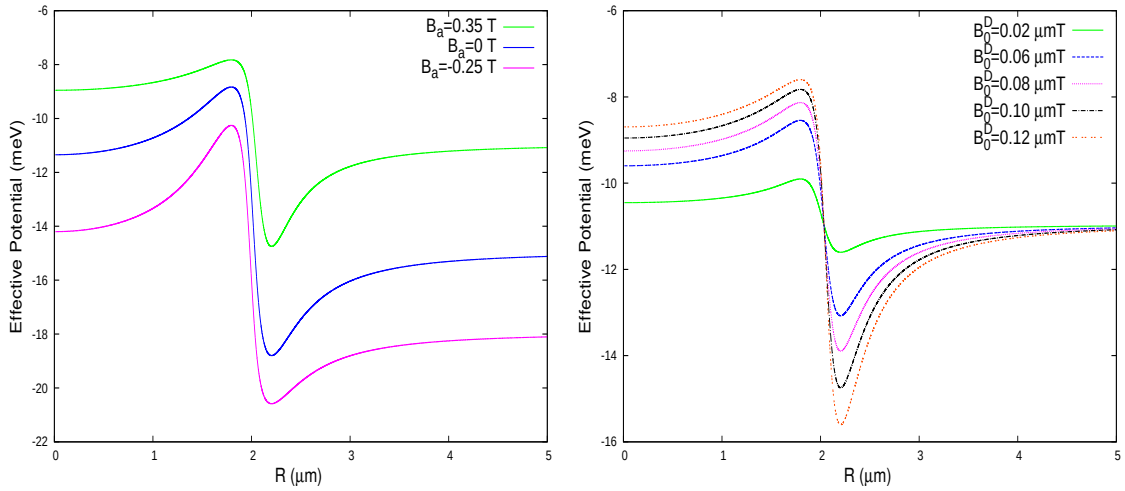

Figure 5-6: Left: Effective potential for a microscale ferromagnetic disk as a function of the radial coordinate R for different applied magnetic fields, B_a, for a heavy hole exciton. Calculated with $B_0^D = 0.1$ μmT, $a = 2$ μm, $d = 0.2$ μm, $S_{e,z} = \frac{1}{2}$, $S_{h,z} = \frac{3}{2}$, $x = 0.01$, $T = 1$ K, $L = 50$ Å, $n_r = 1$, $m_r = 0$ and $m_R = 0$. Right: Effective potential for a microscale ferromagnetic disk as a function of the radial coordinate R for different strengths of the magnetisation of the disk, B_0^D, for a heavy hole exciton. Calculated with $B_a = 0.35$ T, $a = 2$ μm, $d = 0.2$ μm, $S_{e,z} = \frac{1}{2}$, $S_{h,z} = \frac{3}{2}$, $x = 0.01$, $T = 1$ K, $L = 50$ Å, $n_r = 1$, $m_r = 0$ and $m_R = 0$. The values used for $Cd_{1-x}Mn_xTe$ are given in the Table in Appendix K.

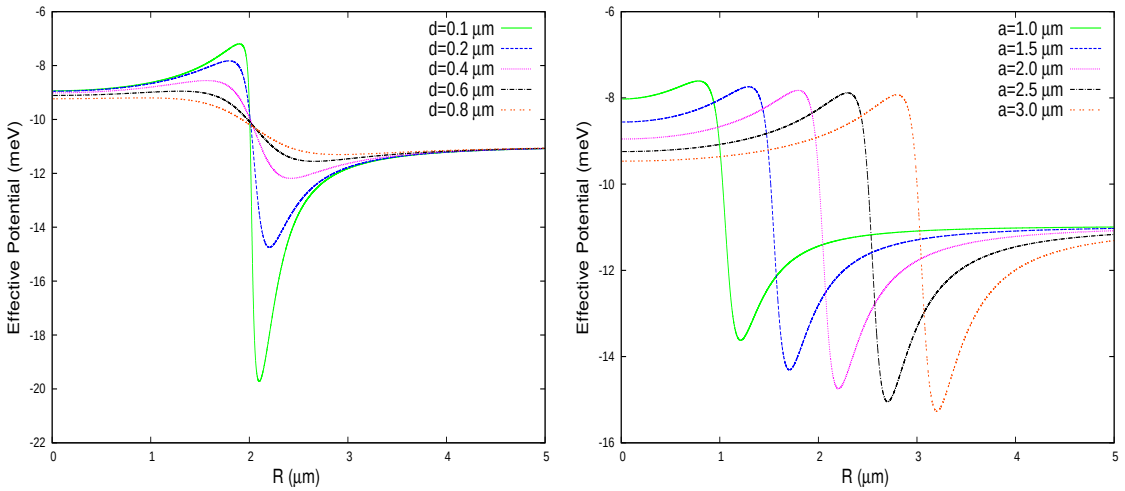

Figure 5-7: Left: Effective potential for a microscale ferromagnetic disk as a function of the radial coordinate R for different distances of the disk to the DMS quantum well, d, for a heavy hole exciton. Calculated with $B_a = 0.35$ T, $B_0^D = 0.1$ μmT, $a = 2$ μm, $S_{e,z} = \frac{1}{2}$, $S_{h,z} = \frac{3}{2}$, $x = 0.01$, $T = 1$ K, $L = 50$ Å, $n_r = 1$, $m_r = 0$ and $m_R = 0$. Right: Effective potential for a microscale ferromagnetic disk as a function of the radial coordinate R for different disk radii, a, for a heavy hole exciton. Calculated with $B_a = 0.35$ T, $B_0^D = 0.1$ μmT, $d = 0.2$ μm, $S_{e,z} = \frac{1}{2}$, $S_{h,z} = \frac{3}{2}$, $x = 0.01$, $T = 1$ K, $L = 50$ Å, $n_r = 1$, $m_r = 0$ and $m_R = 0$. The values used for $Cd_{1-x}Mn_xTe$ are given in the Table in Appendix K.

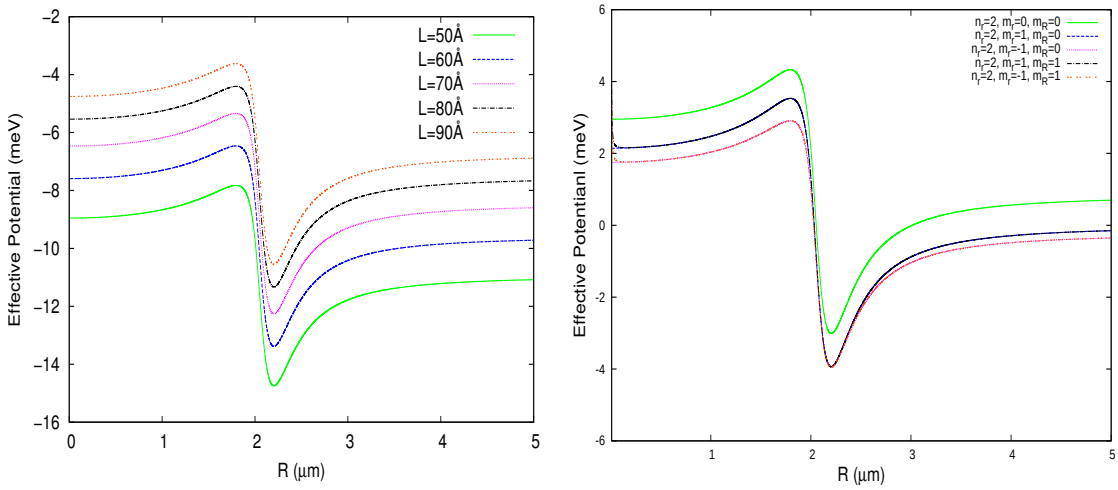

Figure 5-8: Left: Effective potential for a microscale ferromagnetic disk as a function of the radial coordinate R for different quantum well widths, L, for a heavy hole exciton. With $B_a = 0.35$ T, $B_0^D = 0.1$ μmT, $a = 2$ μm, $d = 0.2$ μm, $S_{e,z} = \frac{1}{2}$, $S_{h,z} = \frac{3}{2}$, $x = 0.01$, $T = 1$ K, $n_r = 1$, $m_r = 0$ and $m_R = 0$. Right: Effective potential for a microscale ferromagnetic disk as a function of the radial coordinate R for different values of n_r, m_r and m_R for a heavy hole exciton. Calculated with $B_a = 0.35$ T, $B_0^D = 0.1$ μmT, $a = 2.0$ μm, $d = 0.2$ μm, $S_{e,z} = \frac{1}{2}$, $S_{h,z} = \frac{3}{2}$, $x = 0.01$, $T = 1$ K, $L = 50$ Å. The values used for $Cd_{1-x}Mn_xTe$ are given in the Table in Appendix K.

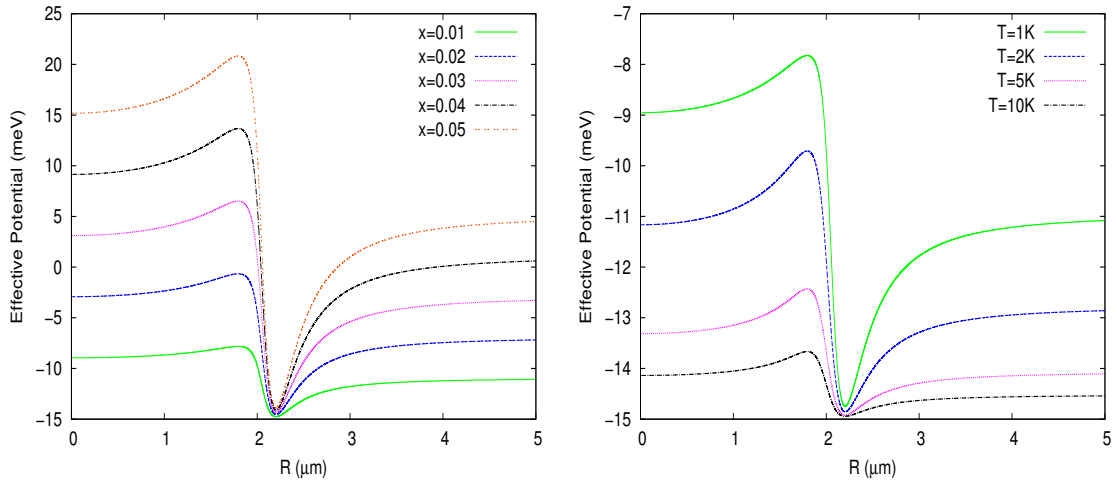

Figure 5-9: Left: Effective potential for a microscale ferromagnetic disk as a function of the radial coordinate R for different values of the magnetic ion concentration, x, for a heavy hole exciton. Calculated with $B_a = 0.35$ T, $B_0^D = 0.1$ μmT, $a = 2$ μm, $d = 0.2$ μm, $S_{e,z} = \frac{1}{2}$, $S_{h,z} = \frac{3}{2}$, $T = 1$ K, $L = 50$ Å, $n_r = 1$, $m_r = 0$, and $m_R = 0$. Right: Effective potential as a function of the radial coordinate R for different temperatures, T, for a heavy hole exciton. Calculated with $B_a = 0.35$ T, $B_0^D = 0.1$ μmT, $a = 2$ μm, $d = 0.2$ μm, $S_{e,z} = \frac{1}{2}$, $S_{h,z} = \frac{3}{2}$, $x = 0.01$, $L = 50$ Å, $n_r = 1$, $m_r = 0$, and $m_R = 0$. The values used for $Cd_{1-x}Mn_xTe$ are given in the Table in Appendix K.

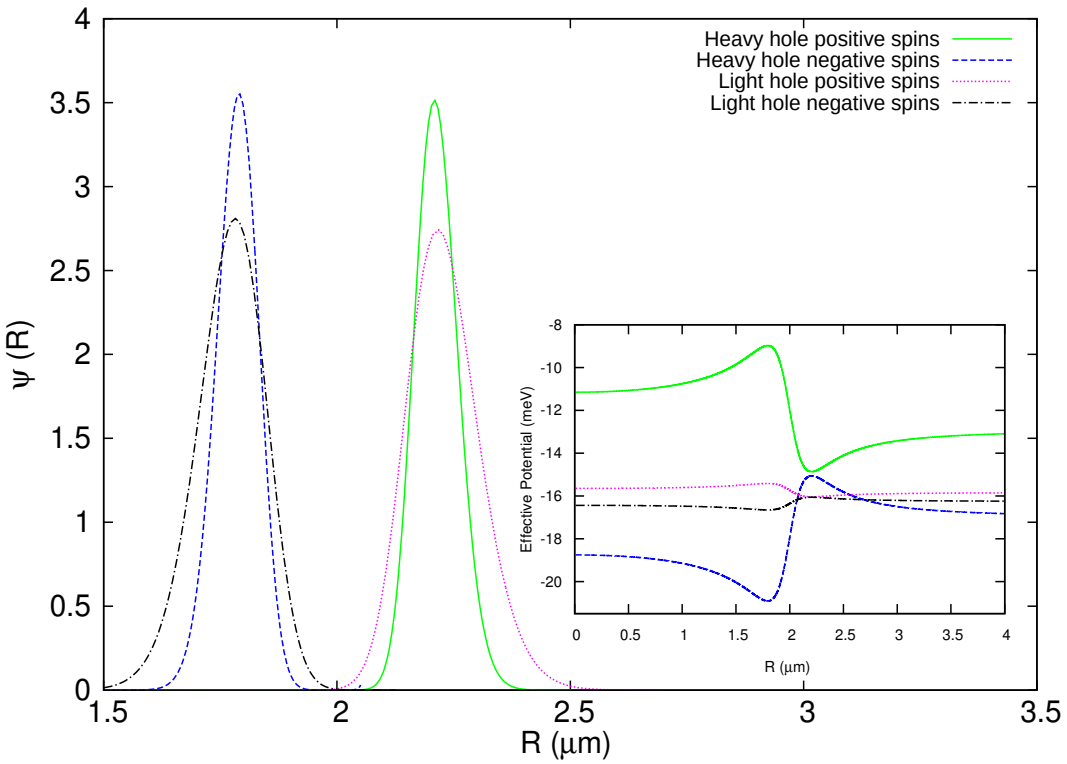

Figure 5-10: The ground state exciton centre of mass radial wavefunction ψ(R) as a function of the radial coordinate R for a heavy and light hole exciton with both σ^+ and σ^- spin components, confined by the magnetic field due to a microscale ferromagnetic disk. The inset shows the effective potential. Calculated with $B_a = 0.35$ T, $B_0^D = 0.1$ μmT, $a = 2$ μm, $d = 0.2$ μm, $x = 0.01$, $T = 1$ K, $L = 50$ Å, $n_r = 1$, $m_r = 0$ and $m_R = 0$. The values used for $Cd_{1-x}Mn_xTe$ are given in the Table in Appendix K.

The eigenfunctions and energies of the Schrödinger Eq. (5.61) containing the effective potentials have been found using the fourth order Runge Kutta method to discretise the equation and the bisection method for root finding, implemented in C++. Care was taken to ensure eigenvalues converged to 10 decimal places with respect to the discretisation step size, which was typically 0.0001μm. It is found that the effective potential can trap more than a single ground state wavefunction, and the wavefunctions for all the heavy and light hole excitons for a single value of x and T are plotted in Figures (5-11) and Appendix J (Figure (J-1)-(J-2)), where the higher members of the series are to be found. More heavy hole exciton radial states are identified as being trapped by the effective potential when $x = 0.09$ and $T = 20$ K, than light hole excitons, because for a heavy hole exciton the sp-d exchange interaction makes a bigger contribution, and creates a deeper potential well, shown in the insert of Figure (5-10). The wavefunction is more confined for the heavy hole exciton than the light hole exciton due to the effective potential being narrower for a given value of x and T for the heavy hole. The wavefunctions for different values of n_r and m_r for a heavy hole exciton can be found in Figure (5-12) and Appendix J (Figure (J-3)-(J-4)). For a heavy hole exciton with $n_r = 1$ and $m_r = 0$ eleven states are found when $x = 0.09$, $T = 20$ K. Increasing n_r to $n_r = 2$ (and still $m_r = 0$) traps an additional twelfth state. Increasing the value of m_r to $m_r = 1$ (and having $n_r = 2$) increases the number again, to thirteen. This can be explained by looking at the effective potential

on the right side of Figure (5-8), where the well is slightly deeper when $n_r = 2$ and $m_r = 1$, meaning more states can be trapped. Increasing the value of n_r results in the wavefunction becoming more confined, and becomes confined further for a higher value of m_r (with $n_r = 2$ and $m_r = 1$) due to a narrower potential well being created by the terms in the effective potential involving m_r.

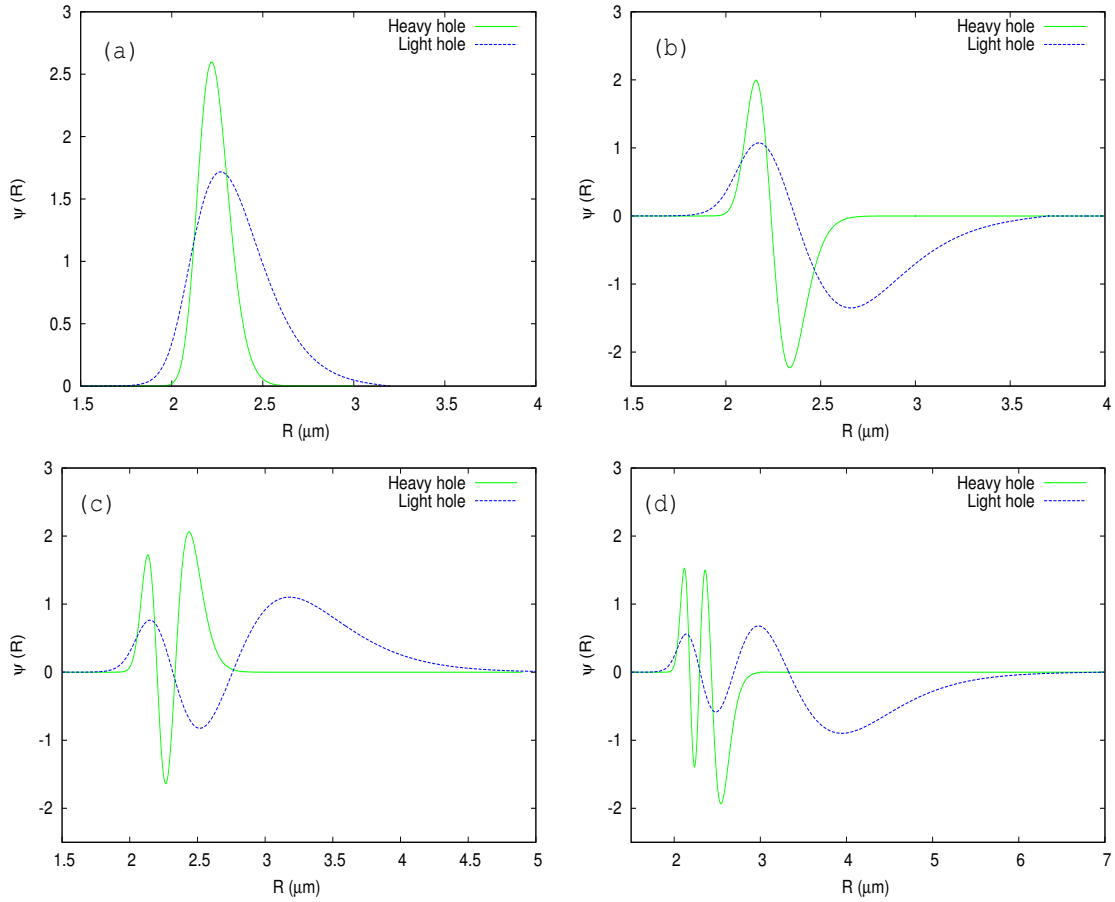

Figure 5-11: (a) Ground state, (b) first excited state, (c) second excited state, and (d) third excited state exciton centre of mass radial wavefunction ψ(R) as a function of the radial coordinate R for a heavy and light hole exciton. Calculated with $B_a = 0.35$ T, $B_0^D = 0.1$ μmT, $a = 2$ μm, $d = 0.2$ μm, $S_{e,z} = \frac{1}{2}$, $S_{h,z} = \frac{3}{2}$, $x = 0.01$, $T = 20$ K, $L = 50$ Å, $n_r = 1$, $m_r = 0$ and $m_R = 0$. The values used for $Cd_{1-x}Mn_xTe$ are given in the Table in Appendix K. Rest given in Appendix J (Figure (J-1)-(J-2)).

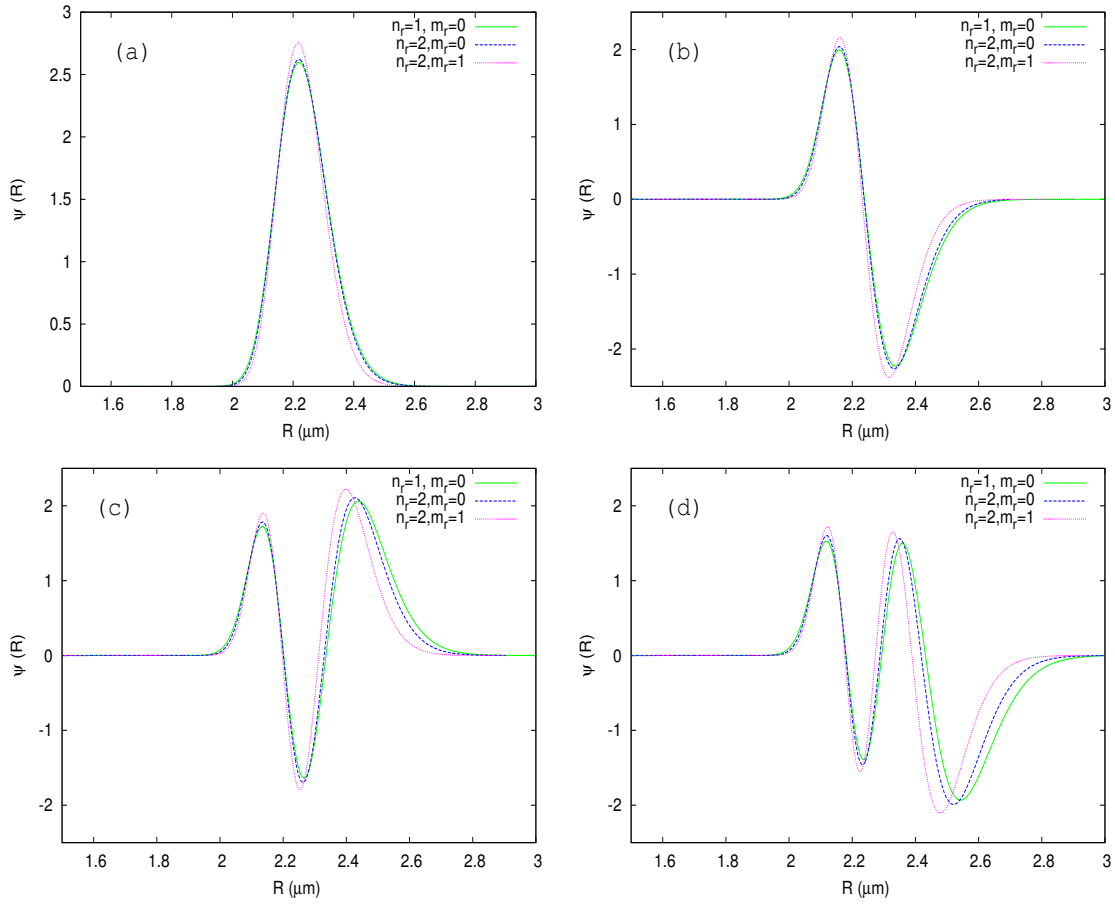

Figure 5-12: (a) Ground state, (b) first excited state, (c) second excited state, and (d) third excited state exciton centre of mass radial wavefunction ψ(R) as a function of the radial coordinate R for a heavy hole for different values of n_r and m_r. Calculated with $B_a = 0.35$ T, $B_0^D = 0.1$ μmT, $a = 2$ μm, $d = 0.2$ μm, $S_{e,z} = \frac{1}{2}$, $S_{h,z} = \frac{3}{2}$, $x = 0.01$, $T = 20$ K, $L = 50$ Å, and $m_R = 0$. The values used for $Cd_{1-x}Mn_xTe$ are given in the Table in Appendix K. Rest given in Appendix J (Figure (J-3)-(J-4)).

The number of excited states changes depending on concentration x and temperature T, and this is shown in Figure (5-13)-(5-16). The number of solutions (where $n = 0$ is the lowest energy state) for $n_r = 1$ and $m_r = 0$ and the corresponding energy E_n for different values of x can be seen in Figure (5-13) for both heavy and light hole excitons. Increasing x increases both the number of solutions and their energies, due to the fact that the sp-d interaction term increases with x, resulting in a deeper well in an overall rising potential, as can be seen in Figure (5-9). The corresponding ground state wavefunction becomes more localised as x is increased, Figure (5-13). The light hole exciton has fewer solutions and lower energies for a given value of x, because for a light hole exciton the sp-d exchange interaction makes a smaller contribution.

The number of solutions for $n_r = 2$ and $m_r = 0$ as well as the corresponding energy for different values of x is plotted in Figure (5-14) for the heavy hole exciton. Increasing n_r increases the number of solutions for the heavy hole exciton for a given value of x. Results for $n_r = 2$ and $m_r = 1$ are also presented. Increasing m_r increases the number of solutions for heavy hole exciton for a given value of x.

Now considering the effect of temperature, the exciton energies found for $n_r = 1$ and $m_r = 0$ for different values of T can be seen in Figure (5-15) for the heavy hole exciton. Decreasing temperature increases both the number of confined exciton states and their energies, which is due to decreasing T increasing the strength of the sp-d interaction. Results for $n_r = 2$ and $m_r = 0$ are also given in Figure (5-15). Increasing n_r results in an increase in the number of solutions for a given value of T. Comparing Figure (5-15) (lower panel) with Figure (5-16) shows the effect of increasing m_r to $m_r = 1$ (with $n_r = 2$), which increases the number of solutions found. This is due to the well being slightly deeper for the case when $n_r = 2$ and $m_r = 1$ which is shown in Figure (5-8), meaning more states are trapped.

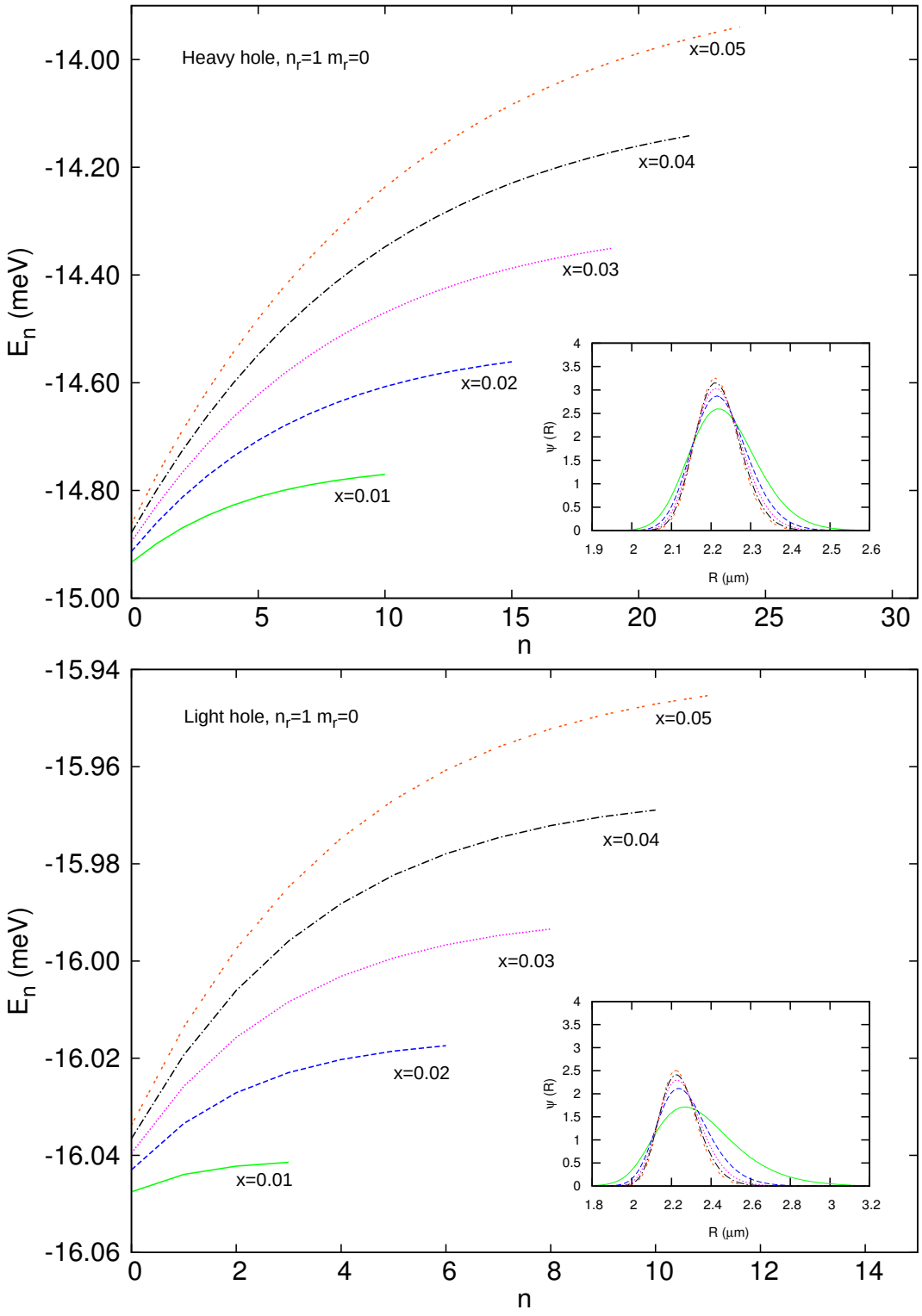

Figure 5-13: Calculated energies E_n of a heavy hole (top) and light hole (bottom) exciton for different magnetic ion concentrations, and the corresponding ground state exciton centre of mass radial wavefunction $\psi(R)$ (insert). Found using $B_a = 0.35$ T, $B_0^D = 0.1$ μmT, $a = 2.0$ μm, $d = 0.2$ μm, $S_{e,z} = \frac{1}{2}$, $S_{h,z} = \frac{3}{2}$, $T = 20$ K, $L = 50$ Å, $n_r = 1$, $m_r = 0$, and $m_R = 0$. The values used for $Cd_{1-x}Mn_xTe$ are given in the Table in Appendix K.

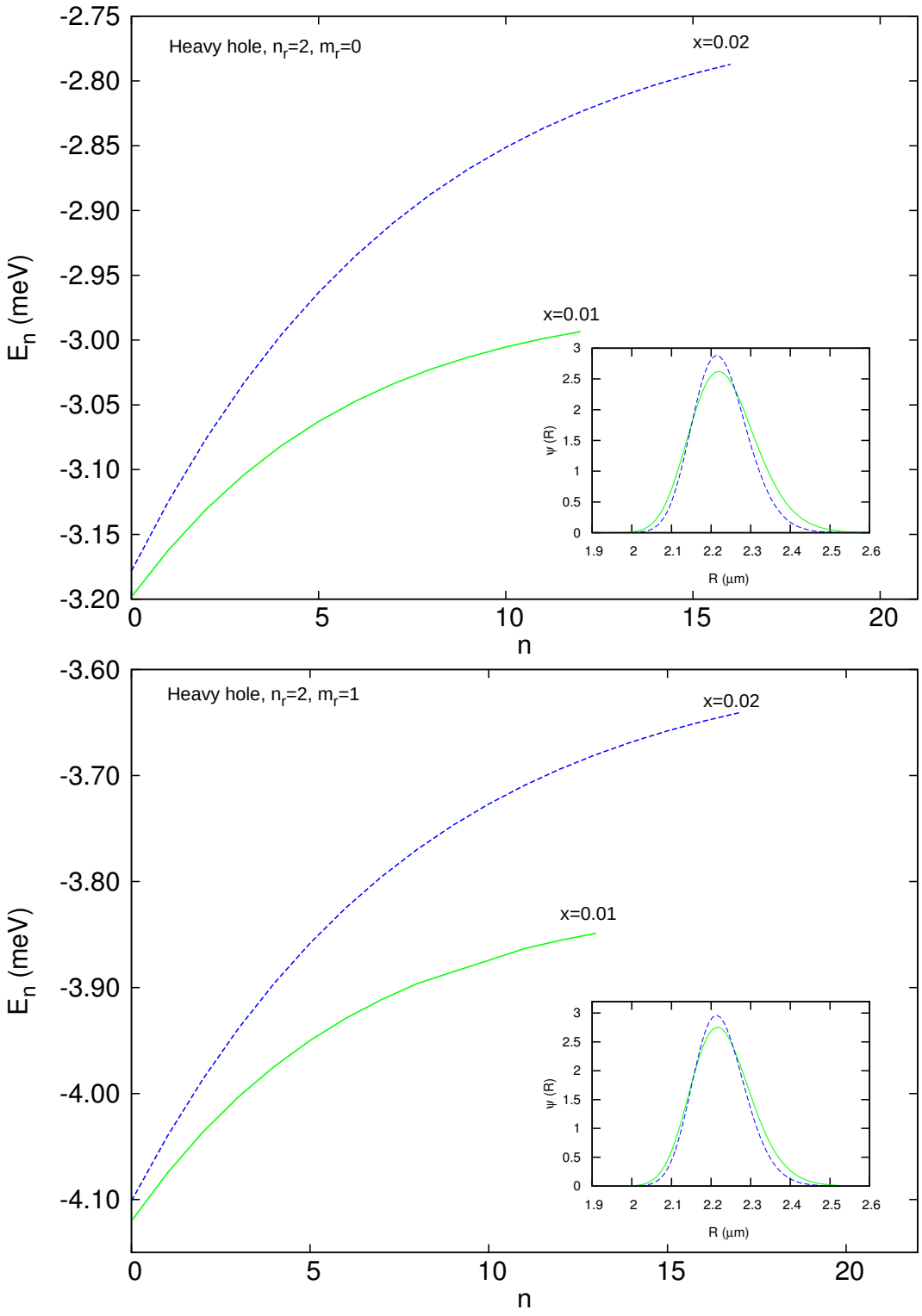

Figure 5-14: Same as previous figure but for the heavy hole with $n_r = 2$, $m_r = 0$ (top) and $n_r = 2$, $m_r = 1$ (bottom).

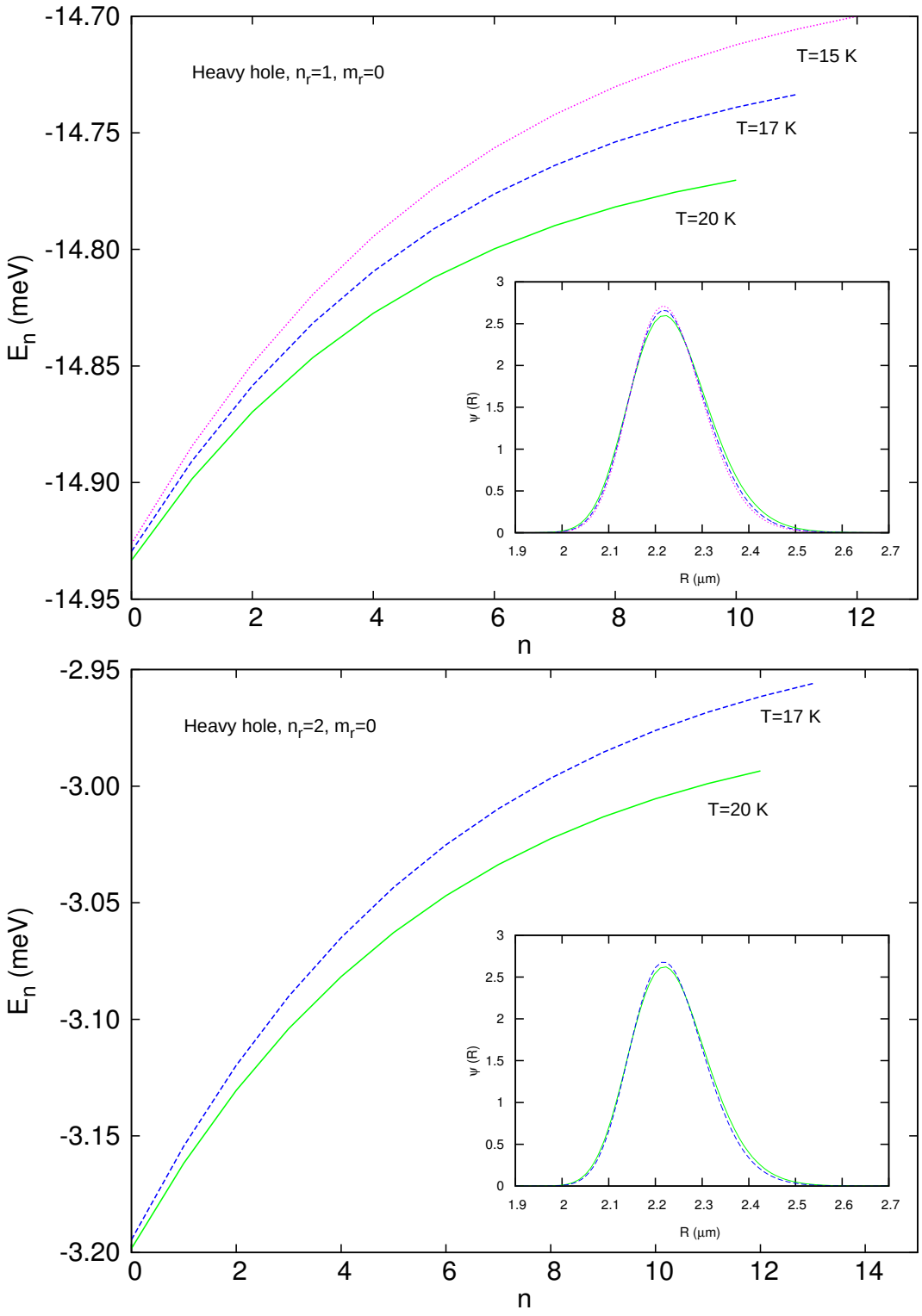

Figure 5-15: Calculated energies E_n of a heavy hole exciton with $n_r = 1$, $m_r = 0$ (top) and $n_r = 2$, $m_r = 0$ (bottom) for different temperatures, and the corresponding ground state exciton centre of mass radial wavefunction $\psi(R)$ (insert). Found with $B_a = 0.35$ T, $B_0^D = 0.1$ μmT, $a = 2.0$ μm, $d = 0.2$ μm, $S_{e,z} = \frac{1}{2}$, $S_{h,z} = \frac{3}{2}$, $x = 0.01$, $L = 50$ Å, and $m_R = 0$. The values used for $Cd_{1-x}Mn_xTe$ are given in the Table in Appendix K.

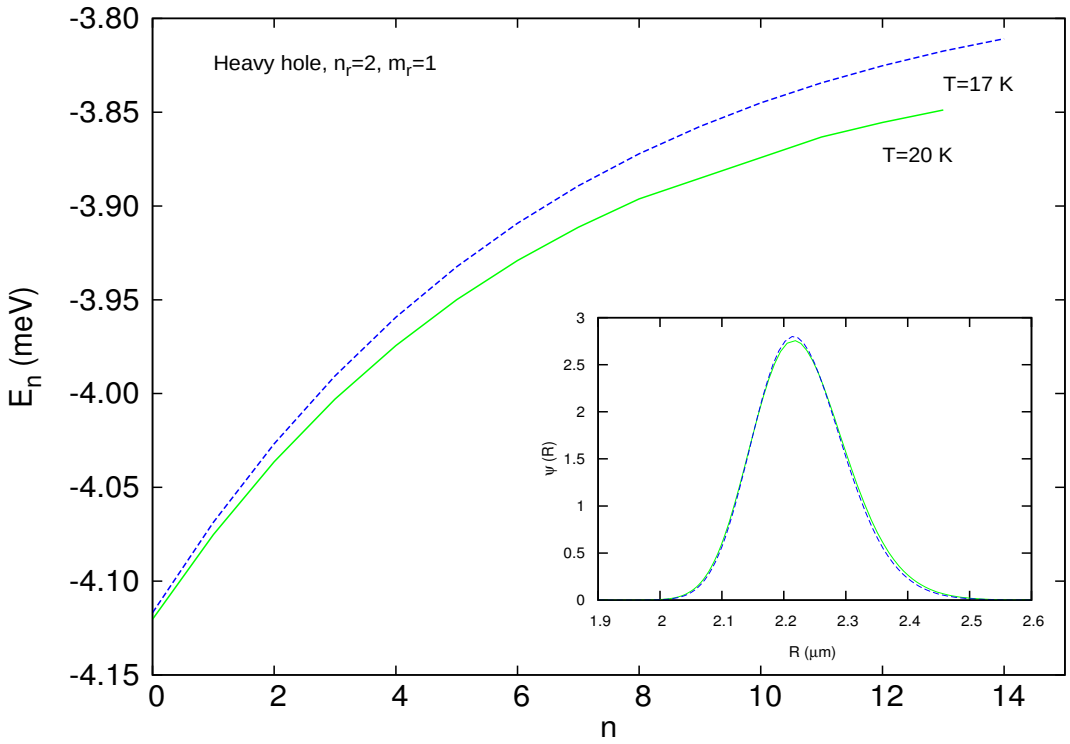

Figure 5-16: Same as previous figure but for $n_r = 2$, and $m_r = 1$.

The effect of the magnetic ion concentration x can be seen in Figure (5-17), where the ground state energy is plotted as a function of the magnetic ion concentration. For a heavy hole exciton with σ^+ spins ($S_{e,z} = \frac{1}{2}$, $S_{h,z} = \frac{3}{2}$) the ground state energy increases when x is increased, due to the fact that increasing x increases the sp-d interaction term, while the ground state energy decreases as x is increased for a heavy hole exciton with σ^- spins ($S_{e,z} = -\frac{1}{2}$ and $S_{h,z} = -\frac{3}{2}$), due to the fact that increasing x when the heavy hole exciton has negative spins increases the sp-d interaction term, which now has a negative contribution. This is the same for the light hole exciton ground state energy as a function of x, which compared to the heavy hole exciton has a lower ground state energy for a given value of x, due to the sp-d interaction making a smaller contribution for light hole excitons. Increasing n_r increases the ground state energy for a given value of x, while increasing m_r (with $n_r = 2$ and $m_r = 1$) slightly decreases the ground state energy as a function of x. For both $n_r = 2$, $m_r = 0$ and $n_r = 2$, $m_r = 1$ the ground state energy increases for increasing x for σ^+ spins.

The effect of the temperature T can be seen in Figure (5-18). For a heavy hole exciton with σ^+ spins the ground state energy increases when T is decreased, due to the increasing sp-d interaction. The opposite applies for a heavy hole exciton with σ^- spins, where decreasing T increases the sp-d interaction term, which makes a negative contribution for this case. This is the same for the light hole exciton ground state energy as a function of temperature, which when compared to the heavy hole exciton has a lower ground state energy for a given value of temperature. Increasing n_r increases the ground state energy for a given value of T, while increasing m_r (with $n_r = 2$ and $m_r = 1$) decreases the ground state energy as a function of T. For both $n_r = 2$, $m_r = 0$ and $n_r = 2$, $m_r = 1$ the ground state energy increases for decreasing T for σ^+ spins.

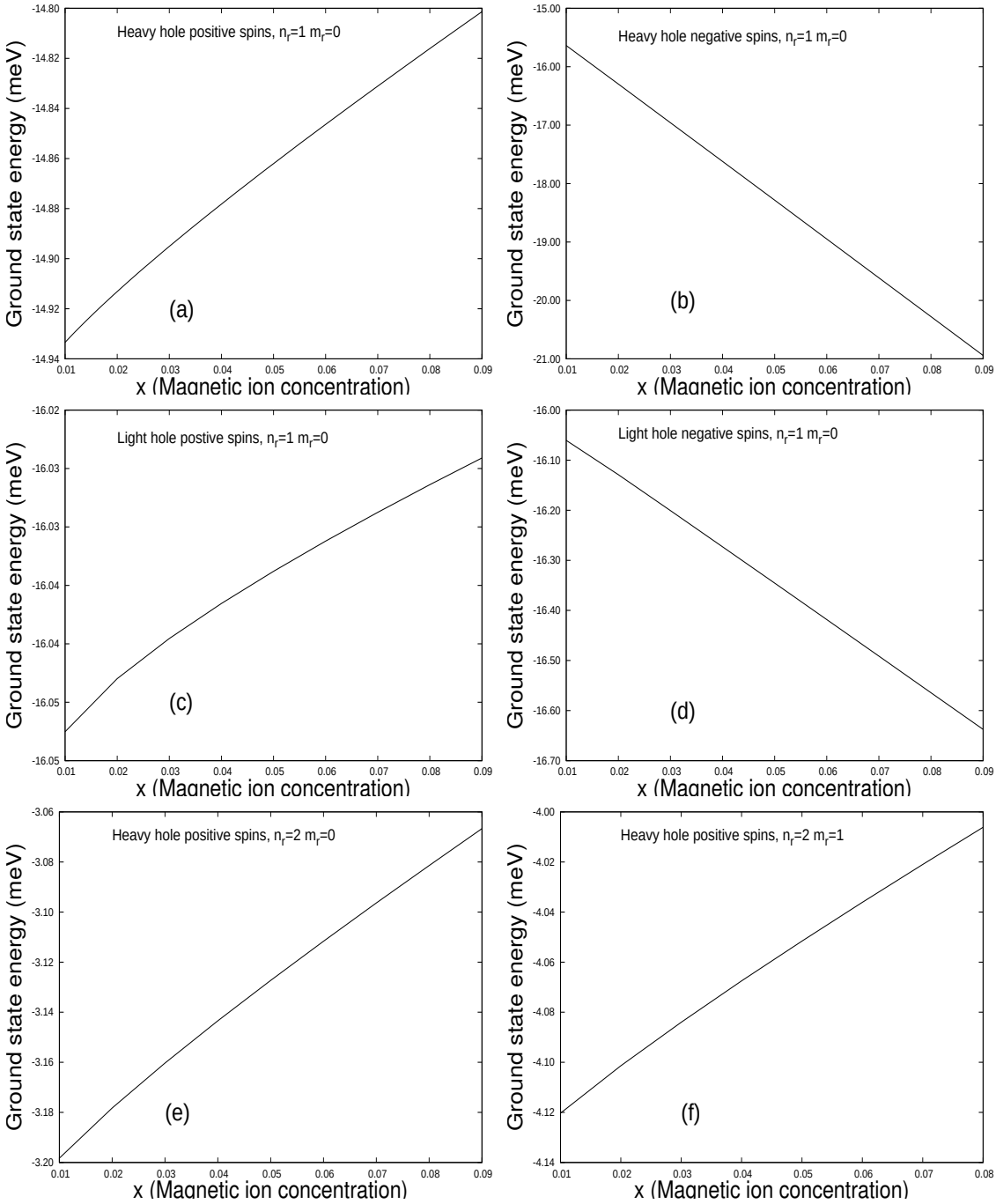

Figure 5-17: Ground state exciton energy as a function of the magnetic ion concentration for a heavy hole exciton with σ^+ (a), and σ^- (b) spin contributions (with $n_r = 1$ and $m_r = 0$), for a light hole exciton with σ^+ (c), and σ^- (d) spin contributions (with $n_r = 1$ and $m_r = 0$,), and for a σ^+ heavy hole exciton with $n_r = 2$, $m_r = 0$ (e), and $n_r = 2$, $m_r = 1$ (f). Calculated with $B_a = 0.35$ T, $B_0^D = 0.1$ μmT, $a = 2.0$ μm, $d = 0.2$ μm, $T = 20$ K, $L = 50$ Å, and $m_R = 0$. The values used for $Cd_{1-x}Mn_xTe$ are given in the Table in Appendix K.

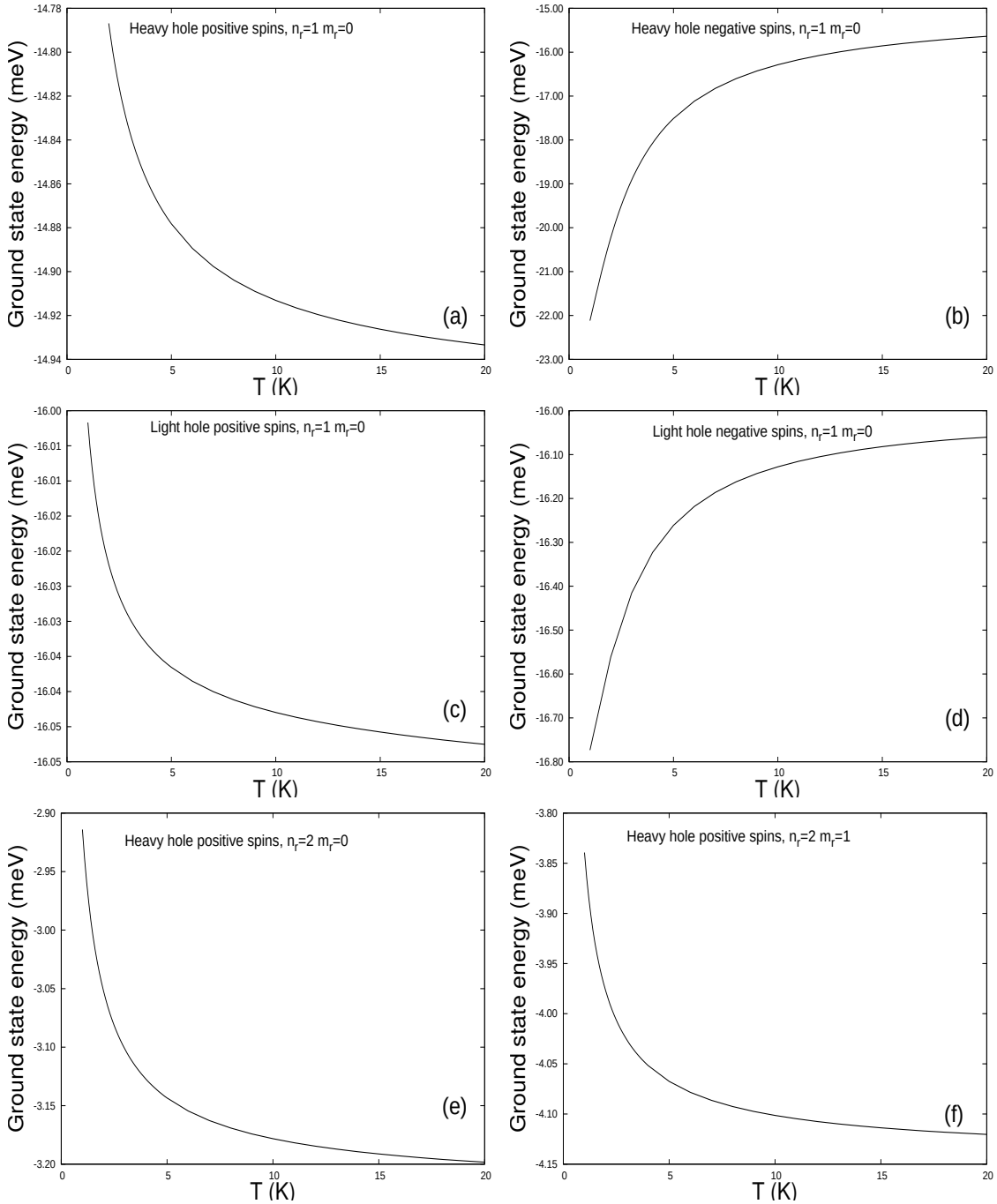

Figure 5-18: Ground state exciton energy as a function of the temperature for a heavy hole exciton with σ^+ (a), and σ^- (b) spin contributions (with $n_r = 1$ and $m_r = 0$,), for a light hole exciton with σ^+ (c), and σ^- (d) spin contributions (with $n_r = 1$ and $m_r = 0$,), and a σ^+ heavy hole exciton with $n_r = 2$, $m_r = 0$ (e), and $n_r = 2$, $m_r = 1$ (f). Calculated with $B_a = 0.35$ T, $B_0^D = 0.1$ μmT, $a = 2.0$ μm, $d = 0.2$ μm, $x = 0.01$ K, $L = 50$ Å, and $m_R = 0$. The values used for $Cd_{1-x}Mn_xTe$ are given in the Table in Appendix K.

5.4 Nanoscale ferromagnetic disk in the vortex state

In this subsection we discuss how excitons behave in a different inhomogeneous magnetic field, that created by a nanoscale ferromagnetic disk in the vortex state given by Eq. (3.4). We again find excitons confined within a DMS quantum well are trapped this time by the magnetic vortex.

A plot of the magnetic field created by a nanoscale ferromagnetic disk in the vortex state with a vortex core ρ_c of 30 nm is shown in Figure (3-4). The corresponding effective potential accounting for the influence on the excitons is given by Eq. (5.63), and is plotted in Figure (5-19) for the nanoscale ferromagnetic disk in the vortex state for a heavy hole exciton with both σ^+ spins and σ^- spins for different values of the magnetic ion concentration x. As the value of x is increased the effective potential varies more significantly, but it converges to the same constant value for all concentrations for distances beyond the radius of the magnetic vortex core where the field becomes negligible. The plots show that an exciton can only be trapped within the region beneath the vortex core, and only heavy and light hole excitons with σ^- spins can be trapped, unlike the case of the microscale ferromagnetic disk which can trap excitons with both σ^+ and σ^- spins. The effective potential given for the nanoscale ferromagnetic disk in the vortex state for a heavy hole exciton with both σ^+ spins and σ^- spins for different temperatures is plotted in Figure (5-20). As the value of T is decreased the effective potential varies more, and again it converges to the same constant value for all temperatures beyond the radius of the magnetic vortex core, where the field becomes negligible. The effective potential for a heavy hole exciton is much deeper than the light hole exciton due to the sp-d interaction making a bigger contribution, Figure (5-21). Changing the values of m_r and m_r just shifts the effective potential up or down, but the shape remains the same for the case of a nanoscale ferromagnetic disk, as shown in Figure (5-21). Decreasing the distance between the nanoscale ferromagnetic disk and the DMS quantum well z increases the depth of the potential well, as well as it becoming narrower due to the magnetic field being stronger closer to the nanoscale ferromagnetic disk, as shown in Figure (5-22).

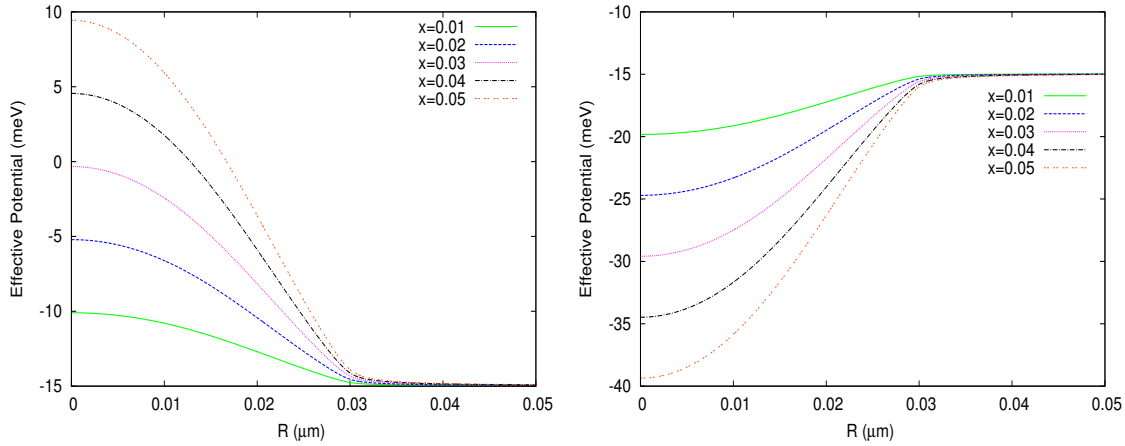

Figure 5-19: Effective potential for a nanoscale ferromagnetic disk as a function of the radial coordinate R for different values of the magnetic ion concentration x, for a heavy hole exciton with σ^+ spins (left) and σ^- spins (right). Calculated with $z = 1$ nm, $\rho_c = 30$ nm, $T = 1$ K, $L = 50$ Å, $n_r = 1$, $m_r = 0$, and $m_R = 0$. The values used for $Cd_{1-x}Mn_xTe$ are given in the Table in Appendix K.

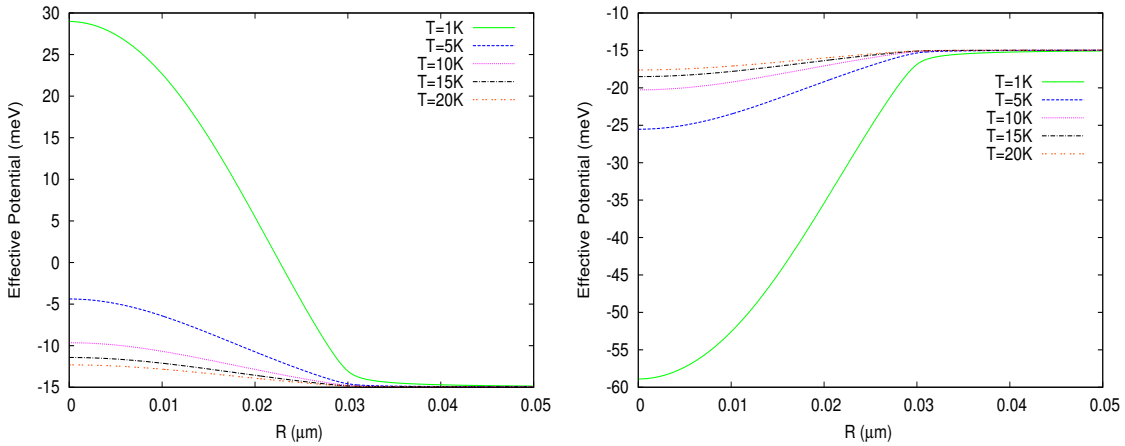

Figure 5-20: Effective potential for a nanoscale ferromagnetic disk as a function of the radial coordinate R for different temperatures T, for a heavy hole exciton with σ^+ spins (left) and σ^- spins (right). Calculated with $z = 1$ nm, $\rho_c = 30$ nm, $x = 0.09$ K, $L = 50$ Å, $n_r = 1$, $m_r = 0$, and $m_R = 0$. The values used for $Cd_{1-x}Mn_xTe$ are given in the Table in Appendix K.

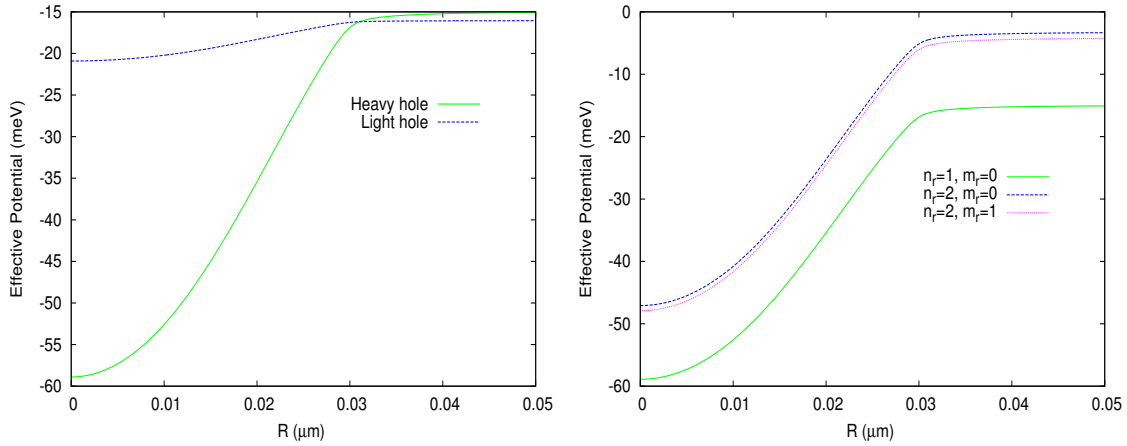

Figure 5-21: Left: Effective potential for a nanoscale ferromagnetic disk as a function of the radial coordinate R for both a heavy and light hole exciton with σ^- spins for $n_r = 1$ and $m_r = 0$. Right: Effective potential for a nanoscale ferromagnetic disk as a function of the radial coordinate R for a heavy exciton with σ^- spins for different values of n_r and m_r. Calculated with $z = 1$ nm, $\rho_c = 30$ nm, $x = 0.09$, $T = 1$ K, $L = 50$ Å, and $m_R = 0$. The values used for $Cd_{1-x}Mn_xTe$ are given in the Table in Appendix K.

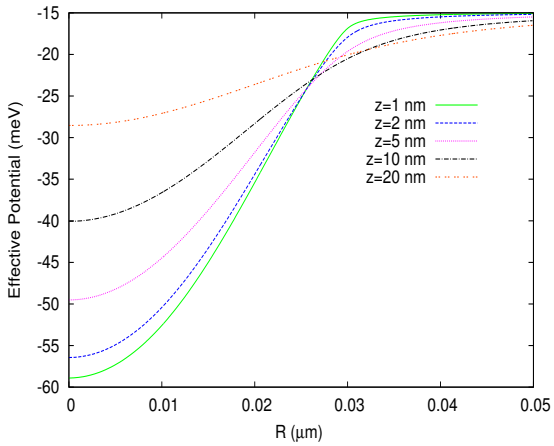

Figure 5-22: Effective potential for a nanoscale ferromagnetic disk as a function of the radial coordinate R for a heavy with σ^- spins for different z values. Calculated with $\rho_c = 30$ nm, $x = 0.09$, $T = 1$ K, $L = 50$ Å, $n_r = 1$, $m_r = 0$ and $m_R = 0$. The values used for $Cd_{1-x}Mn_xTe$ are given in the Table in Appendix K.

Calculated centre of mass radial wavefunctions describing excitons in the lowest energy state trapped by the field just discussed due to a nanoscale ferromagnetic disk for both heavy and light hole cases with σ^- spins are plotted in Figure (5-23). It is found that the heavy hole exciton is more tightly confined than the light hole exciton, due to the potential well being narrower for a heavy hole, see Figure (5-21). Compared to the microscale disk where the excitons were confined to a ring with radial extent $\sim 1\ \mu m$, e.g Figures (5-10), (5-11 (a)), and (5-12 (a)), here the exciton is confined to a point with radial extent almost two order of magnitudes smaller. It is found that the vortex field can trap additional states and the wavefunctions for all the trapped heavy and light hole exciton states are shown in Figure (5-23). The heavy hole exciton has three excited states when $x = 0.09$ and $T = 1$ K, while the light hole exciton has only one for the same values, because for a heavy hole exciton the sp-d exchange interaction makes a bigger contribution, and creates a deeper potential well, shown in Figure (5-21). The wavefunctions for different values of n_r and m_r for a heavy hole exciton are plotted in Figure (5-24). Unlike the case with the microscale ferromagnetic disk the wavefunctions confined by the magnetic field created by the nanoscale ferromagnetic disk for different values of n_r and m_r have the same shape, which can be explained by looking at the potential well in Figure (5-21) for different values of m_r and n_r, which have the all have the same depth and width.

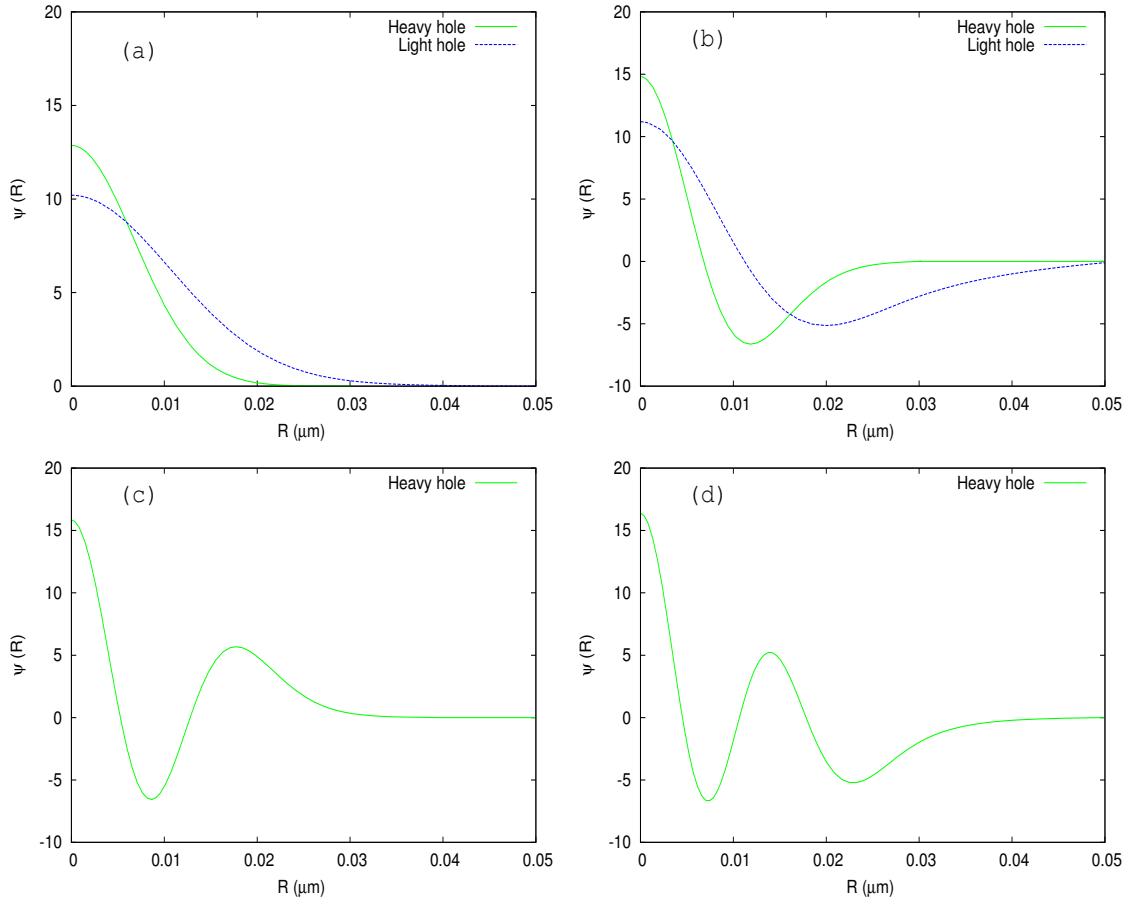

Figure 5-23: (a) Ground state, (b) first excited state, (c) second excited state, and (d) third excited state exciton centre of mass radial wavefunction ψ(R) as a function of the radial coordinate R for a σ^- heavy and light hole exciton for a nanoscale ferromagnetic disk. Calculated with $z = 1$nm, $\rho_c = 30$ nm, $S_{e,z} = -\frac{1}{2}$, $S_{h,z} = -\frac{3}{2}$, $x = 0.09$, $T = 1$ K, $L = 50$ Å, $n_r = 1$, $m_r = 0$ and $m_R = 0$. The values used for $Cd_{1-x}Mn_xTe$ are given in the Table in Appendix K.

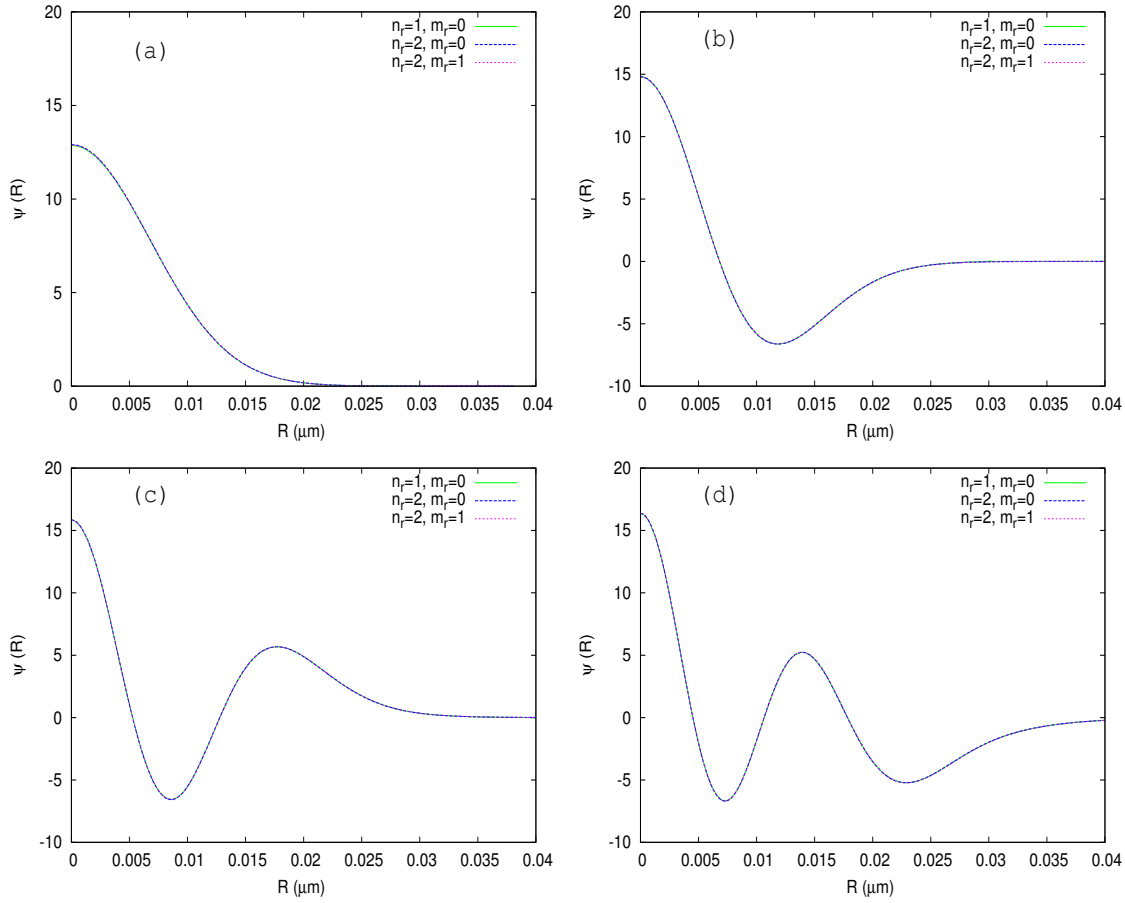

Figure 5-24: (a) Ground state, (b) first excited state, (c) second excited state, and (d) third excited state exciton centre of mass radial wavefunction ψ(R) as a function of the radial coordinate R for a σ^- heavy hole for different values of n_r and m_r for a nanoscale ferromagnetic disk. Calculated with $z = 1$ nm, $\rho_c = 30$ nm, $S_{e,z} = -\frac{1}{2}$, $S_{h,z} = -\frac{3}{2}$, $x = 0.09$, $T = 1$ K, $L = 50$ Å, and $m_R = 0$. The values used for $Cd_{1-x}Mn_xTe$ are given in the Table in Appendix K.

The number of solutions and the corresponding energies for different values of the concentration x are shown in Figure (5-25) for both heavy and light hole excitons. Increasing x increases the number of solutions, and the ground state wavefunction becomes more confined. The corresponding energy and the ground state energy decreases linearly as x is increased. This is the same behaviour as for excitons with σ^- spins confined by a magnetic field created by the microscale ferromagnetic disk. This behaviour is consistent with the variation seen in the effective potential, Figure (5-19), which becomes deeper for σ^- spin excitons. The heavy hole exciton has more solutions than the light hole exciton for a given value of x, because for a heavy hole exciton the sp-d exchange interaction makes a bigger contribution, and creates a deeper potential well. This is the same as was found for the microscale ferromagnetic disk.

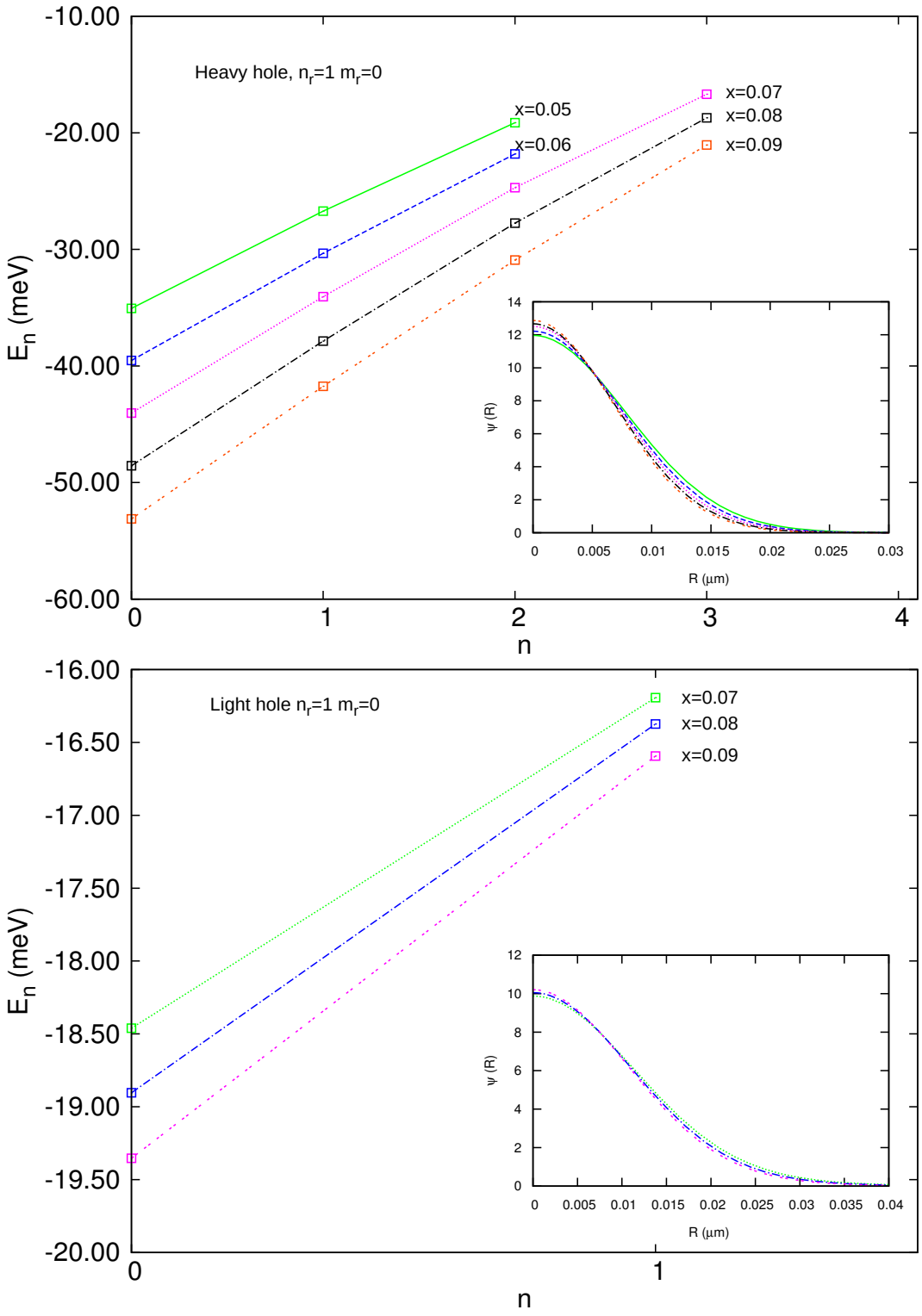

Figure 5-25: Calculated energies E_n of the heavy hole (top) and light hole (bottom) exciton with σ^- spin contributions for different magnetic ion concentrations, and the corresponding ground state exciton centre of mass radial wavefunction $\psi(R)$ (insert). Calculated with $z = 1$ nm, $\rho_c = 30$ nm, $S_{e,z} = -\frac{1}{2}$, $S_{h,z} = -\frac{3}{2}$, $T = 1$ K, $L = 50$ Å, $n_r = 1$, $m_r = 0$, and $m_R = 0$. The values used for $Cd_{1-x}Mn_xTe$ are given in the Table in Appendix K.

The number of solutions and the corresponding energies for different distances between the nanoscale ferromagnetic disk and the DMS quantum well z is shown in Figure (5-26) for a heavy exciton. Increasing z decreases the number of solutions, and the ground state wavefunction becomes less confined. The corresponding energy and the ground state energy increases as z is increased. This can be explained by looking at the effective potential which becomes deeper and narrower as z is decreased resulting in more trapped states, Figure (5-22).

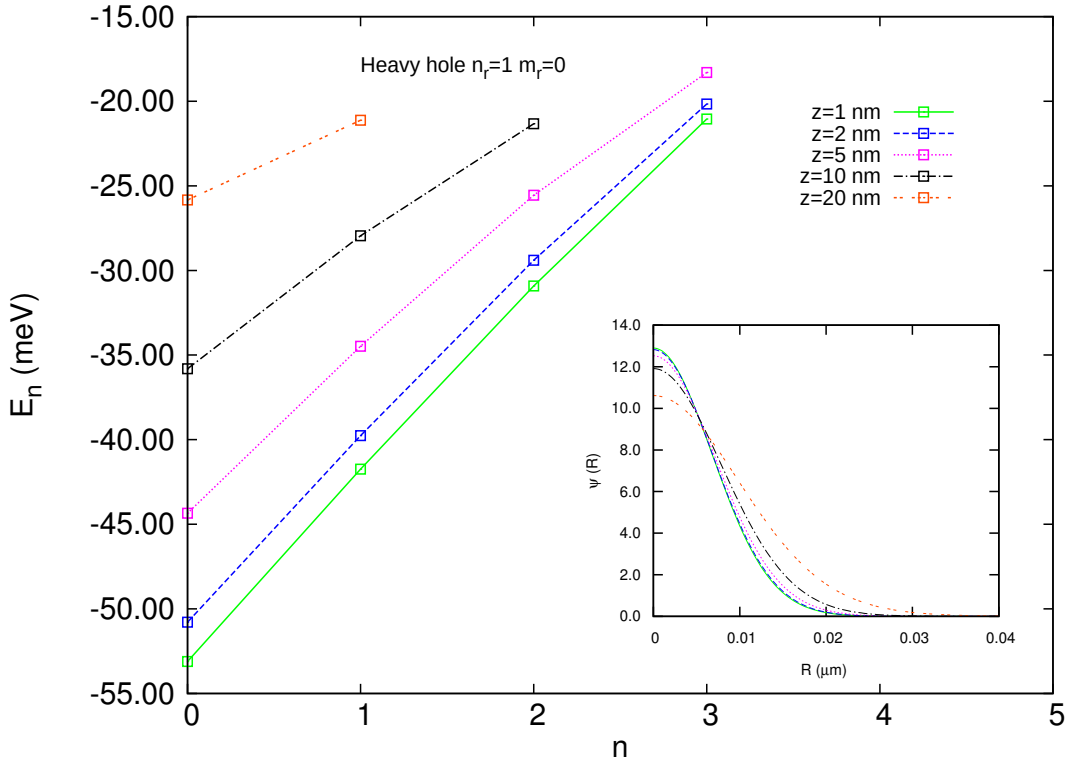

Figure 5-26: Calculated energies E_n of the heavy hole exciton with σ^- spin contributions for different distances between the nanoscale ferromagnetic disk and the DMS quantum well z, and the corresponding ground state exciton centre of mass radial wavefunction $\psi(R)$ (insert). Calculated with $\rho_c = 30$ nm, $S_{e,z} = -\frac{1}{2}$, $S_{h,z} = -\frac{3}{2}$, $T = 1$ K, $x = 0.09$, $L = 50$ Å, $n_r = 1$, $m_r = 0$, and $m_R = 0$. The values used for $Cd_{1-x}Mn_xTe$ are given in the Table in Appendix K.

The effect of the temperature can be seen in Figure (5-27), where the ground state energy is plotted as a function of the temperature. For a heavy hole exciton with σ^- spins the ground state energy increases as T is increased. This is the same for the light hole exciton ground state energy as a function of T. Due to the sp-d interaction increasing as T is decreased, which now makes a negative contribution. Increasing n_r increases the ground state energy for a given value of T, while increasing m_r (with n_r=2 and m_r=1) decreases the ground state energy as a function of T. For a heavy hole exciton with σ^- spins for both n_r=2, m_r=0 and n_r=2, m_r=1 the ground state energy increases for increasing T. The effect of the temperature on the ground state energy for σ^- excitons is the same for both the magnetic field created from the microscale ferromagnetic disk and the nanoscale ferromagnetic disk in the vortex state.

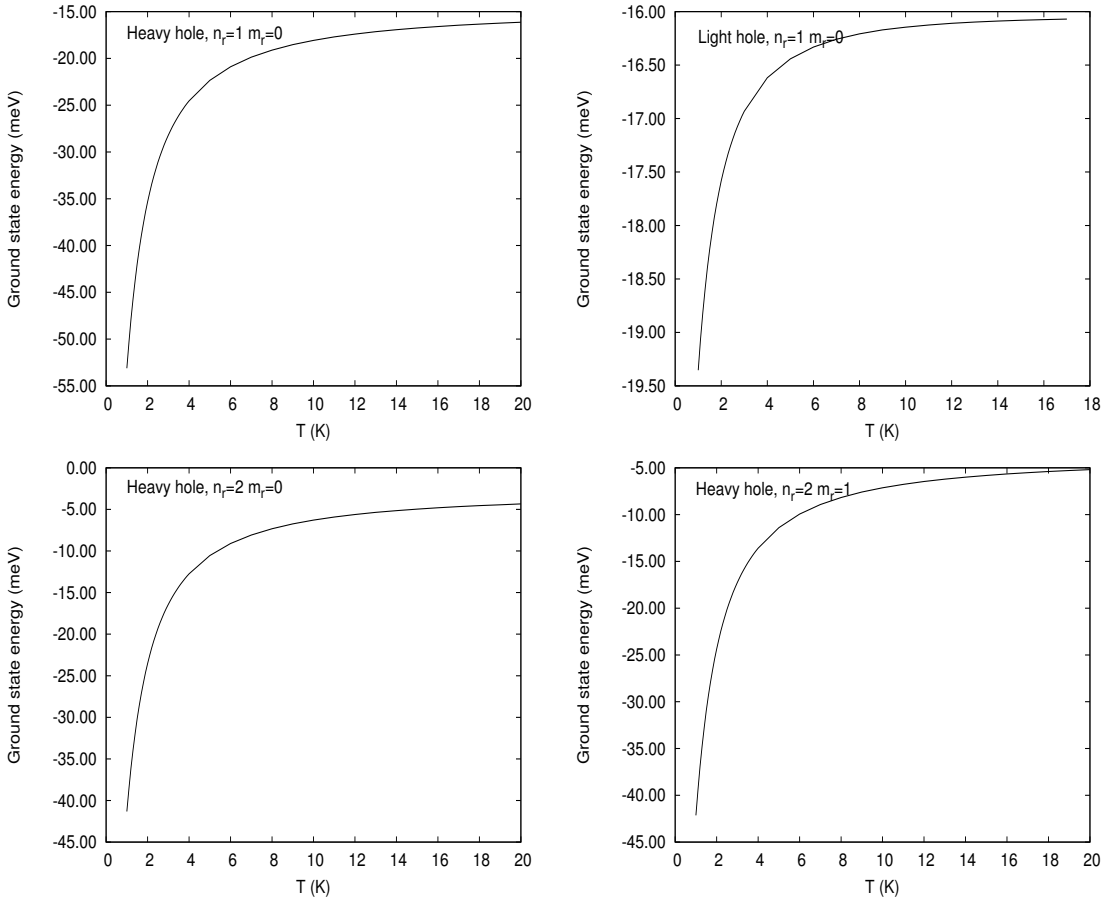

Figure 5-27: Ground state exciton energy as a function of the temperature for a heavy (top left) and light hole exciton (top right) with σ^- spin contributions, and for a σ^- heavy exciton for $n_r = 2$, $m_r = 0$ (bottom left), and $n_r = 2$, $m_r = 1$ (bottom right). Calculated with $z = 1$ nm, $\rho_c = 30$ nm, $x = 0.09$, $L = 50$ Å, and $m_R = 0$. The values used for $Cd_{1-x}Mn_xTe$ are given in the Table in Appendix K.

5.5 Exciton trapping in magnetic wire structures

The centre of mass equation in Eq. (5.61) for excitons in an inhomogeneous magnetic field is for the confinement of excitons using circular (two dimensional) magnetic traps (such as the microscale and nanoscale ferromagnetic disks studied in the previous sections). This needs to be adapted if the model is to be applied to the study of the confinement of excitons using linear magnetic traps (such as those created by a ferromagnetic rectangular strip).

5.5.1 Ferromagnetic strip

Here we discuss the magnetic field created by a ferromagnetic strip. As can be seen in Figure (5-28) the magnetic strip is placed upon the DMS quantum well with the strip width a lying along the x direction, the length of the strip lying along the y direction, and the strip height h is in the z direction. The magnetisation of the strip can either be in the plane of the strip or perpendicular to it.

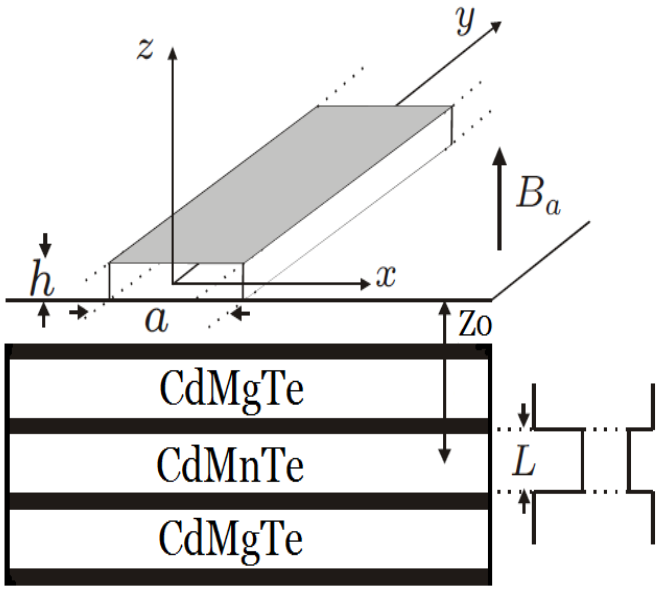

Figure 5-28: Experimental configuration showing the ferromagnetic strip with stripe width a, and thickness h placed upon the DMS quantum well with well width L. The distance from the bottom of the stripe to the middle of the quantum well is given by z_0. B_a is an applied homogeneous magnetic field used to increase the confinement of the exciton. Adapted from Ref. [84].

Since no currents are involved, Maxwell's equations are

$$\vec{\nabla} \cdot \vec{B} = 0, \qquad \vec{\nabla} \times \vec{H} = 0, \tag{5.69}$$

where $\vec{B} = \mu_0(\vec{H} + \vec{M})$ with magnetisation $\vec{M}$ [62]. For reference at saturation the magnetisation of cobalt is $\mu_0 M_s = 1.82$ T, and for nickel $\mu_0 M_s = 0.51$ T [101]. Equations (5.69) imply $\vec{H}$ can be written in terms of the gradient of a scaler potential $\vec{H} = -\vec{\nabla}\Phi$, which leads to

$$\vec{\nabla} \cdot \vec{H} = -\vec{\nabla} \cdot \vec{M} = -\nabla^2 \Phi. \tag{5.70}$$

We see that

$$\Phi(\vec{r}) = -\frac{1}{4\pi} \int \frac{\nabla \cdot \vec{M}(\vec{r}\,')d^3\vec{r}\,'}{|\vec{r} - \vec{r}\,'|} \tag{5.71}$$

If we can find $\Phi(\vec{r})$, then outside the magnet $\vec{M} = 0$, and $\vec{B} = \mu_0 \vec{H} = -\mu_0 \nabla \Phi$. Then

$$\vec{B}(\vec{r}) = \frac{\mu_0}{4\pi} \int \frac{\nabla \cdot \vec{M}(\vec{r}\,')d^3\vec{r}\,'}{|\vec{r} - \vec{r}\,'|}. \tag{5.72}$$

For a single magnetic ferromagnetic strip with magnetisation in the z plane with boundaries $x \in (-a/2, a/2)$, $y \in (-\infty, \infty)$, and $z \in (-h/2, h/2)$ implies

$$\vec{\nabla} \cdot \vec{M} = -M[\delta(z - h/2) - \delta(z + h/2)][\Theta(x + a/2) - \Theta(x - a/2)], \tag{5.73}$$

where the strip length along the y direction is assumed to extend to infinity, Figure (5-28) [102]. Then the magnetic field is obtained from Eq. (5.72) as [102][101]

$$\begin{aligned} B_z(x,z) &= \frac{\mu_0 M}{2\pi} \left[\left[\arctan\left(\frac{x + a/2}{z + h/2}\right) - \arctan\left(\frac{x - a/2}{z + h/2}\right) \right] \right. \\ &\quad \left. + \left[\arctan\left(\frac{x + a/2}{z - h/2}\right) - \arctan\left(\frac{x - a/2}{z - h/2}\right) \right] \right], \end{aligned} \tag{5.74}$$

where

$$z = \left(\frac{h}{2} + z_0\right), \tag{5.75}$$

where z_0 is the distance from the bottom of the ferromagnetic strip to the centre quantum well. For magnetisation in the x direction the corresponding field in the z direction is

$$B_z(x,z) = \frac{\mu_0 M}{2\pi} \left[\frac{1}{2} \mathrm{Ln}\left(\frac{(x + a/2)^2 + (z + h/2)^2}{(x + a/2)^2 + (z - h/2)^2}\right) + \frac{1}{2} \mathrm{Ln}\left(\frac{(x - a/2)^2 + (z + h/2)^2}{(x - a/2)^2 + (z - h/2)^2}\right) \right], \tag{5.76}$$

where Ln is the natural logarithm. A homogeneous magnetic field B_a can be applied in the z direction to increase confinement of the exciton, then the total magnetic field will be $B_z(x,z) + B_a$.

5.5.2 Centre of mass equation

The first term in Eq. (5.1) for the Hamiltonian for a 2D system (consisting of an electron in the conduction band and a hole in the valence band interacting via the Coulomb interaction in the xy plane) in the case of an inhomogeneous magnetic field created by a ferromagnetic strip takes the form [84]:

$$\begin{aligned}\mathcal{H}^{2D}(\vec{R},\vec{r}) &= \frac{\hbar^2}{2m^*_{e,||}}\left\{-i\frac{m^*_{e,||}}{M}\nabla_R - i\nabla_r + \frac{e}{\hbar c}A_Y\left(X+\frac{m^*_{h,||}}{M}x\right)e_Y\right\}^2 \\ &+\frac{\hbar^2}{2m^*_{h,||}}\left\{-i\frac{m^*_{h,||}}{M}\nabla_R + i\nabla_r - \frac{e}{\hbar c}A_Y\left(X-\frac{m^*_{e,||}}{M}x\right)e_Y\right\}^2 - \frac{\gamma e^2}{4\pi\varepsilon_0\varepsilon_r r},\end{aligned} \tag{5.77}$$

where the magnetic field enters via the vector potential which is in the Landau gauge $\vec{A}(\vec{R}) = A_Y(X)e_Y$. The wavefunction transformation used to accommodate the effect of the inhomogeneous magnetic field from a magnetic strip is

$$\Psi(\vec{R},\vec{r}) \to \exp\{-i(e/\hbar c)yA_Y(X)e_Y\}\Psi(\vec{R},\vec{r}), \tag{5.78}$$

and the adiabatic approximation applied to the vector potential, expanding as a power series up to second order, is

$$A_Y\left(X \pm \frac{m^*_{h(e),||}x}{M}\right)e_Y = A_Y(X)e_Y \pm \frac{m^*_{h(e),||}}{M}xB_z(X) + \ldots. \tag{5.79}$$

Then $H^{2D}(\vec{R},\vec{r})$ becomes

$$\widetilde{\mathcal{H}}^{2D}(\vec{R},\vec{r}) = -\frac{\hbar^2}{2\mu}\nabla_r^2 - \frac{\gamma e^2}{4\pi\varepsilon_0\varepsilon_r r} + W_1 + W_2 - \frac{\hbar^2}{2M}\nabla_R^2, \tag{5.80}$$

where

$$\begin{aligned}W_1 &= -\frac{ie\hbar}{c\mu}\xi B_z(X)x\frac{\partial}{\partial y} - \frac{ie\hbar}{Mc}\left(B_z(X)\frac{\partial}{\partial Y}\right)x + \frac{ie\hbar}{Mc}\left(\frac{\partial}{\partial X}B_z(X) + B_z(X)\frac{\partial}{\partial X}\right)y, \\ W_2 &= \frac{e^2}{2Mc^2}B_z(X)^2\left(\frac{\xi^2 M}{\mu}x^2 + r^2\right).\end{aligned} \tag{5.81}$$

The eigenvalues and eigenfunctions of the equation for the exciton relative motion are calculated as before using perturbation theory. The term for the spin Hamiltonian in Eq. (5.52) is here

$$\mathcal{H}^{m_z}(X) = \mu_B\left[g_{e,z}S_{e,z} - \frac{1}{3}g_{g,z}J_{h,z}\right]B_z(X) - \frac{2}{3}\sum_{i=1}^{3}c_iS_{e,i}J_{h,i} \tag{5.82}$$

describing the exciton spin interaction with the inhomogeneous magnetic field, oriented along the z direction [84]. The eigenvalues of $\{\mathcal{H}^{m_z}(X) - E^{m_z}(X)\}\mathcal{L}^{m_z}(X) = 0$ are found to be

$$E^{m_z} = \pm\frac{1}{2}\mu_B g_{ex}B_z(X). \tag{5.83}$$

The total exciton wavefunction is a product of the decoupled motions, with once again it being assumed that there is no coupling between exciton spin and the exciton centre of mass and relative motion. The Schrödinger equation for the exciton centre of mass is

$$\left\{-\frac{\hbar^2}{2}\frac{d}{dX}\left[\frac{1}{M^{eff}(X)}\frac{d}{dX}\right]+V^{eff}(X)-E\right\}\psi(X)=0, \tag{5.84}$$

where the effective mass

$$M^{eff}(X)=\frac{M}{1-\alpha_{m_r}^{n_r}\frac{e^2\mu}{\hbar^2M^2c^2}\gamma^{-4}B_z(X)^2}=\frac{M}{1-\alpha_{m_r}^{n_r}\frac{c_1}{M}\gamma^{-4}B_z(X)^2}, \tag{5.85}$$

and the effective potential

$$\begin{aligned} V^{eff}(X) &= \frac{\hbar^2}{2M^{eff}(X)}Q_Y^2+\beta_{m_r}^{n_r}\frac{e^2\omega}{2\mu c^2}\gamma^{-2}B_z(X)^2+\frac{e\hbar}{2\mu c}\xi B_z(X)m_r \\ &\quad +\frac{1}{2}\mu_B g_{ex}B_z(X)+\mathcal{H}_{s,p-d}(X) \\ &= \frac{\hbar^2}{2M^{eff}(X)}Q_Y^2+\beta_{m_r}^{n_r}4c_2\omega\gamma^{-2}B_z(X)^2+\frac{e\hbar}{2\mu c}\xi B_z(X)m_r \\ &\quad +\frac{1}{2}\mu_B g_{ex}B_z(X)+\mathcal{H}_{s,p-d}(X). \end{aligned} \tag{5.86}$$

γ is calculated from Eq. (5.30), and $\omega=(m_{e,||}^2+m_{h,||}^2)/M$. The wavefunction of the centre of mass motion is decoupled since $\psi(\vec{R})=\exp\{iQ_YY\}\,\psi(X)$ where Q_Y is the wave vector of the centre of mass motion in the Y direction (free direction in the wire) [84].

5.5.3 Results

The magnetic field in the z direction created by a ferromagnetic strip for magnetisation in the x direction given by Eq. (5.76) is plotted in Figure (5-29) and Figure (5-30) for different values of the strip width a, strip height h, and distance between the centre of the ferromagnetic strip and the centre of the quantum well z. The magnetic field in the z direction B_z has a negative peak in the region near the edge of the stripe which corresponds to $x=a/2$, and a positive peak near the other edge at $x=-a/2$ (assuming the centre of the strip lies at $x=0$). As the strip width a is increased B_z peaks at a higher value and becomes more shifted along x as shown in Figure (5-29). Figure (5-29) shows B_z peaks at a higher value as h is increased, as well as becoming steeper. Increasing z decreases the value at which B_z peaks, due to the magnetic field becoming weaker further away from the strip, Figure (5-30). The value of the saturation magnetisation μ_0M_s affects the value at which the magnetic field peaks, and using the value for nickel where $\mu_0M_s=0.51$ T results in the magnetic field peaking at a value that is approximately 25% that of for cobalt, which has $\mu_0M_s=1.82$ T.

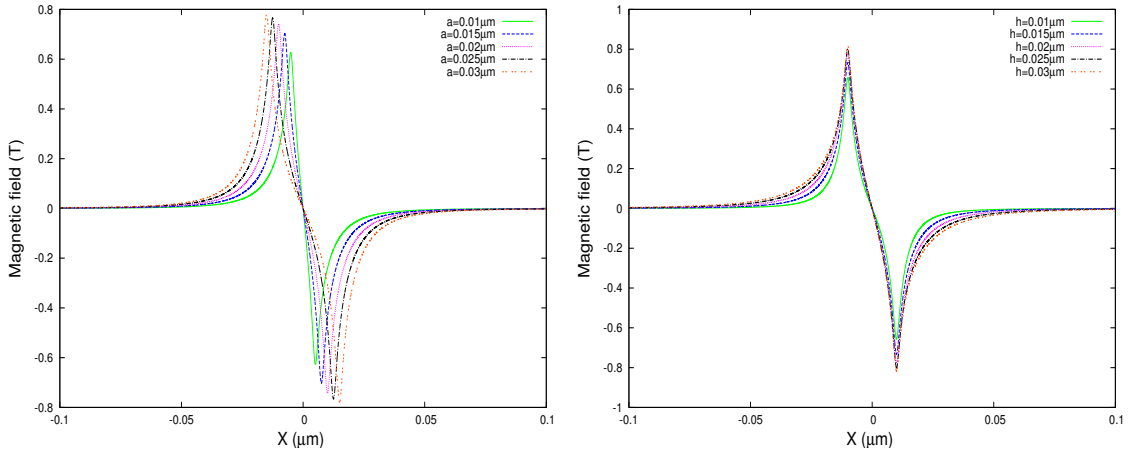

Figure 5-29: Left: Magnetic field in the z direction for a ferromagnetic strip for magnetisation in the x direction as a function of the coordinate along the wire width for different values of the strip width a. Calculated with $B_a = 0$ T, $h = 16$ nm, $z_0 = 1$ nm, $\mu\mathcal{M}_s = 1.82$ T. Right: Magnetic field in the z direction for a ferromagnetic strip for magnetisation in the x direction as a function of the coordinate along the wire width for different values of the strip height h. Calculated with $B_a = 0$ T, $a = 20$ nm, $z_0 = 1$ nm, $\mu_0 M_s = 1.82$ T.

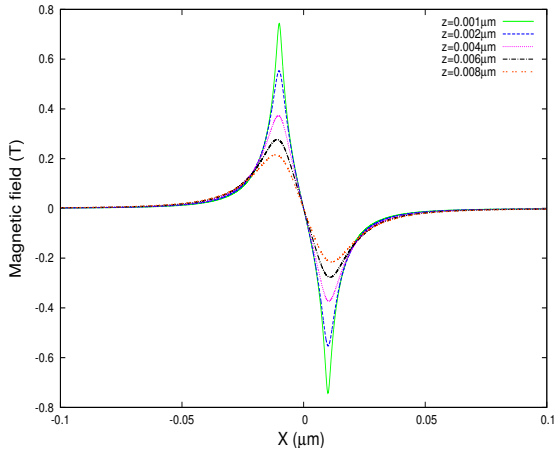

Figure 5-30: Magnetic field in the z direction for a ferromagnetic strip for magnetisation in the x direction as a function of the coordinate along the wire width for different distances between the centre of the ferromagnetic strip and the centre of the quantum well z. Calculated with $B_a = 0$ T, $a = 20$ nm, $h = 16$ nm, and $\mu_0 M_s = 1.82$ T.

Figure (5-31) shows the corresponding effective potential experienced by the exciton centre of mass, for a heavy hole exciton with both σ^+ and σ^- spins for different magnetic ion concentrations x in the DMS. For a heavy and light hole exciton with σ^+ spins the effective potential reaches a maximum when $X < 0$, and a minimum when $X > 0$. While for a heavy and light hole exciton with σ^- spins the effective potential reaches a minimum when $X < 0$, and a maximum when $X > 0$. It can be seen that only heavy and light hole excitons with σ^+ spins can be trapped, unlike the case of the microscale ferromagnetic disk which can trap excitons with both σ^+ and σ^- spins, and the nanoscale ferromagnetic disk that can only trap excitons with σ^- spins. As the value of x is increased the effective potential becomes steeper, and reaches a higher peak value. The effect of the temperature T on the effective potential is shown in Figure (5-32) for a heavy hole exciton with both σ^+ and σ^- spins. As the value of T is decreased the effective potential becomes steeper, as well as peaking at a higher value. The effective potential for a heavy hole exciton with σ^+ spins is shown in Figures (5-33) - (5-34) for different values of the strip width a, strip height h and distance between the centre of the ferromagnetic strip and the centre of the quantum well z. Increasing a and h, and decreasing z increases the depth of the potential well.

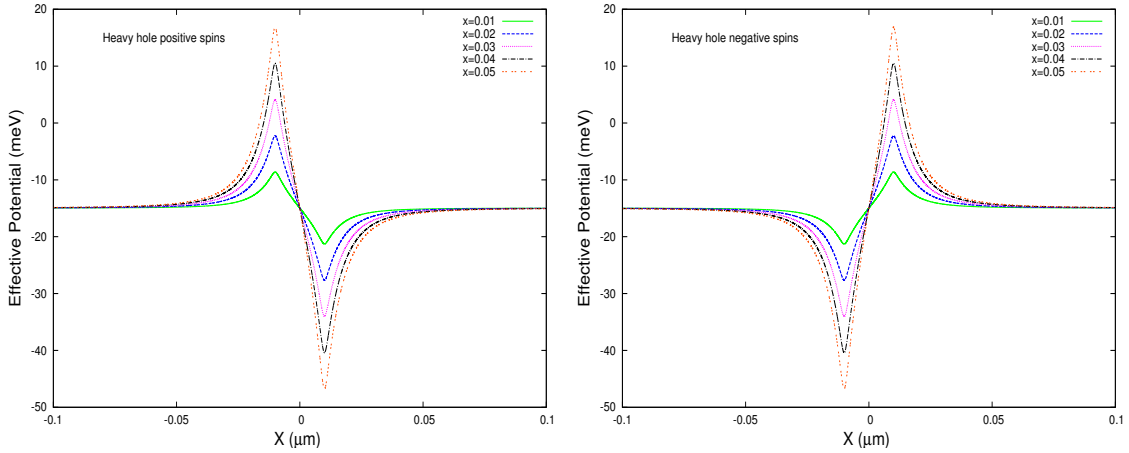

Figure 5-31: Effective potential for a ferromagnetic strip for magnetisation in the x direction as a function of the coordinate along the wire width for different values of the magnetic ion concentration x, for a heavy hole with with σ^+ spins (left) and σ^- spins (right). Calculated with $B_a = 0$ T, $a = 20$ nm, $h = 16$ nm, $z_0 = 1$ nm, $\mu_0 M_s = 1.82$ T, $T = 1$ K, $L = 50$ Å, $n_r = 1$, $m_r = 0$, and $m_R = 0$. The values used for $Cd_{1-x}Mn_xTe$ are given in the Table in Appendix K.

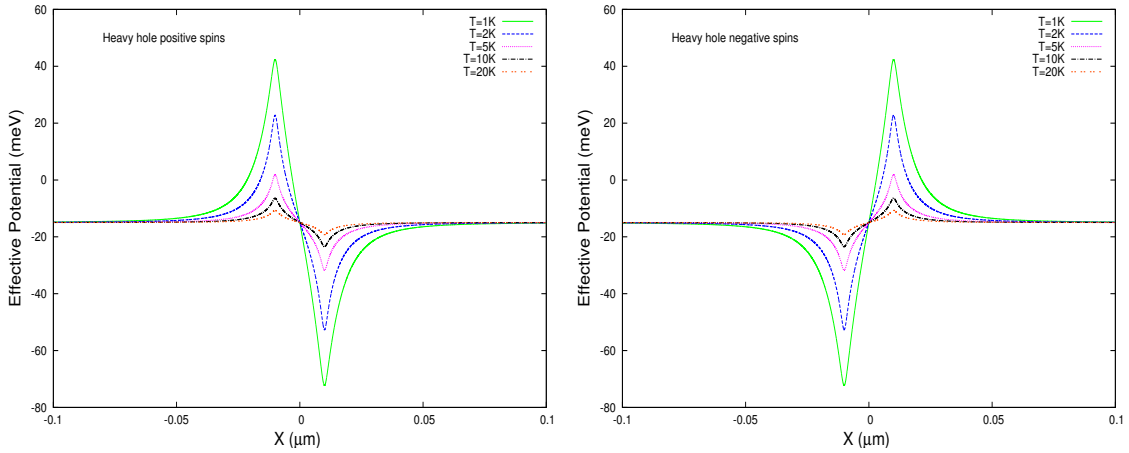

Figure 5-32: Effective potential for a ferromagnetic strip for magnetisation in the x direction as a function of the coordinate along the wire width for different temperatures T, for a heavy hole with σ^+ spins (left) and σ^- spins (right). Calculated with $B_a = 0$ T, $a = 20$ nm, $h = 16$ nm, $z_0 = 1$ nm, $\mu_0 M_s = 1.82$ T, $x = 0.09$ K, $L = 50$ Å, $n_r = 1$, $m_r = 0$, and $m_R = 0$. The values used for $Cd_{1-x}Mn_xTe$ are given in the Table in Appendix K.

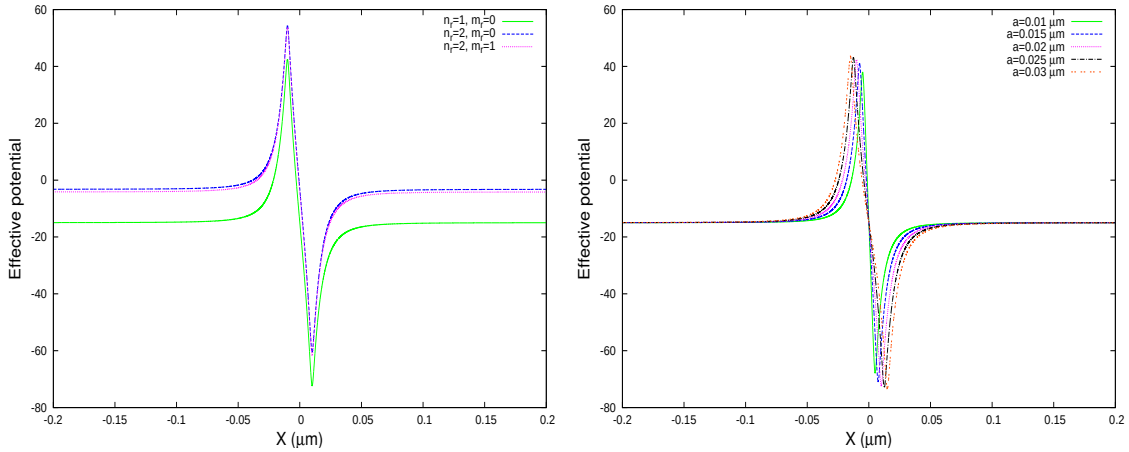

Figure 5-33: Right: Effective potential for a ferromagnetic strip for magnetisation in the x direction as a function of the coordinate along the wire width for a heavy hole with σ^+ spins for different values of n_r and m_r. Calculated with $B_a = 0$ T, $a = 20$ nm $h = 16$ nm, $z_0 = 1$ nm, $\mu\mathcal{M}_s = 1.82$ T ,$T = 1$ K, $x = 0.09$ $L = 50$ Å, and $m_R = 0$. Left: Effective potential for a ferromagnetic strip for magnetisation in the x direction as a function of the coordinate along the wire width for different values of the strip width a for a heavy hole with σ^+ spins. Calculated with $B_a = 0$ T, $h = 16$ nm, $z_0 = 1$ nm, $\mu\mathcal{M}_s = 1.82$ T ,$T = 1$ K, $x = 0.09$ $L = 50$ Å, $n_r = 1$, $m_r = 0$, and $m_R = 0$. The values used for $Cd_{1-x}Mn_xTe$ are given in the Table in Appendix K.

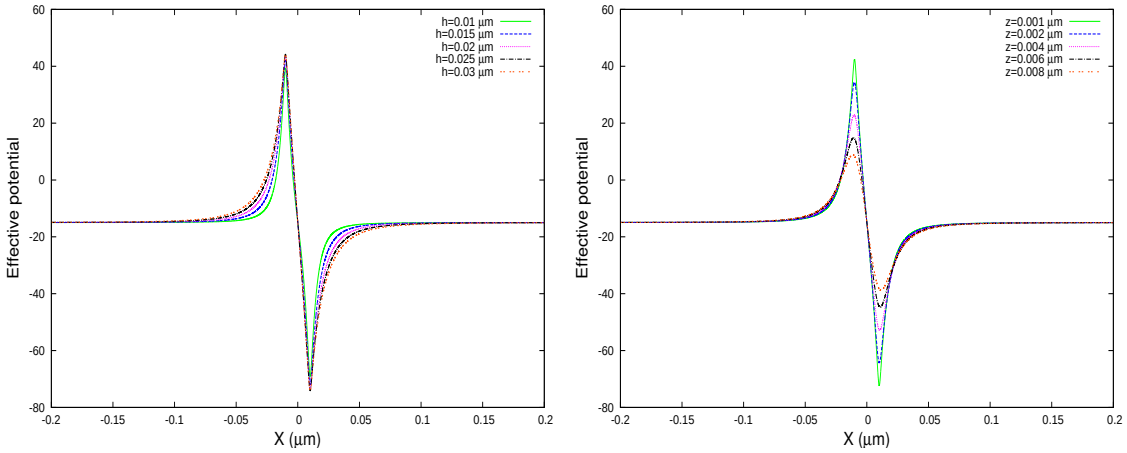

Figure 5-34: Left: Effective potential for a ferromagnetic strip for magnetisation in the x direction as a function of the coordinate along the wire width for different values of the strip height h for a heavy hole with σ^+ spins. Calculated with $B_a = 0$ T, $a = 20$ nm, $z_0 = 1$ nm, $\mu_0 M_s = 1.82$ T, $T = 1$ K, $x = 0.09$ $L = 50$ Å, $n_r = 1$, $m_r = 0$, and $m_R = 0$. Right: Effective potential for a ferromagnetic strip for magnetisation in the x direction as a function of the coordinate along the wire width for different distances between the centre of the ferromagnetic strip and the centre of the quantum well z for a heavy hole with σ^+ spins. Calculated with $B_a = 0$ T, $a = 20$ nm, $h = 16$ nm, $\mu_0 M_s = 1.82$ T, $T = 1$ K, $x = 0.09$ $L = 50$ Å, $n_r = 1$, $m_r = 0$, and $m_R = 0$. The values used for $Cd_{1-x}Mn_xTe$ are given in the Table in Appendix K.

The number of solutions and the corresponding energy for different values of the magnetic ion concentration is plotted in Figure (5-35) for a heavy hole exciton with σ^+ spins. Increasing x increases the number of solutions and the ground state wavefunction becomes more confined, due to the fact that the sp-d interaction term increases with x, resulting in a deeper and narrower potential well, as can be seen in Figure (5-31). The corresponding energy and the ground state energy decreases linearly as x is increased, due to the potential well having a higher negative value for the minimum as x is increased. There are fewer solutions for a given value of x for excitons confined by the magnetic field created by the ferromagnetic strip as compared to the microscale ferromagnetic disk. This is due to the fact that the potential trapping the excitons is alot narrower for the case of the ferromagnetic strip. Compared to the microscale disk where the excitons were confined to a ring with radial extent ~ 1 μm, here the exciton is confined to a point almost two orders of magnitude smaller. There are more solutions for a given value of x for excitons confined by the magnetic field created by the ferromagnetic strip as compared to the nanoscale ferromagnetic disk in the vortex state if the ferromagnetic strip width a is large enough which can be seen in the bottom half of Figure (5-35). As the ferromagnetic strip width is increased the number of solutions increases, due to the effective potential becoming deeper as a is increased, as shown in Figure (5-33).

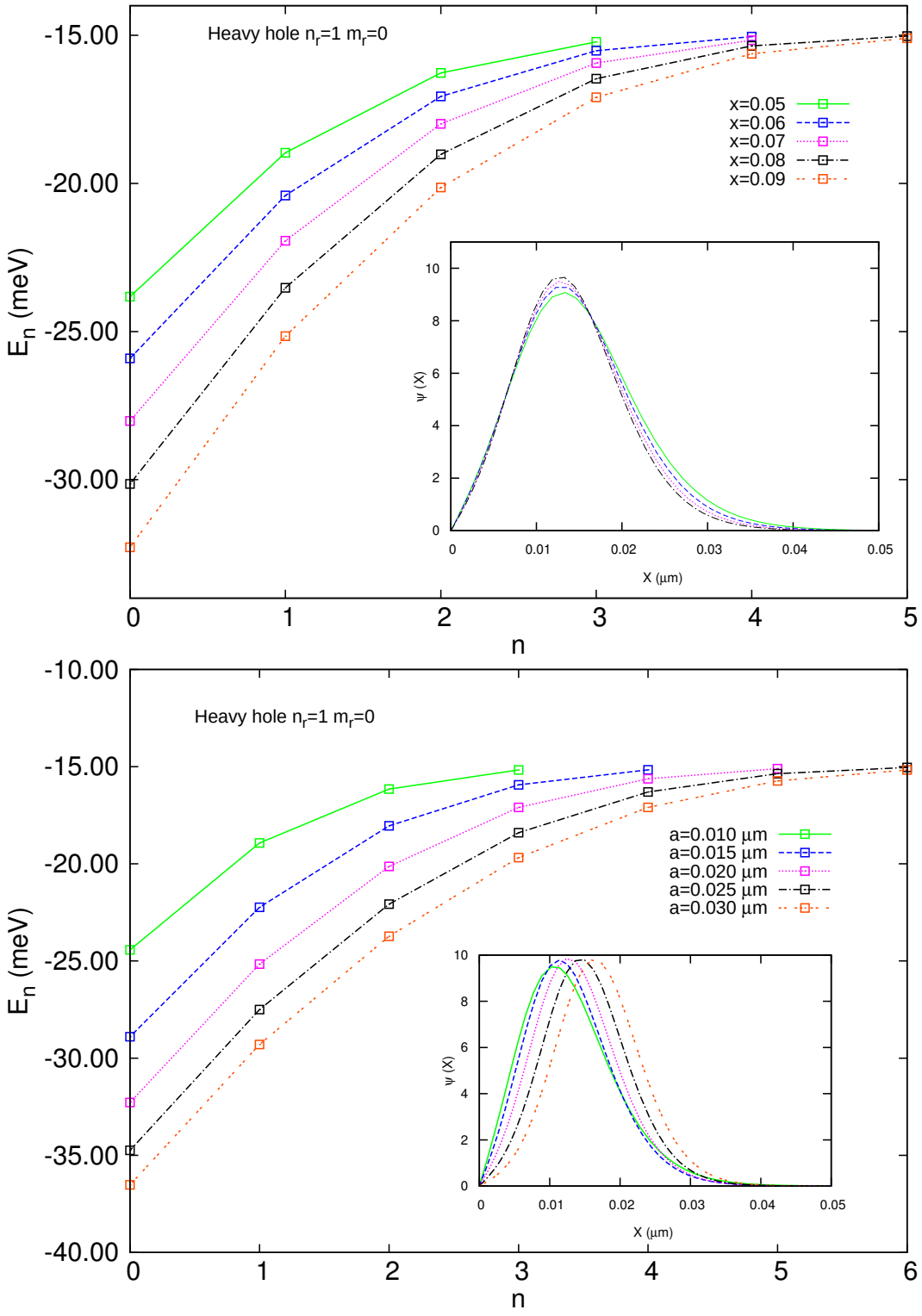

Figure 5-35: Top: Calculated energies E_n of the σ^+ heavy hole exciton for different magnetic ion concentrations, and the corresponding ground state exciton centre of mass radial wavefunction $\psi(X)$ (insert). Bottom: Calculated energies E_n of the σ^+ heavy hole exciton for different values of the disk width a, and the corresponding ground state exciton centre of mass radial wavefunction $\psi(X)$ (insert). Calculated with $B_a = 0$ T, $a = 20$ nm (top), $h = 16$ nm, $z_0 = 1$ nm, $\mu_0 M_s = 1.82$ T, $S_{e,z} = \frac{1}{2}$, $S_{h,z} = \frac{3}{2}$, $x = 0.09$ (bottom), $T = 1$ K, $L = 50$ Å, $n_r = 1$, $m_r = 0$, and $m_R = 0$.

The corresponding value for the ground state energy decreases as the ferromagnetic strip width a is increased as seen in Figure (5-36). This can be explained by looking at the effective potential in Figure (5-33), where the potential peaks at a higher negative value as well as becoming deeper as a is increased. The effect of the ferromagnetic disk height can be seen in Figure (5-36), where the ground state energy decreases as the disk height is increased, again explained by looking at the effective potential in Figure (5-34). Finally, the ground state energy increases as the distance between the bottom of the ferromagnetic strip and the centre of the quantum well is increased as seen in Figure (5-36), due to the potential becoming deeper and peaking at a higher negative value as z is reduced, Figure (5-34).

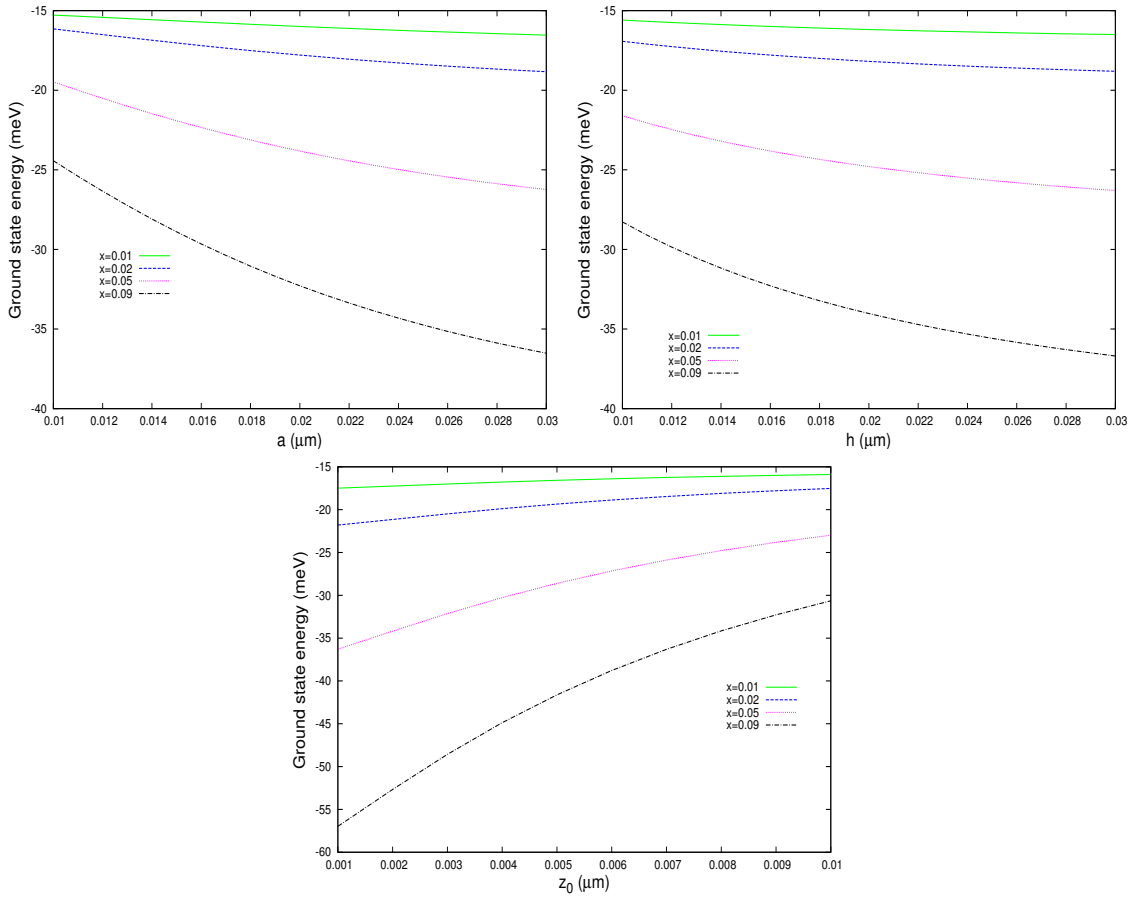

Figure 5-36: Ground state exciton energy for a ferromagnetic strip for different magnetic ion concentrations as a function of the disk radius (top left), disk height (top right) and distance from the bottom of ferromagnetic strip to the centre of the quantum well (bottom) for a σ^+ heavy hole. Calculated with $B_a = 0$ T, $a = 20$ nm (top right, bottom), $h = 16$ nm (top left, bottom), $z_0 = 1$ nm (top left, top right), $\mu_0 M_s = 1.82$ T, $S_{e,z} = \frac{1}{2}$, $S_{h,z} = \frac{3}{2}$, $n_r = 1$, $T = 1$ K, $L = 50$ Å, $n_r = 1$, $m_r = 0$, and $m_R = 0$. The values used for $Cd_{1-x}Mn_xTe$ are given in the Table in Appendix K.

The effect of choosing different magnetic ion concentrations x can be seen in Figure (5-37), where the ground state energy is plotted as a function of the magnetic ion concentration for different temperatures. For a heavy and light hole exciton with σ^+ spins the ground state energy decreases as x is increased. This is opposite to the case of the microscale magnetic disk where the ground state energy increases as x increases for a heavy and light hole exciton with σ^+ spins. This can be explained by comparing the effective potential for the heavy hole exciton with σ^+ spins for the microscale ferromagnetic disk in Figure (5-9) with the ferromagnetic strip with magnetisation in the x direction in Figure (5-31). For the effective potential created by the microscale ferromagnetic disk the minimum value for the potential well (the bottom of the potential well where the excitons becomes trapped) increases as x is increased, but for the effective potential created by the ferromagnetic strip the potential well minimum value occurs at a higher negative value and becomes deeper as x increases. Which results in a lower value for the ground state energy as x is increased for the excitons in the effective potential created by a magnetic field from the ferromagnetic strip. Increasing n_r increases the ground state energy for a given value of x, while increasing m_r (with n_r=2 and m_r=1) decreases the ground state energy as a function of x. This can be again explained by looking at the shape of the effective potential, which is shifted up for $n_r = 2$, and is slightly shifted down for $m_r = 1$ but is still higher than for the case when $n_r = 1$ and $m_r = 0$. For a heavy hole exciton with σ^+ spins for both n_r=2, m_r=0 and n_r=2, m_r=1 the ground state energy decreases for increasing x, which again is opposite to the case of the exciton trapped by the microscale ferromagnetic disk. Due to the potential well minimum occurring at a higher negative value as x increases for the ferromagnetic strip for all values of n_r and m_r.

The effect of varying the temperature T can be seen in Figure (5-38), where the ground state energy is plotted as a function of the temperature. For a heavy and light hole exciton with σ^+ spins the ground state energy increases as T is increased. Increasing n_r increases the ground state energy for a given value of T, while increasing m_r (with n_r=2 and m_r=1) decreases the ground state energy as a function of T. For a heavy hole exciton with σ^+ spins for both n_r=2, m_r=0 and n_r=2, m_r=1 the ground state energy increases for increasing T. This can be explained by looking at Figure (5-31) where the potential peaks at a higher negative value and becomes deeper as T is decreased. This is opposite behaviour to the exciton trapped by the microscale ferromagnetic disk where the ground state energy decreases as T increases for a heavy and light hole exciton with σ^+ spins. This can be explained by comparing the potential created by the ferromagnetic strip when the magnetisation is in the x direction with the potential created by the microscale ferromagnetic disk.

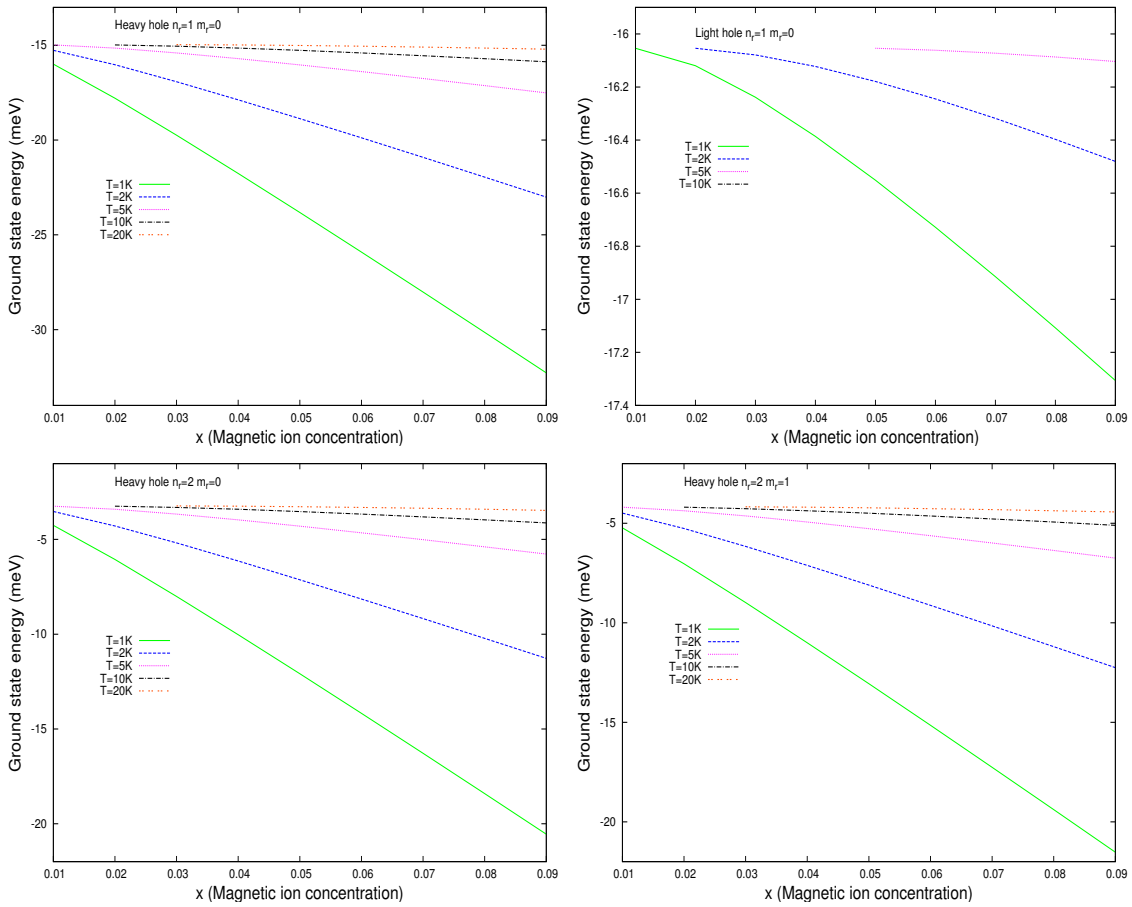

Figure 5-37: Ground state exciton energy for a ferromagnetic strip as a function of the magnetic ion concentration for a heavy (top left) and light (top right) hole exciton with σ^+ spin contributions (with $n_r = 1$ and $m_r = 0$), and for a σ^+ heavy hole exciton with $n_r = 2$, $m_r = 0$ (bottom left), and $n_r = 2$, $m_r = 1$ (bottom right). Calculated with $B_a = 0$ T, $a = 20$ nm, $h = 16$ nm, $z_0 = 1$ nm, $\mu_0 M_s = 1.82$ T, $L = 50$ Å, and $m_R = 0$. The values used for $Cd_{1-x}Mn_xTe$ are given in the Table in Appendix K.

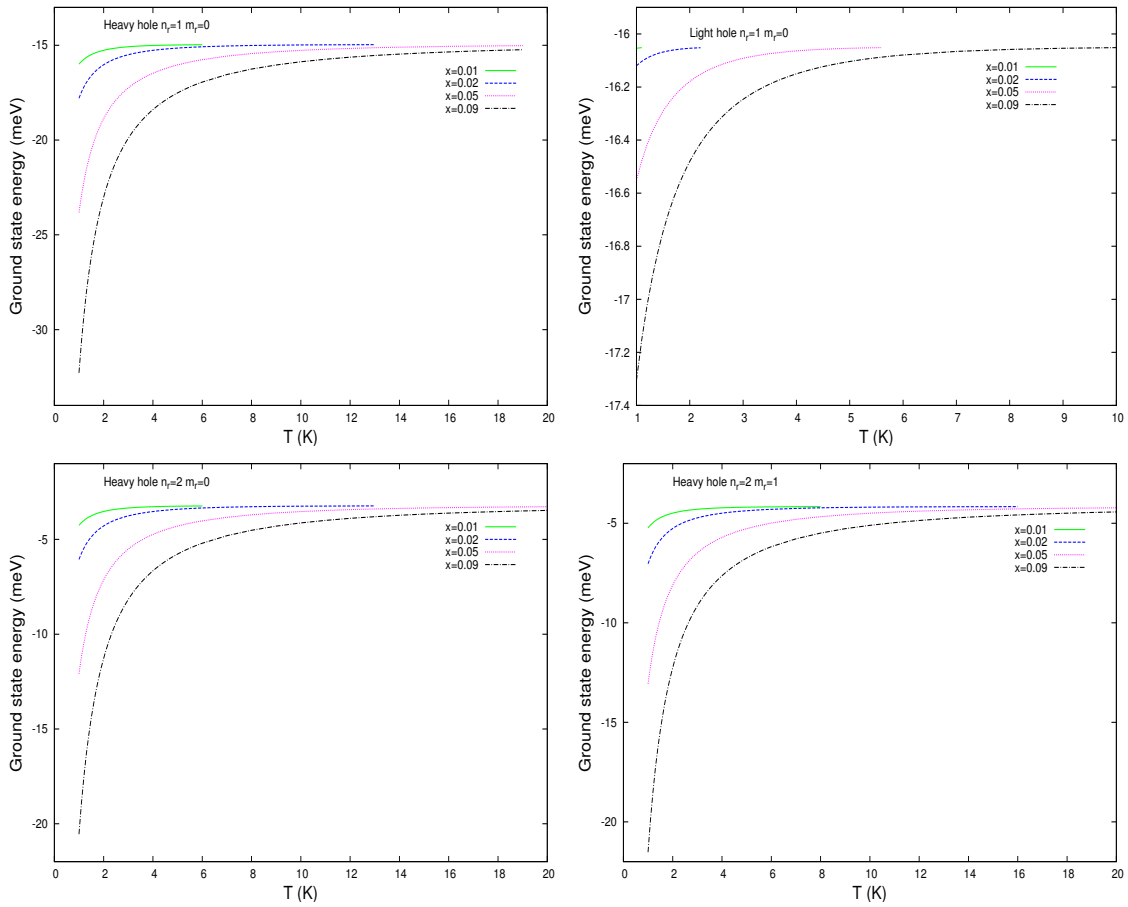

Figure 5-38: Ground state exciton energy for a ferromagnetic strip as a function of the magnetic ion concentration for a heavy (top left) and light (top right) hole exciton with σ^+ spin contributions (with $n_r = 1$ and $m_r = 0$), and for a σ^+ heavy hole exciton with $n_r = 2$, $m_r = 0$ (bottom left), and $n_r = 2$, $m_r = 1$ (bottom right). Calculated with $B_a = 0$ T, $a = 20$ nm, $h = 16$ nm, $z_0 = 1$ nm, $\mu_0 M_s$=1.82 T, $L = 50$ Å, and $m_R = 0$. The values used for $Cd_{1-x}Mn_xTe$ are given in the Table in Appendix K.

The magnetic field created by a ferromagnetic strip for magnetisation in the z direction given by Eq. (5.74) is plotted in Figure (5-39) and Figure (5-40) for different values of the strip width a, strip height h and distance between the centre of the ferromagnetic strip and centre of the quantum well z, using $\mu\mathcal{M}_s = 1.82T$ for cobalt. The magnetic field in the z direction B_z has positive peaks in the regions near the edge of the strip which corresponds to $x = a/2$ and $x = -a/2$, and a negative peak at the centre of the strip (at $x = 0$). The positive peaks increase as the disk width a increases, and as both the disk height h and the distance between the ferromagnetic strip and quantum well z decreases. The negative peak at the centre has a greater negative value as both a and z is reduced, and h is increased.

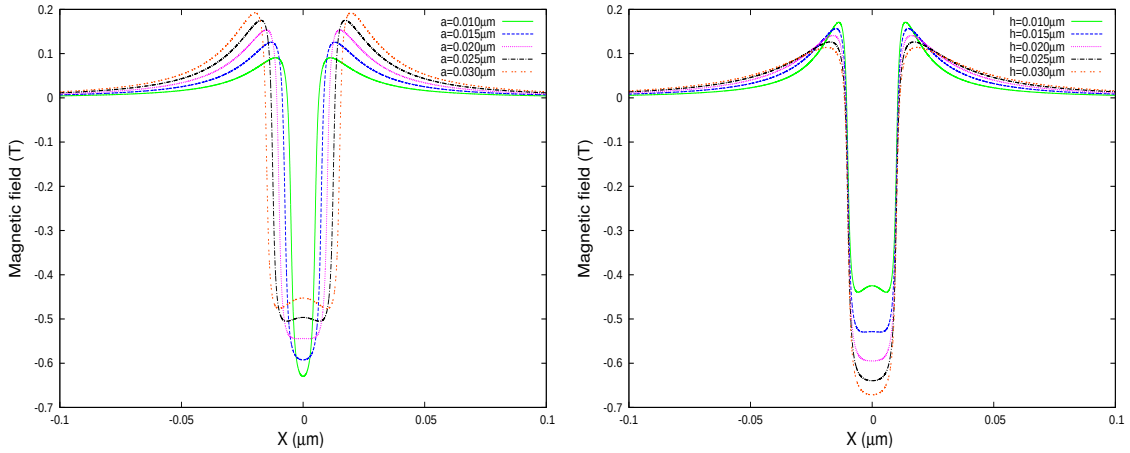

Figure 5-39: Left: Magnetic field for a ferromagnetic strip for magnetisation in the z plane as a function of the coordinate along the wire width for different values of the strip width, a. Calculated with $B_a = 0$ T, $h = 16$ nm, $z_0 = 1$ nm, $\mu\mathcal{M}_s = 1.82$ T. Right: Magnetic field for a ferromagnetic strip for magnetisation in the z direction as a function of the coordinate along the wire width for different values of the strip height, h. Calculated with $B_a = 0$ T, $a = 20$ nm, $z_0 = 1$ nm, $\mu_0 M_s = 1.82$ T.

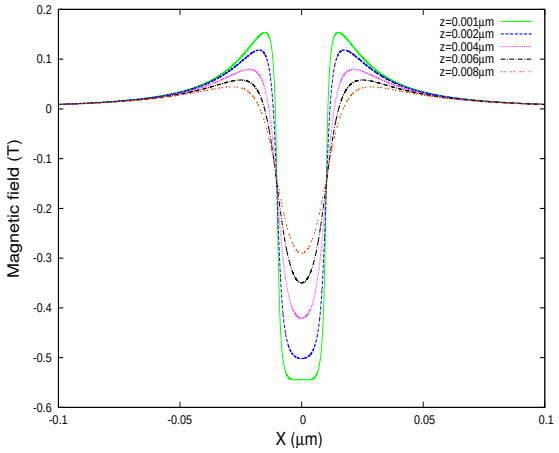

Figure 5-40: Magnetic field for a ferromagnetic strip for magnetisation in the z plane as a function of the coordinate along the wire width for different distances between the ferromagnetic strip and the centre of the quantum well, z. Calculated with $B_a = 0$ T, $a = 20$ nm, $h = 16$ nm, $\mu_0 M_s = 1.82$ T.

The corresponding effective potential for the ferromagnetic strip for magnetisation in the z plane is plotted in Figure (5-41) for a heavy hole exciton with both σ^+ and σ^- spins for different magnetic ion concentrations x. For excitons with σ^+ spins the effective potential reaches a minimum at the centre of the ferromagnetic strip, and has two maximum peaks near the regions which correspond to $x = a/2$ and $x = -a/2$. Conversely, for a heavy or light hole exciton with σ^- spins the effective potential reaches a maximum at the centre of the ferromagnetic strip, and has two negative peaks near the regions which correspond to $x = a/2$ and $x = -a/2$. Excitons with both σ^+ and σ^- spins can be trapped in the negative peaks of the potential, unlike the case for the magnetisation in the x direction for the ferromagnetic strip that only traps excitons with σ^+ spins. For excitons with both σ^+ and σ^- spins the negative peaks in the potentials have a greater negative value and become deeper as x is increased. The effective potential for the ferromagnetic strip for magnetisation in the z plane is plotted in Figure (5-42) for a heavy hole exciton with both σ^+ and σ^- spins for different temperatures. For excitons with both σ^+ and σ^- spins the negative peaks in the potentials have a greater negative value and become deeper as T decreases.

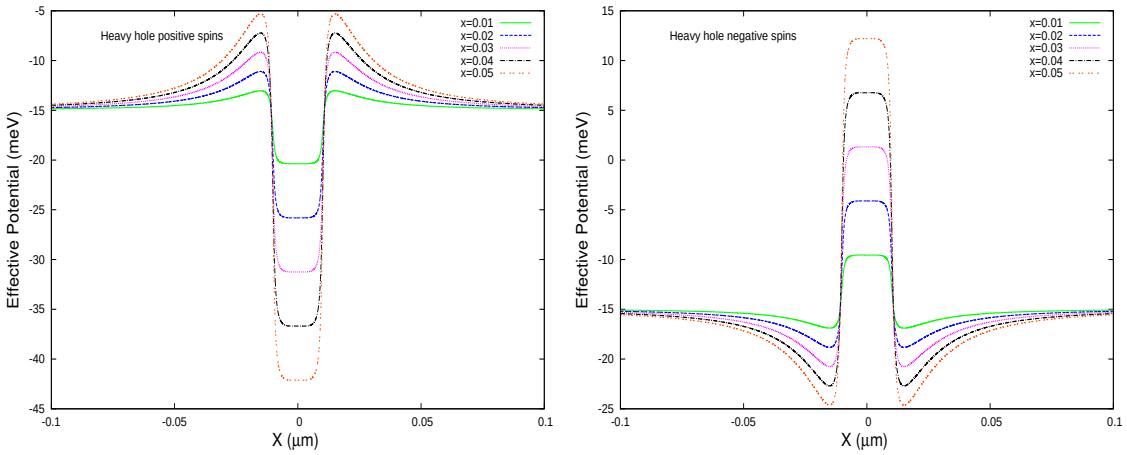

Figure 5-41: Effective potential for a ferromagnetic strip for magnetisation in the z direction as a function of the coordinate along the wire width for different values of the magnetic ion concentration x, for a heavy hole with both σ^+ spins (left) and σ^- spins (right). Calculated with $B_a = 0$ T, $a = 20$ nm, $h = 16$ nm, $z_0 = 1$ nm, $\mu_0 M_s = 1.82$ T, $T = 1$ K, $L = 50$ Å, $n_r = 1$, $m_r = 0$, and $m_R = 0$. The values used for $Cd_{1-x}Mn_xTe$ are given in the Table in Appendix K.

=

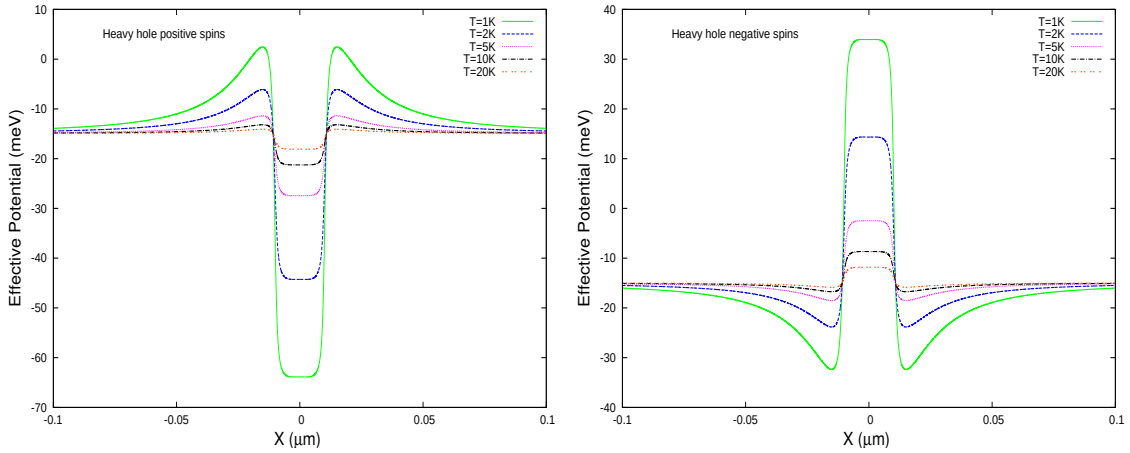

Figure 5-42: Effective potential for a ferromagnetic strip for magnetisation in the z direction as a function of the coordinate along the wire width for different temperatures T, for a heavy hole with both σ^+ spins (left) and σ^- spins (right). Calculated with $B_a = 0$ T, $a = 20$ nm, $h = 16$ nm, $z_0 = 1$ nm, $\mu_0 M_s = 1.82$ T, $x = 0.09$ K, $L = 50$ Å, $n_r = 1$, $m_r = 0$, and $m_R = 0$. The values used for $Cd_{1-x}Mn_xTe$ are given in the Table in Appendix K

The number of solutions and the corresponding energy for different values of the magnetic ion concentration x is plotted in Figure (5-43) for both a σ^+ and σ^- heavy hole exciton for a ferromagnetic strip with magnetisation in the z direction. Increasing x increases the number of solutions, and the ground state wavefunction becomes more confined. The corresponding energy decreases as x is increased, which can be explained by looking at the negative peaks in the potentials shown in Figure (5-41), which peak at a higher negative value and become deeper as x is increased.

There are more solutions for a given value of x for the case of the magnetic field created by the ferromagnetic strip for magnetisation in the z direction for a heavy hole exciton with σ^- spins than there are for a heavy hole exciton with σ^+ spins, due to the potential being narrower for the heavy hole exciton with σ^+ spins, whilst there are more solutions for a given value of x for a heavy hole exciton with σ^+ spins confined by the ferromagnetic strip with magnetisation in the x direction than there is solutions for a heavy hole exciton confined by the ferromagnetic strip with magnetisation in the z plane, as seen by comparing Figure (5-35) and (5-43). This can be explained by comparing the potentials in Figure (5-31) with Figure (5-41), where the potential is deeper for a given value of x for the case when the magnetisation is in the x direction.

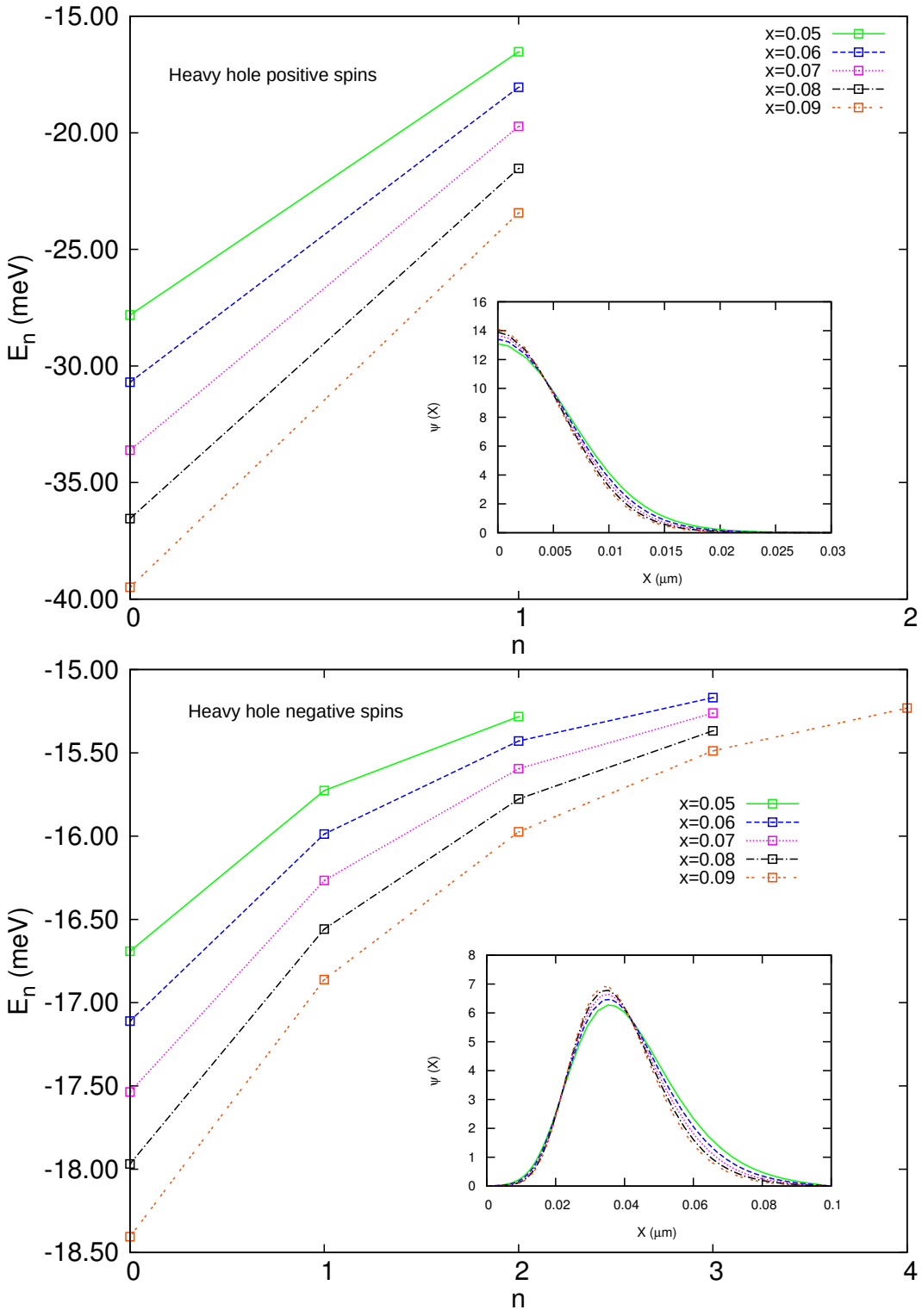

Figure 5-43: Calculated energies E_n of the heavy hole exciton with σ^+ spins (top) and σ^- spins (bottom) for different magnetic ion concentrations, and the corresponding ground state exciton centre of mass radial wavefunction $\psi(R)$ (insert). Calculated with $B_a = 0$ T, $a = 20$ nm, $h = 16$ nm, $z_0 = 1$ nm, $\mu_0 M_s = 1.82$ T, $T = 1$ K, $L = 50$ Å, $n_r = 1$, $m_r = 0$, and $m_R = 0$.

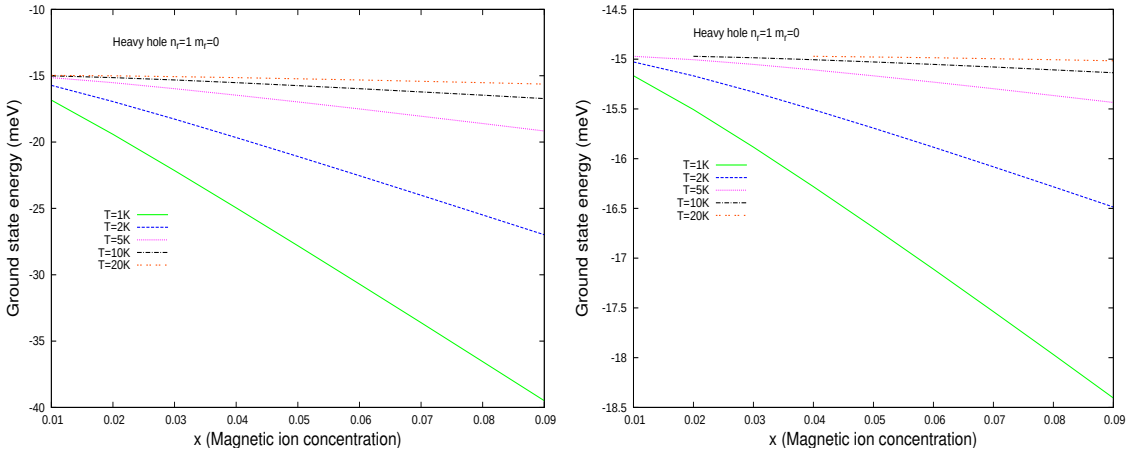

Figure 5-44: Ground state exciton energy as a function of the magnetic ion concentration with different temperatures for a heavy hole with σ^+ spins (left) and σ^- spins (right). Calculated with $B_a = 0$, $a = 20$ nm, $h = 16$ nm, $z_0 = 1$ nm, $\mu_0 M_s = 1.82$ T, $L = 50$ Å, $n_r = 1$, $m_r = 0$, and $m_R = 0$. The values used for $Cd_{1-x}Mn_xTe$ are given in the Table in Appendix K.

The effect of using different concentrations x of the magnetic ion can be seen in Figure (5-44), where the ground state energy is plotted as a function of x and for different temperatures. For a heavy hole exciton with both σ^+ and σ^- spins the ground state energy decreases as x is increased, while the corresponding energy is lower for a given value of x for the heavy hole exciton with σ^+ spins. This is opposite to the case of the microscale ferromagnetic disk where the ground state energy increases as x increases for a heavy hole exciton with σ^+ spins. This can be explained by comparing the potentials in Figure (5-9) for the microscale ferromagnetic disk with the left side of Figure (5-41) for the ferromagnetic strip with magnetisation is in the z plane, where the potential has a higher negative value and becomes deeper as x is increased. The behaviour is the same for the ground state energy for the heavy hole exciton with σ^- spins confined by both the microscale ferromagnetic disk and the ferromagnetic strip for magnetisation in the z plane, where the ground state energy decreases as x increases.

5.6 Summary

To conclude, in this Chapter, a model has been developed for excitons in a dilute magnetic semiconductor in the presence of an inhomogeneous magnetic field. The magnetic fields created by both microscale and nanoscale ferromagnetic disks, and also a ferromagnetic strip, has been considered, with results obtained assuming the dilute magnetic semiconductor is $Cd_{1-x}Mn_xTe$. A variational parameter γ was used to included the effect of the difference between the 2D and 3D Coulomb interaction and calculated for both the heavy and light hole. This parameter γ increases as the well width decreases, and also depends on the quantum numbers n_r and m_r.

The magnetic field created by a microscale ferromagnetic disk is found to trap more than a ground state exciton, and that there are more confined excited state solutions for heavy hole excitons than light hole excitons, due to the sp-d interaction making a smaller contribution for a light hole exciton. Higher values of the magnetic ion concentration x, and decreasing temperature T result in more trapped states, which become increasingly lo-

calised due to the effective potential well that they move in becoming deeper and narrower for increasing x and decreasing T. For heavy and light hole excitons with σ^+ spins the ground state energy increases for increasing magnetic ion concentration and for decreasing temperature, whilst for heavy and light hole exciton with σ^- spins the ground state energy decreases for increasing magnetic ion concentration and decreasing temperature. This is due to the sp-d interaction either making a negative or positive contribution.

It has been found that the magnetic field from a nanoscale ferromagnetic disk traps fewer excitons than the microscale ferromagnetic disk, and can only trap heavy and light hole excitons with σ^- spins. The exciton is confined to a point with radial extent almost two order of magnitudes smaller for the nanoscale ferromagnetic disk. The number of trapped states increases with increasing magnetic ion concentration x and decreasing temperature T for heavy and light hole excitons with σ^- spins.

For a magnetic field created from a ferromagnetic strip the excitons that can be trapped are found to depend on the direction of the magnetisation. When the magnetisation is in the x direction only excitons with σ^+ spins can be trapped, due to the shape of the potential. Increasing the magnetic ion concentration in the dilute magnetic semiconductor x increases the number of excited state solutions, and the wavefunction describing the states becomes more localised. For heavy and light hole excitons with σ^+ spins the ground state energy decreases as x increases, and increases as T increases. This is opposite to the behaviour of excitons confined by the magnetic field from the microscale ferromagnetic strip, which is understood in terms of the behaviour of the effective potential. When the magnetisation is in the z plane the magnetic field from a ferromagnetic strip can trap both σ^+ and σ^- excitons, in the negative peaks of the potential. Increasing x increases the number of solutions for excitons with σ^- spins, and there is more solutions for excitons with σ^- spins than for the case for excitons with σ^+ spins when the magnetisation is in the z plane. There are also more solutions when the magnetisation is in the x direction than the z plane for σ^+ excitons. For σ^+ and σ^- spin excitons the ground state energy decreases as x increases, which is opposite compared to the behaviour of σ^+ excitons confined by a magnetic field created by the microscale ferromagnetic disk, and the same compared to the behaviour of σ^- spin excitons confined by a magnetic field created by the microscale ferromagnetic disk.

Taken together, these results illustrate the opportunities that exist for trapping excitons with different spins in states with different symmetries and spatial extents through the use of inhomogeneous magnetic fields acting upon dilute magnetic semiconductors.

Chapter 6

Conclusion and Further work

6.1 Summary

The use of the spin of quasiparticles, instead of their charge, as a basis for the operation of a new type of electronic devices has attracted the attention of a large interdisciplinary research community. Although still largely theoretical, progress in crystal growth techniques has allowed spintronics research to expand into experimental areas, with the potential of offering devices that are smaller, faster, more energy efficient, and less volatile than traditional charge based electronics. Dilute magnetic semiconductors (DMSs) are ideal candidates for spintronic devices as they exhibit both semiconducting and magnetic properties. Unlike, an ordinary semiconductor, a DMS has a sp-d interaction that can dramatically change the physics of the semiconductor in a magnetic field. This sp-d interaction leads to giant Zeeman splittings of the conduction and valence band, which can be observed at relatively small external magnetic fields. The spin degree of freedom can be utilised in another way, by taking advantage of the large effective g factor present in a DMS, and combining it with a spatially inhomogeneous applied magnetic field, to create a spatially varying Zeeman potential that acts as a confining potential for quasiparticles such as electrons, holes or excitons. These features make DMSs of interest as model systems in the emerging field of spintronics. A fundamental understanding of the spin properties of DMS quantum well structures is essential in furthering progress towards these new devices. The work presented in this thesis is aimed at contributing to this knowledge. It is hoped that the work presented here has furthered the understanding of these materials and structures by looking at hybrid systems combining nanoscale and microscale ferromagnets with DMS quantum wells. This thesis looked at $Cd_{1-x}Mn_xTe$ DMS quantum wells as an interesting system for studying quasiparticles in the presence of an inhomogeneous magnetic field. Many possibilities of using inhomogeneous magnetic fields was proposed, and the results in this thesis illustrate the opportunities that exist for trapping excitons with different spins in states with different symmetries and spatial extents through the use of these different inhomogeneous magnetic fields acting upon the DMS. The giant Zeeman splitting of the different spin components was also looked at.

Firstly, to understand the effects of an inhomogeneous magnetic field on the electrons and holes in a DMS quantum, the splitting on the heavy and light hole modelled using the Luttinger Kohn Hamiltonian was investigated. The inhomogeneous magnetic field that was studied was from a nanoscale ferromagnetic disk in the vortex state, and due to the high effective g factors present in DMSs the particles were found to be confined in a small

region in the quantum well due to the magnetic vortex.

Next, we extended the study by including the Coulomb interaction between the electron and hole, and the Harrison model was used to calculate binding energies in a finite quantum well both with and without the presence of a homogeneous magnetic field. It is believed that this has not previously been studied in this way to calculate the binding energies for this material. The presence of the magnetic field leads to a reduction in the binding energy for a heavy hole with both σ^+ and σ^- spins in the DMS quantum well, and it was found that the binding energy decreases as the magnetic ion concentration in the dilute magnetic semiconductor is increased.

Finally, we have explored the effects of an inhomogeneous magnetic field on excitons in a DMS quantum well. The inhomogeneous magnetic field that were studied were a microscale and nanoscale ferromagnetic disk, and a ferromagnetic strip. The 2D coulomb interaction was used for simplicity, but the variational parameter γ was introduced to included the effect of the difference between the 2D and 3D Coulomb interaction. The different solutions for both a heavy and light hole exciton with both σ^+ and σ^- spins with different n_r and m_r quantum numbers was calculated for different values of the magnetic ion concentration and temperature, which are the two variables that greatly effect the sp-d interaction in a DMS. The number of solutions and the ground state energy was found to depend on the magnetic ion concentration and temperature, as well as the type of magnetic field. These results illustrate the opportunities that exist for trapping excitons with different spins in states with different symmetries and spatial extents through the use of inhomogeneous magnetic fields acting upon dilute magnetic semiconductors.

6.2 Future work

For future work, it would be interesting to extend this study by looking at different inhomogeneous magnetic fields, perhaps one created by a superconducting disk. The model for excitons in the presence of an inhomogeneous magnetic field could be improved by using a finite well, and the effect of the magnetic field on the energy of the exciton confinement in the quantum well direction will need to be included. This study could also be extended to include the valence band coupling since ignoring the valence band coupling is an over simplification, which produces a highly non-parabolic subband structure, which alters the binding energies [72][103][104][105][106]. The non parabolicity for the conduction band and the spin orbit split off band should also be added to get a more accurate picture [72][105]. The use of the effective mass theory in homogeneous bulk semiconductors is well established, however its application to heterostructures, especially with regard to the boundary conditions across an abrupt heterostructure in not so well established [107][108][109][110][111][112][113]. Therefore a more accurate model for excitons in a DMS quantum well should involve the use of envelope function theory, so that proper boundary conditions at the interfaces are automatically obtained [114][115].

The confinement of excitons in a DMS quantum well might be verified experimentally by calculating the optical response of the hybrid structure composed of the ferromagnet deposited on top of the diluted magnetic semiconductor quantum well. Since high values of the effective g factors are fundamental for the localisation and the manufacturing of efficient traps, optical localisation is expected to be observed at sub Kelvin temperatures [48]. Spin flip Raman scattering can provide a high resolution probe of the spin splittings in these hybrid systems [116][117].

Appendix A

Deriving the Kane Hamiltonian and calculating the eigenvalues

This section outlines the derivation of one of the matrix elements of the Kane Hamiltonian given in Eq. (2.19), as well as the eigenvalues. The matrix element $\mathcal{H}_{22}$ is written as

$$\begin{aligned}\left\langle \frac{(X-iY)\uparrow}{\sqrt{2}}\right| \mathcal{H} \left|\frac{(X-iY)\uparrow}{\sqrt{2}}\right\rangle &= \left\langle \frac{(X-iY)\uparrow}{\sqrt{2}}\right| \mathcal{H}_0 \left|\frac{(X-iY)\uparrow}{\sqrt{2}}\right\rangle \\ &+\frac{\hbar}{m_0}\left\langle \frac{(X-iY)\uparrow}{\sqrt{2}}\right| \vec{k}\cdot\vec{p} \left|\frac{(X-iY)\uparrow}{\sqrt{2}}\right\rangle \\ &+\frac{\hbar}{4m_0^2c^2}\left\langle \frac{(X-iY)\uparrow}{\sqrt{2}}\right| \vec{p}\cdot\vec{\sigma}\times\nabla V(\vec{r}) \left|\frac{(X-iY)\uparrow}{\sqrt{2}}\right\rangle. \end{aligned} \tag{A.1}$$

For the first term, expanding out gives

$$\begin{aligned}\left\langle \frac{(X-iY)\uparrow}{\sqrt{2}}\right| \mathcal{H}_0 \left|\frac{(X-iY)\uparrow}{\sqrt{2}}\right\rangle &= \frac{1}{2}\left(\langle X\uparrow|\mathcal{H}_0|X\uparrow\rangle - i\langle X\uparrow|\mathcal{H}_0|Y\uparrow\rangle + i\langle Y\uparrow|\mathcal{H}_0|X\uparrow\rangle \right. \\ &\qquad \left. + \langle Y\uparrow|\mathcal{H}_0|Y\uparrow\rangle\right) \\ &= \frac{1}{2}(E_p - iE_p + iE_p + E_p) \\ &= E_p, \end{aligned} \tag{A.2}$$

where $H_0|X\uparrow\rangle = E_p|X\uparrow\rangle$. For the second

$$\begin{aligned}\frac{\hbar}{m_0}\left\langle \frac{(X-iY)\uparrow}{\sqrt{2}}\right| \vec{k}\cdot\vec{p} \left|\frac{(X-iY)\uparrow}{\sqrt{2}}\right\rangle &= \frac{1}{2}\left(\left\langle X\uparrow\left|\vec{k}\cdot\vec{p}\right|X\uparrow\right\rangle - i\left\langle X\uparrow\left|\vec{k}\cdot\vec{p}\right|Y\uparrow\right\rangle \right. \\ &\qquad \left. -i\left\langle Y\uparrow\left|\vec{k}\cdot\vec{p}\right|X\uparrow\right\rangle + \left\langle Y\uparrow\left|\vec{k}\cdot\vec{p}\right|Y\uparrow\right\rangle\right) \\ &= 0, \end{aligned} \tag{A.3}$$

since $\langle Y\uparrow|k\cdot p|X\uparrow\rangle = -\langle X\uparrow|k\cdot p|Y\uparrow\rangle$ due to the symmetry of the system. For the third part

$$\begin{aligned}
&\frac{\hbar}{4m_0^2c^2}\left\langle\frac{(X-iY)\uparrow}{\sqrt{2}}\right|\vec{p}\cdot\vec{\sigma}\times\nabla V(\vec{r})\left|\frac{(X-iY)\uparrow}{\sqrt{2}}\right\rangle \\
&\quad=-\frac{i\hbar}{8m_0^2c^2}\left(\langle X|\vec{p}\times\nabla V(\vec{r})|Y\rangle\cdot\langle\uparrow|\vec{\sigma}|\uparrow\rangle-\langle Y|\vec{p}\times\nabla V(\vec{r})|X\rangle\cdot\langle\uparrow|\vec{\sigma}|\uparrow\rangle\right) \\
&\quad=-\frac{i\hbar}{4m_0^2c^2}\left\langle X\left|\frac{\partial V}{\partial x}p_y-\frac{\partial V}{\partial y}p_x\right|Y\right\rangle \\
&\quad=-\frac{\Delta_{so}}{3},
\end{aligned}\tag{A.4}$$

since the spin operators act as $\sigma_x|\uparrow\rangle=|\downarrow\rangle$, $\sigma_y|\uparrow\rangle=i|\downarrow\rangle$, and $\sigma_z|\uparrow\rangle=|\uparrow\rangle$. The last step defines the spin orbit energy Δ_{so} [31][30]. Combining, Eq. (A.1) becomes

$$\left\langle\frac{(X-iY)\uparrow}{\sqrt{2}}\right|\mathcal{H}\left|\frac{(X-iY)\uparrow}{\sqrt{2}}\right\rangle=E_p-\frac{\Delta_{so}}{3}.\tag{A.5}$$

Other terms in the Hamiltonian matrix Eq. (2.19) follow by similar analysis.

To calculate the eigenvalues of the Hamiltonian in Eq. (2.19) define the reference energy such that $E_p=-\Delta_{so}/3$, and $E_s=E_g$, which is the band gap energy. The Hamiltonian in Eq. (2.19) then becomes

$$\overline{\mathbf{H}}=\begin{pmatrix}E_g & 0 & kP' & 0\\ 0 & -\frac{2\Delta_{so}}{3} & \frac{\sqrt{2}\Delta_{so}}{3} & 0\\ kP' & \frac{\sqrt{2}\Delta_{so}}{3} & -\frac{\Delta_{so}}{3} & 0\\ 0 & 0 & 0 & 0\end{pmatrix},\tag{A.6}$$

which has the eigenvalue $E'=0$ and the characteristic polynomial

$$E'(E'-E_g)(E'+\Delta_{so})-k^2P'^2\left(E'+\frac{2}{3}\Delta_{so}\right)=0,\tag{A.7}$$

When k^2 is very small, the roots of Eq. (A.7) are expected to be $E'=E_g$, $E'=0$ and $E'=-\Delta_{so}$.

Expand about the extreme of the bands ($E(k)=E(0)+k\frac{\partial f}{\partial k}|_{k=0}+\frac{1}{2}k^2\frac{\partial^2 f}{\partial k^2}|_{k=0}=E(0)+\varepsilon(k^2)$) for small $\vec{k}$ (since its only valid near the band edge where $\vec{k}=0$), and let $E'=E_g+\varepsilon(k^2)$. Putting this into Eq. (A.7) we see

$$\varepsilon=\frac{k^2P'^2(3E_g+2\Delta_{so})}{3E_g(E_g+\Delta_{so})}.\tag{A.8}$$

Then by letting $E'=0+\varepsilon(k^2)$:

$$\varepsilon=\frac{k^2P'^2 2\Delta_{so}+3k^2P'^2\varepsilon k^2}{3\varepsilon k^2(\Delta_{so}-E_g)}=-\frac{2k^2P'^2}{3E_g},\tag{A.9}$$

and by setting $E'=-\Delta_{so}+\varepsilon(k^2)$:

$$\varepsilon=-\frac{k^2P'^2}{3(E_g+\Delta_{so})}.\tag{A.10}$$

Since $E' = E_n(k) - \hbar^2 k^2/2m_0$, the 4 energy bands in Eq. (2.22) are

$$\begin{aligned} E_c(k) &= E_g + \frac{\hbar^2 k^2}{2m_0} + \frac{k^2 P'^2(3E_g + 2\Delta_{so})}{3E_g(E_g + \Delta_{so})}, \\ E_{hh}(k) &= \frac{\hbar k^2}{2m_0}, \\ E_{lh}(k) &= \frac{\hbar k^2}{2m_0} - \frac{2k^2 P'^2}{3E_g}, \\ E_{so}(k) &= -\Delta_{so} + \frac{\hbar k^2}{2m_0} - \frac{k^2 P'^2}{3(E_g + \Delta_{so})}. \end{aligned} \tag{A.11}$$

Appendix B

Diagonalising the 4×4 Luttinger Kohn Hamiltonian Hamiltonian

Here the block diagonalisation of the 4×4 Luttinger Kohn Hamiltonian is summarised. The unitary transformation block diagonalising the 4×4 Luttinger Kohn Hamiltonian is [34][118]

$$U = \begin{pmatrix} v^* & 0 & 0 & -v \\ 0 & w^* & -w & 0 \\ 0 & w^* & w & 0 \\ v^* & 0 & 0 & v \end{pmatrix}, \tag{B.1}$$

where $v = 1/\sqrt{2}\exp(i\phi)$, $w = 1/\sqrt{2}\exp(i\eta)$, with $\phi = \tan^{-1}(k_y/k_x)$ and $\eta = -\phi/3$, we see

$$UU^\dagger = \begin{pmatrix} v^*v + vv^* & 0 & 0 & v^*v - vv^* \\ 0 & w^*w + ww^* & w^*w - ww^* & 0 \\ 0 & w^*w - ww^* & w^*w + ww^* & 0 \\ v^*v - vv^* & 0 & 0 & v^*v + vv^* \end{pmatrix} = \begin{pmatrix} 1 & 0 & 0 & 0 \\ 0 & 1 & 0 & 0 \\ 0 & 0 & 1 & 0 \\ 0 & 0 & 0 & 1 \end{pmatrix}. \tag{B.2}$$

Then

$$\begin{aligned} \mathcal{H}'_{LK} &= U\mathcal{H}_{LK}U^\dagger \\ &= -\begin{pmatrix} v^* & 0 & 0 & -v \\ 0 & w^* & -w & 0 \\ 0 & w^* & w & 0 \\ v^* & 0 & 0 & v \end{pmatrix} \begin{pmatrix} P+Q & -b & c & 0 \\ -b^* & P-Q & 0 & c \\ c^* & 0 & P-Q & b \\ 0 & c^* & b^* & P+Q \end{pmatrix} \end{aligned} \tag{B.3}$$

$$\begin{pmatrix} v & 0 & 0 & v \\ 0 & w & w & 0 \\ 0 & -w^* & w^* & 0 \\ -v^* & 0 & 0 & v^* \end{pmatrix} \tag{B.4}$$

$$= -\begin{pmatrix} v^* & 0 & 0 & -v \\ 0 & w^* & -w & 0 \\ 0 & w^* & w & 0 \\ v^* & 0 & 0 & v \end{pmatrix} \begin{pmatrix} (P+Q)v & -bw - cw^* & -bw + cw^* & (P+Q)v \\ -b^*v - cv^* & (P-Q)w & (P-Q)w & -b^*v + cv^* \\ c^*v - bv* & -(P-Q)w^* & (P-Q)w^* & c^*v + bv^* \\ -(P+Q)v^* & c^*w - b^*w^* & c^*w + b^*w^* & (P+Q)v^* \end{pmatrix} \tag{B.5}$$

$$= - \begin{pmatrix} P+Q & R & 0 & 0 \\ R^* & P-Q & 0 & 0 \\ 0 & 0 & P-Q & R \\ 0 & 0 & R^* & P+Q \end{pmatrix}, \tag{B.6}$$

where $R = |c| - i|b|$. Hence $\mathcal{H}'_{LK} = U\mathcal{H}_{LK}U^\dagger$ is block diagonal.

Appendix C

Magnetic field created by a single vortex in a nanoscale ferromagnetic disk

Here the magnetic field due to a single vortex in a nanoscale ferromagnetic disk is summarised. The resulting expressions are used in the modelling in Chapter 3. To derive the magnetic fields given in Eq. (3.2) and (3.4) we follow reference [62] and start from Maxwell's equations

$$\nabla \cdot \vec{B} = 0, \tag{C.1}$$
$$\nabla \times \vec{H} = \vec{J}, \tag{C.2}$$

where $\vec{J}$ is the current from free charges, zero here, and $\vec{B} = \mu_0(\vec{H} + \vec{M})$ everywhere. Therefore

$$\nabla \times \vec{H} = 0, \tag{C.3}$$
$$\nabla \cdot \vec{H} = -\nabla \cdot \vec{M}. \tag{C.4}$$

These are solved by introducing the magnetic potential Φ such that $\vec{H} = -\nabla\Phi$, so that $\nabla \times \vec{H} = -\nabla \times \nabla\Phi = 0$, and $\nabla^2\Phi = \nabla \cdot \vec{M}$. Comparing with the electrostatic potential from a charge distribution

$$\nabla^2\Phi_{el} = -4\pi\rho(\vec{r}), \qquad \Phi_{el}(\vec{r}) = \int \frac{\rho(\vec{r}\,')d^3\vec{r}\,'}{|\vec{r} - \vec{r}\,'|}, \tag{C.5}$$

we see

$$\Phi(\vec{r}) = -\frac{1}{4\pi}\int \frac{\nabla \cdot \vec{M}(\vec{r}\,')d^3\vec{r}\,'}{|\vec{r} - \vec{r}\,'|}. \tag{C.6}$$

If we can find $\Phi(\vec{r})$, then outside the magnet $\vec{M} = 0$, and $\vec{B} = \mu_0\vec{H} = -\mu_0\nabla\Phi$.

Here by symmetry the magnetisation (Eq. (3.1)) is

$$\vec{M}(\vec{r}) = \left(M_\varphi(\rho)\vec{e}_\varphi + M_z(\rho)\vec{e}_z\right)\left(\Theta(z+d) - \Theta(z)\right), \tag{C.7}$$

where Θ is the Heaviside step function; so that

$$\nabla \cdot \vec{M} = M_z(\rho)\left[\delta(z+d) - \delta(z)\right], \tag{C.8}$$

and

$$\Phi(\vec{r}) = \tilde{\Phi}(\vec{r}) - \tilde{\Phi}(\vec{r} + d\vec{e}_z), \tag{C.9}$$

where

$$\begin{aligned} \tilde{\Phi}(\vec{r}) &= \frac{1}{4\pi} \int \frac{M_z(\rho')\delta(z')d^3\vec{r}\,'}{|\vec{r} - \vec{r}\,'|}, \\ &= \frac{1}{4\pi} \int_0^{\rho_c} \rho' d\rho' \int_0^{2\pi} d\varphi' \frac{M_z(\rho')}{\sqrt{\rho^2 + \rho'^2 + z^2 - 2\rho\rho'\cos(\varphi' - \varphi)}}. \end{aligned} \tag{C.10}$$

Letting $\varphi' - \varphi = \pi + 2\theta$, so $d\varphi' = 2d\theta$ and $\cos(\varphi' - \varphi) = 2\sin^2\theta - 1$, this becomes

$$\tilde{\Phi}(\vec{r}) = \frac{1}{\pi} \int_0^{\rho_c} \frac{\rho' M_z(\rho')d\rho'}{\sqrt{(\rho + \rho')^2 + z^2}} K(k), \tag{C.11}$$

with $K(k)$ the usual elliptical integral of the first kind [63], and

$$k^2 = \frac{4\rho\rho'}{(\rho + \rho')^2 + z^2}. \tag{C.12}$$

Writing the magnetic field as

$$\vec{B}(\vec{r}) = -\mu_0 \nabla\Phi(\vec{r}) = \vec{b}(\vec{r}) - \vec{b}(\vec{r} + d\vec{e}_z), \tag{C.13}$$

where

$$\vec{b}(\vec{r}) = -\mu_0 \nabla\tilde{\Phi}(\vec{r}) = -\frac{\mu_0}{\pi} \nabla \int_0^{\rho_c} \frac{\rho' M_z(\rho')d\rho'}{\sqrt{(\rho + \rho')^2 + z^2}} K(k), \tag{C.14}$$

the z component of $b(\vec{r})$ is

$$\begin{aligned} b_z(\vec{r}) &= -\frac{\mu_0}{\pi} \int_0^{\rho_c} \rho' M_z(\rho')d\rho' \frac{\partial}{\partial z} \frac{K(k)}{\sqrt{(\rho + \rho')^2 + z^2}} \\ &= \frac{\mu_0 z}{\pi} \int_0^{\rho_c} \frac{\rho' M_z(\rho')d\rho'}{(\rho - \rho')^2 + z^2} \frac{E(k)}{\sqrt{(\rho + \rho')^2 + z^2}}, \end{aligned} \tag{C.15}$$

and $E(k)$ is an elliptical integral of the second kind [63]. The ρ component is calculated in the exact same way. From the symmetry of the system the φ of the magnetic field is zero, which is clear from Eq. (C.13), where the derivative with respect to φ for $b_\varphi(\vec{r})$ will give zero.

Appendix D

Eigenfunctions of quasiparticles in the magnetic field of a single vortex of a ferromagnetic disk.

Here the eigenfunctions of quasiparticles in the magnetic field of a single vortex of a ferromagnetic disk in Eq. (3.7) are derived. The Hamiltonian (3.6) does not commute with the z component of the spin, so spin is not a good quantum number; the eigenfunctions are a combination of spin up and spin down wavefunctions. We write

$$\phi(\rho,\varphi,z) = \begin{pmatrix} \phi_\uparrow(\rho,\varphi,z) \\ \phi_\downarrow(\rho,\varphi,z) \end{pmatrix}. \tag{D.1}$$

The Hamiltonian (3.6) is written as

$$\left\{ -\frac{\hbar^2}{2m^*_{e(h)}}\nabla^2_{e(h)} - \frac{1}{2}g^{e(h)}_{eff}\mu_B \begin{pmatrix} B_z & B_\rho\exp(-i\varphi) \\ B_\rho\exp(i\varphi) & -B_z \end{pmatrix} \right\} \phi(\rho,\varphi,z) = E\phi(\rho,\varphi,z), \tag{D.2}$$

where B_z and B_ρ are the transverse and radial components of the magnetic field, and the effects of the vector potential are ignored as negligible in comparison with those due to $\vec{B}$, which are amplified by the effective g factor in the DMS. Substituting Eq. (D.1) into (D.2) gives

$$-\frac{\hbar^2}{2m^*_{e(h)}} \begin{pmatrix} \nabla^2_{e(h)}\phi_\uparrow \\ \nabla^2_{e(h)}\phi_\downarrow \end{pmatrix} - \frac{1}{2}g^{e(h)}_{eff}\mu_B \begin{pmatrix} B_z\phi_\uparrow & B_\rho\exp(-i\varphi)\phi_\downarrow \\ B_\rho\exp(i\varphi)\phi_\uparrow & -B_z\phi_\downarrow \end{pmatrix} = E \begin{pmatrix} \phi_\uparrow \\ \phi_\downarrow \end{pmatrix}. \tag{D.3}$$

The upper and lower entries give two equations

$$\begin{aligned} E\phi_\uparrow(\rho,\varphi,z) &= -\frac{\hbar^2}{2m^*_{e(h)}}\nabla^2_{e(h)}\phi_\uparrow(\rho,\varphi,z) \\ &\quad -\frac{1}{2}g^{e(h)}_{eff}\mu_B\left(B_z\phi_\uparrow(\rho,\varphi,z) + B_\rho\exp(-i\varphi)\phi_\downarrow(\rho,\varphi,z)\right), \end{aligned} \tag{D.4}$$

and

$$E\phi_{\downarrow}(\rho,\varphi,z) = -\frac{\hbar^2}{2m^*_{e(h)}}\nabla^2_{e(h)}\phi_{\downarrow}(\rho,\varphi,z) - \frac{1}{2}g^{e(h)}_{eff}\mu_B\left(B_\rho\exp(i\varphi)\phi_{\uparrow}(\rho,\varphi,z) - B_z\phi_{\downarrow}(\rho,\varphi,z)\right). \quad \text{(D.5)}$$

Then expanding the wavefunctions as $\phi_{\uparrow(\downarrow)}(\rho,\varphi,z) = \sum_m \phi^m_{\uparrow(\downarrow)}(\rho,z)\exp(im\varphi)$ Eq. (D.4) and (D.5) become

$$E\sum_m \phi^m_{\uparrow}(\rho,z)\exp(im\varphi) = -\sum_m \frac{\hbar^2}{2m^*_{e(h)}}\left(\frac{1}{\rho}\frac{\partial}{\partial\rho}\left(\rho\frac{\partial}{\partial\rho}\right) - \frac{m^2}{\rho^2}\right)\phi^m_{\uparrow}(\rho,z)\exp(im\varphi) - \frac{1}{2}g^{e(h)}_{eff}\mu_B\sum_m\Big(B_z\phi^m_{\uparrow}(\rho,z)\exp(im\varphi) + B_\rho\phi^m_{\downarrow}(\rho,z)\exp(i(m-1)\varphi)\Big), \quad \text{(D.6)}$$

and

$$E\sum_m \phi^m_{\downarrow}(\rho,z)\exp(im\varphi) = -\sum_m \frac{\hbar^2}{2m^*_{e(h)}}\left(\frac{1}{\rho}\frac{\partial}{\partial\rho}\left(\rho\frac{\partial}{\partial\rho}\right) - \frac{m^2}{\rho^2}\right)\phi^m_{\downarrow}(\rho,z)\exp(im\varphi) - \frac{1}{2}g^{e(h)}_{eff}\mu_B\sum_m\Big(B_\rho\phi^m_{\uparrow}(\rho,z)\exp(i(m+1)\varphi) - B_z\phi^m_{\downarrow}(\rho,z)\exp(im\varphi)\Big). \quad \text{(D.7)}$$

Multiplying Eq. (D.6) by $\exp(-il\varphi)/2\pi$ and integrating by $d\varphi$ from 0 to 2π gives

$$E\phi^l_{\uparrow}(\rho,z) = -\frac{\hbar^2}{2m^*_{e(h)}}\left(\frac{1}{\rho}\frac{\partial}{\partial\rho}\left(\rho\frac{\partial}{\partial\rho}\right) - \frac{l^2}{\rho^2}\right)\phi^l_{\uparrow}(\rho,z) - \frac{1}{2}g^{e(h)}_{eff}\mu_B\left(B_z\phi^l_{\uparrow}(\rho,z) + B_\rho\phi^{l+1}_{\downarrow}(\rho,z)\right), \quad \text{(D.8)}$$

since the integral

$$\int_0^{2\pi}\exp(im\varphi)\exp(-il\varphi)d\varphi = 2\pi, \quad \text{(D.9)}$$

if $m = l$, and

$$\int_0^{2\pi}\exp(i(m-1)\varphi)\exp(-il\varphi)d\varphi = 2\pi, \quad \text{(D.10)}$$

if $l = m-1$. Then, multiplying Eq. (D.7) by $\exp(-i(l+1)\varphi)/2\pi$ and integrating by $d\varphi$ from 0 to 2π gives

$$E\phi^{l+1}_{\downarrow}(\rho,z) = -\frac{\hbar^2}{2m^*_{e(h)}}\left(\frac{1}{\rho}\frac{\partial}{\partial\rho}\left(\rho\frac{\partial}{\partial\rho}\right) - \frac{(l+1)^2}{\rho^2}\right)\phi^{l+1}_{\downarrow}(\rho,z) - \frac{1}{2}g^{e(h)}_{eff}\mu_B\left(B_\rho\phi^l_{\uparrow}(\rho,z) - B_z\phi^{l+1}_{\downarrow}(\rho,z)\right). \quad \text{(D.11)}$$

Multiplying Eq. (D.8) by $\exp(il\varphi)$ and Eq. (D.11) by $\exp(i(l+1)\varphi)$ gives

$$E\phi^l_{\uparrow}(\rho,z)\exp(il\varphi) = -\frac{\hbar^2}{2m^*_{e(h)}}\nabla^2_{e(h)}\phi^l_{\uparrow}(\rho,z)\exp(il\varphi) - \frac{1}{2}g^{e(h)}_{eff}\mu_B\left(B_z\phi^l_{\uparrow}(\rho,z) + B_\rho\phi^{l+1}_{\downarrow}(\rho,z)\right)\exp(il\varphi), \quad \text{(D.12)}$$

and

$$E\phi_{\downarrow}^{l+1}(\rho,z)\exp(i(l+1)\varphi) = -\frac{\hbar^2}{2m^*_{e(h)}}\nabla^2_{e(h)}\phi_{\downarrow}^{l+1}(\rho,z)\exp(i(l+1)\varphi) - \frac{1}{2}g^{e(h)}_{eff}\mu_B\left(B_\rho\phi_{\uparrow}^{l}(\rho,z) - B_z\phi_{\downarrow}^{l+1}(\rho,z)\right)\exp(i(l+1)\varphi). \tag{D.13}$$

Eq. (D.12) and (D.13) can be combined together as

$$\left[-\frac{\hbar^2}{2m^*_{e(h)}}\nabla^2_{e(h)} - \frac{1}{2}g^{e(h)}_{eff}\mu_B\begin{pmatrix} B_z & B_\rho\exp(-i\varphi) \\ B_\rho\exp(i\varphi) & -B_z \end{pmatrix}\right]\exp(il\varphi)\begin{pmatrix} \phi_{\uparrow}^{l}(\rho,z) \\ \phi_{\downarrow}^{l+1}(\rho,z)\exp(i\varphi) \end{pmatrix}$$

$$= E\exp(il\varphi)\begin{pmatrix} \phi_{\uparrow}^{l}(\rho,z) \\ \phi_{\downarrow}^{l+1}(\rho,z)\exp(i\varphi) \end{pmatrix}. \tag{D.14}$$

Therefore $\phi_{\uparrow}^{l}(\rho,z)\exp(il\varphi)$ is only coupled to $\phi_{\downarrow}^{l+1}(\rho,z)\exp(i(l+1)\varphi)$, so the general form is written as

$$\phi_m(\rho,\varphi,z) = \exp(im\varphi)\begin{pmatrix} \phi_{\uparrow}^{m}(\rho,z) \\ \phi_{\downarrow}^{m+1}(\rho,z)\exp(i\varphi) \end{pmatrix}. \tag{D.15}$$

Appendix E

Spin operators

The spin operators are written as [119]

$$S_z = \begin{pmatrix} \frac{1}{2} & 0 & 0 & 0 & 0 & 0 & 0 & 0 \\ 0 & -\frac{1}{2} & 0 & 0 & 0 & 0 & 0 & 0 \\ 0 & 0 & \frac{1}{2} & 0 & 0 & 0 & 0 & 0 \\ 0 & 0 & 0 & \frac{1}{6} & 0 & 0 & \frac{\sqrt{2}}{3} & 0 \\ 0 & 0 & 0 & 0 & -\frac{1}{6} & 0 & 0 & \frac{\sqrt{2}}{3} \\ 0 & 0 & 0 & 0 & 0 & -\frac{1}{2} & 0 & 0 \\ 0 & 0 & 0 & \frac{\sqrt{2}}{3} & 0 & 0 & -\frac{1}{6} & 0 \\ 0 & 0 & 0 & 0 & \frac{\sqrt{2}}{3} & 0 & 0 & \frac{1}{6} \end{pmatrix}, \tag{E.1}$$

$$S_x = \begin{pmatrix} 0 & \frac{1}{2} & 0 & 0 & 0 & 0 & 0 & 0 \\ \frac{1}{2} & 0 & 0 & 0 & 0 & 0 & 0 & 0 \\ 0 & 0 & 0 & 0 & \frac{1}{2\sqrt{3}} & 0 & \frac{1}{\sqrt{6}} & 0 \\ 0 & 0 & 0 & 0 & \frac{1}{3} & \frac{1}{2\sqrt{3}} & -\frac{1}{3\sqrt{2}} & 0 \\ 0 & 0 & \frac{1}{2\sqrt{3}} & \frac{1}{3} & 0 & 0 & 0 & \frac{1}{3\sqrt{2}} \\ 0 & 0 & 0 & \frac{1}{2\sqrt{3}} & 0 & 0 & 0 & -\frac{1}{\sqrt{6}} \\ 0 & 0 & \frac{1}{\sqrt{6}} & -\frac{1}{3\sqrt{2}} & 0 & 0 & 0 & -\frac{1}{6} \\ 0 & 0 & 0 & 0 & \frac{1}{3\sqrt{2}} & -\frac{1}{\sqrt{6}} & -\frac{1}{6} & 0 \end{pmatrix}, \tag{E.2}$$

and

$$S_y = \begin{pmatrix} 0 & \frac{-1}{2} & 0 & 0 & 0 & 0 & 0 & 0 \\ \frac{1}{2} & 0 & 0 & 0 & 0 & 0 & 0 & 0 \\ 0 & 0 & 0 & 0 & -\frac{1}{2\sqrt{3}} & 0 & -\frac{1}{\sqrt{6}} & 0 \\ 0 & 0 & 0 & 0 & \frac{1}{3} & -\frac{1}{2\sqrt{3}} & -\frac{1}{3\sqrt{2}} & 0 \\ 0 & 0 & \frac{1}{2\sqrt{3}} & -\frac{1}{3} & 0 & 0 & 0 & -\frac{1}{3\sqrt{2}} \\ 0 & 0 & 0 & \frac{1}{2\sqrt{3}} & 0 & 0 & 0 & -\frac{1}{\sqrt{6}} \\ 0 & 0 & \frac{1}{\sqrt{6}} & \frac{1}{3\sqrt{2}} & 0 & 0 & 0 & \frac{1}{6} \\ 0 & 0 & 0 & 0 & \frac{1}{3\sqrt{2}} & \frac{1}{\sqrt{6}} & -\frac{1}{6} & 0 \end{pmatrix}. \tag{E.3}$$

Appendix F

Eigenvalues for the 4 × 4 effective Hamiltonian

The 4×4 effective Hamiltonian given in Eq. (3.45) for a magnetic field $\vec{B} = B\vec{e}_x$ has the characteristic equation

$$E^4 + 2\Delta_{lh}E^3 + E^2\Delta_{lh}^2 - 6c^2E\Delta_{lh} + 9c^4 - 10E^2c^2,$$

where $c = \frac{1}{2\sqrt{3}} g^h_{eff}\mu_B B_x$. With corresponding eigenvalues

$$\begin{aligned} E &= \frac{1}{2}\sqrt{\Delta_{lh}^2 \pm 4\Delta_{lh}c + 16c^2} = \frac{1}{6}\sqrt{\frac{36}{4}\left(\Delta_{lh}^2 \pm \frac{4\Delta_{lh}}{6} g^h_{eff}\mu_B B_x + \frac{16}{6^2}(g^h_{eff}\mu_B B_x)^2\right)} \\ &= \frac{1}{6}\sqrt{9\Delta_{lh}^2 \pm 6\Delta_{lh} g^h_{eff}\mu_B B_x + 4(g^h_{eff}\mu_B B_x)^2}. \end{aligned} \tag{F.1}$$

The eigenvalues can be simplified by applying a Taylor Expansion

$$\begin{aligned} E &\approx -\frac{\Delta_{lh}}{2} - \frac{g^h_{eff}\mu_B B_x}{6} + \frac{1}{6}\Delta_{lh}\left(9 \pm 6\frac{g^h_{eff}\mu_B B_x}{\Delta_{lh}} + \frac{4(g^h_{eff}\mu_B B_x)^2}{\Delta_{lh}}\right)^{\frac{1}{2}} \\ &= -\frac{\Delta_{lh}}{2} - \frac{g^h_{eff}\mu_B B_x}{6} + \frac{1}{2}\left(1 \pm \frac{2g^h_{eff}\mu_B B_x}{3\Delta_{lh}} + \frac{4(g^h_{eff}\mu_B B_x)^2}{9}{\Delta_{lh}}^2\right)^{\frac{1}{2}} \\ &= -\frac{\Delta_{lh}}{2} - \frac{g^h_{eff}\mu_B B_x}{6} + \frac{1}{2}\left(1 \pm \frac{g^h_{eff}\mu_B B_x}{3\Delta_{lh}} + \frac{2(g^h_{eff}\mu_B B_x)^2}{9{\Delta_{lh}}^2} - \frac{1}{8}\frac{4}{9}\frac{(g^h_{eff}\mu_B B_x)^2}{\Delta_{lh}^2}\right). \end{aligned} \tag{F.2}$$

Then the heavy hole and light hole eigenvalues are written as

$$E^{\mp}_{hh} = -\frac{\Delta_{lh}}{2} \mp -\frac{g^h_{eff}\mu_B B_x}{6} + \frac{1}{6}\sqrt{9\Delta_{lh}^2 \pm 6\Delta_{lh} g^h_{eff}\mu_B B_x + 4(g^h_{eff}\mu_B B_x)^2}, \tag{F.3}$$

$$E^{\mp}_{lh} = -\frac{\Delta_{lh}}{2} \mp -\frac{g^h_{eff}\mu_B B_x}{6} - \frac{1}{6}\sqrt{9\Delta_{lh}^2 \pm 6\Delta_{lh} g^h_{eff}\mu_B B_x + 4(g^h_{eff}\mu_B B_x)^2}. \tag{F.4}$$

Appendix G

Derivation of the 2D Hamiltonian consisting of an electron in the conduction band and a hole in the valence band interacting via the Coulomb interaction

This section outlines the derivation of the 2D Hamiltonian consisting of an electron in the conduction band and a hole in the valence band interacting via the Coulomb interaction given in Eq. (5.11) by separating the coordinates into centre of mass and relative coordinates, and applying the wavefunction transformation and adiabatic expansion. Starting with Eq. (5.2) which can be written as

$$\begin{aligned}\mathcal{H}^{2D}(\vec{R},\vec{r}) &= \frac{\hbar^2}{2m^*_{e,||}}\left\{-i\frac{m^*_{e,||}}{M}\nabla_R - i\nabla_r + \frac{e}{\hbar c}\vec{A}\left(\vec{R}+\frac{m^*_{h,||}}{M}\vec{r}\right)\right\}^2 \\ &\quad + \frac{\hbar^2}{2m^*_{h,||}}\left\{-i\frac{m^*_{h,||}}{M}\nabla_R + i\nabla_r - \frac{e}{\hbar c}\vec{A}\left(\vec{R}-\frac{m^*_{e,||}}{M}\vec{r}\right)\right\}^2 - \frac{\gamma e^2}{4\pi\varepsilon_0\varepsilon_r r},\end{aligned} \tag{G.1}$$

by separating the coordinates into the centre of mass and the relative motion coordinates by using

$$\nabla_e = \frac{m^*_{e,||}}{M}\nabla_R + \nabla_r, \qquad \nabla_h = \frac{m^*_{h,||}}{M}\nabla_R - \nabla_r, \tag{G.2}$$

and

$$\vec{A}(\vec{r}_e) = \vec{A}\left(\vec{R}+\frac{m^*_{h,||}}{M}\vec{r}\right), \qquad \vec{A}(\vec{r}_h) = \vec{A}\left(\vec{R}-\frac{m^*_{e,||}}{M}\vec{r}\right). \tag{G.3}$$

Applying the wavefunction given in Eq. (5.4)

$$\Psi(\vec{R},\vec{r}) \rightarrow \exp\left\{-i(e/\hbar c)\vec{r}\cdot\vec{A}(\vec{R})\right\}\tilde{\Psi}(\vec{R},\vec{r}), \tag{G.4}$$

gives

$$\nabla_R \Psi(\vec{R},\vec{r}) = \exp\left\{-i(e/\hbar c)\vec{r}\cdot\vec{A}(\vec{R})\right\}\left(\nabla_R - i\nabla_R\left(\frac{e}{\hbar c}\vec{r}\cdot\vec{A}(\vec{R})\right)\right)\tilde{\Psi}(\vec{R},\vec{r}), \tag{G.5}$$

and

$$\nabla_r \Psi(\vec{R},\vec{r}) = \exp\left\{-i(e/\hbar c)\vec{r}\cdot\vec{A}(\vec{R})\right\}\left(\nabla_r - i\frac{e}{\hbar c}\vec{A}(\vec{R})\right)\tilde{\Psi}(\vec{R},\vec{r}). \tag{G.6}$$

Then Eq. (G.1) becomes

$$\begin{aligned}
\widetilde{\mathcal{H}}^{2D}(\vec{R},\vec{r}) \;=\; & \frac{\hbar^2}{2m^*_{e,||}}\left\{-i\frac{m^*_{e,||}}{M}\nabla_R - i\nabla_r + \frac{e}{\hbar c}\vec{A}\left(\vec{R}+\frac{m^*_{h,||}}{M}\vec{r}\right)\right. \\
& \left. -\frac{em^*_{e,||}}{\hbar cM}\nabla_R\{\vec{r}\cdot\vec{A}(\vec{R})\} - \frac{e}{\hbar c}\vec{A}(\vec{R})\right\}^2 \\
& + \frac{\hbar^2}{2m^*_{h,||}}\left\{-i\frac{m^*_{h,||}}{M}\nabla_R + i\nabla_r - \frac{e}{\hbar c}\vec{A}\left(\vec{R}-\frac{m^*_{e,||}}{M}\vec{r}\right)\right. \\
& \left. -\frac{em^*_{h,||}}{\hbar cM}\nabla_R\{\vec{r}\cdot\vec{A}(\vec{R})\} + \frac{e}{\hbar c}\vec{A}(\vec{R})\right\}^2 \\
& - \frac{\gamma e^2}{4\pi\varepsilon_0\varepsilon_r r}.
\end{aligned} \tag{G.7}$$

By applying the adiabatic expansion in Eq. (5.6), and expanding out and combining terms together Eq. (G.7) becomes

$$\begin{aligned}
\frac{2M}{\hbar^2}\widetilde{\mathcal{H}}^{2D}(\vec{R},\vec{r}) \;=\; & \left[-i\nabla_R - \frac{e}{\hbar c}\nabla_R\left(\vec{r}\cdot\vec{A}(\vec{R})\right)\right]^2 + \frac{M}{\mu}\left[-i\nabla_r + \frac{e}{\hbar c}\xi(\vec{r}\cdot\nabla_R)\vec{A}(\vec{R})\right]^2 \\
& + \left[-i\nabla_R - \frac{e}{\hbar c}\nabla_R(\vec{r}\cdot\vec{A}(\vec{R}))\right]\frac{e}{\hbar c}(\vec{r}\cdot\nabla_R)\vec{A}(\vec{R}) \\
& + \frac{e}{\hbar c}(\vec{r}\cdot\nabla_R)\vec{A}(\vec{R})\left[-i\nabla_R - \frac{e}{\hbar c}\nabla_R(\vec{r}\cdot\vec{A}(\vec{R}))\right] \\
& + \frac{e^2}{\hbar^2 c^2}(\vec{r}\cdot\nabla_R)\vec{A}(\vec{R})\cdot(\vec{r}\cdot\nabla_R)\vec{A}(\vec{R}) \\
& - \frac{2M}{\hbar^2}\frac{\gamma e^2}{4\pi\varepsilon_0\varepsilon_r r}.
\end{aligned} \tag{G.8}$$

This can be simplified with the use of

$$\nabla_R(\vec{r}\cdot\vec{A}(\vec{R})) = \hat{\imath}\left(x\frac{\partial A_X}{\partial X} + y\frac{\partial A_Y}{\partial X}\right) + \hat{\jmath}\left(x\frac{\partial A_X}{\partial Y} + y\frac{\partial A_Y}{\partial Y}\right), \tag{G.9}$$

$$(\vec{r}\cdot\nabla_R)\vec{A}(\vec{R}) = \hat{\imath}\left(x\frac{\partial A_X}{\partial X} + y\frac{\partial A_X}{\partial Y}\right) + \hat{\jmath}\left(x\frac{\partial A_Y}{\partial X} + y\frac{\partial A_Y}{\partial Y}\right), \tag{G.10}$$

and

$$(\vec{r}\cdot\nabla_R)\vec{A}(\vec{R}) = \nabla_R(\vec{r}\cdot\vec{A}(\vec{R})) - \vec{\Xi}. \tag{G.11}$$

Then Eq. (G.8) is rewritten as

$$\frac{2M}{\hbar^2}\widetilde{\mathcal{H}}^{2D}(\vec{R},\vec{r}) = \frac{M}{\mu}\left[-i\nabla_r + \frac{e}{\hbar c}\xi(\vec{r}\cdot\nabla_R)\vec{A}(\vec{R})\right]^2 + \left[i\nabla_R + \frac{e}{\hbar c}\vec{\Xi}\right]^2 - \frac{2M}{\hbar^2}\frac{\gamma e^2}{4\pi\varepsilon_0\varepsilon_r r}. \tag{G.12}$$

With

$$\vec{B}(\vec{R}) = \nabla_R \times \vec{A}(\vec{R}) = \left(\frac{\partial A_Y}{\partial X} - \frac{\partial A_X}{\partial Y}\right)\hat{k}, \tag{G.13}$$

and

$$\vec{r}\times\vec{B}(\vec{R}) = (\hat{i}y - \hat{j}x)B_Z = \vec{\Xi}, \tag{G.14}$$

Eq. (G.12) is rewritten and Eq. (5.7) is obtained

$$\begin{aligned}\widetilde{\mathcal{H}}^{2D}(\vec{R},\vec{r}) &= \frac{\hbar^2}{2\mu}\left(-i\nabla_r + \xi\frac{e}{\hbar c}\left\{(\vec{r}\cdot\nabla_R)\vec{A}(\vec{R})\right\}\right)^2 + \frac{\hbar^2}{2M}\left(i\nabla_R + \frac{e}{\hbar c}\left[\vec{r}\times\vec{B}(\vec{R})\right]\right)^2 \\ &\quad -\frac{\gamma e^2}{4\pi\varepsilon_0\varepsilon_r r}.\end{aligned} \tag{G.15}$$

By applying the gauge $(\vec{r}\cdot\nabla_R)\vec{A}(\vec{R}) = \vec{B}(\vec{R})\times\vec{r}/2 + \nabla_r\left[(\vec{r}\cdot\nabla_R)\left\{\vec{r}\cdot\vec{A}(\vec{R})\right\}\right]/2$, the Hamiltonian is rewritten as

$$\begin{aligned}\widetilde{\mathcal{H}}^{2D}(\vec{R},\vec{r}) &= \frac{\hbar^2}{2\mu}\left(-i\nabla_r + \xi\frac{e}{2\hbar c}\left\{\vec{B}(\vec{R})\times\vec{r}\right\} + \xi\frac{e}{2\hbar c}\nabla_r\left[(\vec{r}\cdot\nabla_R)\left\{\vec{r}\cdot\vec{A}(\vec{R})\right\}\right]\right)^2 \\ &\quad + \frac{\hbar^2}{2M}\left(i\nabla_R + \frac{e}{\hbar c}[\vec{r}\times\vec{B}(\vec{R})]\right)^2 - \frac{\gamma e^2}{4\pi\varepsilon_0\varepsilon_r r}.\end{aligned} \tag{G.16}$$

Applying a further wavefunction transformation in Eq. (5.9)

$$\Psi(\vec{R},\vec{r}) \to \exp\{-i\xi(e/\hbar c)\Omega(r)\}\tilde{\Psi}(\vec{R},\vec{r}), \tag{G.17}$$

where $\Omega(r) = (\vec{r}\cdot\nabla_R)\left\{\vec{r}\cdot\vec{A}(\vec{R})\right\}/2$, gives

$$\nabla_R\Psi(\vec{R},\vec{r}) = \exp\{-i\xi(e/\hbar c)\Omega(r)\}\left(\nabla_R - i\xi\nabla_R\left(\frac{e}{\hbar c}\Omega(r)\right)\right)\tilde{\Psi}(\vec{R},\vec{r}), \tag{G.18}$$

and

$$\nabla_r\Psi(\vec{R},\vec{r}) = \exp\{-i\xi(e/\hbar c)\Omega(r)\}\left(\nabla_r - i\xi\nabla_r\left(\frac{e}{\hbar c}\Omega(r)\right)\right)\tilde{\Psi}(\vec{R},\vec{r}). \tag{G.19}$$

Then Eq. (G.15) becomes Eq. (5.10)

$$\begin{aligned}\widetilde{\mathcal{H}}^{2D}(\vec{R},\vec{r}) &= \frac{\hbar^2}{2\mu}\left(-i\nabla_r + \xi\frac{e}{2\hbar c}[\vec{B}(\vec{R})\times\vec{r}]\right)^2 \\ &\quad + \frac{\hbar^2}{2M}\left(i\nabla_R - \xi\frac{e}{2\hbar c}\nabla_R\left\{(\vec{r}\cdot\nabla_R)\left\{\vec{r}\cdot\vec{A}(\vec{R})\right\}\right\}\right. \\ &\quad \left. + \frac{e}{\hbar c}[\vec{r}\times\vec{B}(\vec{R})]\right)^2 - \frac{\gamma e^2}{4\pi\varepsilon_0\varepsilon_r r}.\end{aligned} \tag{G.20}$$

Expanding this out and combining terms together, while ignoring terms of order r^3 or higher gives Eq. (5.11)

$$\widetilde{\mathcal{H}}^{2D}(\vec{R},\vec{r}) = -\frac{\hbar^2}{2\mu}\nabla_r^2 - \frac{\gamma e^2}{4\pi\varepsilon_0\varepsilon_r r} + W_1 + W_2 - \frac{\hbar^2}{2M}\nabla_R^2. \tag{G.21}$$

Appendix H

Derivation of the perturbation corrections to the eigenvalues of the relative motion Hamiltonian

Here the outline of the derivation of the perturbation corrections to the eigenvalues of the relative motion Hamiltonian used in Chapter 5 is discussed. Firstly

$$\begin{aligned} E_1(n_r, m_r) &= \langle \Phi_0^{n_r,m_r} |W_1| \Phi_0^{n_r,m_r} \rangle \\ &= \left\langle \Phi_0^{n_r,m_r} \left| \frac{e}{2c\mu} \xi \vec{B}(\vec{R}) \cdot \vec{L} + \frac{ie\hbar}{2Mc} \left\{ \vec{B}(\vec{R}) \times \nabla_R - \nabla_R \times \vec{B}(\vec{R}) \right\} \cdot \vec{r} \right| \Phi_0^{n_r,m_r} \right\rangle . \end{aligned} \tag{H.1}$$

The second term has the form

$$\vec{T}_R(\vec{R}) \cdot \langle \Phi_0^{n_r,m_r} \mid \vec{r} \mid \Phi_0^{n_r,m_r} \rangle , \tag{H.2}$$

where the operator $\vec{T}_R(\vec{R})$ is independent of $\vec{r}$. Since $\vec{r}$ is odd under inversion and $|\Phi_0^{n_r,m_r}(\vec{r})|^2$ even, this vanishes so that

$$\begin{aligned} E_1(n_r, m_r) &= \left\langle \Phi_0^{n_r,m_r} \left| \frac{e}{2c\mu} \xi \vec{B}(\vec{R}) \cdot \vec{L} \right| \Phi_0^{n_r,m_r} \right\rangle \\ &= \frac{e\hbar}{2\mu c} \xi B_z(\vec{R}) m, \end{aligned} \tag{H.3}$$

recalling that $\Phi_0^{n_r,m_r}(\vec{r})$ is the inplane hydrogenic wavefunction.

The second order correction is

$$E_2(n_r, m_r) = \langle \Phi_0^{n_r,m_r} |W_2| \Phi_0^{n_r,m_r} \rangle = \frac{e^2}{8\mu c^2} \vec{B}(\vec{R})^2 \left\langle \Phi_0^{n_r,m_r} | r^2 | \Phi_0^{n_r,m_r} \right\rangle . \tag{H.4}$$

Using Eq. (2.19) in Ref [88] this gives

$$\begin{aligned} E_2(n_r, m_r) &= \left(\frac{e^2}{8\mu^2 c^2} \right) \left(\frac{a_B^*}{\gamma} \right)^2 \frac{1}{8} (2n-1)[n(10n^2 - 15n + 11) - 3|m|^2(2n-1) - 3] \\ &= \frac{e^2 a_B^{*2}}{8\mu c^2 \gamma^2} \vec{B}(\vec{R})^2 \beta_{m_r}^{n_r}, \end{aligned} \tag{H.5}$$

where

$$\beta_{m_r}^{n_r} = \begin{cases} \frac{3}{8} & \text{for } n = 1 \text{ and } m = 0, \\ \frac{117}{8} & \text{for } n = 2 \text{ and } m = 0, \\ \frac{45}{4} & \text{for } n = 2 \text{ and } |m| = 1. \end{cases} \tag{H.6}$$

Appendix I

Magnetic field created by a microscale ferromagnetic disk

Here the derivation of the vector potential given in Eq. (5.66) and the magnetic field in Eq. (5.68) for a microscale ferromagnetic disk is summarized. Starting with the magnetisation

$$\vec{M}(\vec{R}) = h\mathcal{M}\delta(Z-d)\Theta(a-R)\vec{e}_z, \tag{I.1}$$

the corresponding vector potential is calculated from the differential form of Amperes law $\vec{\nabla}_R^2\vec{A}(\vec{R}) = -4\pi\vec{\nabla}_R \times \vec{M}(\vec{R})$:

$$\vec{A}(\vec{R}) = \int \frac{\vec{\nabla}_R \times \vec{M}(\vec{R}')}{|\vec{R}-\vec{R}'|} d\vec{R}', \tag{I.2}$$

where

$$\begin{aligned} \vec{\nabla}_R \times \vec{M}(\vec{R}) &= -\frac{\partial M_z}{\partial R}\vec{e}_\varphi = h\mathcal{M}\delta(Z-d)\delta(a-R)\vec{e}_\varphi, \\ &= \frac{h\mathcal{M}}{a}\delta(\cos\theta)\delta(\rho-a)\vec{e}_\varphi. \end{aligned} \tag{I.3}$$

Switching to spherical coordinates (ρ, θ, φ), the φ component of the vector potential is

$$\begin{aligned} A_\varphi(\rho,\theta) &= \frac{h\mathcal{M}}{a}\int \frac{\rho'^2 d\rho' d\varphi' d\theta' \sin\theta' \cos\varphi' \delta(\cos\theta')\delta(\rho'-a)}{[\rho^2+\rho'^2-2\rho\rho'(\cos\theta\cos\theta'+\sin\theta\sin\theta'\cos\varphi')]^{1/2}} \\ &= h\mathcal{M}a\int_0^{2\pi} \frac{\cos\varphi' d\varphi'}{[a^2+\rho^2-2a\rho\sin\theta\cos\varphi']^{1/2}} \\ &= \frac{4h\mathcal{M}a}{[\rho^2+a^2+2a\rho\sin\theta]^{1/2}}\left[\frac{(2-k^2)K(k)-2E(k)}{k^2}\right], \end{aligned} \tag{I.4}$$

in terms of complete elliptic integrals $K(k)$ and $E(k)$ [62], and

$$k = \sqrt{\frac{4a\rho\sin\theta}{a^2+\rho^2+2a\rho\sin\theta}}. \tag{I.5}$$

Reverting to cylindrical coordinates gives

$$A_\varphi(R) = 4h\mathcal{M}\sqrt{\frac{a}{R}}\frac{1}{k}\left[\left(1-\frac{k^2}{2}\right)K(k)-E(k)\right], \tag{I.6}$$

where

$$k = \sqrt{\frac{4aR}{(a+R)^2 + d^2}}. \tag{I.7}$$

The corresponding magnetic field is then given by

$$\vec{B}(\vec{R}) = \vec{\nabla} \times \vec{A}(\vec{R}) = \frac{1}{R}\frac{\partial}{\partial R}(RA_\varphi)\vec{e}_Z - \frac{1}{R}\frac{\partial}{\partial Z}(RA_\varphi)\vec{e}_R. \tag{I.8}$$

Since the radial component of the magnetic field does not trap the exciton within the DMS quantum well, only the z component of the magnetic field is calculated which is given by the first term. For the z component start with

$$RA_\varphi = 2h\mathcal{M}\sqrt{(a+R)^2 + d^2}\left[\left(1 - \frac{k^2}{2}\right)K(k) - E(k)\right], \tag{I.9}$$

which when differentiated gives

$$\begin{aligned}\frac{\partial}{\partial R}(RA_\varphi) &= RA_\varphi \frac{(a+R)}{(a+R)^2 + d^2} \\ &\quad + 2h\mathcal{M}\frac{\sqrt{4aR}}{k}\frac{k^4}{4aR^2}(a^2 - R^2 + d^2)\left\{\left(1 - \frac{k^2}{2}\right)\frac{\partial K(k)}{\partial k^2} - \frac{K(k)}{2} - \frac{\partial E(k)}{\partial k^2}\right\}.\end{aligned} \tag{I.10}$$

Then the z component of the magnetic field is given by

$$\begin{aligned}B_z(R) &= \frac{a+R}{(a+R)^2 + d^2}A_\varphi \\ &\quad + \frac{h\mathcal{M}}{R^2\sqrt{aR}}(a^2 - R^2 + d^2)k^3\left\{\left(1 - \frac{k^2}{2}\right)\frac{\partial K(k)}{\partial k^2} - \frac{K(k)}{2} - \frac{\partial E(k)}{\partial k^2}\right\} \\ &= 2B_0^D \frac{(a+R)}{R\sqrt{(a+R)^2 + d^2}}\left\{-E(k) + \left(1 - \frac{k^2}{2}\right)K(k)\right\} \\ &\quad + B_0^D \frac{(a^2 - R^2 + d^2)}{R^2\sqrt{aR}}k^3\left\{-\frac{\partial}{\partial k^2}E(k) - \frac{1}{2}K(k) + \left(1 - \frac{k^2}{2}\right)\frac{\partial}{\partial k^2}K(k)\right\}.\end{aligned} \tag{I.11}$$

Appendix J

Wavefunctions for the heavy and light hole excitons in the presence of a microscale ferromagnetic disk

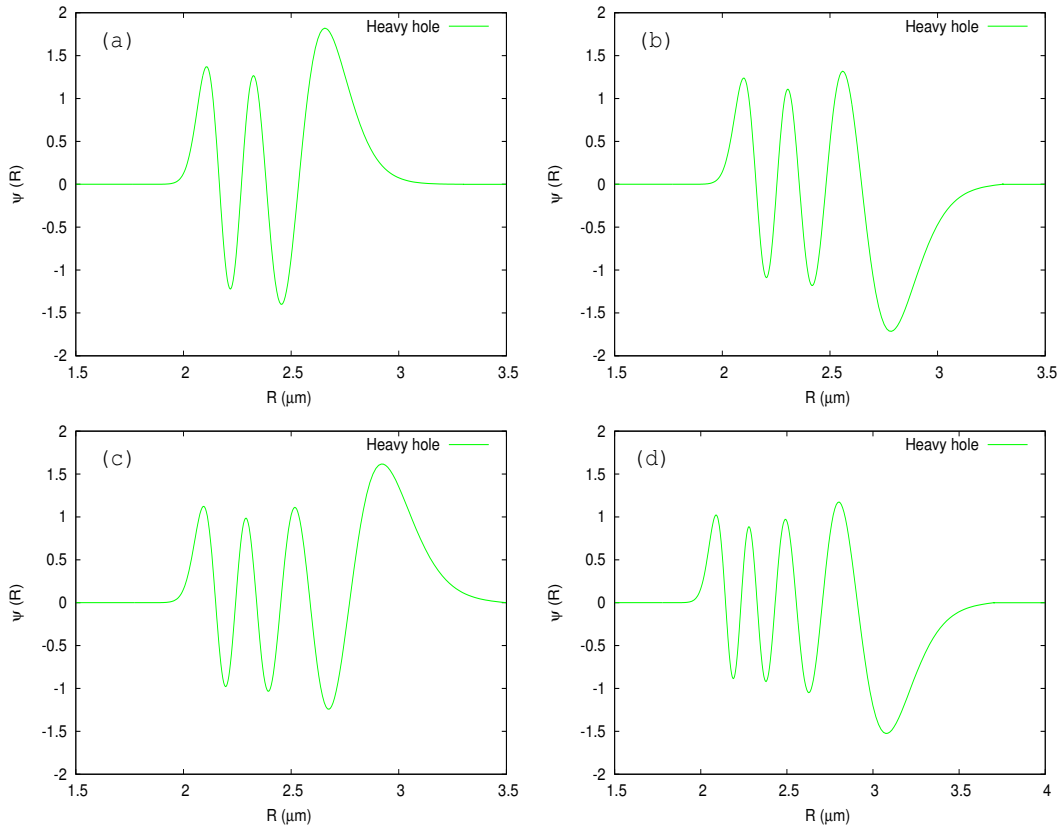

Figure J-1: Fourth, (b) Fifth, (c) Sixth, and (d) Seventh excited state exciton centre of mass radial wavefunction ψ(R) as a function of the radial coordinate R for a heavy hole exciton. Calculated with $B_a = 0.35$ T, $B_0^D = 0.1$ μmT, $a = 2$ μm, $d = 0.2$ μm, $S_{e,z} = \frac{1}{2}$, $S_{h,z} = \frac{3}{2}$, $x = 0.01$, $T = 20$ K, $L = 50$ Å, $n_r = 1$, $m_r = 0$ and $m_R = 0$. The values used for $Cd_{1-x}Mn_xTe$ are given in the Table in Appendix K.

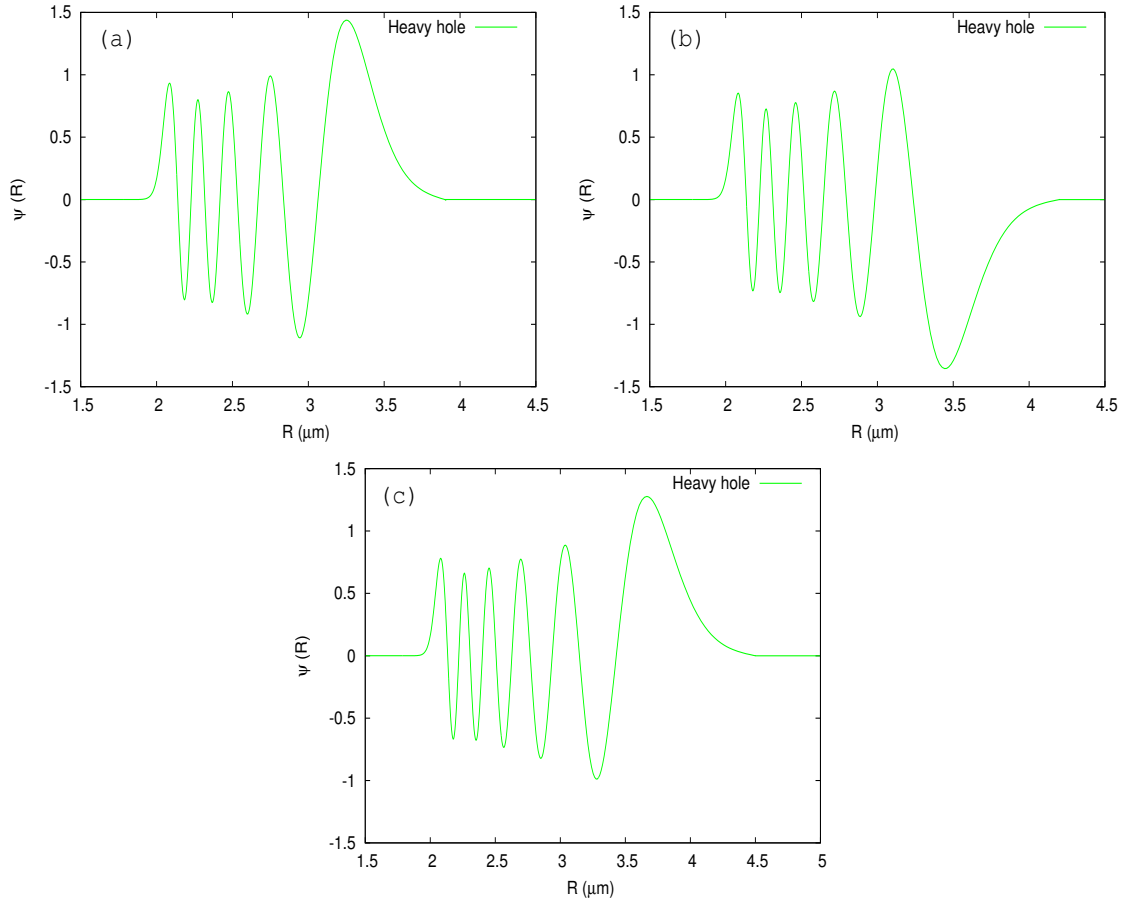

Figure J-2: Eighth, (b) Ninth, and (c) Tenth excited state exciton centre of mass radial wavefunction ψ(R) as a function of the radial coordinate R for a heavy hole exciton. Calculated with $B_a = 0.35$ T, $B_0^D = 0.1$ μmT, $a = 2$ μm, $d = 0.2$ μm, $S_{e,z} = \frac{1}{2}$, $S_{h,z} = \frac{3}{2}$, $x = 0.01$, $T = 20$ K, $L = 50$ Å, $n_r = 1$, $m_r = 0$ and $m_R = 0$. The values used for $Cd_{1-x}Mn_xTe$ are given in the Table in Appendix K.

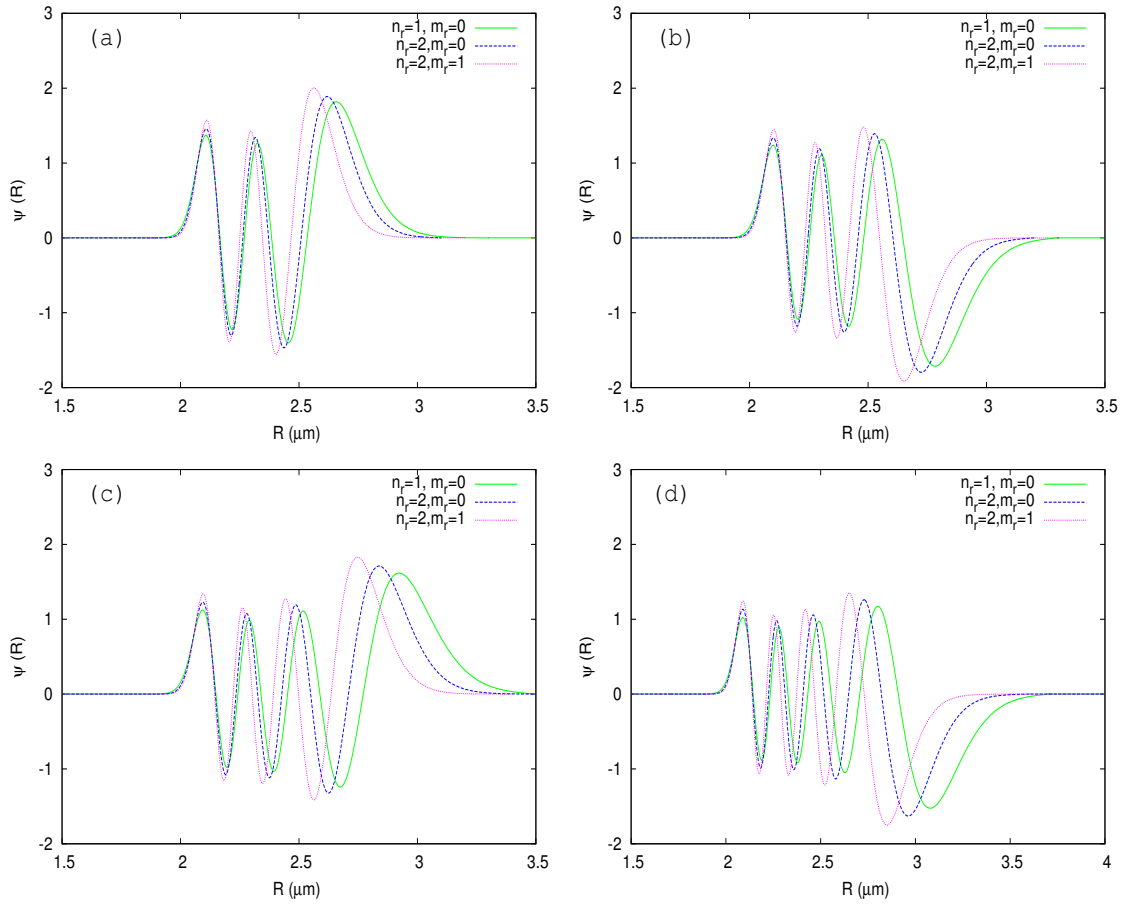

Figure J-3: Fourth, (b) Fifth, (c) Sixth, and (d) Seventh excited state exciton centre of mass radial wavefunction ψ(R) as a function of the radial coordinate R for a heavy hole exciton for different values of n_r and m_r. Calculated with $B_a = 0.35$ T, $B_0^D = 0.1$ μmT, $a = 2$ μm, $d = 0.2$ μm, $S_{e,z} = \frac{1}{2}$, $S_{h,z} = \frac{3}{2}$, $x = 0.01$, $T = 20$ K, $L = 50$ Å, $n_r = 1$, $m_r = 0$ and $m_R = 0$. The values used for $Cd_{1-x}Mn_xTe$ are given in the Table in Appendix K.

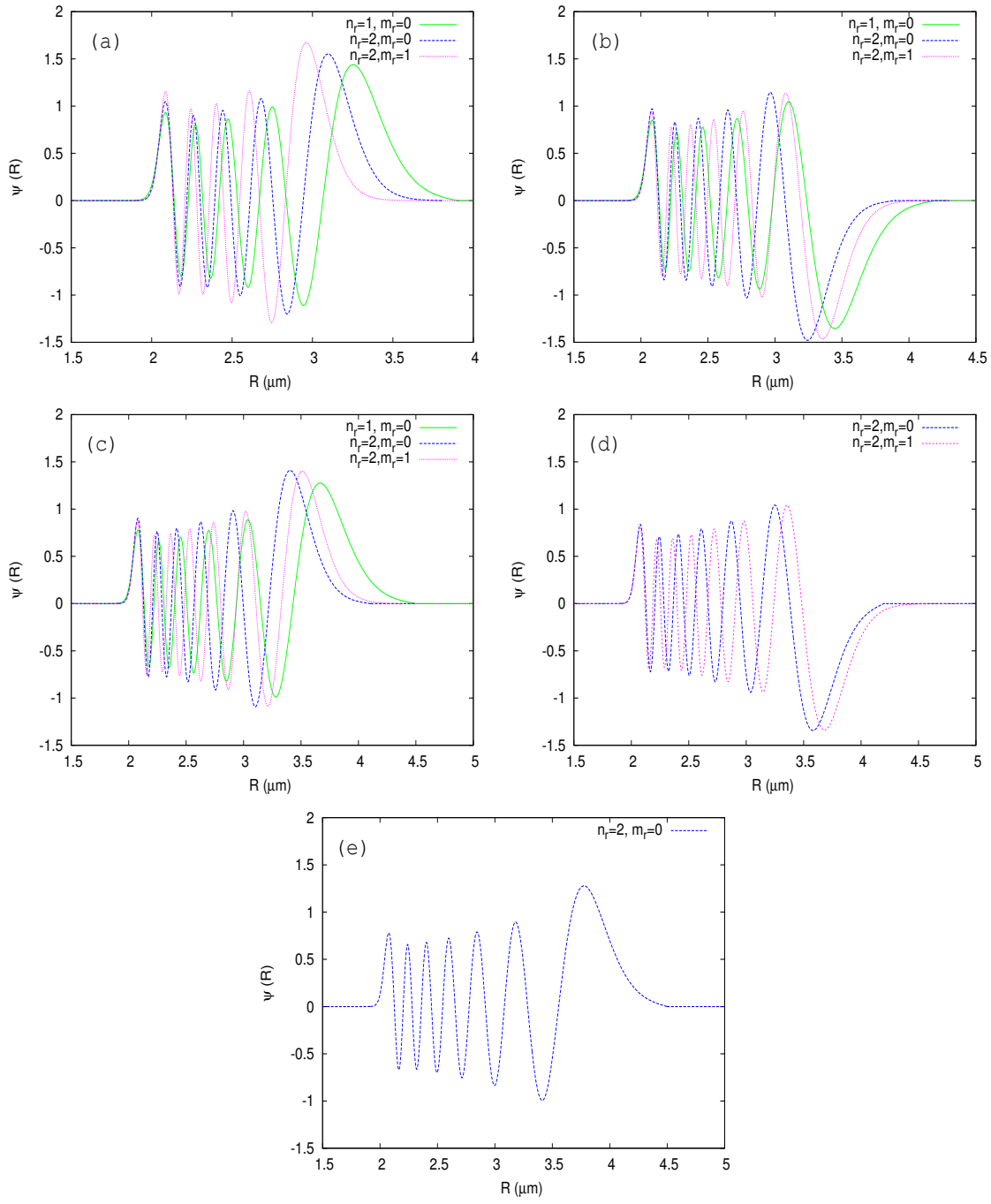

Figure J-4: Eighth, (b) Ninth, (c) Tenth, (d) Eleventh, and (e) Twelfth excited state exciton centre of mass radial wavefunction ψ(R) as a function of the radial coordinate R for a heavy hole exciton for different values of n_r and m_r. Calculated with $B_a = 0.35$ T, $B_0^D = 0.1$ μmT, $a = 2$ μm, $d = 0.2$ μm, $S_{e,z} = \frac{1}{2}$, $S_{h,z} = \frac{3}{2}$, $x = 0.01$, $T = 20$ K, $L = 50$ Å, $n_r = 1$, $m_r = 0$ and $m_R = 0$. The values used for $Cd_{1-x}Mn_xTe$ are given in the Table in Appendix K.

Appendix K

Values used for calculations

	$Cd_{1-x}Mn_xTe$
E_g(eV)	Eq. (1.1)
Δ_{so}(eV)	0.910 [120]
γ_1	4.14 [49]
γ_2	1.09 [49]
γ_3	1.62 [49]
ε_r	9.3 [121]
m_e^*	0.096 m_0 [120][73]
b(eV)	-0.80 [122]
$C_{11}(10^{11}\text{dyn/cm}^2)$	5.60 [122]
$C_{12}(10^{11}\text{dyn/cm}^2)$	3.87 [122]
$N_0\alpha$	0.22 eV [7]
$N_0\beta$	-0.88 eV [7]

Table K.1: Band parameters, deformation potentials, dielectric constant and exchange integrals values for $Cd_{1-x}Mn_xTe$.

Bibliography

[1] R. A. Buhrman J. M. Daughton S. von Molnar M. L. Roukes A. Y. Chtchelkanova S. Wolf, D. D. Awschalom and D. M. Treger. Spintronics: A spin based electronics vision for the future. *Science*, 294(5546):1488, 2001.

[2] S Kreuzer, M Rahm, J Biberger, R Pulwey, J Raabe, D Schuh, W Wegscheider, and D Weiss. Ferromagnet semiconductor hybrid structures: Hall devices and tunnel junctions. *Physica E: Low-dimensional Systems and Nanostructures*, 16(1):137, 2003.

[3] M. N. Baibich, J. M. Broto, A. Fert, F. Nguyen Van Dau, F. Petroff, P. Etienne, G. Creuzet, A. Friederich, and J. Chazelas. Giant Magnetoresistance of (001)Fe/(001)Cr Magnetic Superlattices. *Phys. Rev. Lett*, 61(21):2472, 1988.

[4] H. Akinaga and H. Ohno. Semiconductor spintronics. *IEEE Transitions on Nanotechnology*, 1(1):19, 2002.

[5] K Sato and H Katayama-Yoshida. First principles materials design for semiconductor spintronics. *Semiconductor Science and Technology*, 17(4):367, 2002.

[6] Tatiana G. Rappoport, Mona Berciu, and Boldizsár Jankó. Effect of the Abrikosov vortex phase on spin and charge states in magnetic semiconductor-superconductor hybrids. *Phys. Rev. B*, 74(9):094502, 2006.

[7] J. K. Furdyna. Diluted magnetic semiconductors. *Journal of Applied Physics*, 64(4):R29, 1988.

[8] H. Ohno, A. Shen, F. Matsukura, A. Oiwa, A. Endo, S. Katsumoto, and Y. Iye. (Ga,Mn)As: A new diluted magnetic semiconductor based on GaAs. *Applied Physics Letters*, 69(3):363, 1996.

[9] H. Ohno. Making nonmagnetic semiconductors ferromagnetic. *Science*, 281(5379):951, 1998.

[10] J. K. Furdyna. Diluted magnetic semiconductors: An interface of semiconductor physics and magnetism (invited). *Journal of Applied Physics*, 53(11):7637, 1982.

[11] J. K. Furdyna J. Kossut. *Semiconductor and Semimetals vol. 25.* Academic press Inc, 1988.

[12] J.K. Furdyna, W. Giriat, D.F. Mitchell, and G.I. Sproule. The dependence of the lattice parameter and density of $Zn_{1-x}Mn_xTe$ on composition. *Journal of Solid State Chemistry*, 46(3):349, 1983.

[13] J. M. Hartmann, J. Cibert, F. Kany, H. Mariette, M. Charleux, P. Alleysson, R. Langer, and G. Feuillet. CdTe/MgTe heterostructures: Growth by atomic layer epitaxy and determination of MgTe parameters. *Journal of Applied Physics*, 80(11):6257, 1996.

[14] R. R. Galazka, Shoichi Nagata, and P. H. Keesom. Paramagnetic¯spin-glass¯antiferromagnetic phase transitions in $Cd_{1-x}Mn_xTe$ from specific heat and magnetic susceptibility measurements. *Phys. Rev. B*, 22(7):3344, 1980.

[15] J. K. Furdyna and N. Samarth. Magnetic properties of diluted magnetic semiconductors: A review (invited). *Journal of Applied Physics*, 61(8):3526, 1987.

[16] J. A. Gaj, R. R. Galazka, and M. Nawrocki. Giant exciton Faraday rotation in $Cd_{1-x}Mn_xTe$ mixed crystals. *Solid State Communications*, 25(3):193, 1978.

[17] M. Jaczynski, J. Kossut, and R. R. Galazka. Influence of Exchange Interaction on the Quantum Transport Phenomena in $Hg_{1-x}Mn_xTe$. *physica status solidi (b)*, 88(1):73, 1978.

[18] S. Lee, M. Dobrowolska, J. K. Furdyna, H. Luo, and L. R. Ram-Mohan. Magneto-optical study of interwell coupling in double quantum wells using diluted magnetic semiconductors. *Phys. Rev. B*, 54(23):16939, 1996.

[19] B. Kuhn-Heinrich, W. Ossau, E. Bangert, A. Waag, and G. Landwehr. Zeeman pattern of semimagnetic (CdMn)Te/(CdMg)Te quantum wells in inplane magnetic fields. *Solid State Communications*, 91(6):413, 1994.

[20] T. Stirner, S. Ahmed, and W.E. Hagston. Anisotropic magnetic field effects in diluted magnetic semiconductor quantum wells. *Journal of Crystal Growth*, 159(1-4):1027, 1996.

[21] Ji-Wei Wu, A. V. Nurmikko, and J. J. Quinn. Excitons in semimagnetic semiconductor quantum-well systems: Magnetic polaron effects. *Phys. Rev. B*, 34(2):1080, 1986.

[22] H. H. Cheng, R. J. Nicholas, M. J. Lawless, D. E. Ashenford, and B. Lunn. Magneto-optical studies of the type-I/type-II crossover and band offset in $ZnTe/Zn_{1-x}Mn_xTe$ superlattices in magnetic fields up to 45 T. *Phys. Rev. B*, 52(7):5269, 1995.

[23] B Kuhn-Heinrich, M Popp, W Ossau, E Bangert, A Waag, and G Landwehr. Magneto-optical study of heavy- and light-hole excitons in CdTe/(Cd,Mn)Te single quantum wells. *Semiconductor Science and Technology*, 8(7):1239, 1993.

[24] P Kacman. Spin interactions in diluted magnetic semiconductors and magnetic semiconductor structures. *Semiconductor Science and Technology*, 16(4):R25, 2001.

[25] Martin Kneip. *Magnetization Dynamics in Diluted Magnetic Semiconductor Heterostructures*. Grin Verlag, 2008.

[26] H. Ohno. Properties of ferromagnetic III-V semiconductors. *Journal of Magnetism and Magnetic Materials*, 200(1-3):110, 1999.

[27] Z. Wilamowski A. M. Werpachowska. RKKY coupling in diluted magnetic semiconductors. *Materials Science-Poland*, 24(3):675, 2006.

[28] C. Zener. Interaction between the d shells in the transition metals. *Phys. Rev.*, 81(3):440, 1951.

[29] C. Zener. Interaction between the d-Shells in the Transition Metals. III. Calculation of the Weiss Factors in Fe, Co, and Ni. *Phys. Rev.*, 83(2):299, 1951.

[30] R Winkler. *Spin orbit coupling effects in two dimensional electron and hole systems*. Springer-Verlag Berlin Heidelberg, 2003.

[31] S L Chuang. *Physics of optoelectronic devices*. John Wiley, 1995.

[32] Evan O. Kane. Band structure of indium antimonide. *Journal of Physics and Chemistry of Solids*, 1(4):249, 1957.

[33] J. M. Luttinger and W. Kohn. Motion of Electrons and Holes in Perturbed Periodic Fields. *Phys. Rev.*, 97(4):869, 1955.

[34] W.W Chow and S.W Koch. *Semiconductor laser fundamentals*. Springer, 1999.

[35] T. E. Ostromek. Evaluation of matrix elements of the 8×8 $\mathbf{k}\cdot\mathbf{p}$ Hamiltonian with $\mathbf{k}$-dependent spin-orbit contributions for the zinc-blende structure of GaAs. *Phys. Rev. B*, 54(20):14467, 1996.

[36] Fei Long, W. E. Hagston, P. Harrison, and T. Stirner. The structural dependence of the effective mass and Luttinger parameters in semiconductor quantum wells. *Journal of Applied Physics*, 82(7):3414, 1997.

[37] J. Los, A. Fasolino, and A. Catellani. Generalization of the $\mathbf{k}\cdot\mathbf{p}$ approach for strained layered semiconductor structures grown on high-index-planes. *Phys. Rev. B*, 53(8):4630, 1996.

[38] Craig Pryor. Eight-band calculations of strained InAs/GaAs quantum dots compared with one-, four-, and six-band approximations. *Phys. Rev. B*, 57(12):7190, 1998.

[39] Claudine Hermann and Claude Weisbuch. $\vec{k}\cdot\vec{p}$ perturbation theory in III-V compounds and alloys: a reexamination. *Phys. Rev. B*, 15(2):823, 1977.

[40] H. Mayer and U. Rössler. Spin splitting and anisotropy of cyclotron resonance in the conduction band of GaAs. *Phys. Rev. B*, 44(16):9048, 1991.

[41] G E Pikus G L Bir. *Symmetry and strain induced effects in semiconductors*. John Wiley, 1974.

[42] Calvin Yi-Ping Chao and Shun Lien Chuang. Spin-orbit-coupling effects on the valence-band structure of strained semiconductor quantum wells. *Phys. Rev. B*, 46(7):4110, 1992.

[43] Toshikazu Nishida Yongke Sun, Scott E. Thompson. *Strain effects in Semiconductors, Theory and Device Applications*. Springer New York, 2010.

[44] Shun Lien Chuang. Efficient band-structure calculations of strained quantum wells. *Phys. Rev. B*, 43(12):9649, 1991.

[45] Mi-Ra Kim, Cheol-Hoi Kim, and Baik-Hyung Han. Band-gap renormalization and strain effects in semiconductor quantum wells. *Physica B: Condensed Matter*, 245(1):45, 1998.

[46] Lucio Claudio Andreani, Alfredo Pasquarello, and Franco Bassani. Hole subbands in strained GaAs-$Ga_{1-x}Al_xAs$ quantum wells: Exact solution of the effective-mass equation. *Phys. Rev. B*, 36(11):5887, 1987.

[47] Mona Berciu and Boldizsár Jankó. Nanoscale Zeeman Localization of Charge Carriers in Diluted Magnetic Semiconductor-Permalloy Hybrids. *Phys. Rev. Lett*, 90(24):246804, 2003.

[48] P. Redlinski, T. G. Rappoport, A. Libal, J. K. Furdyna, B. Janko, and T. Wojtowicz. Optical response of a ferromagnetic-diluted magnetic semiconductor hybrid structure. *Applied Physics Letters*, 86(11):3, 2005.

[49] P. Redlinski, T. Wojtowicz, T. G. Rappoport, A. Libal, J. K. Furdyna, and B. Janko. Zero and one dimensional magnetic traps for quasiparticles in diluted magnetic semiconductors. *Phys. Rev. B*, 72(8):085209, 2005.

[50] Tatiana G. Rappoport Mona Berciu and Boldizsár Jankó. Manipulating spin and charge in magnetic semiconductors using superconducting vortices. *Nature*, 435:71, 2005.

[51] F. M. Peeters and A. Matulis. Quantum structures created by nonhomogeneous magnetic fields. *Phys. Rev. B*, 48(20):15166, 1993.

[52] J. A. K. Freire, A. Matulis, F. M. Peeters, V. N. Freire, and G. A. Farias. Confinement of two-dimensional excitons in a nonhomogeneous magnetic field. *Phys. Rev. B*, 61(4):2895, 2000.

[53] S. J. Bending, K. von Klitzing, and K. Ploog. Weak localization in a distribution of magnetic flux tubes. *Phys. Rev. Lett*, 65(8):1060, 1990.

[54] R. P. Cowburn, D. K. Koltsov, A. O. Adeyeye, M. E. Welland, and D. M. Tricker. Single domain circular nanomagnets. *Phys. Rev. Lett*, 83(5):1042, 1999.

[55] Aharoni A. *Introduction to the theory of Ferromagnetism.* Oxford Science Publications, 2nd edition, 2000.

[56] Marcus Steiner. *Micromagnetism and Electrical Resistance of Ferromagnetic Electrodes for Spin-Injection Devices.* Cuvillier Verlag, 2004.

[57] Roman Antos, YoshiChika Otani, and Junya Shibata. Magnetic vortex dynamics. *Journal of the Physical Society of Japan*, 77(3):031004, 2008.

[58] R. Hassdorf K. Shigeto T. Shinjo, T. Okuno and T. Ono. Magnetic Vortex Core Observation in Circular Dots of Permalloy. *Science*, 289(5481):224432, 2000.

[59] J. Raabe, R. Pulwey, R. Sattler, T. Schweinbock, J. Zweck, and D. Weiss. Magnetization pattern of ferromagnetic nanodisks. *Journal of Applied Physics*, 88(7):4437, 2000.

[60] M. Bode O. Pietzsch M. Morgenstern R. Wiesendanger A. Wachowiak, J. Wiebe. Direct observation of internal spin-structure of magnetic vortex cores. *Science*, 298(5593):577, 2002.

[61] A. Hubert and R. Schäfer. *Magnetic Domains*. Springer- Verlag, Berlin, 1998.

[62] J. D. Jackson. *Classical Electrodynamics 3rd ed*. Wiley, New York, 1998.

[63] I. M. Ryzhik I. S. Gradshtein. *Tables of Integrals, Series and Products*. Academic Press, New York, 1980.

[64] Amikam Aharoni. Upper bound to a single-domain behavior of a ferromagnetic cylinder. *Journal of Applied Physics*, 68(6):2892, 1990.

[65] N.A. Usov and S.E. Peschany. Magnetization curling in a fine cylindrical particle. *Journal of Magnetism and Magnetic Materials*, 118(3):L290, 1993.

[66] S.-K. Chang, A. V. Nurmikko, J.-W. Wu, L. A. Kolodziejski, and R. L. Gunshor. Band offsets and excitons in CdTe/(Cd,Mn)Te quantum wells. *Phys. Rev. B*, 37(3):1191, 1988.

[67] Wu Hui-zhen, Yang Ai-ling, Wu Jian-zhong, and Li Zheng-zhi. Exciton Properties of Diluted CdTe/CdMnTe Quantum Wells. *Chinese Physics Letters*, 15(10):734, 1998.

[68] S. R. Jackson, J. E. Nicholls, W. E. Hagston, P. Harrison, T. Stirner, J. H. C. Hogg, B. Lunn, and D. E. Ashenford. Magneto-optical study of excitonic binding energies, band offsets, and the role of interface potentials in CdTe/$Cd_{1-x}Mn_xTe$ multiple quantum wells. *Phys. Rev. B*, 50(8):5392, 1994.

[69] P.Harrison. *Quantum wells, wires, and dots*. Wiley, 2009.

[70] K.K. Bajaj. Use of excitons in materials characterization of semiconductor system. *Materials Science and Engineering: R*, 34(2):59, 2001.

[71] R. C. Miller, D. A. Kleinman, W. T. Tsang, and A. C. Gossard. Observation of the excited level of excitons in GaAs quantum wells. *Phys. Rev. B*, 24(2):1134, 1981.

[72] U. Ekenberg and M. Altarelli. Exciton binding energy in a quantum well with inclusion of valence-band coupling and nonparabolicity. *Phys. Rev. B*, 35(14):7585, 1987.

[73] S B Lev, V I Sugakov, and G V Vertsimakha. Direct and indirect excitons in diluted magnetic semiconductor double-quantum-well structures in external magnetic fields. *Journal of Physics: Condensed Matter*, 16(23):4033, 2004.

[74] V I Sugakov and G V Vertsimakha. Magnetic field dependence of the exciton bandwidth in diluted magnetic semiconductors with quantum wells. *Journal of Physics: Condensed Matter*, 13(24):5635, 2001.

[75] P J Klar, J R Watling, D Wolverson, J J Davies, D E Ashenford, and B Lunn. Magnetic-field induced type I to type II transition in multiple quantum well samples. *Semiconductor Science and Technology*, 12(10):1240, 1997.

[76] William T. Vetterling Brian P. Flannery William H. Press, Saul A. Teukolsky. *Numerical Recipes in Fortran 90*. Cambridge University Press, 1996.

[77] Chikara Onodera, Tadayoshi Shoji, Yukio Hiratate, and Tsunemasa Taguchi. Proposal for $ZnS/Mg_xBe_yZn_{1-x-y}S$ Quantum Wells. *Japanese Journal of Applied Physics*, 47(6):4602, 2008.

[78] Ronald L. Greene, Krishan K. Bajaj, and Dwight E. Phelps. Energy levels of Wannier excitons in $GaAs - Ga_{1-x}Al_xAs$ quantum-well structures. *Phys. Rev. B*, 29(4):1807, 1984.

[79] Ronald L. Greene and K.K. Bajaj. Binding energies of wannier excitons in GaAs-$Ga_{1-x}Al_xAs$ quantum well structures. *Solid State Communications*, 45(9):831, 1983.

[80] J. A. K. Freire, F. M. Peeters, A. Matulis, V. N. Freire, and G. A. Farias. Fine structure of excitons in a quantum well in the presence of a nonhomogeneous magnetic field. *Phys. Rev. B*, 62(11):7316, 2000.

[81] A. B. Dzyubenko. Intraexcitonic transitions in two-dimensional systems in a high magnetic field. *Journal of Experimental and Theoretical Physics Letters*, 66(9):617, 1997.

[82] Z. G. Koinov, G. Collins, and M. Mirassou. Confinement of magnetoexcitons in GaAs quantum well with a superconducting disk on top of the well. *physica status solidi (b)*, 243(15):4046, 2006.

[83] G.A. Farias J.A.K. Freire, V.N. Freire and F.M. Peeters. Exciton trapping in a periodically modulated magnetic field. *Brazilian Journal of Physics*, 32(2):310, 2002.

[84] J A K Freire, F M Peeters, V N Freire, and G A Farias. Exciton trapping in magnetic wire structures. *Journal of Physics: Condensed Matter*, 13(14):3283, 2001.

[85] L. P. Gor'kov and I. E. Dzyaloshinsky. *Zh. Eksp. Teor. Fiz*, 53:717, 1967.

[86] Z. G. Koinov, P. Nash, and J. Witzel. Bethe-salpeter equation for quantum-well exciton states in an inhomogeneous magnetic field. *Phys. Rev. B*, 67(15):155318, 2003.

[87] A.B. Dzyubenko. Intraexcitonic transitions in two-dimensional systems in a high magnetic field. *Journal of Experimental and Theoretical Physics Letters*, 66(9):617, 1997.

[88] X. L. Yang, S. H. Guo, F. T. Chan, K. W. Wong, and W. Y. Ching. Analytic solution of a two-dimensional hydrogen atom. I. Nonrelativistic theory. *Phys. Rev. A*, 43(3):1186, 1991.

[89] L. Schiff. *Quantum Mechanics*. McGraw-Hill Education, 1968.

[90] Y C Lee, W N Mei, and K C Liu. A novel perturbative-variational approach and its application to the impurity states in anisotropic crystals. *Journal of Physics C: Solid State Physics*, 15(14):L469, 1982.

[91] Y. C. Lee and D. L. Lin. Wannier excitons in a thin crystal film. *Phys. Rev. B*, 19(4):1982, 1979.

[92] Tsin-Fu Jiang. An alternative approach to exciton binding energy in a GaAs-Al_xGa_{1-x} as quantum well. *Solid State Communications*, 50(7):589, 1984.

[93] Spiros V. Branis and K. K. Bajaj. Calculation of the exciton binding energies in type-II GaAs/AlAs quantum-well structures: Application of the perturbation-variational expansion method. *Phys. Rev. B*, 45(11):6271, 1992.

[94] Bao-Hua Wei, Youyan Liu, Shi-Wei Gu, and Kin-Wah Yu. Exciton in a quantum-well structure for arbitrary magnetic field strengths. *Phys. Rev. B*, 46(7):4269, 1992.

[95] M. Abramowitz and I. A. Stegun. *Handbook of Mathematical Functions, Chap. 12, 496–502*. Dover, New York, 1965.

[96] Der-San Chuu, Win-Long Won, and Jui-Hsiang Pei. Longitudinal-optical-phonon effects on the exciton binding energy in a semiconductor quantum well. *Phys. Rev. B*, 49(20):14554, 1994.

[97] H. W. van Kesteren, E. C. Cosman, W. A. J. A. van der Poel, and C. T. Foxon. Fine structure of excitons in type-II GaAs/AlAs quantum wells. *Phys. Rev. B*, 41(8):5283, 1990.

[98] I. A. Yugova, I. Ya. Gerlovin, V. G. Davydov, I. V. Ignatiev, I. E. Kozin, H. W. Ren, M. Sugisaki, S. Sugou, and Y. Masumoto. Fine structure and spin quantum beats in InP quantum dots in a magnetic field. *Phys. Rev. B*, 66(23):235312, 2002.

[99] Hongliang Jiang, Duanzheng Yao, Xiaobo Feng, and Shaohua Gong. Spin quantum beats of bright and dark excitonic states in neutral InAs quantum dots. *Journal of Physics: Condensed Matter*, 19(34):346221, 2007.

[100] E. Blackwood, M. J. Snelling, R. T. Harley, S. R. Andrews, and C. T. B. Foxon. Exchange interaction of excitons in GaAs heterostructures. *Phys. Rev. B*, 50(19):14246, 1994.

[101] Alain Nogaret. Electron dynamics in inhomogeneous magnetic fields. *Journal of Physics: Condensed Matter*, 22(25):253201, 2010.

[102] I. S. Ibrahim and F. M. Peeters. Two-dimensional electrons in lateral magnetic superlattices. *Phys. Rev. B*, 52(24):17321, 1995.

[103] D. A. Broido and L. J. Sham. Valence-band coupling and fano-resonance effects on the excitonic spectrum in undoped quantum wells. *Phys. Rev. B*, 34(6):3917, 1986.

[104] K S Chan. The effects of the hole subband mixing on the energies and oscillator strengths of excitons in a quantum well. *Journal of Physics C: Solid State Physics*, 19(6):L125, 1986.

[105] Gerrit E. W. Bauer and Tsuneya Ando. Exciton mixing in quantum wells. *Phys. Rev. B*, 38(9):6015, 1988.

[106] Tohya Hiroshima. Exciton states in strained quantum wells. *Phys. Rev. B*, 36(8):4518, 1987.

[107] M G Burt. An exact formulation of the envelope function method for the determination of electronic states in semiconductor microstructures. *Semiconductor Science and Technology*, 3(8):739, 1988.

[108] M G Burt. Fundamentals of envelope function theory for electronic states and photonic modes in nanostructures. *Journal of Physics: Condensed Matter*, 11(9):53, 1999.

[109] M. G. Burt. Direct derivation of effective-mass equations for microstructures with atomically abrupt boundaries. *Phys. Rev. B*, 50(11):7518, 1994.

[110] M G Burt. The justification for applying the effective-mass approximation to microstructures. *Journal of Physics: Condensed Matter*, 4(32):6651, 1992.

[111] Bradley A. Foreman. Effective-mass hamiltonian and boundary conditions for the valence bands of semiconductor microstructures. *Phys. Rev. B*, 48(7):4964, 1993.

[112] Bradley A. Foreman. Analytic model for the valence-band structure of a strained quantum well. *Phys. Rev. B*, 49(3):1757, 1994.

[113] Bradley A. Foreman. Exact effective-mass theory for heterostructures. *Phys. Rev. B*, 52(16):12241, 1995.

[114] P. Kossacki, J. Cibert, D. Ferrand, Y. Merle d'Aubigné, A. Arnoult, A. Wasiela, S. Tatarenko, and J. A. Gaj. Neutral and positively charged excitons: A magneto-optical study of a p -doped $Cd_{1-x}Mn_xTe$ quantum well. *Phys. Rev. B*, 60(23):16018, 1999.

[115] Calvin Yi-Ping Chao and Shun Lien Chuang. Momentum-space solution of exciton excited states and heavy-hole-light-hole mixing in quantum wells. *Phys. Rev. B*, 48(11):8210, 1993.

[116] A. A. Sirenko, T. Ruf, M. Cardona, D. R. Yakovlev, W. Ossau, A. Waag, and G. Landwehr. Electron and hole g factors measured by spin-flip Raman scattering in $CdTe/Cd_{1-x}Mg_xTe$ single quantum wells. *Phys. Rev. B*, 56(4):2114, 1997.

[117] M. P. Halsall, S. V. Railson, D. Wolverson, J. J. Davies, B. Lunn, and D. E. Ashenford. Spin-flip Raman scattering in $CdTe/Cd_{1-x}Mn_xTe$ multiple quantum wells: A model system for the study of electron-donor binding in semiconductor heterostructures. *Phys. Rev. B*, 50(16):11755, 1994.

[118] D. A. Broido and L. J. Sham. Effective masses of holes at GaAs-AlGaAs heterojunctions. *Phys. Rev. B*, 31(2):888, 1985.

[119] M. Abolfath, T. Jungwirth, J. Brum, and A. H. MacDonald. Theory of magnetic anisotropy in $III_{1-x}Mn_xV$ ferromagnets. *Phys. Rev. B*, 63(5):054418, 2001.

[120] Abraham Moyses Cohen and Gilmar Eugenio Marques. Electronic structure of zinc-blende-structure semiconductor heterostructures. *Phys. Rev. B*, 41(15):10608, 1990.

[121] B. Kuhn-Heinrich, W. Ossau, T. Litz, A. Waag, and G. Landwehr. Determination of the band offset in semimagnetic CdTe/$Cd_{1-x}Mn_x$Te quantum wells: A comparison of two methods. *Journal of Applied Physics*, 75(12):8046, 1994.

[122] Jr. R. L. Harper, R. N. Bicknell, D. K. Blanks, N. C. Giles, J. F. Schetzina, Y. R. Lee, and A. K. Ramdas. Excited confined quantum states in CdMnTe-CdTe superlattices. *Journal of Applied Physics*, 65(2):624, 1989.